

NANOSCALE OPTICAL AND CORRELATIVE MICROSCOPIES FOR  
QUANTITATIVE CHARACTERIZATION OF DNA NANOSTRUCTURES

by

Christopher Michael Green



A dissertation

submitted in partial fulfillment

of the requirements for the degree of

Doctor of Philosophy in Materials Science and Engineering

Boise State University

December 2019

© 2019

Christopher Michael Green

**ALL RIGHTS RESERVED**



## DEDICATION

This dissertation is dedicated to my wife and my parents, without whose support this would not have been possible.

## ACKNOWLEDGMENTS

During my time at Boise State University, I have had the pleasure of working with many incredible individuals who have contributed immensely to my experience, and without whom this work would not have been possible. I am truly grateful for each and every experience, interaction, and challenge that I have been afforded, all of which contributed to my academic and personal growth. To all my friends and colleagues, thank you for enriching my life and my experience so fully.

I would like to thank my advisors, Dr. Wan Kuang and Dr. Will Hughes for the influence they have had. During my graduate career, Wan has taught me to be both confident in and critical of my work. In research, he allowed me much freedom; while this sometimes led to distractions, dead ends, and unfinished work, it was fundamental to my growth as a scientist and led me to discover much about myself. Wan taught me the importance of continually pursuing new skills and knowledge, and I hope to live by that in the future. Dr. Hughes has been a huge source of encouragement, support, and advice throughout my graduate career. By example, and through many discussions, he has taught me to always strive to become the best version of yourself and to never lose sight of the big picture. In addition, his strong emphasis on the importance of maintaining a broad perspective on research, the scientific community, and directions for future work, both short and long term, will have a lasting impact on my future endeavors.

I must also thank Dr. Elton Graugnard for his support and guidance. Elton has always been a strong source of motivation, as well as a steadfast advocate of and contributor to the

work described in this dissertation. I cannot fully express my appreciation for his openness to discussion any time I needed advice, suggestions, or feedback on research or any ideas that struck me. Our discussions, and particularly his contributions, were fundamental to much of the work described here. Too often I failed to recognize the merit of his suggestions until long after our conversations, and in hindsight I thank him for his patience and constant support.

I would like to express my gratitude to Chad Watson, Jessica Economy, Dr. Natalya Hallstrom, Dr. Reza Zadegan, Dr. Paul Davis, Dr. William Knowlton, and Dr. Hao Chen for their support and guidance throughout my graduate career. Each has contributed to my experience in unique and fundamental ways, and I cannot thank them enough for all that they have done.

Lastly, I'd like to recognize all the graduate students and post-docs that I have had the pleasure of befriending during my time in Boise. I cannot imagine this experience without them, and I am grateful for all the amazing conversations, social interactions, and support that they have provided me. I am truly fortunate to have made such good friends and to work alongside such talented individuals.

## ABSTRACT

Methods to engineer nanomaterials and devices with uniquely tailored properties are highly sought after in fields such as manufacturing, medicine, energy, and the environment. The macromolecule deoxyribonucleic acid (DNA) enables programmable self-assembly of nanostructures with near arbitrary shape and size and with unprecedented precision and accuracy. Additionally, DNA can be chemically modified to attach molecules and nanoparticles, providing a means to organize active materials into devices with unique or enhanced properties. One particularly powerful form of DNA-based self-assembly, DNA origami, provides robust structures with the potential for nanometer-scale resolution of addressable sites. DNA origami are assembled from one large DNA "scaffold" strand and many unique, short "staple" strands; each staple programmatically binds the scaffold at several distant domains, and the coordinated interactions of many staples with the scaffold act to fold the scaffold into a desired shape. The utility of DNA origami has been demonstrated through multiple applications, such as plasmonic and photonic devices, electronic device patterning, information storage, drug delivery, and biosensors. Despite the promise of DNA nanotechnology, few products have successfully translated from the laboratory to industry.

Achieving high yield and high-precision synthesis of stable DNA nanostructures is one of the biggest challenges to applications of DNA nanostructures. For adoption in manufacturing, methods to measure and inspect assembled structures (i.e. metrology) are essential. Common high-resolution imaging techniques used to characterize DNA

nanostructures, such as atomic force microscopy and transmission electron microscopy, cannot facilitate high-throughput characterization, and few studies have been directed towards the development of improved methods for nanoscale metrology. DNA-PAINT super-resolution microscopy enables high-resolution, multiplexed imaging of reactive sites on DNA nanostructures and offers the potential for inline optical metrology. In this work, nanoscale metrologies utilizing DNA-PAINT were developed for DNA nanostructures and applied to characterize DNA origami arrays and single site defects on DNA origami.

For metrology of DNA origami arrays, an embedded, multiplexed optical super-resolution methodology was developed to characterize the periodic structure and defects of two-dimensional arrays. Images revealed the spatial arrangement of structures within the arrays, internal array defects, and grain boundaries between arrays, enabling the reconstruction of arrays from the images. The nature of the imaging technique is also highly compatible with statistical methods, enabling rapid statistical analysis of synthesis conditions. To obtain a greater understanding of DNA origami defects at the scale of individual strands, correlative super-resolution and atomic force microscopies were enabled through the development of a simple and flexible method to bind DNA origami directly to cover glass, simultaneously passivating the surface to single-stranded DNA. High-resolution, correlative microscopy was performed to characterize DNA origami, and spatial correlation in super-resolution optical and topographic images of 5 nm was achieved, validating correlative microscopy for single strand defect metrology. Investigations of single strand defects showed little correlation to structural defects on DNA origami, revealing that most site defects occur on strands that are present in the

structure, contrary to prior reports. In addition, the results suggest that the structural stability of DNA origami was decreased by DNA-PAINT imaging.

The presented work demonstrated the development and application of advanced characterization techniques for DNA nanostructures, which will accelerate fundamental research and applications of DNA nanotechnology.

## TABLE OF CONTENTS

DEDICATION .....	iv
ACKNOWLEDGMENTS .....	v
ABSTRACT.....	vii
TABLE OF CONTENTS.....	x
LIST OF TABLES .....	xiii
LIST OF FIGURES .....	xiv
LIST OF ABBREVIATIONS.....	xxix
LIST OF SYMBOLS .....	xxxv
CHAPTER ONE: INTRODUCTION.....	1
1.1 DNA Nanotechnology .....	1
1.2 Super-Resolution Optical Microscopy.....	9
1.3 Atomic Force Microscopy .....	14
1.4 References.....	17
CHAPTER TWO: METROLOGY OF DNA ARRAYS BY SUPER-RESOLUTION MICROSCOPY.....	25
2.1 Abstract.....	27
2.2 Introduction.....	27
2.3 Experimental.....	29
2.3.1 Crystal-PAINT Imaging.....	29
2.4 Results and Discussion.....	31

2.4.1 2x2-Tile Array Imaging .....	31
2.4.2 Unbounded Array Imaging .....	33
2.4.3 Analysis of 2x2-Tile Arrays.....	36
2.5 Conclusions.....	39
2.6 Acknowledgements.....	39
2.7 References.....	40
2.8 Supporting Information.....	43
2.8.1 Materials and Methods.....	43
2.8.2 Counting method and statistics .....	48
2.8.3 Supporting Figures.....	49
<b>CHAPTER THREE: INVESTIGATIONS OF STRAND DEFECTS IN DNA ORIGAMI WITH CORRELATIVE DNA-PAINT AND ATOMIC FORCE MICROSCOPY .....</b>	<b>73</b>
3.1 Introduction.....	74
3.2 Results.....	75
3.2.1 Cross-compatible Substrate for Correlative Imaging .....	75
3.2.2 Correlative DNA-PAINT/AFM Microscopy.....	77
3.2.3 Correlative Defect Metrology .....	79
3.3 Conclusion .....	84
3.4 References.....	85
3.5 Supporting Information.....	92
3.5.1 Materials and Methods.....	92
3.5.2 Characterization and Analysis .....	101
3.5.3 Supplemental Figures.....	111
3.5.4 Supplemental Tables .....	137

3.5.5 References.....	144
CHAPTER FOUR: SUMMARY AND FUTURE WORK .....	145

## LIST OF TABLES

Table 2.1	Thermocycler recipe for cross-shaped DNA origami tile synthesis. ....	44
Table 2.2	Individual tile counting statistics .....	51
Table 2.3	Peak fitting statistics for unconfined tile arrays.....	56
Table 2.4	Self-limiting 2x2-tile array defect counting statistics.....	58
Table 2.6	Strand sequences for cross-shaped DNA origami tile (body strands) .....	64
Table 2.7	Strand sequences for cross-shaped DNA origami tile (edge strands).....	70
Table 2.8	Strand sequences for DNA-PAINT imager strands .....	72
Table 3.1	List of internal staples for DNA origami cross-tile. ....	137
Table 3.2	List of internal docking staples for DNA origami cross-tile.....	141
Table 3.3	List of edge staples for DNA origami cross-tile. ....	142
Table 3.4	List of modified oligomers for imaging and filtration. ....	143
Table 3.5	Thermocycler recipe for DNA origami synthesis. ....	143

## LIST OF FIGURES

- Figure 1.1 The scale of natural and man-made objects, from small to nanoscale ( $10^{-2}$  to  $10^{-10}$  m). Adapted from reference.<sup>1</sup> ..... 2
- Figure 1.2 Examples of the self-assembly of organic molecules. (a) Block-copolymer self-assembly can be combined with lithographically-defined guide patterns to produce nanoscale patterns with long-range coherence.<sup>10</sup> (b) Colloids with domains of varying polarity self-assemble into various structures.<sup>11</sup> (c) Nanoparticles functionalized with ssDNA self-assemble in a manner resembling atomic crystals.<sup>12</sup> (d) Nanostructures can be self-assembled from DNA into structures with nearly arbitrary size and shape. .... 3
- Figure 1.3 The progression of DNA nanotechnology. Structurally rigid DNA constructs were first demonstrated by Mirkin's group (nanoparticle-templated DNA bonds, left) and Seeman's group (hybridization-based DNA bonds, right) in 1996. The field of DNA nanotechnology has greatly expanded since its origination, and DNA has proven to be powerful material for programmable, nanoscale control of self-assembly. Figure reproduced from Jones et al.<sup>12</sup> ..... 5
- Figure 1.4 Gold nanoparticle (AuNP) plasmonic devices scaffolded by DNA origami. (a) AFM image of AuNPs and quantum dots arranged on DNA origami nanotubes.<sup>28</sup> (b) TEM images and predicted geometries of helical AuNP assemblies for plasmonic devices with distinct chirality, constructed with 10 nm (top) and 16 nm (bottom) AuNPs.<sup>29</sup> (c) Geometric model and TEM image of a plasmonic toroidal metamolecule constructed of four DNA origami and 24 AuNPs. The toroidal metamolecules showed strong chiroptical response and were compatible with uniform axial alignment on surfaces.<sup>30</sup> (d) Schematic illustration and TEM image of AuNR helical superstructures scaffolded by DNA origami. The TEM image shows a right-handed plasmonic structure consisting of 16 AuNRs and DNA origami (+/- 1 origami).<sup>31</sup> Figure reproduced from references.<sup>28-31</sup> ..... 6
- Figure 1.5 Hierarchical assembly of discrete DNA origami arrays. (a) Strand-level, reduced complexity schematic of a square DNA origami tile. (b) Tile schematic depicting reactive edge sites and the positions of hairpins extended from the origami. (c) Tile array schematic depicting an assembled array composed of 4x4 unique tiles with hairpins extended to depict the Mona Lisa upon proper array formation. (d)-(f) AFM images of 2x2, 4x4, and 8x8 tile arrays assembled using the programmed assembly method.

	Each size of array has individual origami with hairpins extended from the surface to depict the Mona Lisa, as shown in (c). Figure reproduced from Tikhomirov et al. <sup>43</sup> .....	8
Figure 1.6	Super-resolution with single molecule localization microscopy. An averaged fluorescence image is provided to represent optical imaging with all fluorophores emitting simultaneously. With single molecule localization microscopy, emitters are spatially isolated by spreading observations out over time. Within individual images, single emitters are identified and fitted with a PSF to approximate the sub-pixel location of each emitter. During imaging, thermal drift results in lateral shifts of the imaging frame and is corrected using fiducial markers or correlational methods. Finally, a high-resolution image is rendered using the sub-pixel locations of all identified emitters.....	12
Figure 1.7	Atomic Force Microscopy. (a) Simplified schematic of an AFM and sample. As the tip is raster scanned across the surface, variations in the sample topography cause the tip and cantilever to be deflected and is observed as movement of a laser spot on a photodetector. (b) SEM images of AFM cantilever (i) and AFM tip (ii). Figure reproduced from reference. <sup>58</sup> .....	16
Figure 2.1	(a) Schematic depicting the cross-shaped DNA origami tiles used for Xtal-PAINT. Each set of sticky-ends on tile arms contain two 8 nucleotide (nt) defect labels (orange strands, M1) and six 5 nt sticky-ends (black strands). Six 8 nt docking sites extend from the center of the top of each tile (blue strands, M2). The lattice sites are aligned parallel to the central indent of the tile to delineate individual tile orientation for Xtal-PAINT imaging. Two biotinylated strands extend from the bottom of each tile arm (green circles) for immobilization to avidin-functionalized glass substrates. (b) Schematic of ideal sticky-end hybridization between A and B tiles. Bound tiles within an array are rotated 90° relative to neighboring tiles, which can be observed by the orientation of the lattice sites in Xtal-PAINT images. As shown in the magnified view of hybridization between A and B tile sticky-ends, all but 3 nt of the defect labels are bound, deactivating the strands as docking sites. (c) Xtal-PAINT and (d) AFM images of individual tiles corresponding to the tile schematics in (a). Scale bars, 50 nm. (e) Schematic of a 2x2-tile array depicting imager strand docking to unbound defect labels. ....	30
Figure 2.2	(a) Xtal-PAINT images of a single tile, 2-tile array, 3-tile array, and 2x2-tile array immobilized on glass by protein binding, with lattice sites (blue) and defect labels (yellow). (b) Schematics of the tiles and arrays deduced from the corresponding Xtal-PAINT images in (a) with defect labels (yellow) and lattice sites (blue). (c) AFM height images of tiles and arrays on mica, analogous to the structures depicted in (a). Scale bars, 50 nm. AFM height scale bar, 4 nm. ....	32

- Figure 2.3 Xtal-PAINT image of an unbounded DNA origami array. (a) Image of lattice sites revealing the array periodicity, (b) defect label image revealing the array perimeter and missing tiles, and (c) combined images of a tile array resolved by Xtal-PAINT. Slight misalignment of the lattices in the arrays results in grain boundaries in the defect label image, suggesting that the large array coalesced from smaller tile arrays. Tile array models were deduced from the Xtal-PAINT images and overlaid on the images in the lower half of the figure. Lattice misalignment and grain boundaries are accounted for by modeling the structure as three arrays distinguished by color (red, orange, and yellow grids). Mean localization precision for defect label and lattice images were  $8.5 \pm 5.0$  nm and  $10.4 \pm 6.1$  nm, respectively. Scale bar, 500 nm..... 34
- Figure 2.4 Xtal-PAINT image of unbounded tile arrays. (a) Combined defect label (yellow) and lattice (blue) images of tile arrays annealed for 24 hours near 38 °C. The four largest arrays are identified in the image by i-iv. (b) Magnified images of the tile arrays corresponding to i-iv in a. (i) Tile array (also shown in Figure 3) with dimensions of approximately  $1 \times 1 \mu\text{m}^2$ . Within the array, missing sites suggest tile vacancies. (ii) and (iii) Small tile arrays of  $\sim 0.5 \times 0.5 \mu\text{m}^2$  (iv) Large tile array that appears to extend out of the focal plane and TIRF illumination field, potentially caused by curvature induced by crystallization. (c) Radial distribution function of the full lattice image with peak at 87.4 nm, corresponding to the nearest neighbor distance between hybridized tiles. Higher order peaks were observed at 123 nm, 195 nm, and 275 nm, corresponding to the 2nd, 4th, and 7th nearest neighbor distances, respectively. Mean localization precision for defect label and lattice images were  $8.5 \pm 5.0$  nm and  $10.4 \pm 6.1$  nm, respectively. Scale bars, 1  $\mu\text{m}$ . ..... 35
- Figure 2.5 Quantitative analysis of 2x2-tile array defect label images. (a) Histograms displaying the results of hybridization defect counting for 2x2-tile arrays annealed at 25°C, 30°C, and 35°C. The legend at top indicates the structures analyzed to determine the probabilities of hybridization defects. Binomial distributions were generated from the data to calculate the probability of hybridization defects  $p_d$  for bound tile arms.  $p_d$  was observed to decrease as the temperature of anneal was increased. (b) Experimental and fitted  $g(r)$  for defect label images of 2x2-tile arrays annealed at 25 °C, 30 °C, and 35 °C. The first three peaks are identified with a 2x2-tile array model. The fitted  $g(r)$  were generated by spectral decomposition of the experimental distributions into a linear combination of the single tile ( $X_1$ ), 2-tile array ( $X_2$ ), 3-tile array ( $X_3$ ), and 2x2-tile array ( $X_4$ ) spectra.  $\text{Fit} = a_1X_1 + a_2X_2 + a_3X_3 + a_4X_4$ , where  $a_1 - a_4$  represent the fraction of tiles in each size of array out of the total number of tiles. For the fits of the 25 °C, 30 °C, and 35 °C distributions, the adjusted R-square (adj.  $R^2$ ) values were 0.614, 0.722, and 0.926, respectively. .... 37

- Figure 2.6 Strand diagram for cross-shaped DNA origami A-tile. Strand diagram exported from caDNAno and altered to depict modifications to the tile for Xtal-PAINT imaging and tile array formation. Individual strand sequences and imager strand sequences can be found in Tables 2.1-3. Original design and naming convention for individual strands were adopted from Liu et al. .... 49
- Figure 2.7 Schematic depicting step-wise Xtal-PAINT imaging. (a) Schematic depicting defect label imaging of tile arrays bound to glass coverslip by biotin-avidin binding, with 3 nM imager strand M1' in solution. Biotinylated bovine serum albumin (BSA-Biotin) was used to functionalize the surface and immobilize tile structures by protein binding. (b) Rinse to remove imager strand M1' and deactivate remaining strands with 10 nM M1\* imager passivation strands. Imager passivation strands were observed to effectively deactivate imager strands even when added directly to the imaging solution. (c) Lattice site imaging with 3 nM imager strand M2'. All buffer solutions contain 0.5x TBE 18mM MgCl<sub>2</sub>, and 15,000 frames were captured at 6.66 Hz during each imaging step. .... 50
- Figure 2.8 Xtal-PAINT and AFM images of individual tiles. (a,b) For A-tiles and B-tiles imaged by Xtal-PAINT, probability histograms for the number of defect label sites counted per tile are shown (grey bars), where p is the probability of resolving defect label sites on an individual tile arm, and N is the total number of tiles counted. Binomial distributions (red) were generated from the results of counting to calculate p given that each tile has four arms. The data for individual tile counting statistics can be found in Table 2.2. (c) Xtal-PAINT image of individual B-tiles displaying defect labels (yellow) and lattice sites (blue). Scale bar, 500 nm. (d) AFM image of individual B-tiles on mica, imaged in fluid (0.5x TBE with 12 mM MgCl<sub>2</sub> and 2mM NiCl<sub>2</sub>). Image dimensions, 500 nm x 500 nm. To reduce homogeneous interactions between tiles, tile solutions were heated to 30 °C prior to deposition in fluid wells and on mica. .... 51
- Figure 2.9 Self-limiting 2x2-tile array design and Xtal-PAINT images. (a) and (b) Schematics of A-tile and B-tile, respectively, for self-limiting 2x2-tile arrays. Sticky-ends from two arms of each tile were replaced with 3 nt poly-Thymine extensions to deactivate the arms for sticky-end hybridization. Defect label strands on the passivated arms were replaced with modified defect label strands that lack 5' sticky-ends. (c) Xtal-PAINT image of 2x2-tile arrays annealed at 35 °C, displaying defect labels (yellow) and lattice sites (blue). Individual tiles, 2-tile, 3-tile, and 2x2-tile arrays were resolved in the image. Scale bar, 1 μm. .... 52
- Figure 2.10 Xtal-PAINT and AFM images of unconstrained tile arrays. (a) and (b) Schematics of A-tile and B-tile, respectively, for unconstrained tile arrays. Defect labels and sticky-ends reside on the outermost helices of each tile

arm, and the central helices of each arm were passivated to blunt-end stacking interaction by 3 nt poly-Thymine extensions. (c) and (d) Xtal-PAINT and AFM image of unconstrained tile arrays on a coverslip and on mica, respectively. In the Xtal-PAINT image, large tile structures were observed that appear to consist of several overlapping tile arrays, consistent with structures observed in AFM images of tile arrays on mica. Scale bars, 1  $\mu\text{m}$ . ..... 53

Figure 2.11 Xtal-PAINT lattice images of large tile arrays with curvature. Inverted grayscale Xtal-PAINT lattice images of large tile arrays that were unable to flatten on the surface, indicated by indistinct, blurred regions of the array and/or curved lattice site paths. Blurring was observed in all of the arrays due to imager strand binding to lattice sites located outside of the focal plane. This effect was rarely observed in tile arrays smaller than 1  $\mu\text{m}$  x 1  $\mu\text{m}$ , though it is unlikely that the curvature observed in large arrays was caused by global curvature since no tube-like structures were observed. Rather, tile arrays were unable to relax or flatten on the surface due to immobilization by biotin-avidin binding. Large tile arrays are more likely to experience large fluctuations away from planarity due to local fluctuations of the solution, and any deformation that occurs in tile arrays while binding to the surface may be trapped in the structure. Scale bar, 1  $\mu\text{m}$ . ..... 54

Figure 2.12 Analysis of cross-shaped DNA origami tile dimensions. (a) and (b) Topographic profiles of a cross-shaped DNA origami tile in the directions perpendicular to and parallel to the central indent of the tile, respectively. The dimensions of the tile along both directions are approximately 100 nm, in agreement with the dimensions reported by Liu et. al. Scale bars, 50 nm. AFM height color bar, 5.5 nm. (c) Cando-generated model of the cross-shaped DNA origami tile. The contraction in the dimensions of the Cando model due to curvature and twist were calculated by the difference between the path length of the helices and the straight-line distance between each end of a tile arm. The observed contraction in the length of the tile arm was approximately 12%. (d) Radial distribution function of an Xtal-PAINT lattice image of unconstrained tile arrays. The first peak was observed at 10 nm (peak 1). The peak corresponding to the center to center distance between bound tiles in a tile array was observed at 87.4 nm (peak 2), a ~13% contraction in the dimensions of the tile relative to the tile dimensions observed in AFM images of tiles on mica in a,b. This result is in agreement with the contraction observed in the Cando tile model. Additional peaks were observed at 123 nm, 195 nm, and 275 nm (peaks 3-5), corresponding to the 2<sup>nd</sup>, 4<sup>th</sup>, and 7<sup>th</sup> nearest neighbor distances for a square lattice with a lattice constant of 87 nm. Peak positions were determined by fitting individual peaks with Gaussian functions. Statistics for the results of peak fitting for peaks 2-5 are provided in Table 2.4. .... 55

- Figure 2.13 Results of defect quantification for 2x2-tile arrays. (a-c) For self-limiting 2x2-tile array samples annealed at 25, 30, and 35 °C, respectively, probability histograms for the number of hybridization defects observed per 2x2-tile array are shown (grey bars), where  $N$  is the number of 2x2-tile arrays counted and  $p_d$  is the probability of observing a hybridization defect on tile arms bound by sticky-end hybridization for each sample. Binomial distributions (red) were generated from the results of counting to calculate  $p_d$ . The number of defects was observed to decrease linearly with anneal temperature as expected due to the decreased stability of sticky-end hybridization between defective structures. These results provide evidence that annealing inhibits hybridization between defective structures. The data for 2x2-tile array defect counting can be found in Table 2.5. (d-g) Examples of 2x2-tile arrays imaged by Xtal-PAINT with 0, 1, 2, and 3 defects, respectively. (d) Example of counting window for 2x2-tile array defect counting. Counting results for sample annealed at 25 °C are shown..... 57
- Figure 2.14 AFM images of tile arrays formed by constant temperature annealing. (a-c) AFM images of unconstrained tile arrays on mica, annealed for three hours at 35, 37, and 40 °C, respectively, in 0.5x TBE 8mM MgCl<sub>2</sub>. As expected, the average size of tile arrays was observed to decrease with anneal temperature, and few arrays were observed in the sample annealed at 40 °C. All samples were prepared in parallel and immediately deposited on mica after annealing, though cooling of each solution on contact with mica likely contributed to a small degree of array formation in each case. The images indicate that the temperature of formation of tile arrays by sticky-end hybridization in 0.5x TBE 8mM MgCl<sub>2</sub> is near 40 °C. Scale bars, 1 μm. 58
- Figure 2.15 Simulated radial distribution function of rigid and flexible tile models. (a) Probability distribution of tile defect label positions for a rigid tile model, generated by Monte Carlo methods ( $N=10^5$ ). For a rigid model, each point distribution is rotationally symmetric. (b) Probability distribution of tile defect label positions for a “flexible” tile model with an additional degree of freedom to account for twisting, generated by Monte Carlo methods ( $N=10^5$ ). In comparison to the rigid model, the point distributions of the flexible tile model are elongated tangent to the tile. Scale bars, 50 nm. Probability color bar, linear from 0 to 1 AU. (c) Radial distribution functions of the rigid and flexible tile models plotted with the experimental  $g(r)$  for comparison. For a valid comparison of the shape of each distribution, the contribution of random tile positions was removed from the experimental distribution by subtracting 1 and all distributions were normalized by the maximum values of each distribution (corrections validated in Figure 2.17). The shape, position, and relative height of the second peak of the experimental distribution could not be accounted for with a rigid tile model, demonstrating the need for a tile model that accounted for the effect of arm twist on the positions of defect labels..... 59

- Figure 2.16 Simulated radial distribution functions for tile arrays. (a) Probability distributions of defect label positions for the flexible models of individual tiles, 2-tile arrays, 3-tile arrays, and 2x2-tile arrays. Scale bars, 100 nm. (b) Simulated images of tile structures with uniform spacing, random orientation, and random defect label positions defined by the corresponding probability distributions in a. The densities of tiles and arrays were equivalent for all images. (c) Radial distribution functions of simulated tiles and arrays corresponding to a and b. For each structure,  $g(r)$  was calculated from a stack of 16 images, each image containing 625 evenly spaced structures, a total of  $10^4$  simulated structures. (d) Peak fitting of  $g(r)$  for the simulated distributions. Each distribution was approximated as a sum of Gaussian distributions, and the results of fitting were used for linear decomposition of experimental spectra. .... 60
- Figure 2.17 Radial distribution function for randomized position and tile distribution. (a) Simulated  $g(r)$  for a sample with a non-uniform but known distribution of tiles and arrays. To determine if the distribution of tile arrays in an Xtal-PAINT image could be quantified from  $g(r)$ , the simulated  $g(r)$  was fitted with a linear combination of the individual tile, 2-tile array, 3-tile array, and 4-tile array spectra. The fitted  $g(r)$  is plotted along with the simulated  $g(r)$ . The distribution of tiles and arrays was accurately predicted by the fraction of each component in the fitted  $g(r)$ , validating the use of  $g(r)$  to quantify distributions of tile arrays. (b) Simulated  $g(r)$  and fitted spectra for a uniform distribution of tile arrays with randomized positions within the image. (c) Simulated  $g(r)$  and fitted spectra for a non-uniform distribution of tile arrays with randomized positions within the image. The spectra used for fitting did not have randomized positions (Figure 2.16), though at low point densities the contribution of randomness can be effectively removed by subtracting 1 from  $g(r)$ . This is demonstrated by the fitted spectra in b and c. .... 61
- Figure 2.18 Linear decomposition of experimental  $g(r)$  into simulated spectra. (a-c) Experimental, fitted, and component  $g(r)$  for constrained 2x2-tile array samples annealed at 25, 30, and 35 °C, respectively. The fitted  $g(r)$  were generated by spectral decomposition of the experimental  $g(r)$  into a linear combination of spec single tile ( $X_1$ ), 2-tile array ( $X_2$ ), 3-tile array ( $X_3$ ), and 2x2-tile array ( $X_4$ ) spectra.  $\text{Fit} = a_1X_1 + a_2X_2 + a_3X_3 + a_4X_4$ , where  $a_1$ - $a_4$  represent the fraction of tiles in each size of tile array out of the total number of tiles. The isolated component spectra are shown in Figure 2.16. The fraction of tiles bound by sticky-end hybridization ( $a_2$ - $a_4$ ) was observed to decrease with anneal temperature. The deviation of fitted  $g(r)$  from experimental  $g(r)$  also decreased with anneal temperature due to a decrease in the fraction of tile structures that are not accounted for by the isolated component spectra (Figure 2.19). .... 62
- Figure 2.19 Xtal-PAINT and AFM images of extended 2x2-tile arrays. (a) AFM image of a self-limiting 2x2-tile array sample on mica. In the image, several tile

arrays were observed that failed to terminate at 2x2-tile arrays. The tile array magnified in the image demonstrates out-of-plane sticky-end hybridization, which enables tile arrays to extend beyond the intended 2x2-tile structure. Several larger tile arrays were also observed in the image. (b) Xtal-PAINT image of a self-limiting 2x2-tile array sample. Several large tile structures were resolved that failed to terminate at 2x2-tile arrays due to out-of-plane sticky-end hybridization, closely resembling tile arrays observed in a. Scale bars, 1  $\mu\text{m}$ . Inset scale bar, 250 nm..... 63

Figure 3.1 Hydroxylated cover glass for DNA-PAINT and AFM imaging of DNA origami. (a) Depiction of cover glass preparation for imaging. Pre-cleaned borosilicate cover glass were exposed to glow discharge in a reduced atmosphere of air to activate the surface through hydroxylation. (b) Strand diagram overlaid on DNA-PAINT image, (c) high resolution AFM image, (d) areal AFM image, and (e) DNA-PAINT image of DNA origami cross-tiles on hydroxylated cover glass. Scale bars, 50 nm. .... 77

Figure 3.2 20  $\mu\text{m}$  x 20  $\mu\text{m}$  correlative DNA-PAINT/AFM image of DNA origami cross-tiles. The large area AFM image was acquired with 10 nm pixel size, and the inset images were acquired with 2.5 nm pixel size. To distinguish features on the surface in AFM images, the height and amplitude error channels were superimposed..... 78

Figure 3.3 Spatial correlation of docking sites in DNA-PAINT and AFM images. (a) DNA-PAINT SRM, (b) AFM, and (c) correlative DNA-PAINT/SRM image of DNA origami cross-tiles. Scale bars, 250 nm. (d-f) Spatial correlation, dispersion, and 2D dispersion histogram, respectively, of 286 docking sites in two correlated DNA-PAINT and AFM images (Figure 3.26).  $P_{\text{AFM}}$  and  $P_{\text{SRM}}$  represent the positions of corresponding docking sites in AFM and SRM images, respectively, with horizontal (X, red) and vertical (Y, blue) positions indicated.  $\Delta P$  represents the deviation in position of corresponding sites in DNA-PAINT and AFM.  $dX$  and  $dY$  represent the relative deviation between corresponding sites in the x and y axes, respectively. The mean spatial deviation between the images was  $5 \pm 3$  nm, depicted by a black circle near the origin. .... 80

Figure 3.4 Correlation of defects in DNA-PAINT and AFM images. (a) Strand diagram of the DNA origami cross-tile depicting the positions of docking sites (red) at one corner of each arm. (b) Magnified strand diagram depicting (i) active docking sites that are successfully imaged with DNA-PAINT, (ii) inactive docking sites that do not appear in DNA-PAINT images but appear in AFM images, and (iii) unincorporated docking sites that do not appear in both DNA-PAINT and AFM images. (c) Superimposed DNA-PAINT center-of-mass and AFM topography image with unresolved sites (yellow), AFM defects (blue), and unresolved sites correlated to AFM defects (green). Full resolution images can be found in Figures 3.23 and 3.24. (d)

	Tables summarizing the results of defect quantification for the images in c and d, respectively. The four cases are distinguished by the states of docking sites in DNA-PAINT and AFM images (✓ - no defect, □ - defect). (e) Donut chart of the site distribution corresponding to the three possible states of docking sites depicted in b.....	83
Figure 3.5	DNA origami cross-tile caDNA <sub>no</sub> schematic. <sup>6</sup> Modified caDNA <sub>no</sub> schematic of the twist-corrected DNA origami cross-tile, <sup>7,8</sup> altered to more closely depict the geometry of the intended structure. Individual staple strand sequences can be found in Tables 3.1-3.3.....	111
Figure 3.6	Schematic of glow discharge vacuum chamber and fluidic well. (a) Schematic diagram of the custom glow discharge vacuum chamber used for hydroxylation of cover glass. <sup>9</sup> For glow discharge treatment, power to the RF (radio frequency) generator was supplied for 75 seconds, during which the chamber pressure was held at 2 torr. (b) 3D CAD model of custom, reusable fluidic well, designed and machined in house. The base plate and cover glass mount were machined from aluminum, and the screws, o-ring, and cover glass were purchased separately.....	112
Figure 3.7	Selective passivation of cover glass by hydroxylation. The first four TIRF frames of image acquisition of hydroxylated cover glass (a) without DNA origami and (b) with DNA origami cross-tiles adsorbed onto the surface. The imaging buffer for both samples was 0.5X TBE with 35 mM MgCl <sub>2</sub> , pH 8.3, and 3 nM Cy3b-labeled imager strands. The samples were imaged under identical experimental conditions, and the color range is identical for all images. ....	113
Figure 3.8	Comparison of DNA-PAINT images on BSA-passivated and hydroxylated cover glass. (a) Depiction of DNA origami cross-tiles bound to cover glass by protein-binding (top) and by hydroxylation (bottom), with (b) multiplexed DNA-PAINT imaging and (c) localization uncertainty distributions shown for each, respectively. The localization lists corresponding to the images in (b) were corrected for xy-drift and rendered at 5.35 nm/px; no filters were applied to the list prior to image rendering. Nonspecific binding events are indicated in DNA-PAINT images by localizations randomly distributed between structures and in the localization uncertainty distribution by a second population of events with higher localization uncertainty. The second population of events was speculated to result from nonspecific binding events lasting less than one full frame of acquisition. Scale bars, 500 nm.....	114
Figure 3.9	High resolution AFM topography image of DNA origami cross-tiles on hydroxylated cover glass. Tapping mode topography images were acquired in fluid (0.5x TBE, 18 mM MgCl <sub>2</sub> ). The image shown is 1 μm x 1 μm and was captured with 1000 pts/line and 3 Hz scan rate. The pores observed on	

the surface were suspected to result from phase separation during cooling of the borosilicate glass after formation. AFM height scale bar, 4.2 nm.115

- Figure 3.10 Schematic depicting correlative DNA-PAINT/AFM imaging. For correlative imaging, samples were mounted on an inverted microscope and viewed in brightfield to locate substrate registration marks and perform a programmed stage movement to a specified ROI. DNA-PAINT images of origami within the ROI were then acquired in TIRF illumination by a 561-nm laser source. Fluorescent events were identified in each frame and localized to sub-pixel coordinates, then the positions of each event were corrected for xy-drift by tracking fiducial markers as a function of time and generating a translational correction for events in each frame. Super-resolution microscopy (SRM) images were rendered from the corrected localization list, and pseudo-colors were assigned to each image to indicate the imager strand used. After SRM imaging, substrates were removed from the fluidic chamber and transferred for AFM characterization in fluid. The substrate was viewed optically to identify registration marks and move to the ROI imaged with SRM. Topographic images were acquired in fluid tapping mode using protocol provided in the methods. After AFM imaging and image processing, SRM and AFM images were roughly aligned using corresponding structures in the images. The positions of corresponding docking sites in each image were used to generate a projective transformation to transform SRM to AFM and correct for global image aberrations (Figure 3.14). The corrected SRM and AFM images were then combined by averaging. AFM schematic adapted from Bruker Dimension Icon/FastScan Bio help files.<sup>10</sup> ..... 116
- Figure 3.11 2  $\mu\text{m}$  x 2  $\mu\text{m}$  correlative DNA-PAINT/AFM image. Correlative SRM/AFM image of DNA origami cross-tiles on cover glass. Two color DNA-PAINT imaging was performed on the sample with imager strands M1' (red/yellow) and M3' (cyan). The AFM image was captured with 1  $\text{nm}^2$  pixel size and rendered in greyscale. .... 117
- Figure 3.12 5  $\mu\text{m}$  x 5  $\mu\text{m}$  correlative DNA-PAINT/AFM image. Correlative SRM/AFM image of DNA origami cross-tiles on cover glass. Two color DNA-PAINT imaging was performed on the sample with imager strands M1' (red/yellow) and M3' (cyan). The AFM image was captured with 2.5 nm x 2.5 nm pixel size and rendered in greyscale. .... 118
- Figure 3.13 20  $\mu\text{m}$  x 20  $\mu\text{m}$  correlative DNA-PAINT/AFM image. Correlative SRM/AFM image of DNA origami cross-tiles on cover glass. Two color DNA-PAINT imaging was performed on the sample with imager strands M1' (red/yellow) and M3' (cyan). The AFM image was captured with 10 nm x 10 nm pixel size and rendered in greyscale. .... 119

- Figure 3.14 Nonlinear deviations between AFM and SRM images. Global image aberrations often occur in optical and topographic images due to optical aberrations and suboptimal AFM imaging conditions. The aberrations manifest as nonlinear deviations between images acquired on different systems and should be corrected to better represent the correlation between images. (a) Correlative SRM/AFM image of DNA origami cross-tiles with nonlinear deviation in the positions of individual structures within the images. (b) Vector field visualizing the deviation in position of a subset of structures within the image; vectors begin on the AFM structure and end on the SRM structure. (c) Correlative SRM/AFM image from (a) after correcting for global image aberrations. Deviations between individual structures in the image were small and randomly oriented after the correction. .... 120
- Figure 3.15 Correlative DNA-PAINT/AFM image 1a. High-resolution, correlative SRM/AFM image of DNA origami cross-tiles on cover glass for quantifying spatial correlation and single-site defect metrology. Two-color DNA-PAINT imaging was performed on the sample with imager strands M1' (red/yellow) and M3' (cyan). The AFM image was captured with 1 nm<sup>2</sup> pixel size and rendered in greyscale. Image is 2 x 2 μm<sup>2</sup>..... 121
- Figure 3.16 Correlative DNA-PAINT/AFM image 1b. Second correlated image of the DNA origami cross-tile sample from Figure 3.15. Identical imaging parameters and dimensions. .... 122
- Figure 3.17 Locating docking sites in DNA-PAINT and AFM images. To quantify the quality of correlation between SRM and AFM images, the positions of docking sites were identified independently in SRM images (a) and AFM images (b), depicted by red cross-marks in each image. For DNA-PAINT images, POI were identified within the images and mapped to the localization list to identify all events corresponding to each POI. The position of individual POI were then determined from the average position of the corresponding events. For AFM images, the positions of docking sites were approximated based on the design of the origami. The relative positions and deviations in position for the images are plotted in Figure 3.18..... 123
- Figure 3.18 Correlation of docking site positions in AFM and DNA-PAINT images. (a,b) Plots of the x and y coordinates of 286 sites in the AFM images ( $X_1$ ,  $Y_1$ ) relative to the SRM images ( $X_2$ ,  $Y_2$ ). The correlation between individual sites within the images is represented by the slope of the fitted lines; for both fits, the slope  $b = 1.000$  and  $R^2 = 1.000$ . The results show strong correlation between the images with deviations randomly distributed in the x and y directions. (c,d) Plots of the regular residuals for the fits in (a,b). The residuals provide a better visualization of the position-dependence of deviations between the images. (e) Histogram of the magnitude of

deviations for sites within the images. The standard deviation in site positions between the SRM and AFM images was 5.85 nm. (f) Histogram of the localization uncertainty for events in the SRM image corresponding to the correlated images. The root mean square localization uncertainty was 6.5 nm. .... 124

Figure 3.19 Cumulative first detections of DNA-PAINT sites. (a) Plot of the cumulative first detections for an SRM image of DNA origami cross-tiles acquired in standard imaging buffer with imager strand M1'. The experimental data was fitted to extract the exponential and linear components; the exponential component was found to have a rate constant of  $k_I = 0.00267 \text{ sec}^{-1}$ . (b) Plot of the extracted exponential and linear components. The exponential component, representing the cumulative first detections of active docking sites, surpasses 99% of the predicted population of active sites by 60 minutes of imaging. (c) Plot of the detection efficiency ( $p_{det}$ ) measured for SRM images rendered every 5 minutes. For the fitted exponential decay, the rate constant  $k = 0.00214 \text{ sec}^{-1}$ . (d) Histogram of fluorescent event lifetimes. The dissociation rate constant ( $k_{off}$ ) was calculated from the exponential decay fit to be  $k_{off} = 1.24 \text{ sec}^{-1}$ . From the list of POI,  $[IP_e] / [P_e]$  was found to be 0.0022, and  $k_I = 0.00277 \text{ sec}^{-1}$ . (e). Plot comparing the progressions of DNA-PAINT detection predicted with each method. .... 125

Figure 3.20 Point-masking procedure for structure classification. (a) DNA-PAINT images were rendered at 20x magnification. (b) Maxima in the images surpassing a threshold of two detections were identified, generating a binary image of maxima. (c) Points within the maxima image were dilated to 50 nm squares, causing structures within 100 nm of other structures to be joined. (d) Structures in the dilated image were filtered by area, removing structures with areas larger than expected for a single structure. (e) Filtered image of dilated structures. The center of masses of filtered structures within the image were recorded. (f) The coordinates of filtered structures were used to generate a montage image of structures meeting the criteria for classification. .... 126

Figure 3.21 Neural pattern recognition for structure classification. (a) Subset of structures identified with the method described in Section 3.5.2.4 and depicted in Figure 3.20, chosen for automated classification. (b) An input vector is generated for each image. The count of maxima in the image is determined, then the radial distribution is calculated for the image. For the input, the count is vertically concatenated with the radial distribution, generating a row vector for the image. The final input matrix contains the input for individual images separated by column. (c) The inputs are fed into a neural network for classification. The output distinguishes between 5 classes for input images. The network was trained using over 4000 images per class. (d) The montage of input images labelled with the results of classification. The class values represent the number of POI detected for

each structure. With this method, thousands of structures can be classified in seconds. (e) Table of the results of automated and manual counting of five image samples containing 500 structures each. For all five samples, the detection efficiency determined from automated classification was within 1% of the value obtained by manual classification..... 127

Figure 3.22 AFM detection of unincorporated sites – Image 2a. Correlative SRM/AFM image of DNA origami cross-tiles synthesized with intentional unincorporated site defects. The DNA-PAINT image was rendered with detections located at the average position of the associated POI for improved visualization. The positions of the defects on individual origami are indicated by the structure diagram in the bottom left, along with simulated SRM detections. Within the image, unincorporated sites which were correctly identified are marked by white circles. One tile arm was obscured by imaging artifacts, but all other unincorporated sites were successfully detected..... 128

Figure 3.23 AFM detection of unincorporated sites – Image 2b. Second correlated image of DNA origami cross-tiles with intentional defects. Within the image, unincorporated sites which were correctly identified are marked by white circles. All 24 sites within the image were correctly identified.... 129

Figure 3.24 Quantifying unincorporated site detection with AFM. (a) DNA origami cross-tile strand diagram depicting an unincorporated site defect. (b) To quantify the structural difference between incorporated and unincorporated sites on DNA origami, the edge lengths of DNA origami cross-tiles were measured for intentional unincorporated sites (red) and sites without apparent defects (blue). The image shown is an inverted local slope image to aid visualization, and unincorporated sites are indicated by black arrows, corresponding to the structure diagram in the bottom left. Scale bar, 50 nm. (c) Box and whisker plots summarizing the distribution of edge lengths for unincorporated sites (‘Missing site’, red) and incorporated sites (‘Control’, blue), with a box spanning the 50<sup>th</sup> percentile and split by the median line, connected to the minimum and maximum values. The mean is indicated by a small box, and one outlier in the Missing site measurements is indicated by an ‘x’. (d) Table of the values from the box and whisker plot. The means are separated by greater than three standard deviations, indicating a significant difference between the edge length of incorporated and unincorporated sites. For the unincorporated sites examined, the double-stranded helix edge length was expected to be reduced by 5.4 nm (16 nt) by the defect, in close agreement with the measured  $6 \pm 3$  nm difference in the means. .... 130

Figure 3.25 Correlative defect metrology of DNA origami cross-tiles. AFM topography images with local contrast enhanced and background removed (a,b) and DNA-PAINT images (c,d) with colored circles indicating AFM defects

(blue), inactive DNA-PAINT sites (yellow), and correlated defects (green) identified independently in AFM and SRM images, prior to correlation. The DNA-PAINT image was rendered with detections located at the average position of the associated POI for improved visualization. (e) Table of the results of defect quantification. The fraction of inactive DNA-PAINT sites correlated to AFM defects was 0.23, less than the value expected to result from false AFM detections alone. The results suggest that the fraction of inactive sites missing from the structure is lower than the detectable limit for the experiment, and the rate of strand incorporation for the sites examined was greater than 0.97. For structures within the ROIs shown in (b) and (d), the detection efficiency of DNA-PAINT sites was 0.86; for the full SRM image, the detection efficiency was 0.815 (Section 3.5.2.4). . 131

- Figure 3.26 Correlative defect metrology of DNA origami cross-tiles. Correlative defect metrology as described in Figure 3.25, performed on a second tile sample. The percentage of inactive DNA-PAINT sites correlated to AFM defects was 7.7%, and the rate of strand incorporation for the sites examined was greater than 0.98. Scale bars, 250 nm. .... 132
- Figure 3.27 Rate of detection plot. The rate of observed detections for the sample shown in Figure 3.25 decreased by  $24.7 \pm 1.7\%$  over the course of DNA-PAINT image acquisition, close to the fraction of active DNA-PAINT sites with defects in AFM ( $18 \pm 2\%$ , Figure 3.25). Based on the results of a recent study demonstrating photo-induced depletion of docking sites during DNA-PAINT imaging,<sup>11</sup> it is speculated that the decrease in detection rate resulted from photo-induced damage to docking sites. Individual fluorophores can also become photo-bleached during imaging, though fluorophores exposed to TIRF illumination while imaging represent only about 1 in  $10^5$  of the total population for the given sample..... 133
- Figure 3.28 Docking site-targeted filtration – seqPAGE. (a) Depiction of Acrydite-immobilized ssDNA in a polyacrylamide matrix. For docking site-targeted PAGE filtration, Acrydite-modified ssDNA was incorporated in a polyacrylamide gel at a concentration of 3  $\mu\text{M}$ . The modified ssDNA polymerizes with acrylamide during polymerization of the gel, immobilizing the strands in the gel. A 7 nt domain of the ssDNA was complementary to docking site M1; migrating strands interact weakly with the immobilized strands if the docking site is present. (b) seqPAGE gel image of docking site strands. 5 nmoles of the indicated strands were added to the wells. The docking site length was 7 nt, White boxes indicate the bands removed from the gel after filtration. .... 134
- Figure 3.29 Docking site-targeted filtration – dpxPAGE. (a) Strand diagram depicting docking site strands hybridized to duplexing strands. The 8 nt hybridized domain was found to be stable during PAGE filtration when cooled to 5 C in 0.5x TBE with 12.5 mM  $\text{MgCl}_2$ . (b) dpxPAGE filtration of 1:1 and 2:1

strand concentrations [47pT-M1']:[47pt-M1] for 1 nmole and 4 nmole of strand 47pT-M1 added to the wells. The total mass of ssDNA added to each well, from left to right, was 33.4 ng, 50.2 ng, 16.7 ng, 134 ng, and 201 ng. Sharp duplexed bands were observed for ratios of 1:1 and 2:1 for up to 50 ng of ssDNA added to the wells. (c) dpxPAGE filtration of docking sites with 8 nt and 9 nt duplexed domains. The duplexing strand 47pT-M1' was included in the 3<sup>rd</sup> and 8<sup>th</sup> wells for reference. Docking sites and duplex strands were mixed at 1:1 ratio (3 nmoles total) and annealed from 90 C to 20 C over 20 minutes, then the annealed solutions were added to each well. White boxes indicate the bands removed from the gel after PAGE filtration. .... 135

Figure 3.30 Results of docking site-targeted filtration. Six sets of DNA origami cross-tiles were synthesized with 7 nt or 8 nt docking sites with no filtration, PAGE-filtration, seqPAGE-filtration (7 nt only), or dpxPAGE-filtration (8 nt only). DNA-PAINT imaging was performed on each set and classified to calculate the detection efficiency (p) for docking sites filtered by each method. (a) Histogram of the experimental counts of classified structures with two, three, or four active docking sites (grey bars), and the counts expected for a binomial distribution fitted to the results (black bars). The parameters of the binomial distribution for each sample can be found in (c). (b) Plot of the rate of SRM defects (1-p) for each origami set. For both 7 nt and 8 nt docking sites, the rate of defects decreased after PAGE-filtration, and the lowest rates of defects were achieved for the docking site-targeted filtration methods. .... 136

## LIST OF ABBREVIATIONS

°	Degrees
°C	Degrees Celsius
2D	Two-dimensional
3D	Three-dimensional
A, T, C, G	Adenine, Thymine, Cytosine, Guanine
Ac, Acry	Acrydite
adj. R <sup>2</sup>	Adjusted R-squared, adjusted coefficient of determination
AFM	Atomic force microscopy
AGE	Agarose gel electrophoresis
Apo	Apochromatic aberration correction
APS	Ammonium persulfate
ATP	Adenosine triphosphate
Au	Gold
AuNP	Gold nanoparticle
AuNR	Gold nanorod
BCP	Block-copolymer
bp	Base pair
BSA	Bovine serum albumin

BSA-Biotin	Biotin-labeled bovine serum albumin
CAD	Computer-aided drawing
CFI	Chrome-free infinity-corrected (Nikon)
cm	Centimeter
Cy	Cyanine fluorophores
dB	Decibels
DI	Deionized
DNA	Deoxyribonucleic acid
dpxPAGE	Duplexed PAGE
DSA	Directed self-assembly
dsDNA	Double-stranded DNA
EDTA	Ethylenediaminetetraacetic acid
EMCCD	Electron-multiplying charge-coupled device
ESI	Electronic supplementary information
Exp.	Experimental
FEA	Finite element analysis
Fig.	Figure
fM	Femtomolar
fps	Frames per second
fr.	Frame
HCl	Hydrochloric acid
HPLC	High performance liquid chromatography

HR	High-resolution
Hz	Hertz
in.	Inch
ITRS	International technology roadmap for semiconductor manufacturing
LUT	Lookup table
m	Meter
MEMS	Microelectromechanical device
mg	Milligram
MgCl <sub>2</sub>	Magnesium chloride
mm	Millimeter
mM	Millimolar
ms	Millisecond
mV	Millivolt
mW	Milliwatt
N <sub>2</sub>	Nitrogen gas
NA	Numerical aperture
NaCl	Sodium chloride
ng	Nanogram
NiAc	Nickel (II) acetate
NiCl <sub>2</sub>	Nickel chloride
nm	Nanometer
nM	Nanomolar

nmole	Nanomole
no.	Numero, number
NPR	Neural pattern recognition
nt	Nucleotide
PAGE	Polyacrylamide gel electrophoresis
PAINT	Points accumulation for imaging in nanoscale topography
PALM	Photo-activated localization microscopy
pM	Picomolar
POI	Point of interest
PSF	Point spread function
pT	Polythymine
px	Pixel
QD	Quantum dot
R <sup>2</sup>	R-squared, coefficient of determination
rcf	Relative centrifugal force
RF	Radio frequency
RMS	Root mean square
RMSE	Root mean square error
ROI	Region of interest
ROS	Reactive oxygen species
SemiSynBio	Semiconductor synthetic biology
seqPAGE	Sequence-targeted PAGE

SiO <sub>2</sub>	Silicon dioxide, silica
SMLM	Single molecule localization microscopy
SNR	Signal-to-noise ratio
SNP	Spherical nucleic acid
SRC	Semiconductor Research Corporation
SRM	Super-resolution microscopy
ssDNA	Single-stranded DNA
STM	Scanning tunneling microscopy
STORM	Stochastic optical reconstruction microscopy
SYBR	Synergy brands, Inc.
TBD	To be determined
TBE	Tris-borate EDTA buffer
TE	Tris-EDTA
TEM	Transmission electron microscopy
TEMED	Tetramethylethylenediamine
TIRF	Total internal reflection fluorescence
U,D,L,R	Up, down, left, right
UV	Ultra-violet light
V	Volts
Vis	Visible light
Xtal	Crystal
μg	Microgram

$\mu\text{L}$	Microliter
$\mu\text{m}$	Micrometer
$\mu\text{M}$	Micromolar

## LIST OF SYMBOLS

$\bar{\sigma}_{loc}$	Localization uncertainty
$\bar{D}$	Average detections per frame
[I]	Concentration of imager strands
[I <sub>e</sub> ]	Concentration of imager strands at equilibrium
[IP]	Concentration of imager strands bound to POI
[IP <sub>e</sub> ]	Concentration of imager strands bound to POI at equilibrium
[P]	Concentration of active sites/POI
[P <sub>e</sub> ]	Concentration of active sites/POI at equilibrium
$a_i$	Fraction of tiles corresponding to spectra $X_i$
$A_i$	Number of active sites in population $i$
$B_i$	Intensity of background signal for event $i$
$c$	Linear correction factor for nonspecific events
$d$	Diameter
$dt$	Derivative with respect to time
$D_{total}$	Total number of detections
$dx$	Spatial deviation between $P_{AFM}$ and $P_{SRM}$ in the x-axis
$dy$	Spatial deviation between $P_{AFM}$ and $P_{SRM}$ in the y-axis
$f(x 4,p)$	Binomial probability distribution for 4-trials of random variable $x$

$g(r)$	Radial distribution function
$I_i$	Intensity of event $i$ determined as the height of a fitted gaussian PSF
$k_i$	Reaction rate constant for population $i$
$k_{\text{off}}$	Dissociation rate constant
$k_{\text{on}}$	Association rate constant
$n$ (Chapter 1)	Refractive index of medium
$n$ (Chapter 3)	total number of sites examined
$N(t)$	Cumulative first detections at time $t$
$N_{\text{total}}$	Total number of active sites
$p_{00}$	Probability of an unresolved site in SRM with defect in AFM
$p_{01}$	Probability of an unresolved site in SRM with no defect in AFM
$p_{10}$	Probability of a resolved site in SRM with defect in AFM
$p_{11}$	Probability of a resolved site in SRM with no defect in AFM
$p_{\text{Act.}}$	Probability of an incorporated docking site being active for imaging
$P_{\text{AFM}}$	Position in AFM image
$p_{\text{dD}}$	Probability of observing a defect in AFM
$p_{\text{dDet.}}$	Probability of correctly identifying a defect in AFM
$p_{\text{det}}$	Probability of detection of individual docking sites
$p_{\text{Det.}}$	Probability of detecting an active docking site in SRM
$p_{\text{dImg.}}$	Probability of defect induced by imaging
$p_{\text{Inc.}}$	Probability of staple strand incorporation during synthesis
$p_{\text{nD}}$	Probability of not observing a defect in AFM

$p_{\text{off}}$	Probability of not resolving a docking site in SRM
$p_{\text{on}}$	Probability of resolving a docking site in SRM
$\text{PSF}_G(x,y,i)$	Symmetric 2D gaussian point spread function fitted to point $i$ centered at spatial coordinates $(X_i, Y_i)$
$P_{\text{SRM}}$	Position in SRM image
$t_{\text{total}}$	Total time of image acquisition
$X_i$ (Chapter 2)	Spectra of tile array with $i$ tiles
$X_i$ (Chapter 3)	x-coordinate of fitted gaussian PSF for event $i$
$x_m$	x-coordinate of site $m$ in AFM image
$X_m$	x-coordinate of site $m$ in DNA-PAINT image
$Y_i$	y-coordinate of fitted gaussian PSF for event $i$
$y_m$	y-coordinate of site $m$ in AFM image
$Y_m$	y-coordinate of site $m$ in DNA-PAINT image
$\Delta P$	Spatial deviation between $P_{\text{AFM}}$ and $P_{\text{SRM}}$
$\Delta T$	Change in temperature
$\sigma_i^2$	Sigma of event $I$ determined from the width of a fitted gaussian PSF
$\sigma_{xy}$	Standard deviation of sites in DNA-PAINT from AFM
$\theta$	Half-angle of light converging to spot
$\theta(t)$	Fraction of active sites detected at time $t$
$\lambda_0$	Wavelength of light from an emitter

## CHAPTER ONE: INTRODUCTION

### **1.1 DNA Nanotechnology**

The field of nanotechnology is built on the principle that matter often exhibits new or enhanced properties at scales below 100 nm (Figure 1.1 provided for scale).<sup>1</sup> This occurs when the dimensions of structures shrink below the characteristic lengths of phenomena that give rise to macroscopic properties, resulting in new chemical and physical properties.<sup>2</sup> At the nanoscale, properties become strongly dependent on size and structure, and the ability to control matter at this scale allows one to engineer materials and devices with unique properties and behaviors. For example, nanoscale films can be applied to optics as antireflective, self-cleaning, scratch-resistant, and electrically conductive coatings, and nanoscale additives to textiles can produce antimicrobial, stain-resistant, and strengthened fabrics.<sup>3</sup> In principle, the structure and properties of materials could be uniquely tailored to optimize performance for individual applications, a capability that is highly sought after in fields such as manufacturing, medicine, textiles, energy, and space. For nanoscale device fabrication, top-down lithography is undoubtedly the most predominant and capable method, enabling high fidelity production of logic and memory chips with complex architectures and nanoscale feature dimensions.<sup>4</sup> While the performance of top-down lithography is unmatched, the costs, challenges, and complexity of nanoscale patterning with photolithography have limited its use to products with the largest production volumes.

As alternatives to top-down manufacturing techniques, methods that enable bottom-up assembly of nanoscale components into macroscale systems have been explored

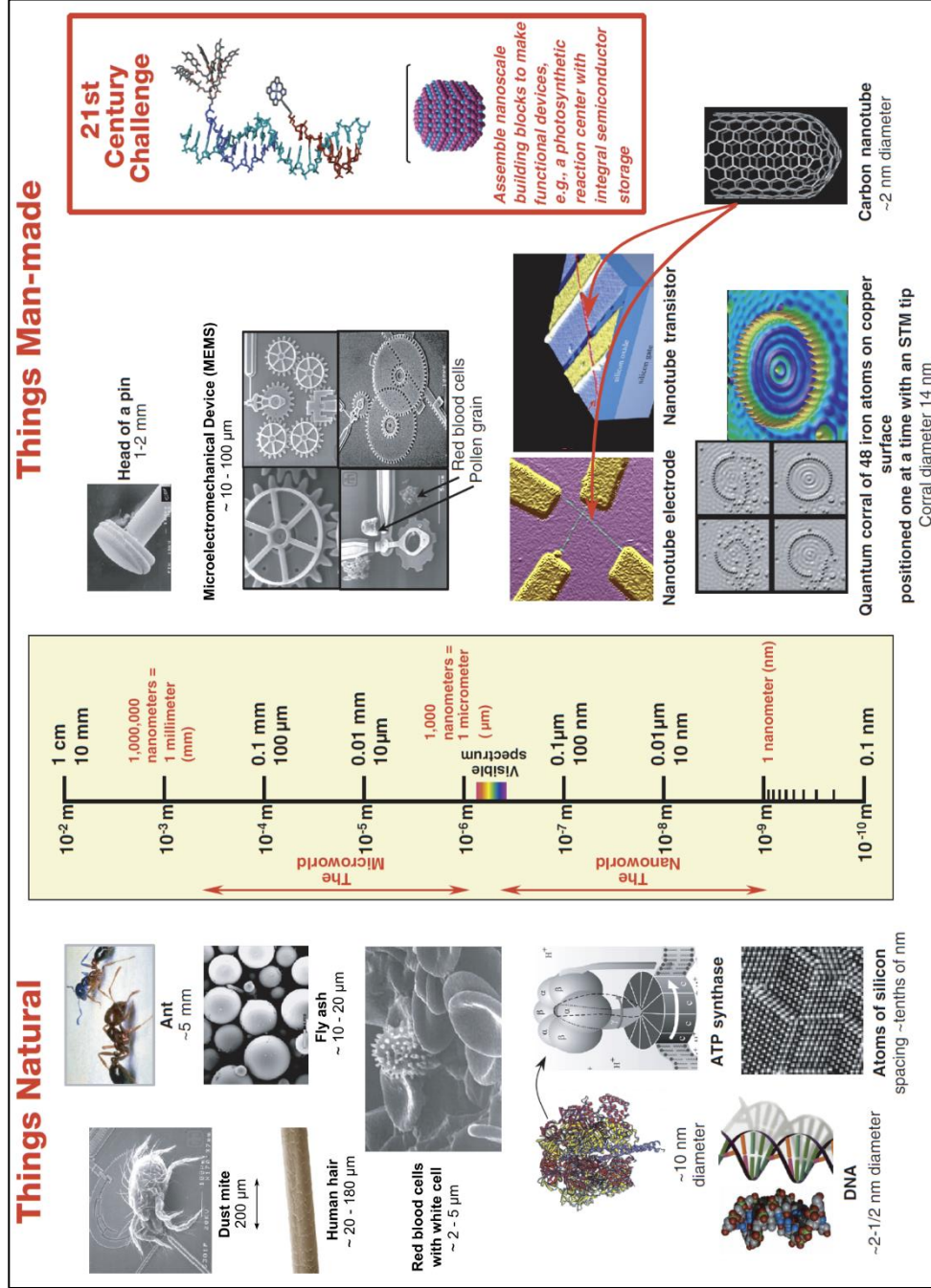
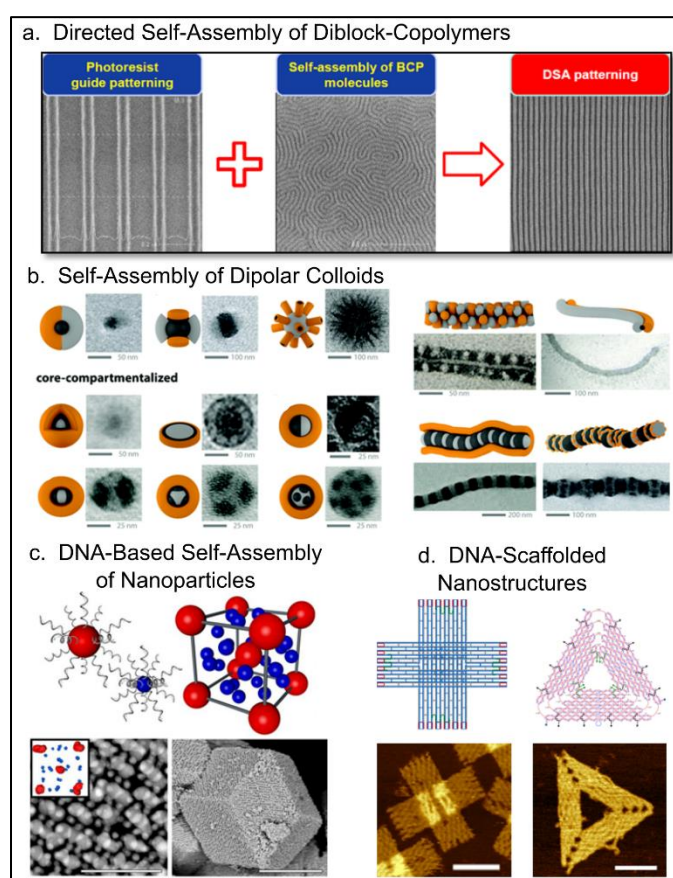


Figure 1.1 The scale of natural and man-made objects, from small to nanoscale ( $10^{-2}$  to  $10^{-10}$  m). Adapted from reference.<sup>1</sup>

extensively over the past two decades.<sup>5-8</sup> Many of the systems explored for bottom-up nanomanufacturing utilize self-assembly, i.e., the autonomous assembly of components into ordered structures without external intervention. Self-assembly typically occurs in weakly interacting systems with some degree of specificity in interactions, enabling thermally driven relaxation into energetically favorable, organized arrangements.<sup>9</sup> The majority of self-assembling systems involve organic molecules due to the prevalence of weak interactions between them (Figure 1.2). For example, polymers and colloids with



**Figure 1.2** Examples of the self-assembly of organic molecules. (a) Block-copolymer self-assembly can be combined with lithographically-defined guide patterns to produce nanoscale patterns with long-range coherence.<sup>10</sup> (b) Colloids with domains of varying polarity self-assemble into various structures.<sup>11</sup> (c) Nanoparticles functionalized with ssDNA self-assemble in a manner resembling atomic crystals.<sup>12</sup> (d) Nanostructures can be self-assembled from DNA into structures with nearly arbitrary size and shape.

domains of varying solvophobicity, such as block-copolymers, can self-assemble into ordered structures with nanoscale features (Figure 1.2a). Self-assembly is also highly prevalent in biological systems such as lipids, carbohydrates, proteins, and nucleic acids. The hybridization of DNA through base-pairing is one of the most powerful examples of self-assembly.<sup>12</sup>

Biological systems rely on information encoded onto DNA, a chain-like molecule consisting of linear sequences of four unique bases, adenine (A), thymine (T), guanine (G), and cytosine (C), connected to a deoxyribose phosphate backbone. DNA strands with complementary sequences can hybridize antiparallel to one another through hydrogen bonding according to the simple pairing rules that A binds T and C binds G, forming a stiff, linear double helix with a persistence length of approximately 50 nm and well-known dimensions that are determined by the number of complementary base pairs.<sup>13,14</sup> Conveniently, DNA can be produced synthetically at low cost and with desired sequence and length through solid state synthesis using the phosphoramidite method.<sup>15,16</sup> The specificity and simplicity of DNA-DNA interactions, predictable geometry, and freedom to construct strands of arbitrary sequence/length make DNA an excellent system for programmable self-assembly of materials with nanoscale feature control.<sup>17,18</sup>

The potential for long-range order through predetermined self-assembly makes DNA an ideal candidate for bottom-up nanomanufacturing. Figure 1.3 (adopted from Jones et al.<sup>12</sup>) visualizes the broad progression of DNA-based techniques from their inception in 1996 when two research groups, led by Chad Mirkin and Nadrian Seeman, simultaneously demonstrated conceptually distinct techniques for assembling rigid, DNA-based



of stable, discrete DNA nanostructures of near arbitrary shape and size. DNA origami uses a single long “scaffold” strand, commonly derived from viral DNA, and many unique, short

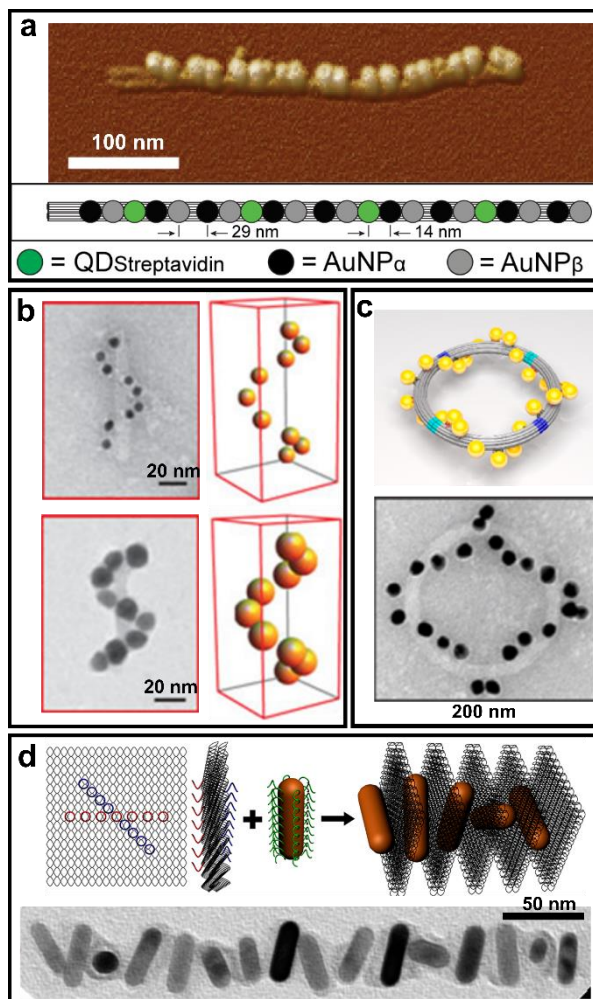


**Figure 1.4** Gold nanoparticle (AuNP) plasmonic devices scaffolded by DNA origami. (a) AFM image of AuNPs and quantum dots arranged on DNA origami nanotubes.<sup>28</sup> (b) TEM images and predicted geometries of helical AuNP assemblies for plasmonic devices with distinct chirality, constructed with 10 nm (top) and 16 nm (bottom) AuNPs.<sup>29</sup> (c) Geometric model and TEM image of a plasmonic toroidal metamolecule constructed of four DNA origami and 24 AuNPs. The toroidal metamolecules showed strong chiroptical response and were compatible with uniform axial alignment on surfaces.<sup>30</sup> (d) Schematic illustration and TEM image of AuNR helical superstructures scaffolded by DNA origami. The TEM image shows a right-handed plasmonic structure consisting of 16 AuNRs and DNA origami (+/- 1 origami).<sup>31</sup> Figure reproduced from references.<sup>28-31</sup>

“staple” strands that are synthesized with sequences chosen to strategically bind the scaffold strand in several distant locations. Upon thermal annealing, the staple strands hybridize to the scaffold strand, and the coordinated interactions of many staples with the scaffold strand act to fold the scaffold into a desired shape.<sup>27</sup> The power of DNA origami for constructing highly complex nanostructures was demonstrated in the original publication of the technique, in which topographic images with 6 nm pixels were written onto several DNA origami by modification of staple strands to possess double-stranded DNA hairpin extensions.<sup>27</sup> Within several years, DNA origami had been successfully used to template proteins,<sup>32</sup> gold and silver nanoparticles,<sup>33-35</sup> quantum dots,<sup>36,37</sup> and carbon nanotubes.<sup>38</sup> Several examples of gold nanoparticle plasmonic devices templated by DNA origami are shown in Figure 1.4 to demonstrate the flexibility of the technique.

Hierarchical assembly of DNA origami into 1D and 2D periodic superstructures has been demonstrated in the literature using various methods to join origami end-to-end, such as multi-scaffolded structures,<sup>39,40</sup> blunt-end stacking,<sup>41</sup> and sticky-end hybridization.<sup>42</sup> The most versatile method for assembling large, discrete DNA origami arrays with uniquely addressable sites to date was demonstrated by Tikhomirov et al., shown in Figure 1.5, in which arrays of up to 8x8 unique DNA origami were assembled with dimerization yields of 95%.<sup>43,44</sup> Sticky-end hybridization has also been demonstrated to enable high yield dimerization, and DNA origami tile arrays, based on the work by Liu et al.,<sup>42</sup> were synthesized using the sticky-end method and characterized in this work.

One of the biggest challenges to commercialization of DNA nanotechnology is the difficulty in achieving high-precision synthesis of stable DNA nanostructures at high yields.<sup>45</sup> While large-scale DNA origami synthesis has been demonstrated at high

chemistry-scale yields ( $> 90\%$ ),<sup>46</sup> current semiconductor manufacturing techniques require defect densities less than  $10/\text{cm}^2$  for memory and less than  $1/\text{cm}^2$  for logic.<sup>47</sup> If the average DNA origami is approximated as  $10^{-5}$  cm per side and the synthesis yield is rounded up to 99%, this would equate to  $10^{10}$  origami per  $\text{cm}^2$  and an approximate defect density of

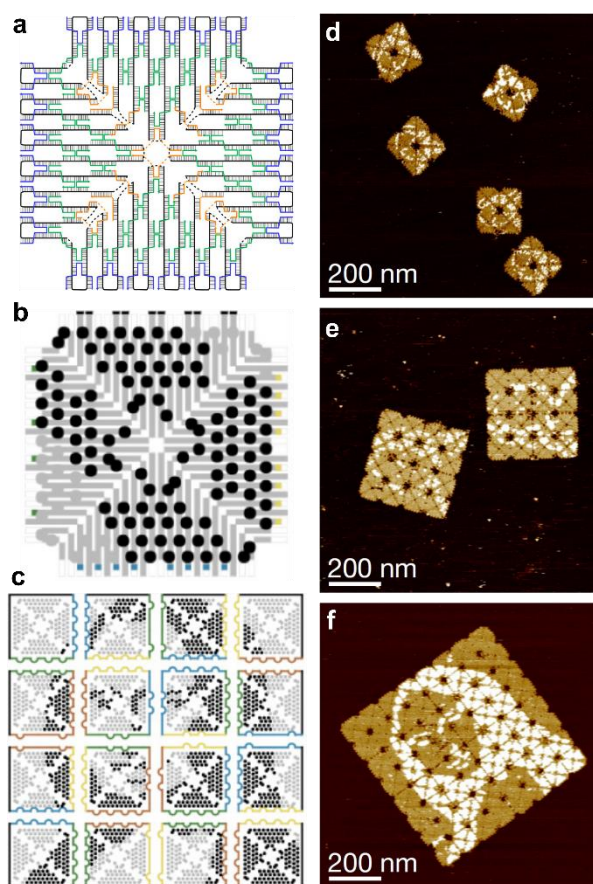


**Figure 1.5** Hierarchical assembly of discrete DNA origami arrays. (a) Strand-level, reduced complexity schematic of a square DNA origami tile. (b) Tile schematic depicting reactive edge sites and the positions of hairpins extended from the origami. (c) Tile array schematic depicting an assembled array composed of  $4 \times 4$  unique tiles with hairpins extended to depict the Mona Lisa upon proper array formation. (d)-(f) AFM images of  $2 \times 2$ ,  $4 \times 4$ , and  $8 \times 8$  tile arrays assembled using the programmed assembly method. Each size of array has individual origami with hairpins extended from the surface to depict the Mona Lisa, as shown in (c). Figure reproduced from Tikhomirov et al.<sup>43</sup>

$10^8/\text{cm}^2$ . From this perspective, it is obvious that DNA-based patterning is incompatible with current state-of-the-art semiconductor manufacturing techniques and device

architectures. While this may seem like a dooming argument for DNA-based semiconductor patterning, it ignores the potential for development of new, defect-tolerant device architectures that could accommodate chemistry-scale device yields, and such possibilities have been acknowledged in the 2018 Semiconductor Synthetic Biology Roadmap.<sup>45</sup>

Beyond the ability to pattern at the nanoscale, commercialization in a high-volume manufacturing environment requires methods to measure and quantify assembled structures (i.e., metrology). This is particularly important for DNA-based patterns due to the challenges imposed by the size and composition of DNA nanostructures. Common high-resolution imaging techniques used to characterize DNA nanostructures, such as atomic force microscopy (AFM) and transmission electron microscopy (TEM), cannot facilitate high-throughput characterization. As an alternative, super-resolution optical fluorescence microscopy (SRM), a technique developed for sub-diffraction-limit imaging of biological specimens,<sup>48</sup> has been demonstrated for sub-5 nm optical characterization of DNA origami.<sup>49</sup> The technique known as “DNA-PAINT” (DNA Points Accumulation for Imaging in Nanoscale Topography)<sup>50</sup> utilizes the programmable nature of DNA hybridization to produce optimal conditions for super-resolution imaging. These methods will be discussed in the following sections and serve as the basis for the work described in Chapters 2 and 3.

## **1.2 Super-Resolution Optical Microscopy**

The diffraction limit has long been the greatest weakness of optical microscopy, and this limit is well described by the Rayleigh criterion for the minimum resolvable distance between two point-source objects:

$$d = \frac{0.61 \lambda_0}{n \sin(\theta)} = \frac{0.61 \lambda_0}{NA} \quad (1)$$

where  $\lambda_0$  is the wavelength of light traveling through a medium with refractive index  $n$  and converging to a spot with half-angle  $\theta$ . The product of the refractive index and the sine of the half-angle is often referred to as the numerical aperture (NA) and is dependent on the optical system and imaging medium, which can reach up to 1.6 for modern oil immersion microscope objectives. Thus, a maximum resolution of approximately  $\lambda_0/3$  can be achieved when imaging multiple emitters simultaneously, though this does not apply for a single point-source emitter. Unlike multiple neighboring emitters, the position of an individual point-source emitter can be determined with nearly arbitrary accuracy if enough photons are detected.<sup>48</sup> This principle is the basis of super-resolution techniques utilizing single molecule localization microscopy (SMLM), a method by which single emitters are spatially isolated in images and fitted (i.e., “localized”) with a point spread function (PSF) to approximate their position with sub-pixel accuracy.

SMLM techniques achieve spatial isolation of emitters by spreading out observations in time, capturing many images in which only a small fraction of available emitters are detected. By localizing the emitters in each frame, then combining the information from many individual frames, an image can be reconstructed with sub-pixel resolution using the localized coordinates of the single emitters. Several techniques for isolating single emitters have been developed that utilize light sources to temporarily switch a stochastically-determined subset of fluorophores or fluorescent proteins into “on” states for imaging, such as stochastic optical reconstruction microscopy (STORM)<sup>48</sup> and photo-activated localization microscopy (PALM).<sup>51,52</sup> These methods are highly flexible and have been developed for multiplexed, 3D, and live cell imaging. While these methods are powerful

for biological imaging, they are limited in resolution to about 20 nm due to dependence on a finite population of fluorophores permanently bound to a sample. During imaging, fluorophores can become permanently photobleached and unable to emit, limiting the total number of photons collected per fluorophore.

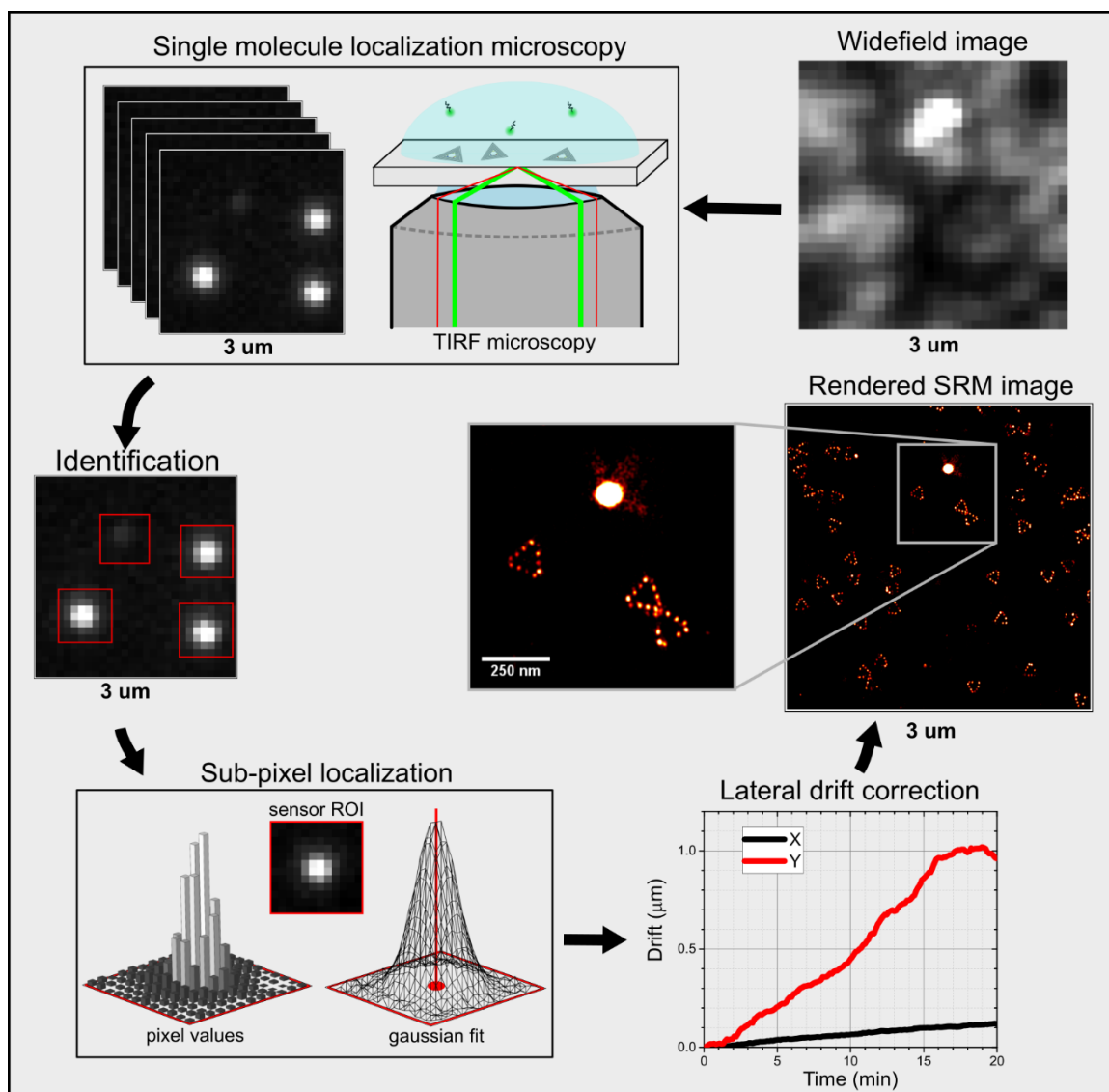


**Figure 1.6 Super-resolution with single molecule localization microscopy.** An averaged fluorescence image is provided to represent optical imaging with all fluorophores emitting simultaneously. With single molecule localization microscopy, emitters are spatially isolated by spreading observations out over time. Within individual images, single emitters are identified and fitted with a PSF to approximate the sub-pixel location of each emitter. During imaging, thermal drift results in lateral shifts of the imaging frame and is corrected using fiducial markers or correlational methods. Finally, a high-resolution image is rendered using the sub-pixel locations of all identified emitters.

To circumvent the limits associated with permanently bound emitters, the technique known as PAINT (Points Accumulation for Imaging in Nanoscale Topography)<sup>53</sup> utilizes

diffusing fluorophores that stochastically bind to immobilized targets. Typically, dyes are chosen with fluorescence that is highly sensitive to the chemical environment or possess favorable specificity of adsorption/desorption to a target structure. In this way, emission is enhanced upon binding to a target structure, decreasing the background signal from diffusing dyes. To further decrease background noise, the method could be combined with total internal reflection fluorescence (TIRF), limiting sample illumination to within about 100 nm of the surface to reduce excitation of diffusing dyes.<sup>54</sup> By tuning the concentration of fluorophores in solution and the illumination intensity to the binding characteristics of the fluorophore and sample, the density of emitters on a sample can be finely controlled for single molecule localization.<sup>53</sup> Spatial resolution of 20 nm has been achieved with this technique, as well as 3D imaging. The biggest challenges associated with PAINT are limited specificity of dye-sample interactions, which determines the contrast in super-resolution images, dependence on special dyes with high sensitivity to the chemical environment, and a limited ability to tune the strength of dye-sample interactions.<sup>50</sup>

Shortly after the development of PAINT, Jungmann et al.<sup>50</sup> developed a new SMLM technique to overcome the limitations of PAINT by exploiting the specificity of DNA hybridization. The technique known as DNA-PAINT utilizes ssDNA-labelled fluorophores (i.e., ‘imager’ strands) to transiently bind complementary ssDNA domains (i.e., ‘docking’ strands) on target structures. The use of DNA hybridization to control dye-sample interactions provides several significant improvements relative to the limitations associated with PAINT: (1) dye-sample interaction specificity is not determined by the properties of the fluorophore, thus no special dyes are required, (2) binding kinetics can be finely tuned by the length and sequence of the complementary DNA domains to maximize the number

of photons collected, and (3) dye-sample interactions gain the high specificity of DNA hybridization, greatly increasing the signal-to-noise ratio (SNR) in super-resolution images.<sup>49</sup> Further, multiplexed imaging can be achieved with a single fluorophore in sequential acquisitions by varying the imager strand ssDNA sequence.<sup>55</sup> In combination with statistical analysis of the adsorption/desorption kinetics of imager strand hybridization, multiplexed imaging can even be achieved in a single acquisition with one unique imager strand by variation of the lengths and redundancy of docking strands on a target structure.<sup>56</sup> While the technique is currently limited due to the lack of fluorogenic imager strands (i.e., species that only fluoresce upon binding to a sample), the method has enabled sub-5nm imaging of DNA origami and is a promising foundation for inline nanometrology of DNA origami in manufacturing.<sup>57</sup>

### **1.3 Atomic Force Microscopy**

Unlike optical microscopy, AFM circumvents the limits of light as a probe by use of a physical tip to interact with a sample, analogous to a tiny record player (Figure 1.7).<sup>58</sup> AFM uses a sharp tip, typically etched from silicon or silicon nitride with a radius of curvature on the order of nanometers, suspended on a cantilever to trace the surface of a sample by raster scanning the tip across the surface and recording any deflections of the cantilever caused by deviations in the sample topography. To observe such deflections, a laser spot is focused on the backside of the cantilever, reflecting onto a sensor that records the laser spot position. When tip-sample interactions cause the cantilever to flex, the position of the laser spot on the sensor changes. If the tip, cantilever, and laser/cantilever/sensor geometry are known, the position of the laser spot on the sensor can be translated into deflection amplitude of the tip at each position, providing a measure of

the height of features on the surface. Thus, the topography of a sample can be reconstructed from vertical deflections of the tip as it is raster scanned laterally across the surface by piezoelectric elements, enabling sub-nanometer lateral and vertical resolution in ideal conditions.<sup>59</sup>

As described above, early methods of AFM relied on flexibility of the cantilever to modulate the force of tip interactions with samples, greatly limiting the utility of the technique due to a force-dependence on the amplitude of cantilever deflection. To overcome this challenge, an additional piezoelectric element was added to the system to modulate the height of the tip/cantilever (or the sample itself) with the topography of the sample. In this way, the amplitude of deflections of the cantilever provide a measure of the local slope of features on the sample rather than a measure of the height itself, and changes in the height are instead reflected in the position of the piezoelectric element. This modification allowed deflections of the cantilever to be minimized, providing consistent, predictable, and tunable tip-sample forces during imaging.<sup>59</sup>

Initial applications of AFM relied on raster scanning of a tip in constant contact with a sample, referred to as contact mode imaging. Additional modes have since been developed, the most common being tapping modes and non-contact modes. Tapping modes are of particular interest for imaging soft samples such as DNA. In tapping mode, the tip is driven to oscillate at or near the resonant frequency of the cantilever, typically by a

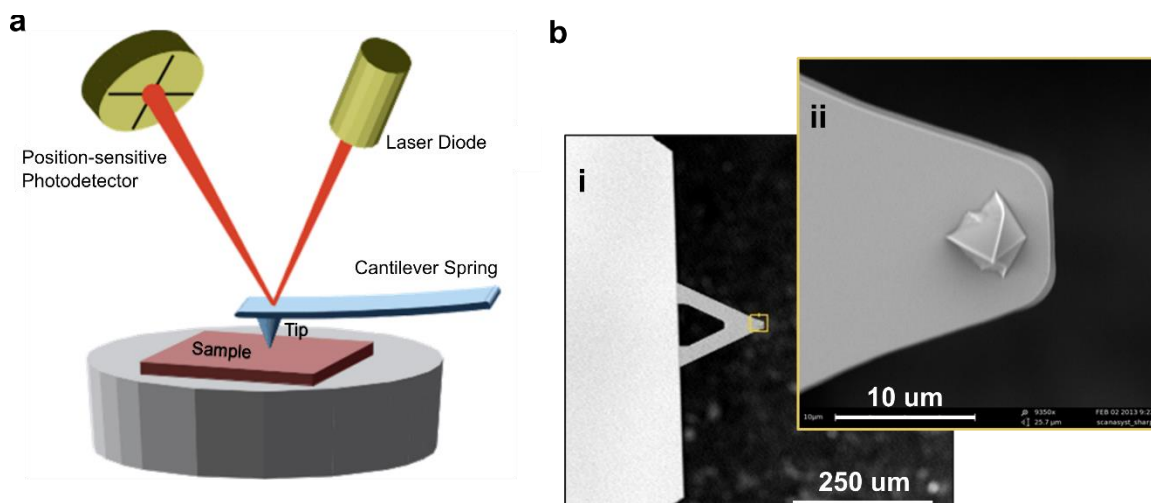


**Figure 1.7 Atomic Force Microscopy.** (a) Simplified schematic of an AFM and sample. As the tip is raster scanned across the surface, variations in the sample topography cause the tip and cantilever to be deflected and is observed as movement of a laser spot on a photodetector. (b) SEM images of AFM cantilever (i) and AFM tip (ii). Figure reproduced from reference.<sup>58</sup>

piezoelectric element. As the tip interacts with a sample, the amplitude, frequency, and phase of oscillations can shift relative to the drive signal, providing various information on tip-sample interactions. Changes in the amplitude of oscillations are typically used as feedback for the piezoelectric to modulate the vertical position of the cantilever with sample topography.<sup>59</sup> Tapping mode imaging can greatly reduce damage to samples by decoupling tip-sample interaction forces from lateral movement of the tip during raster scanning. While vertical forces can still be large during interactions, such interactions only occur intermittently and are spatially discrete, reducing damage caused by the tip.<sup>60</sup>

The force of tip-sample interactions is determined by several factors, such as the amplitude of tip deflection, tip geometry, and intermolecular forces. While most of these factors can be tuned externally, intermolecular forces between the tip and sample are difficult to control, particularly when imaging in ambient conditions. The nonlinear dependence of intermolecular forces on distance results in rapid changes of interaction

forces as the tip approaches the surface, often causing the tip to snap to the surface.<sup>59</sup> Additionally, humidity in ambient conditions can result in the condensation of water vapor on the sample, introducing additional forces by the formation of a water meniscus between the tip and sample. Capillary forces arise from movement of the water meniscus with the tip and can be strong enough to damage soft samples.<sup>61</sup>

If imaging is instead performed in fluid, such as a buffer, these effects can be negated, and the strength of intermolecular interactions can also be reduced.<sup>62</sup> Relative to ambient conditions, imaging in fluid can provide significantly higher resolution while decreasing the force of tip-sample interactions. The ability to image in fluid also enables in situ imaging of biological specimens and samples such as DNA nanostructures, and topographic images resolving the DNA double helix have been demonstrated with fluid imaging.<sup>63,64</sup> While AFM is not compatible with high-throughput characterization for inline nanometrology, it can provide high-resolution structural information that is not accessible in SRM images, and the complementary natures of AFM and SRM are ideal for correlative imaging. AFM is often used to supplement SRM imaging in the following chapters, and Chapter 3 discusses the development of high-resolution correlative DNA-PAINT and AFM for fundamental studies of strand defects in DNA origami.

#### 1.4 References

- 1 Small wonders, endless frontiers: A review of the National Nanotechnology Initiative. (National Academies Press, 2002).
- 2 Poole Jr, C. P. & Owens, F. J. Introduction to nanotechnology. (John Wiley & Sons, 2003).
- 3 US National Nanotechnology Initiative: Nanotechnology & You, <<https://www.nano.gov/you/nanotechnology-benefits>> (

- 4 Liddle, J. A. & Gallatin, G. M. Lithography, metrology and nanomanufacturing. *Nanoscale* **3**, 2679-2688, doi:10.1039/c1nr10046g (2011).
- 5 Whitesides, G. M. & Grzybowski, B. Self-assembly at all scales. *Science* **295**, 2418-2421, doi:DOI 10.1126/science.1070821 (2002).
- 6 Philp, D. & Stoddart, J. F. Self-assembly in natural and unnatural systems. *Angew Chem Int Edit* **35**, 1154-1196, doi:DOI 10.1002/anie.199611541 (1996).
- 7 Ariga, K., Hill, J. P., Lee, M. V., Vinu, A., Charvet, R. & Acharya, S. Challenges and breakthroughs in recent research on self-assembly. *Sci Technol Adv Mat* **9**, doi:10.1088/1468-6996/9/1/014109 (2008).
- 8 Grzelczak, M., Vermant, J., Furst, E. M. & Liz-Marzan, L. M. Directed Self-Assembly of Nanoparticles. *Acs Nano* **4**, 3591-3605, doi:10.1021/nn100869j (2010).
- 9 Israelachvili, J. N. *Intermolecular and surface forces*. (Academic press, 2015).
- 10 Lee, J. W. *Directed Self-Assembly Process and Materials Development*. (Dongjin Semichem Co. Ltd., 2012).
- 11 Groschel, A. H. & Muller, A. H. Self-assembly concepts for multicompartment nanostructures. *Nanoscale* **7**, 11841-11876, doi:10.1039/c5nr02448j (2015).
- 12 Jones, M. R., Seeman, N. C. & Mirkin, C. A. Nanomaterials. Programmable materials and the nature of the DNA bond. *Science* **347**, 1260901, doi:10.1126/science.1260901 (2015).
- 13 Watson, J. D. & Crick, F. H. The structure of DNA. *Cold Spring Harb Symp Quant Biol* **18**, 123-131, doi:10.1101/sqb.1953.018.01.020 (1953).
- 14 Manning, G. S. The persistence length of DNA is reached from the persistence length of its null isomer through an internal electrostatic stretching force. *Biophys. J.* **91**, 3607-3616 (2006).
- 15 Beaucage, S. & Caruthers, M. H. Deoxynucleoside phosphoramidites—a new class of key intermediates for deoxypolynucleotide synthesis. *Tetrahedron Lett.* **22**, 1859-1862 (1981).

- 16 Beaucage, S. L. & Iyer, R. P. Advances in the synthesis of oligonucleotides by the phosphoramidite approach. *Tetrahedron* **48**, 2223-2311 (1992).
- 17 Seeman, N. C. DNA in a material world. *Nature* **421**, 427-431, doi:10.1038/nature01406 (2003).
- 18 Seeman, N. C. DNA nanotechnology: novel DNA constructions. *Annu. Rev. Biophys. Biomol. Struct.* **27**, 225-248, doi:10.1146/annurev.biophys.27.1.225 (1998).
- 19 Mirkin, C. A., Letsinger, R. L., Mucic, R. C. & Storhoff, J. J. A DNA-based method for rationally assembling nanoparticles into macroscopic materials. *Nature* **382**, 607-609, doi:10.1038/382607a0 (1996).
- 20 Li, X. J., Yang, X. P., Qi, J. & Seeman, N. C. Antiparallel DNA double crossover molecules as components for nanoconstruction. *JACS* **118**, 6131-6140, doi:DOI 10.1021/ja960162o (1996).
- 21 Winfree, E., Liu, F. R., Wenzler, L. A. & Seeman, N. C. Design and self-assembly of two-dimensional DNA crystals. *Nature* **394**, 539-544, doi:Doi 10.1038/28998 (1998).
- 22 Wei, B., Dai, M. & Yin, P. Complex shapes self-assembled from single-stranded DNA tiles. *Nature* **485**, 623-626, doi:10.1038/nature11075 (2012).
- 23 Zheng, J. P., Birktoft, J. J., Chen, Y., Wang, T., Sha, R. J., Constantinou, P. E., Ginell, S. L., Mao, C. D. & Seeman, N. C. From molecular to macroscopic via the rational design of a self-assembled 3D DNA crystal. *Nature* **461**, 74-77, doi:10.1038/nature08274 (2009).
- 24 Zheng, J. W., Constantinou, P. E., Micheel, C., Alivisatos, A. P., Kiehl, R. A. & Seeman, N. C. Two-dimensional nanoparticle arrays show the organizational power of robust DNA motifs. *Nano Lett.* **6**, 1502-1504, doi:10.1021/nl060994c (2006).
- 25 He, Y., Ye, T., Su, M., Zhang, C., Ribbe, A. E., Jiang, W. & Mao, C. D. Hierarchical self-assembly of DNA into symmetric supramolecular polyhedra. *Nature* **452**, 198-U141, doi:10.1038/nature06597 (2008).

- 26 Ke, Y., Ong, L. L., Shih, W. M. & Yin, P. Three-dimensional structures self-assembled from DNA bricks. *Science* **338**, 1177-1183, doi:10.1126/science.1227268 (2012).
- 27 Rothemund, P. W. Folding DNA to create nanoscale shapes and patterns. *Nature* **440**, 297-302, doi:10.1038/nature04586 (2006).
- 28 Klein, W. P., Schmidt, C. N., Rapp, B., Takabayashi, S., Knowlton, W. B., Lee, J., Yurke, B., Hughes, W. L., Graugnard, E. & Kuang, W. Multiscaffold DNA origami nanoparticle waveguides. *Nano Lett.* **13**, 3850-3856, doi:10.1021/nl401879r (2013).
- 29 Kuzyk, A., Schreiber, R., Fan, Z., Pardatscher, G., Roller, E. M., Hogege, A., Simmel, F. C., Govorov, A. O. & Liedl, T. DNA-based self-assembly of chiral plasmonic nanostructures with tailored optical response. *Nature* **483**, 311-314, doi:10.1038/nature10889 (2012).
- 30 Urban, M. J., Dutta, P. K., Wang, P., Duan, X., Shen, X., Ding, B., Ke, Y. & Liu, N. Plasmonic Toroidal Metamolecules Assembled by DNA Origami. *J. Am. Chem. Soc.* **138**, 5495-5498, doi:10.1021/jacs.6b00958 (2016).
- 31 Lan, X., Lu, X., Shen, C., Ke, Y., Ni, W. & Wang, Q. Au nanorod helical superstructures with designed chirality. *J. Am. Chem. Soc.* **137**, 457-462, doi:10.1021/ja511333q (2015).
- 32 Kuzyk, A., Laitinen, K. T. & Torma, P. DNA origami as a nanoscale template for protein assembly. *Nanotechnology* **20**, 235305, doi:10.1088/0957-4484/20/23/235305 (2009).
- 33 Ding, B., Deng, Z., Yan, H., Cabrini, S., Zuckermann, R. N. & Bokor, J. Gold nanoparticle self-similar chain structure organized by DNA origami. *J. Am. Chem. Soc.* **132**, 3248-3249, doi:10.1021/ja9101198 (2010).
- 34 Hung, A. M., Micheel, C. M., Bozano, L. D., Osterbur, L. W., Wallraff, G. M. & Cha, J. N. Large-area spatially ordered arrays of gold nanoparticles directed by lithographically confined DNA origami. *Nat Nanotechnol* **5**, 121-126, doi:10.1038/nnano.2009.450 (2010).

- 35 Pal, S., Deng, Z., Ding, B., Yan, H. & Liu, Y. DNA-origami-directed self-assembly of discrete silver-nanoparticle architectures. *Angew. Chem. Int. Ed. Engl.* **49**, 2700-2704, doi:10.1002/anie.201000330 (2010).
- 36 Bui, H., Onodera, C., Kidwell, C., Tan, Y., Graugnard, E., Kuang, W., Lee, J., Knowlton, W. B., Yurke, B. & Hughes, W. L. Programmable periodicity of quantum dot arrays with DNA origami nanotubes. *Nano Lett.* **10**, 3367-3372, doi:10.1021/nl101079u (2010).
- 37 Ko, S. H., Gallatin, G. M. & Liddle, J. A. Nanomanufacturing with DNA Origami: Factors Affecting the Kinetics and Yield of Quantum Dot Binding. *Adv. Funct. Mater.* **22**, 1015-1023, doi:10.1002/adfm.201102077 (2012).
- 38 Eskelinen, A. P., Kuzyk, A., Kaltiainenaho, T. K., Timmermans, M. Y., Nasibulin, A. G., Kauppinen, E. I. & Torma, P. Assembly of single-walled carbon nanotubes on DNA-origami templates through streptavidin-biotin interaction. *Small* **7**, 746-750, doi:10.1002/sml.201001750 (2011).
- 39 Endo, M., Sugita, T., Katsuda, Y., Hidaka, K. & Sugiyama, H. Programmed-assembly system using DNA jigsaw pieces. *Chemistry* **16**, 5362-5368, doi:10.1002/chem.200903057 (2010).
- 40 Li, Z., Liu, M., Wang, L., Nangreave, J., Yan, H. & Liu, Y. Molecular behavior of DNA origami in higher-order self-assembly. *J. Am. Chem. Soc.* **132**, 13545-13552, doi:10.1021/ja106292x (2010).
- 41 Woo, S. & Rothmund, P. W. Programmable molecular recognition based on the geometry of DNA nanostructures. *Nat Chem* **3**, 620-627, doi:10.1038/nchem.1070 (2011).
- 42 Liu, W., Zhong, H., Wang, R. & Seeman, N. C. Crystalline two-dimensional DNA-origami arrays. *Angew. Chem. Int. Ed. Engl.* **50**, 264-267, doi:10.1002/anie.201005911 (2011).
- 43 Tikhomirov, G., Petersen, P. & Qian, L. Fractal assembly of micrometre-scale DNA origami arrays with arbitrary patterns. *Nature* **552**, 67-71, doi:10.1038/nature24655 (2017).

- 44 Tikhomirov, G., Petersen, P. & Qian, L. Programmable disorder in random DNA tilings. *Nat Nanotechnol* **12**, 251-259, doi:10.1038/nnano.2016.256 (2017).
- 45 2018 Semiconductor Synthetic Biology Roadmap. 32 (Semiconductor Research Corporation, 2018).
- 46 Bathe, M., Chrisey, L. A., Herr, D. J. C., Lin, Q., Rasic, D., Woolley, A. T., Zadegan, R. M. & Zhirnov, V. V. Roadmap on biological pathways for electronic nanofabrication and materials. *Nano Futures* **3**, doi:10.1088/2399-1984/aaf7d5 (2019).
- 47 Sreenivasan, S. V. Nanoimprint lithography steppers for volume fabrication of leading-edge semiconductor integrated circuits. *Microsyst Nanoeng* **3**, 17075, doi:10.1038/micronano.2017.75 (2017).
- 48 Rust, M. J., Bates, M. & Zhuang, X. Sub-diffraction-limit imaging by stochastic optical reconstruction microscopy (STORM). *Nat. Methods* **3**, 793-795, doi:10.1038/nmeth929 (2006).
- 49 Schnitzbauer, J., Strauss, M. T., Schlichthaerle, T., Schueder, F. & Jungmann, R. Super-resolution microscopy with DNA-PAINT. *Nat Protoc* **12**, 1198-1228, doi:10.1038/nprot.2017.024 (2017).
- 50 Jungmann, R., Steinhauer, C., Scheible, M., Kuzyk, A., Tinnefeld, P. & Simmel, F. C. Single-molecule kinetics and super-resolution microscopy by fluorescence imaging of transient binding on DNA origami. *Nano Lett.* **10**, 4756-4761, doi:10.1021/nl103427w (2010).
- 51 Betzig, E., Patterson, G. H., Sougrat, R., Lindwasser, O. W., Olenych, S., Bonifacino, J. S., Davidson, M. W., Lippincott-Schwartz, J. & Hess, H. F. Imaging intracellular fluorescent proteins at nanometer resolution. *Science* **313**, 1642-1645, doi:10.1126/science.1127344 (2006).
- 52 Hess, S. T., Girirajan, T. P. & Mason, M. D. Ultra-high resolution imaging by fluorescence photoactivation localization microscopy. *Biophys. J.* **91**, 4258-4272, doi:10.1529/biophysj.106.091116 (2006).

- 53 Sharonov, A. & Hochstrasser, R. M. Wide-field subdiffraction imaging by accumulated binding of diffusing probes. *Proc Natl Acad Sci U S A* **103**, 18911-18916, doi:10.1073/pnas.0609643104 (2006).
- 54 Axelrod, D. Total internal reflection fluorescence microscopy in cell biology. *Traffic* **2**, 764-774 (2001).
- 55 Jungmann, R., Avendano, M. S., Woehrstein, J. B., Dai, M., Shih, W. M. & Yin, P. Multiplexed 3D cellular super-resolution imaging with DNA-PAINT and Exchange-PAINT. *Nat. Methods* **11**, 313-318, doi:10.1038/nmeth.2835 (2014).
- 56 Wade, O. K., Woehrstein, J. B., Nickels, P. C., Strauss, S., Stehr, F., Stein, J., Schueder, F., Strauss, M. T., Ganji, M., Schnitzbauer, J., Grabmayr, H., Yin, P., Schwille, P. & Jungmann, R. 124-Color Super-resolution Imaging by Engineering DNA-PAINT Blinking Kinetics. *Nano Lett.*, doi:10.1021/acs.nanolett.9b00508 (2019).
- 57 Graugnard, E., Hughes, W. L., Jungmann, R., Kostianen, M. A. & Linko, V. Nanometrology and super-resolution imaging with DNA. *MRS Bull.* **42**, 951-959, doi:10.1557/mrs.2017.274 (2017).
- 58 Meyers, D. Atomic Force Microscope: A Tiny Record Player, <<https://undergrad.research.ucsb.edu/2014/03/atomic-force-microscope-tiny-record-player/>> (2014).
- 59 Haugstad, G. Atomic force microscopy: understanding basic modes and advanced applications. (John Wiley & Sons, 2012).
- 60 <Hansma-Laney\_DNA Binding to Mica Correlates with Cationic Radius\_BiophysJ\_1996.pdf>.
- 61 Zitzler, L., Herminghaus, S. & Mugele, F. Capillary forces in tapping mode atomic force microscopy. *Physical Review B* **66**, 155436 (2002).
- 62 Hansma, P. K., Cleveland, J. P., Radmacher, M., Walters, D. A., Hillner, P. E., Bezanilla, M., Fritz, M., Vie, D., Hansma, H. G., Prater, C. B., Massie, J., Fukunaga, L., Gurley, J. & Elings, V. Tapping Mode Atomic-Force Microscopy in Liquids. *Appl. Phys. Lett.* **64**, 1738-1740, doi:Doi 10.1063/1.111795 (1994).

- 63 Leung, C., Bestembayeva, A., Thorogate, R., Stinson, J., Pyne, A., Marcovich, C., Yang, J., Drechsler, U., Despont, M. & Jankowski, T. Atomic force microscopy with nanoscale cantilevers resolves different structural conformations of the DNA double helix. *Nano Lett.* **12**, 3846-3850 (2012).
- 64 Ido, S., Kimura, K., Oyabu, N., Kobayashi, K., Tsukada, M., Matsushige, K. & Yamada, H. Beyond the helix pitch: direct visualization of native DNA in aqueous solution. *ACS nano* **7**, 1817-1822 (2013).

CHAPTER TWO: METROLOGY OF DNA ARRAYS BY SUPER-RESOLUTION  
MICROSCOPY

This chapter was published by the Royal Society of Chemistry in the journal *Nanoscale* and should be referenced appropriately.\*

Reference:

Green, Christopher M., Kelly Schutt, Noah Morris, Reza M. Zadegan, William L. Hughes, Wan Kuang, and Elton Graugnard. "*Metrology of DNA arrays by super-resolution microscopy.*" *Nanoscale* 9, no. 29 (2017): 10205-10211.

Reproduced/modified by permission of the Royal Society of Chemistry.

## **Metrology of DNA Arrays by Super-Resolution Microscopy**

Christopher M. Green<sup>a</sup>

Kelly Schutt<sup>a</sup>

Noah Morris<sup>b</sup>

Reza M. Zadegan<sup>a</sup>

William L. Hughes<sup>a</sup>

Wan Kuang<sup>b</sup>

Elton Graugnard<sup>a</sup>

Accepted for publication in:

*Nanoscale*

April 27, 2017

<sup>a</sup>*Micron School of Materials Science & Engineering,  
Boise State University, 1910 University Dr., Boise, ID 83725, USA*

<sup>b</sup>*Department of Electrical & Computer Engineering,  
Boise State University, 1910 University Dr., Boise, ID 83725, USA*

## 2.1 Abstract

Recent results in the assembly of DNA into structures and arrays with nanoscale features and patterns have opened the possibility of using DNA for sub-10 nm lithographic patterning of semiconductor devices. Super-resolution microscopy is being actively developed for DNA-based imaging and is compatible with inline optical metrology techniques for high volume manufacturing. Here, we combine DNA tile assembly with state-dependent super-resolution microscopy to introduce crystal-PAINT as a novel approach for metrology of DNA arrays. Using this approach, we demonstrate optical imaging and characterization of DNA arrays revealing grain boundaries and the temperature dependence of array quality. For finite arrays, analysis of crystal-PAINT images provides further quantitative information of array properties. This metrology approach enables defect detection and classification and facilitates statistical analysis of self-assembled DNA nanostructures.

## 2.2 Introduction

As the costs and challenges of semiconductor device scaling increase,<sup>1</sup> new materials and technologies that enable precise patterning and placement of nanostructures are sought to supplement or replace current photolithography techniques.<sup>2</sup> For example, nanoscale patterning through directed self-assembly of block-copolymer (BCP) structures has been acknowledged as a viable and inexpensive lithographic mask via the International Technology Roadmap for Semiconductor manufacturing.<sup>3,4</sup> While progress has been made in the precise control of BCP self-assembly, defect densities and directed self-assembly of complex patterns remain challenges for manufacturing.<sup>5</sup> As an alternative technology, the potential for programmable, long-range order through self-assembly makes DNA an

attractive material for bottom-up fabrication of nanoscale patterns,<sup>6</sup> as well as for templated-assembly of electronic and photonic devices with nanometer precision.<sup>7-10</sup>

Within the last two decades, DNA-based techniques such as origami,<sup>6</sup> tiles,<sup>9</sup> and bricks<sup>11</sup> have demonstrated precise control over the size, shape, arrangement, and assembly of DNA nanostructures and nanocomponents. While much work is still needed to approach commercial viability, lithographically confined DNA origami and large crystalline arrays of DNA origami show potential as self-assembled lithographic masks<sup>12</sup> and templates for precise nanoparticle assemblies.<sup>13-18</sup> As a result of these advances, the Semiconductor Research Corporation recently listed DNA-controlled sub-10 nm manufacturing as a technical area for its future roadmap.<sup>19</sup>

Beyond the ability to pattern at the nanoscale, metrology of patterned structures is a crucial capability in semiconductor device manufacturing that poses increasing challenges (e.g., cost, throughput, accuracy) as the device dimensions decrease.<sup>20,21</sup> For example, locating dislocations within a nanoscale BCP pattern requires tedious inspection of high-resolution scanning electron micrographs. Likewise, common high-resolution imaging techniques used for characterization of DNA nanostructures, such as atomic force microscopy (AFM) and transmission electron microscopy (TEM), cannot accommodate high throughput characterization. Currently, few studies have focused on developing DNA nanostructure characterization techniques that meet the demands of commercial manufacturing.<sup>22-25</sup> Super-resolution fluorescence microscopy has proven to be a powerful tool for biological imaging, and in the case of DNA-based nanostructures, the technique known as DNA-PAINT enables non-destructive, multiplexed optical imaging with resolution down to ~5 nm.<sup>26-29</sup> Based on conventional optical microscopy, super-resolution

offers the potential for inline optical metrology of DNA nanostructures, a capability crucial for manufacturing.

## 2.3 Experimental

### 2.3.1 Crystal-PAINT Imaging

As a proof-of-principle of the ability to incorporate defect metrology with DNA-based patterning, we report a two-step super-resolution methodology for characterizing the periodic structure and quality of two-dimensional (2D) DNA origami arrays. We demonstrate the ability to perform defect characterization by integrating DNA-PAINT docking sites with sticky-end hybridization strands, creating state-dependent docking sites that deactivate when bound in an array. In this way, information on the state of each tile arm (deactivated/bound or active/unbound) is acquired in parallel with spatial information during imaging. Furthermore, we incorporate docking sites near the center of individual structures for characterization of array periodicity, thereby enabling step-wise characterization of the crystalline structure and single defect identification – a technique that will be referred to as crystal-PAINT characterization (Xtal-PAINT).<sup>28</sup> Using this technique, we reconstruct arrays of cross-shaped DNA origami tiles and identify grain boundaries occurring between arrays. In addition, utilizing statistical methods, we quantify the dimensions and size distributions of tile arrays and identify tile curvature and twist due to stress in the structure.

For DNA nanostructure assemblies formed by hybridization, binding of DNA origami tiles is dependent on unique sets of short, single-stranded DNA “sticky-ends” extended from the DNA origami tiles, as illustrated in Figure 2.1. Array growth is promoted through

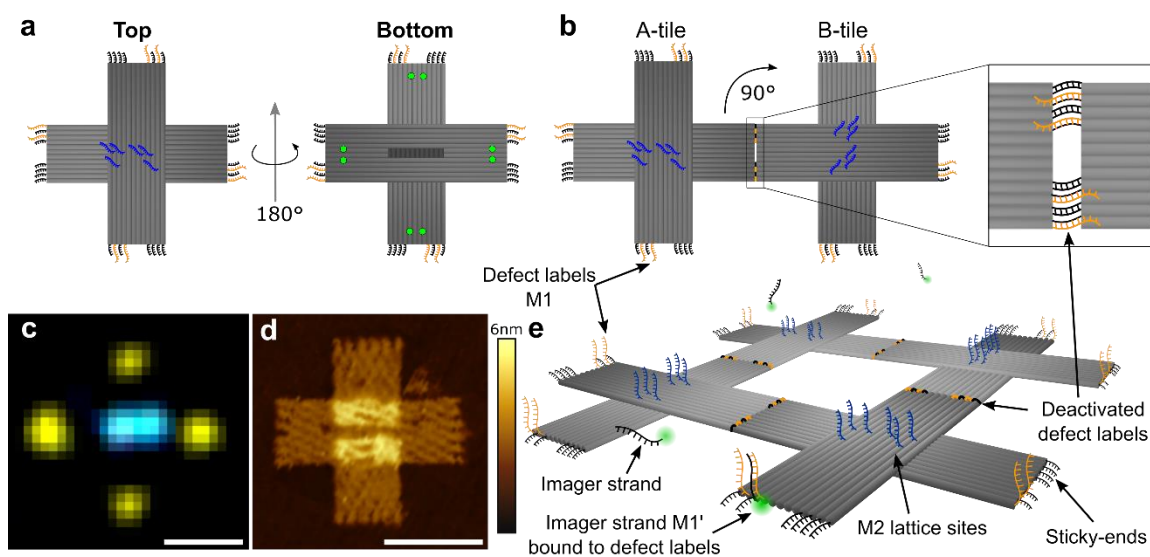


**Figure 2.1** (a) Schematic depicting the cross-shaped DNA origami tiles used for Xtal-PAINT. Each set of sticky-ends on tile arms contain two 8 nucleotide (nt) defect labels (orange strands, M1) and six 5 nt sticky-ends (black strands). Six 8 nt docking sites extend from the center of the top of each tile (blue strands, M2). The lattice sites are aligned parallel to the central indent of the tile to delineate individual tile orientation for Xtal-PAINT imaging. Two biotinylated strands extend from the bottom of each tile arm (green circles) for immobilization to avidin-functionalized glass substrates. (b) Schematic of ideal sticky-end hybridization between A and B tiles. Bound tiles within an array are rotated  $90^\circ$  relative to neighboring tiles, which can be observed by the orientation of the lattice sites in Xtal-PAINT images. As shown in the magnified view of hybridization between A and B tile sticky-ends, all but 3 nt of the defect labels are bound, deactivating the strands as docking sites. (c) Xtal-PAINT and (d) AFM images of individual tiles corresponding to the tile schematics in (a). Scale bars, 50 nm. (e) Schematic of a  $2 \times 2$ -tile array depicting imager strand docking to unbound defect labels.

hybridization of structures with complementary sticky-end sets.<sup>14</sup> DNA-PAINT provides a convenient method for detecting hybridization defects between individual structures bound through sticky-end interactions. For DNA-PAINT, oligomers are extended from DNA origami tiles to provide short, single-stranded DNA “docking sites” to which complementary, fluorophore-labeled DNA “imager strands” can transiently hybridize.<sup>27</sup> To enable super-resolution imaging of array defects, we combine origami sticky-ends with DNA-PAINT docking sites, and this is the basis for defect identification with Xtal-PAINT.

To implement Xtal-PAINT, a subset of sticky-ends were modified to facilitate either DNA-PAINT or sticky-end hybridization (M1, orange strands in Fig. 2.1). Modified sticky-ends (defect labels) retain the ability to hybridize for array formation but also serve as docking sites until such binding occurs. Upon binding to another origami, defect labels hybridize to complementary sticky-ends and are in a bound state and deactivated to DNA-PAINT imaging (Fig. 2.1b,e). Thus, defect labels are in unbound and active state at defects within an array (e.g., missing tiles) and at array boundaries. For array lattice imaging, docking sites (M2, blue strands in Fig. 2.1) extend from the center of each tile in a specific pattern to delineate the directionality of the cross-tile, as seen in Figure 2.1. Biotinylated strands have been incorporated onto the bottom of the tiles for binding to substrates functionalized with avidin binding sites (Fig. 2.6).<sup>30</sup> Figure 2.1c shows a super-resolution image of an A-tile, where the defect labels (pseudo-colored, yellow) and lattice sites (pseudo-colored, blue) were imaged with two-color imaging, discussed below. The image clearly demonstrates the ability to resolve the ends of the origami arms and to determine the orientation of the origami. For comparison, Figure 2.1d shows an atomic force microscope (AFM) height image of an individual A-tile imaged in fluid on mica. All materials and methods are described in detail in the ESI.

## **2.4 Results and Discussion**

### **2.4.1 2x2-Tile Array Imaging**

To validate Xtal-PAINT, imaging was initially performed on individual tiles and self-limiting 2x2-tile arrays (Figs 2.7-9). The 2x2-tile arrays were constrained by replacing two adjacent sticky-end sets from A and B tiles with inert poly-thymine extensions (Fig. 2.9). Arrays were formed in solution by constant temperature annealing and immediately

deposited in a fluid well for Xtal-PAINT and on mica for AFM imaging. Super-resolution imaging of defect labels and lattice sites was performed in two steps by Exchange-PAINT,<sup>28</sup> a technique for multiplexed DNA-PAINT that eliminates the need for spectrally distinct imaging probes. Two distinct Cy3b-labeled imager strands (M1' and M2'), complementary to the defect labels (M1) and lattice sites (M2), respectively, were introduced to the fluid well separately for imaging (Fig. 2.7). In Figure 2.2a, Xtal-PAINT images of structures progressing from individual origami tiles to self-limited 2x2-tile arrays are shown. Using spatial and state-dependent information from individual structures in

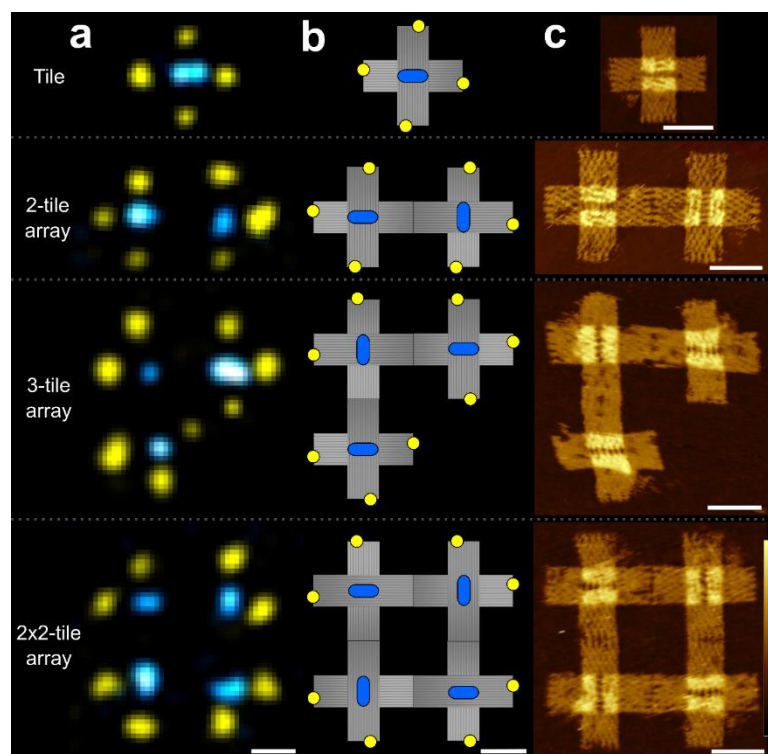


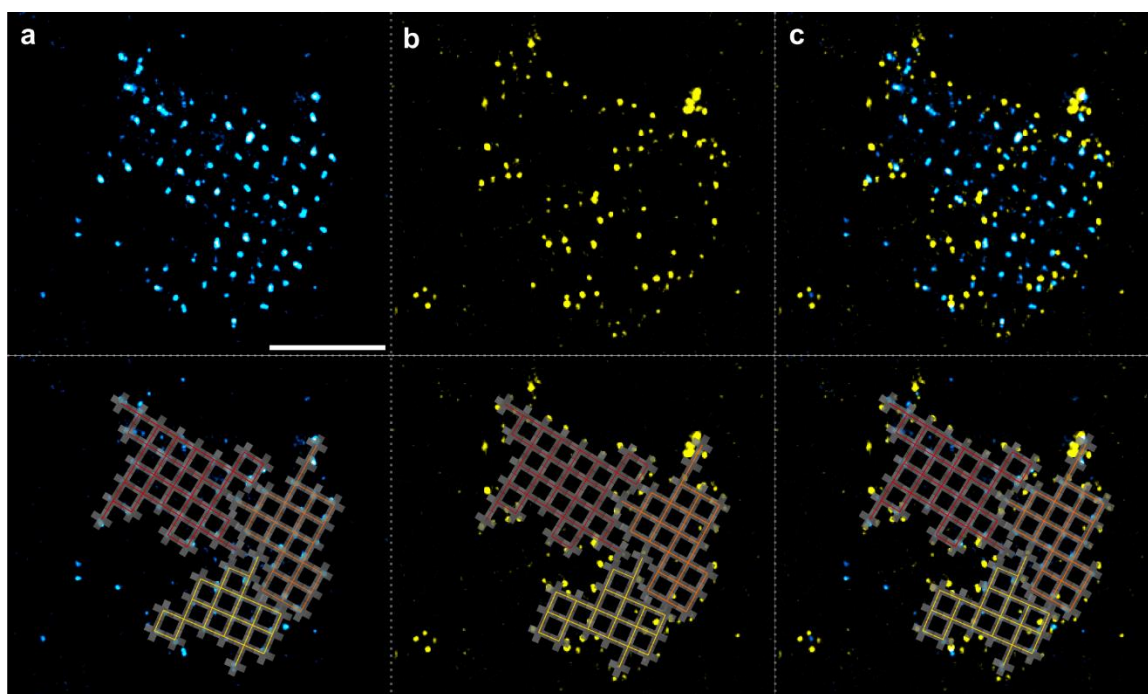
**Figure 2.2** (a) Xtal-PAINT images of a single tile, 2-tile array, 3-tile array, and 2x2-tile array immobilized on glass by protein binding, with lattice sites (blue) and defect labels (yellow). (b) Schematics of the tiles and arrays deduced from the corresponding Xtal-PAINT images in (a) with defect labels (yellow) and lattice sites (blue). (c) AFM height images of tiles and arrays on mica, analogous to the structures depicted in (a). Scale bars, 50 nm. AFM height scale bar, 4 nm.

Xtal-PAINT images, tiles and arrays were deduced (Fig. 2.2b) and compared to AFM images of analogous structures on mica (Fig. 2.2c). Tile arrays reconstructed from Xtal-PAINT images geometrically resemble arrays imaged by AFM on mica, and the relative orientations of lattice sites and defect labels were consistent with the tile design. Defect labels were resolved on unbound tile arms and were successfully deactivated on bound arms. These data validate the Xtal-PAINT approach to imaging lattices and defects within DNA origami arrays.

#### 2.4.2 Unbounded Array Imaging

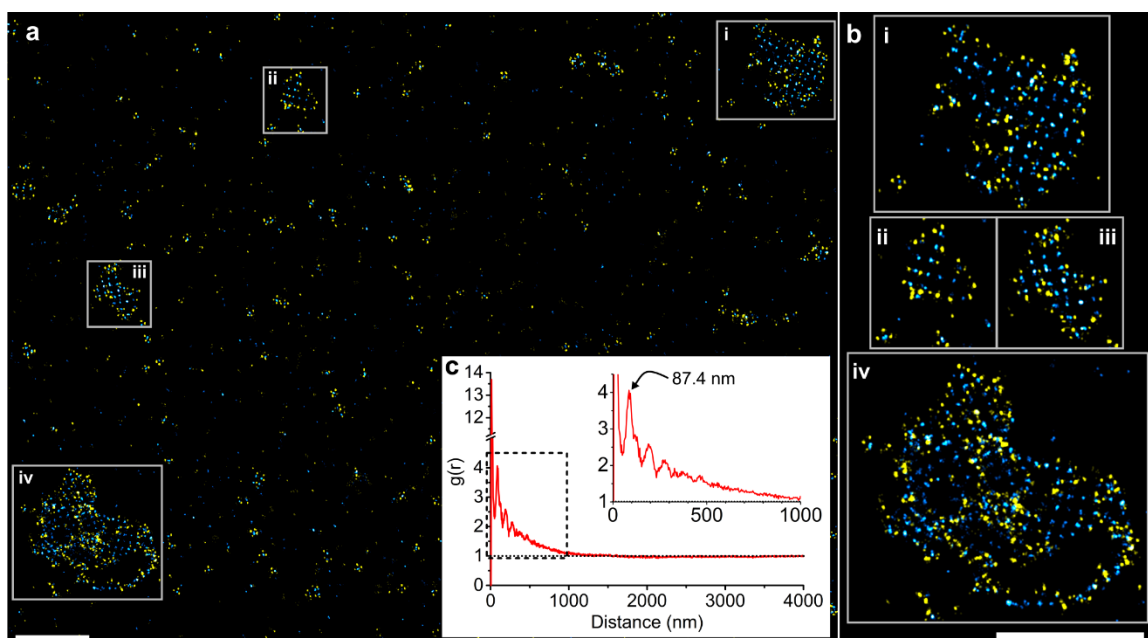
To demonstrate Xtal-PAINT imaging of unconstrained arrays, tile arrays were assembled in solution and immediately deposited in a fluid well (Fig. 2.10). Resulting two-color images for an array consisting of approximately 81 tiles are shown in Figures 2.3 and 2.4. The Xtal-PAINT images in Figure 3 reveal a distinct crystalline array that is easily identified by the periodicity of the lattice sites (blue, Fig. 2.3a). The yellow defect label image in Figure 2.3b displays a well-defined external boundary, as well as defects within the array along paths resembling boundaries between separate arrays. Closer inspection of the lattice sites in Figure 2.3a reveals three grains with slightly misaligned lattices that meet at the grain boundaries observed in Figure 2.3b. In crystallography, this type of defect is referred to as a low angle grain boundary. A polycrystalline array model was deduced from Xtal-PAINT images and overlaid on each image in the lower half of Figure 2.3 to aid visualization. Individual grains in the simulated array are distinguished by color. The ability to resolve grain boundaries with Xtal-PAINT demonstrates a potential application of the technique to observe and quantify nucleation and growth of DNA origami crystals.

Figure 2.4 shows a larger region of a Xtal-PAINT image containing the tile array analyzed in Figure 2.3 (labeled as i in Fig. 2.4). Within the image, multiple small arrays were observed, and four arrays were observed that each consisted of more than ten tiles, with upwards of 150 tiles estimated in the largest array. The largest array shows a high degree of disorder, partially resulting from the inability to relax or flatten after immobilization by protein binding to the surface (Fig. 2.11). To characterize the average dimensions of the tiles and the extent of short and long range order for the sample, a radial



**Figure 2.3** Xtal-PAINT image of an unbounded DNA origami array. (a) Image of lattice sites revealing the array periodicity, (b) defect label image revealing the array perimeter and missing tiles, and (c) combined images of a tile array resolved by Xtal-PAINT. Slight misalignment of the lattices in the arrays results in grain boundaries in the defect label image, suggesting that the large array coalesced from smaller tile arrays. Tile array models were deduced from the Xtal-PAINT images and overlaid on the images in the lower half of the figure. Lattice misalignment and grain boundaries are accounted for by modeling the structure as three arrays distinguished by color (red, orange, and yellow grids). Mean localization precision for defect label and lattice images were  $8.5 \pm 5.0$  nm and  $10.4 \pm 6.1$  nm, respectively. Scale bar, 500 nm.

distribution function,  $g(r)$ , was calculated from the lattice image and plotted in Figure 2.4c. Several clear peaks were observed in the  $g(r)$ , and individual peaks were identified by comparison to the expected dimensions of the tile and tile arrays. The first and largest peak, occurring at  $\sim 10$  nm, results from the elongated pattern of lattice sites on individual tiles and provides an approximate measure of the resolution of our system, in agreement with the mean localization precision for the lattice image.<sup>31,32</sup> The second peak, centered at 87 nm, is the center-to-center distance between neighboring tiles. Higher order peaks were



**Figure 2.4** Xtal-PAINT image of unbounded tile arrays. (a) Combined defect label (yellow) and lattice (blue) images of tile arrays annealed for 24 hours near 38 °C. The four largest arrays are identified in the image by i-iv. (b) Magnified images of the tile arrays corresponding to i-iv in a. (i) Tile array (also shown in Figure 3) with dimensions of approximately 1 x 1  $\mu\text{m}^2$ . Within the array, missing sites suggest tile vacancies. (ii) and (iii) Small tile arrays of  $\sim 0.5 \times 0.5 \mu\text{m}^2$  (iv) Large tile array that appears to extend out of the focal plane and TIRF illumination field, potentially caused by curvature induced by crystallization. (c) Radial distribution function of the full lattice image with peak at 87.4 nm, corresponding to the nearest neighbor distance between hybridized tiles. Higher order peaks were observed at 123 nm, 195 nm, and 275 nm, corresponding to the 2nd, 4th, and 7th nearest neighbor distances, respectively. Mean localization precision for defect label and lattice images were  $8.5 \pm 5.0$  nm and  $10.4 \pm 6.1$  nm, respectively. Scale bars, 1  $\mu\text{m}$ .

also observed at 123 nm, 195 nm, and 275 nm, corresponding to the 2nd, 4th, and 7th nearest neighbor distances, respectively (Fig. 2.12). For reference, from AFM images the dimensions of individual tiles on mica were approximately 100 nm per side, 13 nm longer than the center-to-center spacing of tiles imaged by Xtal-PAINT in solution. This 13% difference is likely caused by out-of-plane curvature of tiles immobilized by protein-binding in the fluid cell compared to lying flat on mica; Cando analysis of the tile indicates a ~12% reduction of tile dimensions from curvature and twist, consistent with the dimensions observed in Xtal-PAINT (Fig. 2.12).<sup>33</sup> The correlation length ( $g(r) \rightarrow 1$ ) of the distribution indicates that order persists until nearly 1.6  $\mu\text{m}$ , approximately equal to the largest dimension of array iv from Figure 2.4. The lack of distinct peaks beyond 300 nm suggests that large arrays were typically polycrystalline, consistent with the array analyzed in Figure 2.3. Thus, the results of Figure 2.4 validate the use of Xtal-PAINT in characterizing 2D crystalline DNA origami arrays. In comparison to AFM imaging, two-color Xtal-PAINT images were typically captured in ~75 minutes under conservative imaging conditions and could be expanded to capture over  $10^5 \mu\text{m}^2$  without increasing capture time, while AFM imaging of an equal area would be impractical.

#### 2.4.3 Analysis of 2x2-Tile Arrays

For bounded arrays, such as the 2x2-tile array system shown in Figure 2.2 and 2.8, a greater depth of information can be obtained by analysis of defect label images, which reveal both hybridization defects between bound arms as well as missing or extra tiles from the finite array. To demonstrate the utility of such an analysis, a temperature dependence study was performed on the 2x2-tile array system. 2x2-tile arrays were formed by constant temperature annealing at 25 °C, 30 °C, and 35 °C for 24 hours and imaged with Xtal-

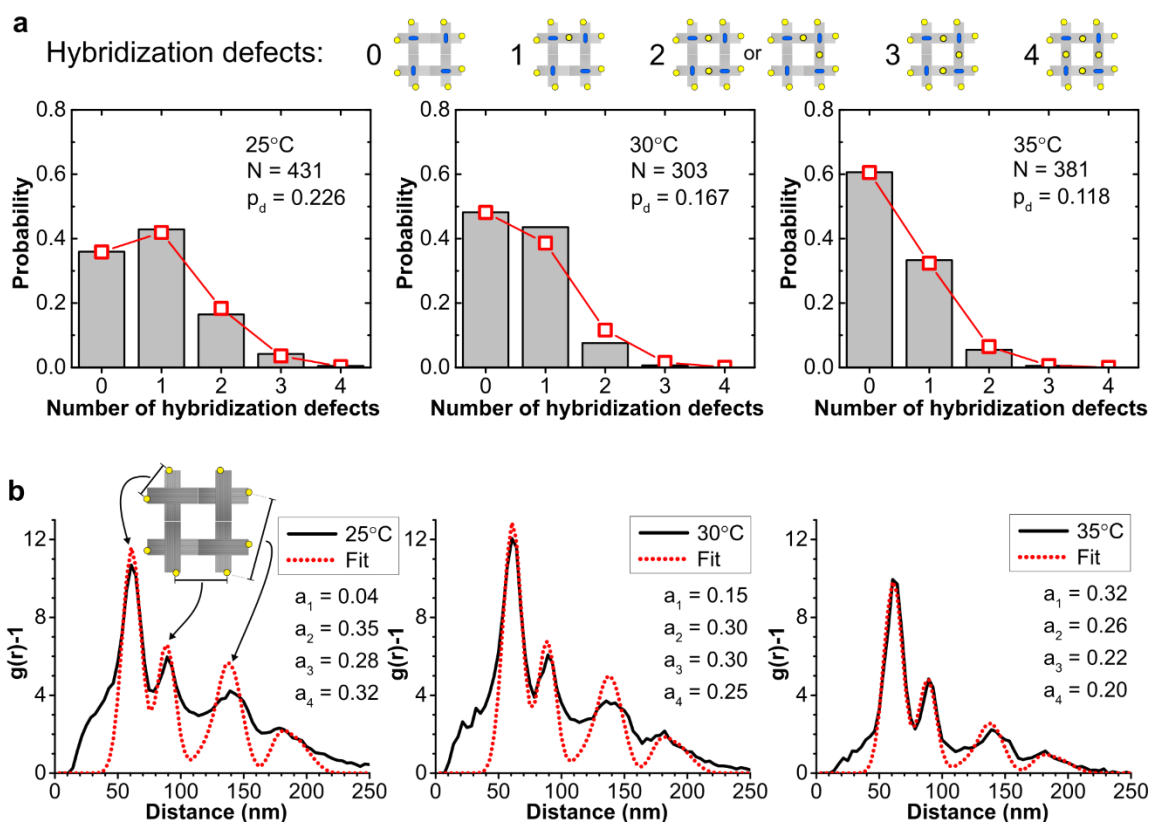


**Figure 2.5** Quantitative analysis of 2x2-tile array defect label images. (a) Histograms displaying the results of hybridization defect counting for 2x2-tile arrays annealed at 25°C, 30°C, and 35°C. The legend at top indicates the structures analyzed to determine the probabilities of hybridization defects. Binomial distributions were generated from the data to calculate the probability of hybridization defects  $p_d$  for bound tile arms.  $p_d$  was observed to decrease as the temperature of anneal was increased. (b) Experimental and fitted  $g(r)$  for defect label images of 2x2-tile arrays annealed at 25 °C, 30 °C, and 35 °C. The first three peaks are identified with a 2x2-tile array model. The fitted  $g(r)$  were generated by spectral decomposition of the experimental distributions into a linear combination of the single tile ( $X_1$ ), 2-tile array ( $X_2$ ), 3-tile array ( $X_3$ ), and 2x2-tile array ( $X_4$ ) spectra.  $\text{Fit} = a_1X_1 + a_2X_2 + a_3X_3 + a_4X_4$ , where  $a_1 - a_4$  represent the fraction of tiles in each size of array out of the total number of tiles. For the fits of the 25 °C, 30 °C, and 35 °C distributions, the adjusted R-square (adj.  $R^2$ ) values were 0.614, 0.722, and 0.926, respectively.

PAINT. For the temperature dependence of hybridization defects, resolved 2x2-tile arrays were analyzed by counting the number of defects observed on bound arms (Fig. 2.13). Histograms of the results are shown in Figure 2.5a (grey bars). The probability of hybridization defects  $p_d$  for bound tile arms was determined from the results of counting and used to generate binomial distributions for each sample. A negative correlation was

observed between  $p_d$  and the annealing temperature since annealing at higher temperatures inhibits binding between defective structures. These data provide a direct observation that annealing tiles closer to the array melting temperature ( $\sim 40^\circ\text{C}$ ) improved array quality (Fig. 2.14).

While hybridization defects form when docking sites fail to deactivate between bound tile arms, additional defects include missing or extra tiles within a finite array. To study the temperature dependence of the 2x2-tile array size distribution,  $g(r)$  were calculated from defect label images and are shown in Figure 2.5b (black). The experimental  $g(r)$  were decomposed into linear combinations of spectra for single tiles, 2-tile, 3-tile, and 2x2-tile arrays (Figs 2.15,16). These component spectra were simulated using Monte Carlo methods using a curved and twisted tile model (Fig. 2.15). The fitted spectra (red) are overlaid on the experimental  $g(r)$  in Figure 2.5b for comparison (Figs 2.17,18). The results allow quantitative determination of the distribution of tile arrays for each sample. Overall, excellent fits were obtained when the data was modeled using a twisted origami model despite the fact that the experimental data were purely two-dimensional (focal plane). Use of three-dimensional DNA-PAINT techniques may yield additional information valuable to the analysis of array formation.<sup>28,34,35</sup>

The distribution of tile arrays determined by spectral decomposition (Fig. 2.5b) indicates that the fraction of tiles not bound in arrays increased with anneal temperature while the fraction of tiles bound within 2-tile, 3-tile, and 2x2-tile arrays decreased. The quality of fitting (indicated by adj.  $R^2$ ) was also observed to increase with anneal temperature, indicating that the fraction of improperly formed arrays decreased with anneal temperature. Though the tiles were designed to form 2x2-tile arrays, larger tile structures

often form due to agglomeration or out of plane hybridization (Figs 2.9,19); such structures were not accounted for in the simulated distributions for 2x2-tile arrays and are indicated by a decrease in the quality of fitting at lower anneal temperature. These observations validate the use of statistical methods with Xtal-PAINT for quantitative and qualitative studies of DNA origami and origami arrays, and similar techniques can be developed for DNA nanostructures in general.

## 2.5 Conclusions

In summary, we have introduced a versatile optical metrology technique for stepwise, selective characterization of DNA arrays by means of DNA-PAINT and state-dependent docking sites. This approach revealed grain boundaries in tile arrays and provided information on the temperature dependence of array quality. Prior studies of DNA tiling have relied solely on AFM for structural characterization, but AFM imaging influences surface tiling and is not suited for large area imaging in manufacturing. While the Xtal-PAINT image in Figure 4 clearly highlights that there are challenges for creating large-scale ordered arrays with DNA origami tiles, our technique demonstrates the ability to image and quantitatively analyze these structures and gain the insight necessary to improve array formation. Xtal-PAINT provides an approach for large area, inline, defect detection and classification for DNA arrays with the statistical analysis relevant for high volume manufacturing.

## 2.6 Acknowledgements

We thank Bernard Yurke and Hao Chen for valuable discussions and insight, and we thank Paul Davis and Kari Livingston for assistance in AFM imaging. We thank Peng Yin for assistance with super-resolution imaging, localization software, and DNA-PAINT

samples. We thank Mingjie Dai for valuable assistance. We thank Friedrich Simmel and Ali Rafat for valuable discussions and DNA origami tile samples. This work was supported by the National Science Foundation through the Scalable NanoManufacturing grant (CMMI-1344915).

## 2.7 References

- 1 M. M. Waldrop, *Nature*, 2016, **530**, 144–147.
- 2 K. Galatsis, K. L. Wang, M. Ozkan, C. S. Ozkan, Y. Huang, J. P. Chang, H. G. Monbouquette, Y. Chen, P. Nealey and Y. Botros, *Adv. Mater.*, 2010, **22**, 769–778.
- 3 R. A. Segalman, *Mater. Sci. Eng. R Reports*, 2005, **48**, 191–226.
- 4 M. Neisser and S. Wurm, *Adv. Opt. Technol.*, 2015, **4**, 235–240.
- 5 V. Mishra, G. H. Fredrickson and E. J. Kramer, *ACS Nano*, 2012, **6**, 2629–2641.
- 6 P. W. K. Rothmund, *Nature*, 2006, **440**, 297–302.
- 7 F. A. Aldaye, A. L. Palmer and H. F. Sleiman, *Science*, 2008, **321**, 1795–1799.
- 8 E. Winfree, F. Liu, L. A. Wenzler and N. C. Seeman, *Nature*, 1998, **394**, 539–44.
- 9 C. Lin, Y. Liu, S. Rinker and H. Yan, *Chemphyschem*, 2006, **7**, 1641–7.
- 10 E. P. Gates, A. M. Dearden and A. T. Woolley, *Crit. Rev. Anal. Chem. / CRC*, 2014, **44**, 354–70.
- 11 Y. Ke, L. L. Ong, W. M. Shih and P. Yin, *Science*, 2012, **338**, 1177–83.
- 12 C. T. Diagne, C. Brun, D. Gasparutto, X. Baillin and R. Tiron, *ACS Nano*, 2016, **10**, 6458–6463.
- 13 A. M. Hung, C. M. Micheel, L. D. Bozano, L. W. Osterbur, G. M. Wallraff and J. N. Cha, *Nat. Nanotechnol.*, 2010, **5**, 121–6.
- 14 W. Liu, H. Zhong, R. Wang and N. C. Seeman, *Angew. Chemie*, 2011, **123**, 278–281.

- 15 A. Aghebat Rafat, T. Pirzer, M. B. Scheible, A. Kostina and F. C. Simmel, *Angew. Chemie - Int. Ed.*, 2014, **53**, 7665–7668.
- 16 S. Woo and P. W. K. Rothmund, *Nat. Commun.*, 2014, **5**, 4889.
- 17 S. P. Surwade, F. Zhou, B. Wei, W. Sun, A. Powell, C. O'Donnell, P. Yin and H. Liu, *J. Am. Chem. Soc.*, 2013, **135**, 6778–81.
- 18 G. Tikhomirov, P. Petersen and L. Qian, *Nat. Nanotechnol.*, 2017, **12**, 251–259.
- 19 SemiSynBio Consortium and Roadmap, 2016.
- 20 E. Vogel, *Nat. Nanotechnol.*, 2007, **2**, 25–32.
- 21 J. A. Liddle and G. M. Gallatin, *ACS Nano*, 2016, **10**, 2995–3014.
- 22 B. Liang, A. Nagarajan, M. W. Hudoba, R. Alvarez, C. E. Castro and S. Soghrati, *J. Biomech. Eng.*, 2017, **139**, 41003.
- 23 D. J. Kauert, T. Kurth, T. Liedl and R. Seidel, *Nano Lett.*, 2011, **11**, 5558–5563.
- 24 I. H. Stein, V. Schüller, P. Böhm, P. Tinnefeld and T. Liedl, *Chemphyschem*, 2011, **12**, 689–95.
- 25 D. Mathur and I. L. Medintz, *Anal. Chem.*, 2017, **89**, 2646–2663.
- 26 L. Schermelleh, R. Heintzmann and H. Leonhardt, *J. Cell Biol.*, 2010, **190**, 165–175.
- 27 R. Jungmann, C. Steinhauer, M. Scheible, A. Kuzyk, P. Tinnefeld and F. C. Simmel, *Nano Lett.*, 2010, **10**, 4756–61.
- 28 R. Jungmann, M. S. Avendaño, J. B. Woehrstein, M. Dai, W. M. Shih and P. Yin, *Nat. Methods*, 2014, **11**, 313–8.
- 29 R. Iinuma, Y. Ke, R. Jungmann, T. Schlichthaerle, J. B. Woehrstein and P. Yin, *Science*, 2014, **344**, 65–9.
- 30 J. L. Guesdon, T. Ternynck and S. Avrameas, *J. Histochem. Cytochem.*, 1979, **27**, 1131–1139.
- 31 M. Ovesny, Charles University in Prague, 2016.

- 32 R. E. Thompson, D. R. Larson and W. W. Webb, *Biophys. J.*, 2002, **82**, 2775–83.
- 33 C. E. Castro, F. Kilchherr, D.-N. Kim, E. L. Shiao, T. Wauer, P. Wortmann, M. Bathe and H. Dietz, *Nat. Methods*, 2011, **8**, 221–229.
- 34 H. P. Kao and A. S. Verkman, *Biophys. J.*, 1994, **67**, 1291–1300.
- 35 B. Huang, W. Wang, M. Bates and X. Zhuang, *Science*, 2008, **319**, 810–3.

## 2.8 Supporting Information

### 2.8.1 Materials and Methods

#### 2.8.1.1 DNA Origami Synthesis

Single stranded M13mp18 DNA (scaffold strand) was purchased from Bayou Biolabs (Catalog # P-107) at 1.0  $\mu\text{g}/\mu\text{L}$  in 1 x TE buffer (10 mM Tris-HCl, 1 mM EDTA, pH 8.0). Scaffold concentration was calculated to be 420 nM using the molecular weight of M13mp18/19, as reported by New England Biolabs. Staple strands were purchased unfiltered from Integrated DNA Technologies in 1 x TE buffer at 100  $\mu\text{M}$  or dry and rehydrated with 1 x TE buffer to 100  $\mu\text{M}$ . Biotinylated staple strands were purchased HPLC purified from Integrated DNA Technologies dry and rehydrated with 1 x TE buffer to 100  $\mu\text{M}$ .

Individual cross-shaped DNA origami tiles were prepared with 10 nM scaffold strand, 50 nM body staples, and 100 nM edge staples in 0.5 x TBE  $\text{Mg}^{2+}$  buffer (44.5 mM Tris, 44.5 mM boric acid, 1 mM EDTA, 12.5 mM  $\text{MgCl}_2$ ). Thermal annealing was performed in an Eppendorf Mastercycler Nexus Gradient thermal cycler using the recipe reported in Table 2.1. After annealing, tiles were stained with 0.2 x SYBR® Gold nucleic acid gel stain and filtered by agarose gel electrophoresis (uncooled, 0.8 % Agarose, 0.5 x TBE, 8 mM  $\text{MgCl}_2$ ) at 70 V for 2 hours. Filtered tiles were cut from the gel and retrieved by compressing the gel between glass slides.

**Table 2.1 Thermocycler recipe for cross-shaped DNA origami tile synthesis.**

Step	Starting temp.	Cycles	$\Delta T$ per Cycle	Time per Cycle
#	(°C)	#	(°C)	(min)
1	70	1	0	15
2	70	50	-0.1	0.75
3	65	50	-0.1	0.75
4	60	50	-0.1	0.75
5	55	50	-0.1	2
6	50	50	-0.1	2
7	45	50	-0.1	2
8	40	50	-0.1	1.5
9	35	50	-0.1	1.5
10	30	20	-0.5	0.5
11	20	1	0	Hold

### 2.8.1.2 Tile Array Synthesis

Prior to mixing tiles for array formation, all tile solutions were diluted to 1 nM with buffer (0.5 x TBE, 8 mM MgCl<sub>2</sub>) and annealed at 30°C for ten minutes to reduce homogenous tile interactions. Unconstrained tile arrays were assembled by mixing equal parts of A and B tiles at 1 nM in buffer (0.5 x TBE, 8 mM MgCl<sub>2</sub>) and annealing for 24 hours from 38.5 to 35°C at 3 hours per 0.5°C. After annealing, unconstrained tile arrays were immediately deposited into a fluid well and onto mica (coverslip and mica heated to

35°C prior to deposition). For 2x2-tile arrays, tile polymerization was limited by replacing the sticky-ends of the R and D arms of tile A (Figure 2.9a) and L and D arms of tile B (Figure 2.9b) with inert 3 nt polyThymine (pT) extensions, leaving only the defect label strands. 2x2-tile arrays were assembled by mixing equal parts of A and B tiles at 1 nM in buffer (0.5 x TBE, 8 mM MgCl<sub>2</sub>) and annealing for 24 hours at constant temperature (25, 30, or 35°C). After annealing, 2x2-tile arrays were immediately deposited onto mica, then the array solution was diluted by 4x with buffer (0.5 x TBE, 8 mM MgCl<sub>2</sub>) and deposited into fluid wells.

### 2.8.1.3 AFM imaging

Samples for individual A and B tiles were diluted to 1 nM tiles in buffer (0.5 x TBE, 8 mM MgCl<sub>2</sub>) and annealed for 10 minutes at 30°C prior to deposition on mica. After annealing, 15 µL of the tile solution was deposited onto freshly cleaved mica (see above). After 4 min, an additional 100 µL of buffer was added to the mica surface and gently removed by drawing the excess solution up with a pipette to remove any tiles in solution. This rinsing step was repeated three times. After rinsing, 80 µL of buffer with nickel (0.5 x TBE, 8 mM MgCl<sub>2</sub>, 1 mM nickel (II) acetate) was deposited for imaging. AFM images of individual tiles were acquired in Peak Force Tapping mode in fluid on a Dimension Icon (Bruker) using ScanAsyst fluid probes (Bruker). Typical scanning parameters were 30 Hz scan rate, 256 lines, 1 µm x 1 µm area.

Samples for AFM imaging of unconstrained tile arrays and 2x2-tile arrays were prepared by depositing 15 µL of tile arrays at 1 nM (individual tile concentration) in buffer (0.5 x TBE, 8 mM MgCl<sub>2</sub>) onto freshly cleaved mica (Ted Pella, 25 mm x 75 mm Grade V1 mica sheets, 7.8 mm punched diameter). After four minutes the solution was removed

by rinsing with 4 mL DI water and dried with an N<sub>2</sub> gun. AFM images of tile arrays were acquired in Peak Force Tapping mode in air on a MultiMode 8 (Bruker) using ScanAsyst HR probes (Bruker). Typical scanning parameters were 0.8 Hz scan rate, 1024 lines, 10 μm x 10 μm area.

#### 2.8.1.4 Fluid well construction

Open fluid wells were constructed from treated plastic microscope slides (Ted Pella, catalog number: 260225) and Gold Seal® #1 square cover glass (Ted Pella, catalog number: 260341). A ½ in. hole was drilled into the center of the plastic microscope slide using a ½ in. glass and tile bit. For fiducial markers, 50 μL of 200 fM gold nanoparticles in methanol (Nanopartz, 150 nm silane polymer-coated spherical AuNPs, part #: E11-150-Silane-2.5 \*custom order) were deposited onto the coverslip. Treated coverslips were attached to drilled microscope slides with two-part epoxy.

#### 2.8.1.5 Fluid well sample preparation

Fluid wells were rinsed twice with 200 μL DI water, then 200 μL of 1 mg/mL biotin-labeled bovine serum albumin (Sigma-Aldrich, catalog number: A8549) in buffer 1 (1 x Tris-HCl, 150 mM NaCl) was deposited in the fluid well. After two minutes, the fluid well was rinsed twice with 200 μL buffer 1, and 200 μL of 1mg/mL NeutrAvidin (ThermoFisher Scientific, catalog number: 31000) in buffer 1 was deposited in the fluid well. After two minutes, the fluid well was rinsed twice with 200 uL buffer 2 (0.5 x TBE with 8 mM MgCl<sub>2</sub>). For unconstrained tile arrays and 2x2-tile arrays, the fluid wells were heated to the temperature of the final array annealing step for sample deposition. 200 μL of buffer 2 was deposited in fluid wells prior to heating. For individual tile samples, fluid wells were not heated for deposition (fluid well deposition temperature ~20°C).

Before deposition into fluid wells, individual tile samples were diluted to 100 pM in buffer 2 and 2x2-tile arrays were diluted to 250 pM in buffer 2. Tile or tile array solutions were deposited in the fluid well, and after two minutes the fluid well was rinsed with 200  $\mu$ L of 0.1% Tween-20 (Sigma-Aldrich, catalog number: P9416) in buffer 3 (0.5 x TBE, 18 mM MgCl<sub>2</sub>). After five minutes, the fluid well was rinsed twice with 200  $\mu$ L of buffer 3, then 200  $\mu$ L of buffer 3 was deposited in preparation for imaging.

#### 2.8.1.6 Optical Setup

Fluorescence imaging was performed on a Nikon Eclipse TiU microscope equipped with a Nikon TIRF illuminator and a Nikon CFI Apo TIRF 100x NA 1.49 objective. An additional 1.5x magnification was used to achieve a total magnification of 150x and a pixel size of 107 nm. A 561 nm laser (Coherent Sapphire) was used for illumination with a 0.5x stop down (~8 mW TIRF illumination). A Chroma TRF49909 ET-561nm filter set was used to spectrally filter laser output. A Princeton Instruments ProEM EMCCD camera, using the imaging software LightField, was set to 25x EM gain and a data acquisition rate of 6.66 Hz. 15,000 frames were captured during each acquisition step (Figure 2.7). Focal drift was corrected in real time with an optical system and feedback loop developed in house.

#### 2.8.1.7 Super-resolution Xtal-PAINT imaging

For Xtal-PAINT imaging, two imager strand solutions and one rinsing solution were prepared. Cy3b-labeled imager strands were purchased dual HPLC-filtered from Bio-Synthesis dry and rehydrated to 10  $\mu$ M with 1 x TE buffer. The rinsing strand, M1\*, was purchased from Integrated DNA Technologies dry and rehydrated to 100  $\mu$ M with 1 x TE buffer. For imager solution 1, Cy3b-labeled imager strand M1' was diluted to 3 nM in

buffer 3. For imager solution 2, Cy3b-labeled imager strand M2' was diluted to 3 nM in buffer 3. For the rinsing solution, rinsing strand M1\* was diluted to 10 nM in buffer 3. For imaging, 200  $\mu$ L of imager solution 1 was first introduced to the fluid well for imaging. After imaging, the fluid well was washed with the rinsing solution to remove and passivate any remaining M1' imager strands. Following rinsing, 200  $\mu$ L of imager strand M2' was introduced to the fluid well for imaging.

Image localization, drift correction, and image post-processing were performed with the ThunderSTORM<sup>30</sup> plugin for ImageJ,<sup>31</sup> available for download at <http://zitmen.github.io/thunderstorm/>, and exported at 40x magnification. Defect label images were pseudo-colored using the 'Cyan Hot' LUT available in ImageJ, and lattice site images were pseudo-colored using the 'Yellow' LUT available in ImageJ.

## 2.8.2 Counting method and statistics

### 2.8.2.1 Counting

Self-limiting 2x2-tile array hybridization defect counting was performed using ImageJ to track the progress of counting. Hybridization defect counting was performed only on structures that could be confidently identified as 2x2-tile arrays by the presence of defect labels and lattice sites in a recognizable pattern. 2x2-tile arrays were counted by the number of defect labels resolved on bound tile arms (within the array). The number of 2x2-tile arrays counted was reported for each case; counting data is available in Table 2.5.

### 2.8.2.2 Statistical analysis with radial distribution function $g(r)$

The radial distribution functions of experimental and simulated images were calculated using the 'Radial Distribution Function' plugin for ImageJ which is accessible at [http://imagejdocu.tudor.lu/doku.php?id=macro:radial\\_distribution\\_function](http://imagejdocu.tudor.lu/doku.php?id=macro:radial_distribution_function).

## 2.8.3 Supporting Figures

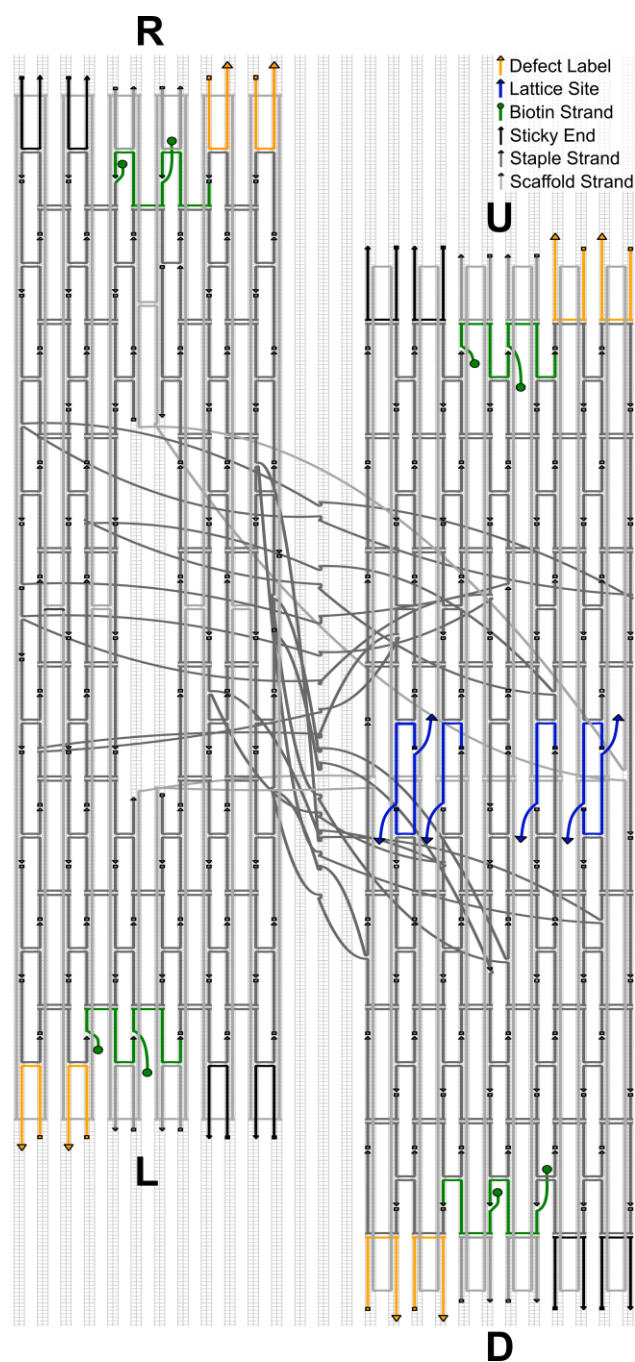


**Figure 2.6** Strand diagram for cross-shaped DNA origami A-tile. Strand diagram exported from caDNAno and altered to depict modifications to the tile for Xtal-PAINT imaging and tile array formation. Individual strand sequences and imager strand sequences can be found in Tables 2.1-3. Original design and naming convention for individual strands were adopted from Liu et al.

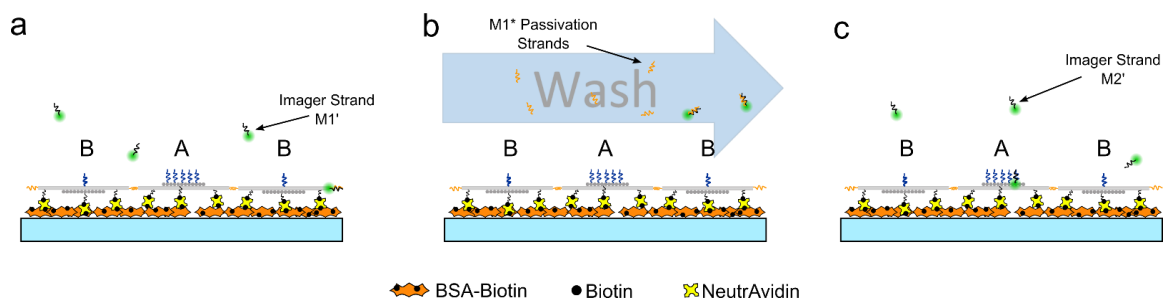


**Figure 2.7** Schematic depicting step-wise Xtal-PAINT imaging. (a) Schematic depicting defect label imaging of tile arrays bound to glass coverslip by biotin-avidin binding, with 3 nM imager strand M1' in solution. Biotinylated bovine serum albumin (BSA-Biotin) was used to functionalize the surface and immobilize tile structures by protein binding. (b) Rinse to remove imager strand M1' and deactivate remaining strands with 10 nM M1\* imager passivation strands. Imager passivation strands were observed to effectively deactivate imager strands even when added directly to the imaging solution. (c) Lattice site imaging with 3 nM imager strand M2'. All buffer solutions contain 0.5x TBE 18mM MgCl<sub>2</sub>, and 15,000 frames were captured at 6.66 Hz during each imaging step.

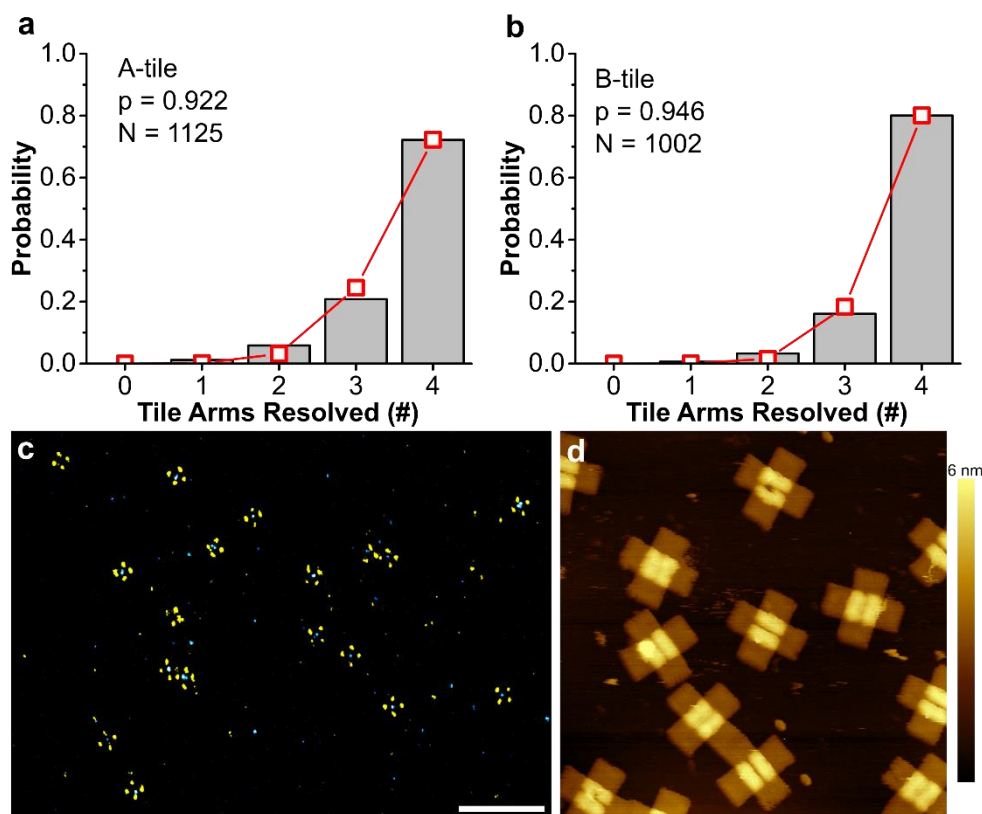


**Figure 2.8** Xtal-PAINT and AFM images of individual tiles. (a,b) For A-tiles and B-tiles imaged by Xtal-PAINT, probability histograms for the number of defect label sites counted per tile are shown (grey bars), where  $p$  is the probability of resolving defect label sites on an individual tile arm, and  $N$  is the total number of tiles counted. Binomial distributions (red) were generated from the results of counting to calculate  $p$  given that each tile has four arms. The data for individual tile counting statistics can be found in Table 2.2. (c) Xtal-PAINT image of individual B-tiles displaying defect labels (yellow) and lattice sites (blue). Scale bar, 500 nm. (d) AFM image of individual B-tiles on mica, imaged in fluid (0.5x TBE with 12 mM  $MgCl_2$  and 2mM  $NiCl_2$ ). Image dimensions, 500 nm x 500 nm. To reduce homogeneous interactions between tiles, tile solutions were heated to 30 °C prior to deposition in fluid wells and on mica.

**Table 2.2** Individual tile counting statistics

	Count (A-tile)	Count (B-tile)	Probability (A-tile)	Probability (B-tile)	Binomial PDF (A-tile)	Binomial PDF (B-tile)
Number of Arms Resolved	#arrays	#arrays	-	-	-	-
4	812	802	0.722	0.800	0.723	0.801
3	234	161	0.208	0.161	0.245	0.183
2	66	33	0.059	0.033	0.031	0.016
1	13	6	0.012	0.006	0.002	0.001
*0	0	0	0.000	0.000	0.000	0.000





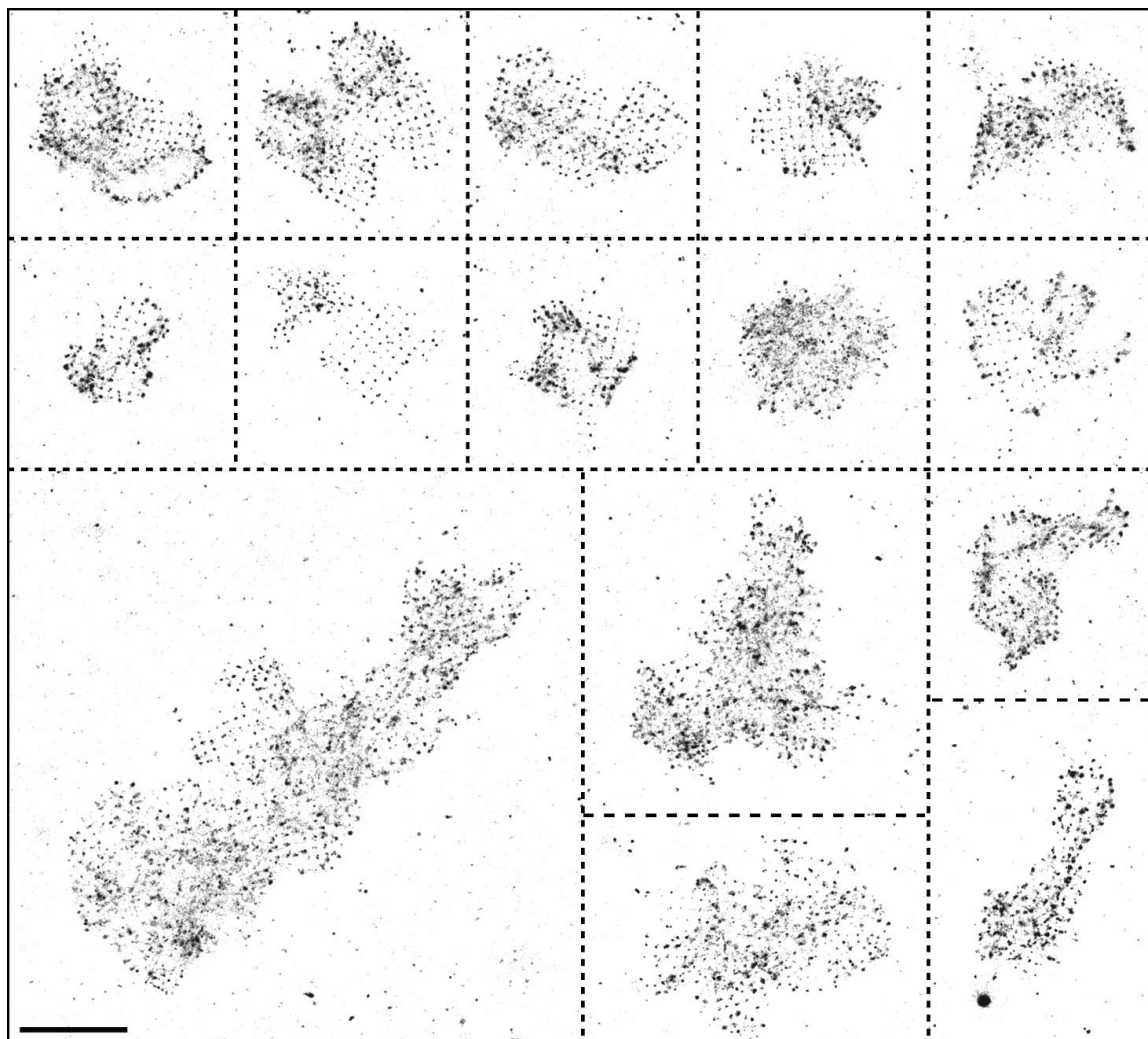


**Figure 2.11** Xtal-PAINT lattice images of large tile arrays with curvature. Inverted grayscale Xtal-PAINT lattice images of large tile arrays that were unable to flatten on the surface, indicated by indistinct, blurred regions of the array and/or curved lattice site paths. Blurring was observed in all of the arrays due to imager strand binding to lattice sites located outside of the focal plane. This effect was rarely observed in tile arrays smaller than  $1\ \mu\text{m} \times 1\ \mu\text{m}$ , though it is unlikely that the curvature observed in large arrays was caused by global curvature since no tube-like structures were observed. Rather, tile arrays were unable to relax or flatten on the surface due to immobilization by biotin-avidin binding. Large tile arrays are more likely to experience large fluctuations away from planarity due to local fluctuations of the solution, and any deformation that occurs in tile arrays while binding to the surface may be trapped in the structure. Scale bar,  $1\ \mu\text{m}$ .

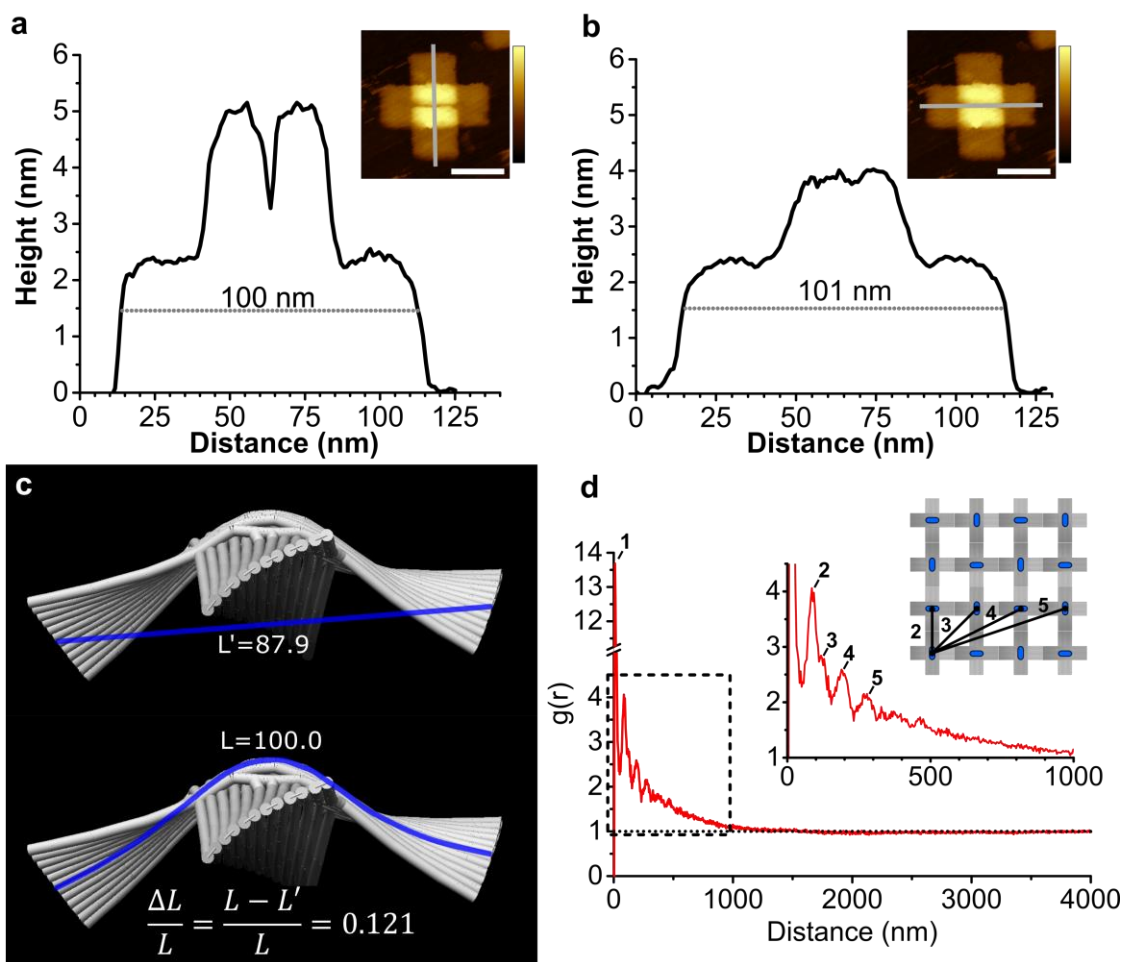


**Figure 2.12** Analysis of cross-shaped DNA origami tile dimensions. (a) and (b) Topographic profiles of a cross-shaped DNA origami tile in the directions perpendicular to and parallel to the central indent of the tile, respectively. The dimensions of the tile along both directions are approximately 100 nm, in agreement with the dimensions reported by Liu et. al. Scale bars, 50 nm. AFM height color bar, 5.5 nm. (c) Cando-generated model of the cross-shaped DNA origami tile. The contraction in the dimensions of the Cando model due to curvature and twist were calculated by the difference between the path length of the helices and the straight-line distance between each end of a tile arm. The observed contraction in the length of the tile arm was approximately 12%. (d) Radial distribution function of an Xtal-PAINt lattice image of unconstrained tile arrays. The first peak was observed at 10 nm (peak 1). The peak corresponding to the center to center distance between bound tiles in a tile array was observed at 87.4 nm (peak 2), a ~13% contraction in the dimensions of the tile relative to the tile dimensions observed in AFM images of tiles on mica in a,b. This result is in agreement with the contraction observed in the Cando tile model. Additional peaks were observed at 123 nm, 195 nm, and 275 nm (peaks 3-5), corresponding to the 2<sup>nd</sup>, 4<sup>th</sup>, and 7<sup>th</sup> nearest neighbor distances for a square lattice with a lattice constant of 87 nm. Peak positions were determined by fitting individual peaks with Gaussian functions. Statistics for the results of peak fitting for peaks 2-5 are provided in Table 2.4.

**Table 2.3 Peak fitting statistics for unconfined tile arrays**

	Peak position		Peak width		sigma	FWHM	Height	Statistics	
	Value (nm)	Standard Error	Value (nm)	Standard Error	Value (nm)	Value (nm)	Value	Reduced Chi-Sqr	Adj. R-Square
<b>Peak 2</b>	87.40071	0.51087	26.5205	5.14706	13.26025	31.2255	1.63016	0.01118	0.94422
<b>Peak 3</b>	122.7505	7.59605	20.76644	18.22743	10.38322	24.45061	0.46998	0.15444	0.94465
<b>Peak 4</b>	194.92566	6.28781	30.5346	18.75183	15.2673	35.95175	0.65668		
<b>Peak 5</b>	275.39338	11.32762	37.26473	32.74182	18.63236	43.87586	0.43181		

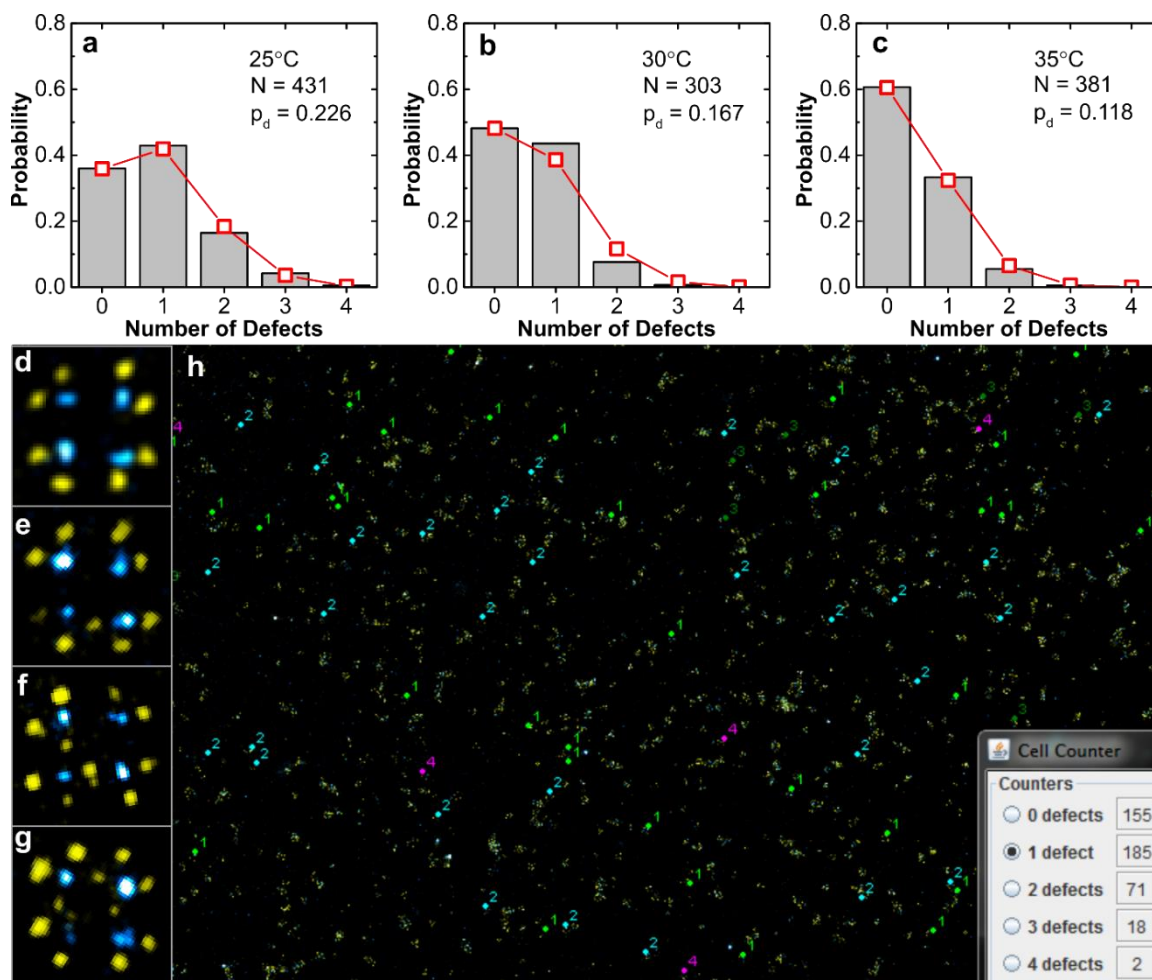


**Figure 2.13** Results of defect quantification for 2x2-tile arrays. (a-c) For self-limiting 2x2-tile array samples annealed at 25, 30, and 35 °C, respectively, probability histograms for the number of hybridization defects observed per 2x2-tile array are shown (grey bars), where N is the number of 2x2-tile arrays counted and  $p_d$  is the probability of observing a hybridization defect on tile arms bound by sticky-end hybridization for each sample. Binomial distributions (red) were generated from the results of counting to calculate  $p_d$ . The number of defects was observed to decrease linearly with anneal temperature as expected due to the decreased stability of sticky-end hybridization between defective structures. These results provide evidence that annealing inhibits hybridization between defective structures. The data for 2x2-tile array defect counting can be found in Table 2.5. (d-g) Examples of 2x2-tile arrays imaged by Xtal-PAINT with 0, 1, 2, and 3 defects, respectively. (d) Example of counting window for 2x2-tile array defect counting. Counting results for sample annealed at 25 °C are shown.

**Table 2.4 Self-limiting 2x2-tile array defect counting statistics**

	Count (25°C)	Count (30°C)	Count (35°C)	Probability (25°C)	Probability (30°C)	Probability (35°C)	Binomial PDF (25°C)	Binomial PDF (30°C)	Binomial PDF (35°C)
Number of Defects	#arrays	#arrays	#arrays	-	-	-	-	-	-
0	155	146	231	0.360	0.482	0.606	0.359	0.481	0.605
1	185	132	127	0.429	0.436	0.333	0.419	0.386	0.324
2	71	23	21	0.165	0.076	0.055	0.184	0.116	0.065
3	18	2	2	0.042	0.007	0.005	0.036	0.016	0.006
4	2	0	0	0.005	0.000	0.000	0.003	0.001	0.000

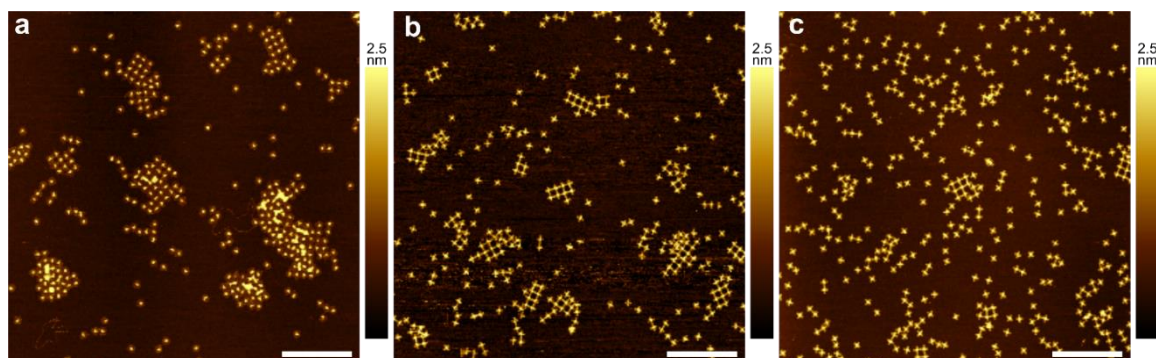


**Figure 2.14** AFM images of tile arrays formed by constant temperature annealing. (a-c) AFM images of unconstrained tile arrays on mica, annealed for three hours at 35, 37, and 40 °C, respectively, in 0.5x TBE 8mM MgCl<sub>2</sub>. As expected, the average size of tile arrays was observed to decrease with anneal temperature, and few arrays were observed in the sample annealed at 40 °C. All samples were prepared in parallel and immediately deposited on mica after annealing, though cooling of each solution on contact with mica likely contributed to a small degree of array formation in each case. The images indicate that the temperature of formation of tile arrays by sticky-end hybridization in 0.5x TBE 8mM MgCl<sub>2</sub> is near 40 °C. Scale bars, 1 μm.

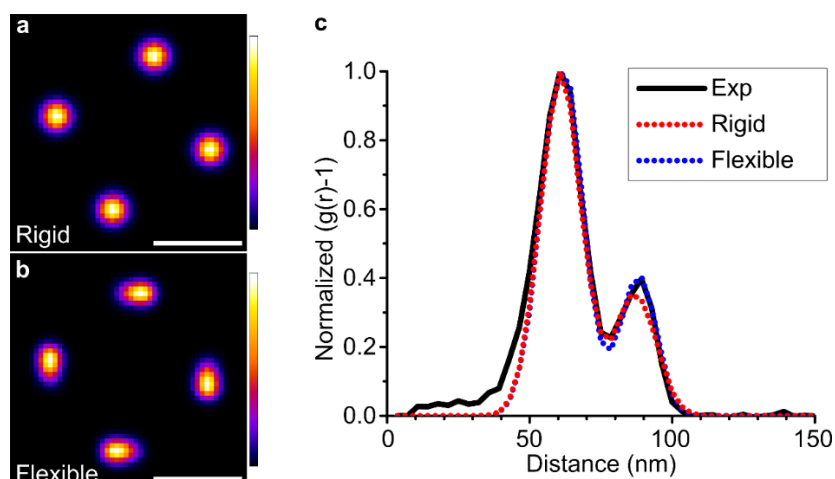


**Figure 2.15** Simulated radial distribution function of rigid and flexible tile models. (a) Probability distribution of tile defect label positions for a rigid tile model, generated by Monte Carlo methods ( $N=10^5$ ). For a rigid model, each point distribution is rotationally symmetric. (b) Probability distribution of tile defect label positions for a “flexible” tile model with an additional degree of freedom to account for twisting, generated by Monte Carlo methods ( $N=10^5$ ). In comparison to the rigid model, the point distributions of the flexible tile model are elongated tangent to the tile. Scale bars, 50 nm. Probability color bar, linear from 0 to 1 AU. (c) Radial distribution functions of the rigid and flexible tile models plotted with the experimental  $g(r)$  for comparison. For a valid comparison of the shape of each distribution, the contribution of random tile positions was removed from the experimental distribution by subtracting 1 and all distributions were normalized by the maximum values of each distribution (corrections validated in Figure 2.17). The shape, position, and relative height of the second peak of the experimental distribution could not be accounted for with a rigid tile model, demonstrating the need for a tile model that accounted for the effect of arm twist on the positions of defect labels.

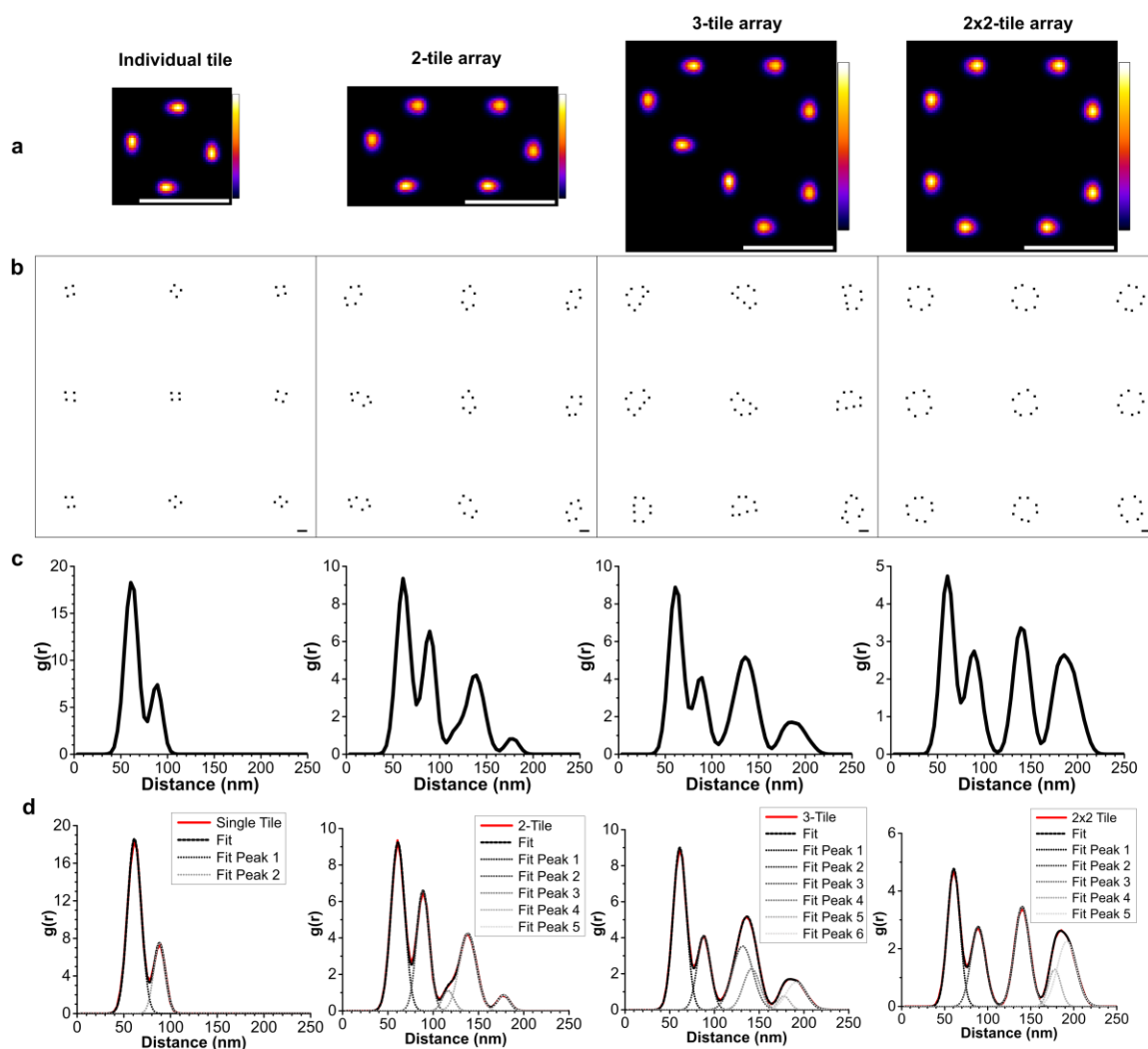


**Figure 2.16** Simulated radial distribution functions for tile arrays. (a) Probability distributions of defect label positions for the flexible models of individual tiles, 2-tile arrays, 3-tile arrays, and 2x2-tile arrays. Scale bars, 100 nm. (b) Simulated images of tile structures with uniform spacing, random orientation, and random defect label positions defined by the corresponding probability distributions in a. The densities of tiles and arrays were equivalent for all images. (c) Radial distribution functions of simulated tiles and arrays corresponding to a and b. For each structure,  $g(r)$  was calculated from a stack of 16 images, each image containing 625 evenly spaced structures, a total of  $10^4$  simulated structures. (d) Peak fitting of  $g(r)$  for the simulated distributions. Each distribution was approximated as a sum of Gaussian distributions, and the results of fitting were used for linear decomposition of experimental spectra.

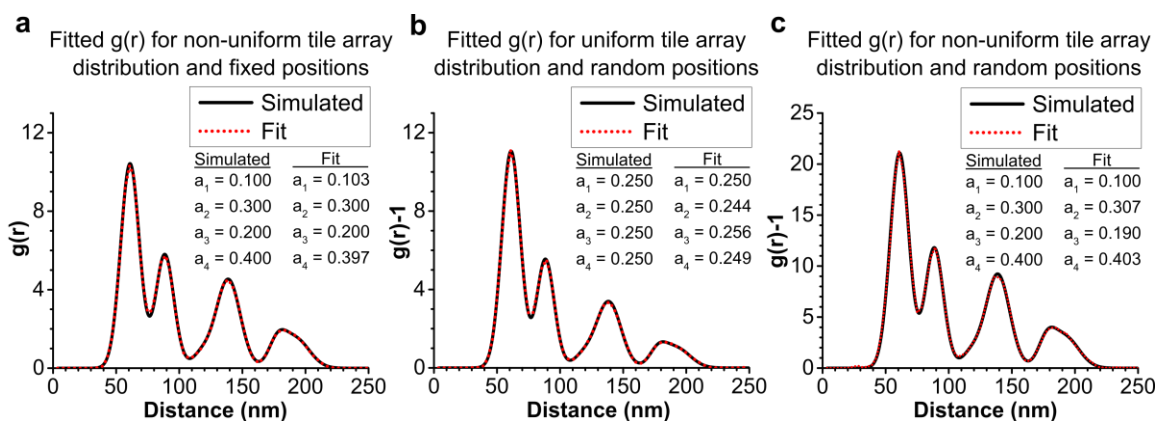


**Figure 2.17 Radial distribution function for randomized position and tile distribution.** (a) Simulated  $g(r)$  for a sample with a non-uniform but known distribution of tiles and arrays. To determine if the distribution of tile arrays in an Xtal-PAINT image could be quantified from  $g(r)$ , the simulated  $g(r)$  was fitted with a linear combination of the individual tile, 2-tile array, 3-tile array, and 4-tile array spectra. The fitted  $g(r)$  is plotted along with the simulated  $g(r)$ . The distribution of tiles and arrays was accurately predicted by the fraction of each component in the fitted  $g(r)$ , validating the use of  $g(r)$  to quantify distributions of tile arrays. (b) Simulated  $g(r)$  and fitted spectra for a uniform distribution of tile arrays with randomized positions within the image. (c) Simulated  $g(r)$  and fitted spectra for a non-uniform distribution of tile arrays with randomized positions within the image. The spectra used for fitting did not have randomized positions (Figure 2.16), though at low point densities the contribution of randomness can be effectively removed by subtracting 1 from  $g(r)$ . This is demonstrated by the fitted spectra in b and c.

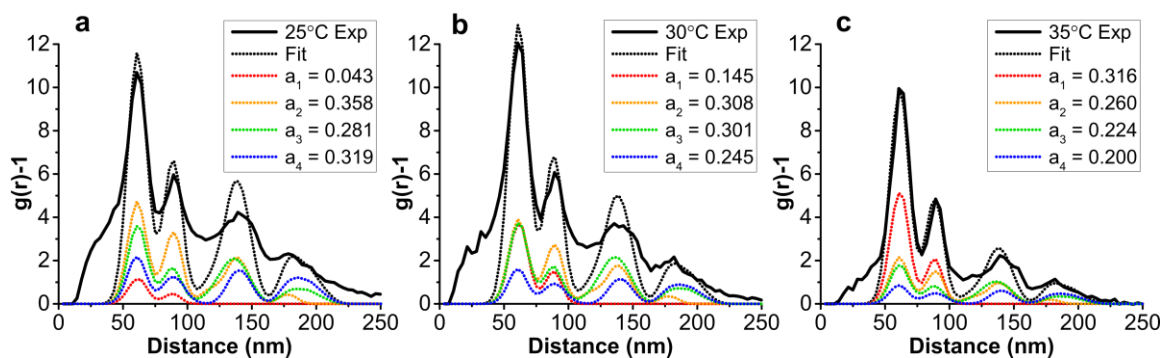


**Figure 2.18** Linear decomposition of experimental  $g(r)$  into simulated spectra. (a-c) Experimental, fitted, and component  $g(r)$  for constrained  $2 \times 2$ -tile array samples annealed at 25, 30, and 35 °C, respectively. The fitted  $g(r)$  were generated by spectral decomposition of the experimental  $g(r)$  into a linear combination of spec single tile ( $X_1$ ), 2-tile array ( $X_2$ ), 3-tile array ( $X_3$ ), and  $2 \times 2$ -tile array ( $X_4$ ) spectra.  $\text{Fit} = a_1X_1 + a_2X_2 + a_3X_3 + a_4X_4$ , where  $a_1$ - $a_4$  represent the fraction of tiles in each size of tile array out of the total number of tiles. The isolated component spectra are shown in Figure 2.16. The fraction of tiles bound by sticky-end hybridization ( $a_2$ - $a_4$ ) was observed to decrease with anneal temperature. The deviation of fitted  $g(r)$  from experimental  $g(r)$  also decreased with anneal temperature due to a decrease in the fraction of tile structures that are not accounted for by the isolated component spectra (Figure 2.19).

**Table 2.5** Statistics for fitting of experimental  $g(r)$

	a1		a2		a3		a4		Statistics	
	Value	Standard Error	Reduced Chi-Sqr	Adj. R-Square						
25 °C	0.04254	0.06067	0.35795	0.19343	0.28067	0.22905	0.31885	0.17504	2.09289	0.61456
30 °C	0.14535	0.06201	0.30843	0.19088	0.30118	0.22692	0.24504	0.17802	1.89167	0.72172
35 °C	0.31642	0.04411	0.25982	0.1232	0.22424	0.14351	0.19952	0.11692	0.32711	0.92639

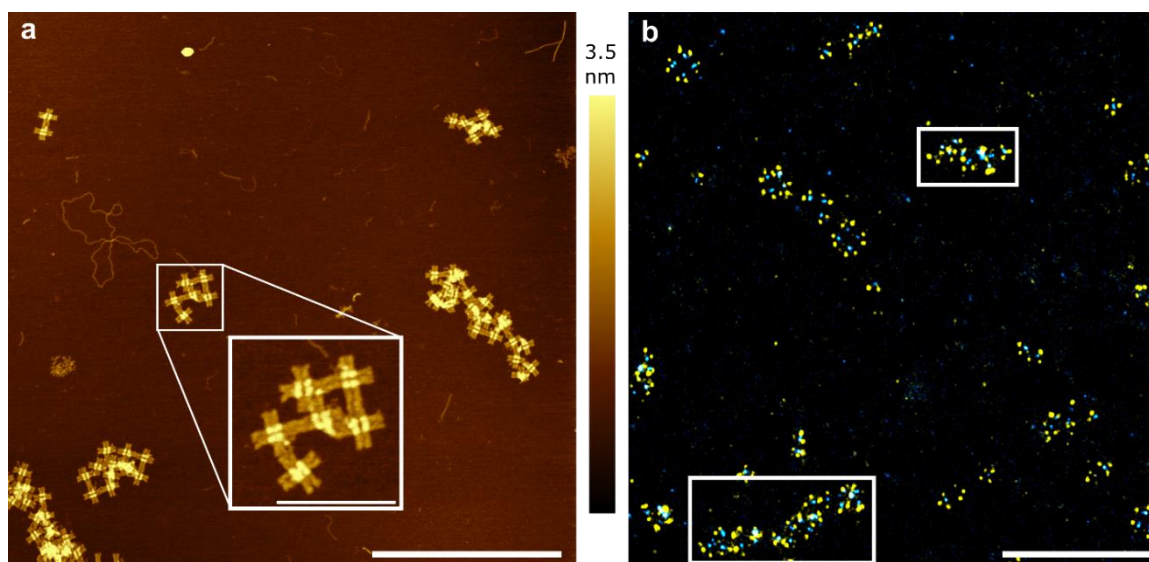


**Figure 2.19** Xtal-PAINT and AFM images of extended 2x2-tile arrays. (a) AFM image of a self-limiting 2x2-tile array sample on mica. In the image, several tile arrays were observed that failed to terminate at 2x2-tile arrays. The tile array magnified in the image demonstrates out-of-plane sticky-end hybridization, which enables tile arrays to extend beyond the intended 2x2-tile structure. Several larger tile arrays were also observed in the image. (b) Xtal-PAINT image of a self-limiting 2x2-tile array sample. Several large tile structures were resolved that failed to terminate at 2x2-tile arrays due to out-of-plane sticky-end hybridization, closely resembling tile arrays observed in a. Scale bars, 1  $\mu\text{m}$ . Inset scale bar, 250 nm.

**Table 2.6 Strand sequences for cross-shaped DNA origami tile (body strands)**

Name	Sequence	Length (bp)	Type
CO-M-001	AGCTAATGCAGAACGCGCCTGTTTTAATATCC	32	
CO-M-002	CATCCTAATTTGAAGCCTTAAATCTTTTATCC	32	
CO-M-003 [B]	5Biosg\ TTTTTTTTTT TGAATCTTGAGAGATAACCCACAAAACAATGA	42	Biotin-labeled
CO-M-004 [B]	5Biosg\ TTTTT AATAGCAATAGATGGGCGCATCGTACAGTATC	37	Biotin-labeled
CO-M-005	GGCCTCAGCTTGCATGCCTGCAGGGAATTCGT	32	
CO-M-006	AATCATGGTGGTTTTTCTTTTCACCCGCCTGG	32	
CO-M-007	CCCTGAGAGAGTTGCAGCAAGCGGGTATTGGG	32	
CO-M-008	CGCCAGGGTCATAGCTGTTTCTGGACGGCCA	32	
CO-M-009 [c]	GTGCCAAGGAAGATCGCACTCCAGATAGGTCA	32	
CO-M-010	CGTTGGTGTAGCTATCTTACCGAATTGAGCGC	32	
CO-M-011 [c]	TAATATCAACCAACGCTAACGAGCCCGACTTG	32	
CO-M-012	CGGGAGGTTTTACGAGCATGTAGAACATGTTC	32	
CO-M-013	CTGTCCAGACGACGACAATAAACAAACCAATC	32	
CO-M-014	AATAATCGCGTTTTAGCGAACCTCGTCTTTCC	32	
CO-M-015	AGAGCCTACAAAGTCAGAGGGTAAGCCCTTTT	32	
CO-M-016	TAAGAAAAGATTGACCGTAATGGGCCAGCTTT	32	
CO-M-017	CCGGCACCCACGACGTTGTA AAACTGTGAAAT	32	
CO-M-018	TGTTATCCGGGAGAGGCGGTTTGCTCCACGCT	32	
CO-M-019	GGTTTGCCCCAGCAGGCGAAAATCAATCGGCC	32	
CO-M-020	AACGCGCGGCTCACAATTCACACCCAGGGTT	32	
CO-M-021	TTCCCAGTGCTTCTGGTGCCGGAAGTGGAAC	32	
CO-M-022	AAACGGCGGTAAGCAGATAGCCGAACTGAAC	32	
CO-M-023	ACCCTGAAATTTGCCAGTTACAAATTCTAAGA	32	
CO-M-024	ACGCGAGGGCTGTCTTTTCCTATCAAGTAATT	32	
CO-M-025	AATATAAAGTACCGACAAAAGGTAATTCCAAG	32	
CO-M-026	AACGGGTAGAAAGCTTATCCGGTAATAAACAG	32	

CO-M-027	CCATATTAATTAGACGGGAGAATTACAAAGTTACC	35	
CO-M-028	GTCGGATTCTCCACCAGGCA	20	
CO-M-029	AAGCGCCAATTAAGTTGGGTAACGAACATACG	32	
CO-M-030	AGCCGGAAGCCAGCTGCATTAATGCTGTTTGATGGTGTCTTCTGTAG	48	
CO-M-031	CCTGTCTGCATAAAGTGTAAGCGATGTGCT	32	
CO-M-032	GCAAGGCGTTCGCCATTCAGGCTGCGCAACTG	32	
CO-M-033	GGAAGCGCTTTATCCCAATCCAAAAAGCAAAT	32	
CO-M-034	CAGATATATTAACCATACGGAAATTACCCAAAAGAACTGGCATGATTA	49	
CO-M-035	AGGCATTTTCGAGCCAGTACTCATCG	26	
CO-M-036	AGAACAAGTACCGCGCCAATAGCTAAGAAAC	32	
CO-M-037	GATTTTTTACAGAGAGAATAACATAAAAAACAG	32	
CO-M-038	TTGGGAAGCAGCTGGCTTAAAGCTAGCTATTTTTGAGAGATCTGGAGCA	49	
CO-M-039	CCTAATGAACTGCCCGCTTTCCAGCCCTTATA	32	
CO-M-040	AATCAAAAGAATAGCCCTTTAAATATGCATTCTACTAATAGTAGTAACATTAT	53	
CO-M-041	GAGATAGGTTGTCAGGATTAG	22	
CO-M-042	TTGCGCTCGTGAGCTAACTCACATGATAGCCC	32	
CO-M-043	TATTACGCGGCGATCGGTGCGGGCGAGGATTT	32	
CO-M-044	CAGCCTTTGTTTAAACGTCAAAAATTTTCAATT	32	
CO-M-045	GGAATCATCAAGCCGTTTTTATTTGTTATATA	32	
CO-M-046 [c]	CCAACATGTTGTGCCCGTATA	21	
CO-M-047	ACTATATGCTCCGGCTTAGGTTGGTCATCGTA	32	
CO-M-048	ACCTGAGCAGAGGCGAATTATTCAGAAAATAG	32	
CO-M-049	AGAAGTATAATAGATAATACATTTCTCTTCGC	32	
CO-M-050	TAAAACATCTTTAATGCGCGAACTTAATTGCG	32	
CO-M-051	CTATTAGTCGCCATTA AAAATACCATAGATTA	32	
CO-M-052	GAGCCGTCTAGACTTTACAAACAATTCGACAA	32	
CO-M-053	AATCGCGCAAAAGAAGTTAGTTAGCTTAAACAGCTTGATACGCCACGC	49	
CO-M-054	TTTTTAACTAAATGCTGATGCAAAATTGAGAA	32	
CO-M-055	TCGCCATATTTAACAACGTTGCGGGTTTTAAGCCCAATAGGAACCTTGTCGTC	54	
CO-M-056	CAAGACAAAAATCATAGGCTGAGACAAACAT	32	
CO-M-057	CAAGAAAAATTGCTTTGAATACCAAGTTACAA	32	

CO-M-058	CTCGTATGGTGCACTAACAACTAGAACGAAC	32	
CO-M-059	CACCAGCAGGCACAGATTTAATTTCTCAATCATAAGGGAACCGAACTGA	49	
CO-M-060	TGCTGGTAATATCCAGAACAATATAAGCGTAA	32	
CO-M-061	GAATACGTGAAGATAAAACAGAGGATCTAAAA	32	
CO-M-062	TATCTTTAAAAATCCTTTGCCCGAACCGGACCTGC	35	
CO-M-063	CGAAACAAAGTAATAACGGA	20	
CO-M-064	TTCGCCTGCAAAAATTAATTACATTAATAGTGA	32	
CO-M-065	ATTTATCAAGAACGCGAGAAAAC TAGTATAAAGCCAATAAAGAATACAC	49	
CO-M-066	ATATGCGTTATACAAATCTTACCTTTTCAA	32	
CO-M-067	TATATTTGACGCTGAGAAGAGTCTAACAAT	32	
CO-M-068	TGATTTGATACATCGGGAGAAACACAACGGAG	32	
CO-M-069	TTTGGATTATACCTGATAAATGTGTGCAAAATCGTTATTA	40	
CO-M-070	ATTTTAAAGGAATTGAGGAAGGTTTGAGCGG	32	
CO-M-071	TCAGTATTAACCCTTCTGACCTGATACCGCCA	32	
CO-M-072	GCCATTGCAACAGGAAAAACGCTCTGGCCAAC	32	
CO-M-073 [c]	AGAGATAGAACACCGCCTGCAACAAAATCAAC	32	
CO-M-074	AGTAGAAAAGTTTGAGTAACATTA	24	
CO-M-075	ATTTGTATCATCGCTTCTGAATTACAGTAACA	32	
CO-M-076	GTACCTTTATTACCTTTTTTAATGCGATAGCT	32	
CO-M-077 [c]	TAGATTAAGTTAATTTTCATCTTCTTAGTATC	32	
CO-M-078	TCATAATTACTAGAAAAAGCCTGTTGACCTAA	32	
CO-M-079	ATTTAATGATCCTTGAAAACATAGGAAACAGT	32	
CO-M-080	ACATAAATACGTCAGATGAATATATGGAAGGA	32	
CO-M-081 [c]	TTAGAACCAATATAATCCTGATTGTCATTTTG	32	
CO-M-082	CGGAACAATATCTGGTCAGTTGGCGTGCCACG	32	
CO-M-083	CTGAGAGCAATAAAAGGGACATTCATGGAAAT	32	
CO-M-084 [c]	ACCTACATTTTGACGCTCAATCGTCAGTCACA	32	
CO-M-085	CGACCAGTCAGCAGCAAATGAAAATCAAACCC	32	
CO-M-086 [B]	$\gamma$ Biosgl TTTTTTTTTT TCAATCAAAGAAACCACCAGAAGGATGATGGC	42	Biotin-labeled
CO-M-087 [B]	$\gamma$ Biosgl TTTTT AATTCATCTACCATATCAAAATTATAGATTTT	37	Biotin-labeled

CO-M-088	CAGGTTTACAATATATGTGAGTGATTAATTTT	32	
CO-M-089	CCCTTAGAGTTTGAAATACCGACCCACCGGAA	32	
CO-M-090	ATAAGCAAAAATTCGCGTTAAATTTTGTAA	32	
CO-M-091	CTCATATAAAAGATTCAAAAGGGTAAGATTGT	32	
CO-M-092 [B]	5Biosgl TTTT CGAACGAGAAATGGTCAATAACCTTTAGAACC	37	Biotin-labeled
CO-M-093 [B]	5Biosgl TTTTTTTTT ATAGTCAGGGAAGCCCGAAAGACTCAATTCTG	42	Biotin-labeled
CO-M-094	ACCACATTTTACGAGGCATAGTAATGACTATT	32	
CO-M-095 [c]	CAAGAGTAATCAACGTAACAAAGCTTAGGAAT	32	
CO-M-096 [c]	CAGTGAATGCGCATAGGCTGGCTGACCTTCAT	32	
CO-M-097 [c]	CTATCATAAATTCATCAGTTGAGATTGCTCATT	32	
CO-M-098	CGCGTTTTAATCAGGTCTTTACCCGAGCAACA	32	
CO-M-099	ATATTTTCTGTAACAGTTGATTCCTCAAATAT	32	
CO-M-100	CCGGAGACGCAAGGATAAAAATTTGTTAGCT	32	
CO-M-101	ATCAGCTCAAGCCCCAAAAACAGGGAGAAAGG	32	
CO-M-102	AATCAGAAATTTTAAACCAATAGGAACGCCA	32	
CO-M-103	ATTTCAACAGTCAAATCACCATCACGGTTGAT	32	
CO-M-104	TCATTCCAATTTGGGGCGCGAGCTAAGCCTTT	32	
CO-M-105	AAATCAAAAATTCGAGCTTCAAAGTGAAGTT	32	
CO-M-106	GTAGAAAGACCCTCGTTTACCAGAATGACCAT	32	
CO-M-107 [c]	CAGACCAGAAGGCTTGCCCTGACGTATTACAG	32	
CO-M-108	CAGAACGAGAAAGAGGACAGATGAACGGTGTA	32	
CO-M-109 [c]	AAAACCAAATAACGGAACAACATAGAAACAC	32	
CO-M-110 [c]	ACCGGAAGAGTTCAGAAAACGAGACGACGATA	32	
CO-M-111	GGCATCAAATAAAGTACGGTGTCGAACCCAG	32	
CO-M-112	TTCAACCGAATACTTTGCGGGAGGAAAAGGT	32	
CO-M-113	TCAAAAATTCATCATATGTACCCATATGATA	32	
CO-M-114	CTAGCATGAATTCGCGTCTGGCTGTCCGAAATCGGC AAAATTCGGGAAA	50	
CO-M-115	GACCCTGTTTCTAGCTGATAAATTCGTA AAA	32	
CO-M-116	AACAGTTAACAGAGCCGCCAGAACCCG	32	
CO-M-117	CTTTAAACCAAATCCAACAGTTGAGTGTGTTCTG TAGAAGA ACTCAAAC TTTGAATGG	59	

CO-M-118	TAAAACGAAATAGCGAGAGGCTTTCTCAAATG	32	
CO-M-119	CCAACCTTGTAGTAAATTGGGCTTTACGTAA	32	
CO-M-120	AAGTTTTGGTTGGGAAGAAAAATCGAGATGGTTCAATATTTATCGGCCT	49	
CO-M-121	AGAGTACCTATTCATTGAATCCCCTGCAAAAG	32	
CO-M-122 [c]	CATCCAATAATGCTGTAGCTCAACATGTTT	30	
CO-M-123	AGAGGGTAAATCGGTTGTACAAAAGCATTAA	32	
CO-M-124	CCAGCTTAAATCGATGAACGGTAAAATGCCGG	32	
CO-M-125	AACAAGAGCATCAACATTAATGTGAGCGAGTAACAACCTAAGGAAACCGAG GAAA	56	
CO-M-126	CTGAATCTAAATCATAACAGGCAAGTCAGAGCATGAAAGGGGCTGGGGTG	49	
CO-M-127	GTCATAAATTTAATTGCTCCTTTTCTTAATTG	32	
CO-M-128	GTCAGGACCCAGAGGGGTAATAGGCGGAATC	32	
CO-M-129	AACGAGGCGCAGACGGAACCTTAATCATTGTGTATACCA	40	
CO-M-130 [D]	CTGGCTCAAATTACCTTATGCGATAATGACAATTACTTGTGA	42	M2' Dock
CO-M-131 [D]	CCAATACTTAAAATGTTAGACTGGTAGCATTTTACTTGTGA	42	M2' Dock
CO-M-132 [ND]	GCTTAGAGGATAAGAGGTCATTTTTGAAACAT	32	
CO-M-133 [D]	ATAAAGCCGCAAAGAATTAGCAAACCACCCTTACTTGTGA	42	M2' Dock
CO-M-134 [D]	CTGAGAGTCTACAAGGCTATCAGACTTGAGCTTACTTGTGA	42	M2' Dock
CO-M-135 [D]	CATTTGGGATTATCACCGTCACCGGTCATTGCTTACTTGTGA	42	M2' Dock
CO-M-136 [ND]	CTCAGAGCACCGCCACCCTCAGAGATTAAGCA	32	
CO-M-137 [ND]	GAAAGTATTCGGAACCTATTATTCTGCGGATG	32	
CO-M-138 [ND]	CCACAGACACAACTACAACGCCTGATAGCGT	32	
CO-M-139 [D]	CAACCATCCGATAGTTGCGCCGACTTAAAGAATTACTTGTGA	42	M2' Dock
CO-M-140	ATAACCGATCATCTTTGACCCCAGCGATTATACCAAGTTCATGTTACTTAGCC GG	56	
CO-M-141	TGAGACTCGAGTTTCGTCACCAGTAGCCCTCATATGATGAAAGACTACC	49	
CO-M-142	GAACCACCATGCCCCCTGCCTATTTAAGAGGC	32	
CO-M-143	CCAGCAAAAAGCCGCCACCCTCAGACGCCACCA	32	
CO-M-144	CGCAATAATAACGGAATATTCATTAAGGTGAAATTAGAG	40	
CO-M-145	TCCCTCAGATCACAGTAGCACCAAAATATTGTAGTACCGCAATAAGAG	49	
CO-M-146	GTAACACTCTCAAGAGAAGGATTAGGATTA	30	

CO-M-147	AGAATTCGTAACGATCTAAAGTTCATGTACC	32	
CO-M-148	TAAAACACTATATTCGGTCGCTGATTTGAGG	32	
CO-M-149	GGGAGTTAAACGAAAGAGGCGTCGCTCAACAGTAGGGCTTATCCAATCG	49	
CO-M-150	TTCCAGACGGTTTATCAGCTTGGCGCTTGCA	32	
CO-M-151	AGGAGGTTGCCTTGAGTAAACATAATTTAGGCAG	33	
CO-M-152	AGCAAGGCACCAGAGCCACCACCGCATTGAC	32	
CO-M-153	AGACTCCTTTGAGGGAGGGAAGGTTTACCATT	32	
CO-M-154	TCAACCGATATTACGCAGTATGTTAGCAAACG	32	
CO-M-155	TCACCGGACGGAAACGTCACCAATGGCGACAT	32	
CO-M-156	GGGTCAGTGAGGCAGGTCAGACGAAATCAAAA	32	
CO-M-157	GGGATAGCGCTCAGTACCAGGCGGTTTTAACG	32	
CO-M-158	AATTGTATCGTTAGTAAATGAATTCATTTTCA	32	
CO-M-159	CAACCTAAAAGGCCGCTTTTGGGGAGCCTTT	32	
CO-M-160	CCCTCAGCTACGTAATGCCACTACGAAGGCAC	32	
CO-M-161	GGGATTTTAAAAAGGCTCCAAAAGGATCGTCA	32	
CO-M-162	CGTCGAGATCAGAGCCACCCTTTCTGTAT	32	
CO-M-163	GATATTCAGTGTACTGGTAATAAGATAAGTGC	32	
CO-M-164	CGATAGCATTGGCCATCTTTTCATTTGGCCTT	32	
CO-M-165	TAGAAAATGCGCCAAAGACAAAAGGAAACCAT	32	
CO-M-166	GTTTACCAACATACATAAAGGTGGCAACATAT	32	
CO-M-167	TATTAGCGGCACCCTAATCAGTAGTTCATATG	32	
CO-M-168 [c]	ATACAGGACAAACAAATAAATCCTAGCCCCCT	32	
CO-M-169	CGCCACCCGGGTTGATATAAGTATTTTTGATG	32	
CO-M-170	TCTCAAAGCTAAACAATTTCAACTCAGAAC	32	
CO-M-171	GGGTAAAAAGCGAAAGACAGCATCGTTGAAAA	32	
CO-M-172	GGTAGCAATTCATGAGGAAGTTCCATTAAAC	32	
CO-M-173	GCGGAGTGATAATAATTTTTTACGGAACGAG	32	
CO-M-174 [B]	5Biosg\ TTTTT ATAGGTGTCTCAGAACCGCCACCCAGTTTCA	37	Biotin-labeled
CO-M-175 [B]	5Biosg\ TTTTTTTTTT CCAGAATGAAGCGTCATACATGGCAGCCCGGA	42	Biotin-labeled
CO-M-176	TCAAGTTTCGGCATTTTCGGTCATCATTAAAG	32	

CO-M-177	AAAAGAAACACAATCAATAGAAAACGACAGAA	32	
----------	----------------------------------	----	--

**Table 2.7 Strand sequences for cross-shaped DNA origami tile (edge strands)**

**A-Tile Edge Strands**

CO-A-D1*	CGTAACGTTAATATTTTGTAAATATTTAAATTGTAAAATACATCT	45	M1 dock/sticky-ends
CO-A-D2*	GTTCATGAGTAATGTGTAGGTTTTTAAATGCATGCCATACATCT	45	M1 dock/sticky-ends
CO-A-D3*	TTTATTAGATACATTTTCGCTAGATTTAGTTTGACCTTT	38	Blocking
CO-A-D4*	TTTATCAAAAAGATTAAGAAAAGCAAAGCGGATTGCTTT	38	Blocking
CO-A-D5*	AGTGTATAACGCCAAAAGGAACAATAATGCAGATACTGTAT	42	sticky-ends
CO-A-D6*	GACATGATATTCATTACCCAAATCTTGACAAGAACCGTGTAT	42	sticky-ends
CO-A-L1*	CGAATTCCTGAACAAGAAAAATCAACAATAGATAAGATACATCT	45	M1 dock/sticky-ends
CO-A-L2*	AGCATTTGCACCCAGCTACAAAAGATTAGTTGCTATTATACATCT	45	M1 dock/sticky-ends
CO-A-L3*	TTTAATAATAAGAGCAAGAGAATTGAGTTAAGCCCTTT	38	Blocking
CO-A-L4*	TTTGTGTTGAGGGGACGACGAACCGTGCATCTGCCATTT	38	Blocking
CO-A-L5*	GCAAACCCGGGTACCGAGGTCTCGACTCTAGAGGATCTGTAT	42	sticky-ends
CO-A-L6*	CTGTTAGCTGATTGCCCTTCACAGTGAGACGGCAACTGTAT	42	sticky-ends
CO-A-R1	CTGTTGTTAAATAAGAATAAAGTGTGATAAATAAGGCTGTAT	42	sticky-ends
CO-A-R2	GCAAAAAATCGTCGCTATTAATAACCTTGCCTCTGTGTAT	42	sticky-ends
CO-A-R3	TTTAAATAAAGAAATTGCGTTAGCACGTAAAACAGTTT	38	Blocking
CO-A-R4	TTTTATTCCTGATTATCAGAGCGGAATTATCATCATTT	38	Blocking
CO-A-R5	AGCATTGCTGAACCTCAAATAATCTAAAGCATCACCTATACATCT	45	M1 dock/sticky-ends
CO-A-R6	CGAATACATTGGCAGATTCACCTGAAATGGATTATTTATACATCT	45	M1 dock/sticky-ends
CO-A-U1	GACATAATAAGTTTATTTTGTGCGCAAAGACACCACGGTGTAT	42	sticky-ends
CO-A-U2	AGTGTGTTAGCGGTTTTTCATGCCTTTAGCGTCAGACTGTAT	42	sticky-ends
CO-A-U3	TTTAATTACCGTTCCAGTGAAAGCGCAGTCTCTGTTT	38	Blocking
CO-A-U4	TTTGGTTTAGTACCGCCACATCACCGTACTCAGGATTT	38	Blocking
CO-A-U5	GTTCAACTAAAGGAATTGCGAAGAATAGAAAGGAACAATACATCT	45	M1 dock/sticky-ends
CO-A-U6	CGTAAGAGGACTAAAGACTTTCGGCTACAGAGGCTTTATACATCT	45	M1 dock/sticky-ends

### B-Tile Edge Strands

CO-B-D1*	TTACGGTTAAATAAGAATAAAGTGTGATAAATAAGGCTGTAT	42	sticky-ends
CO-B-D2*	TGAACAAATCGTCGCTATTAAATAACCTTGCTTCTGTGTAT	42	sticky-ends
CO-B-D3*	TTTAAATAAAGAAATTGCGTTAGCACGTAACAGTTT	38	Blocking
CO-B-D4*	TTTTATTCTGATTATCAGAGCGGAATTATCATCATTT	38	Blocking
CO-B-D5*	ACACTTGCTGAACCTCAAATAATCTAAAGCATCACCTATACATCT	45	M1 dock/sticky-ends
CO-B-D6*	ATGTCACATTGGCAGATTCACCTGAAATGGATTATTTATACATCT	45	M1 dock/sticky-ends
CO-B-L1*	AACAGCGTTAATATTTTGTAAATTTAAATTGTAAATACATCT	45	M1 dock/sticky-ends
CO-B-L2*	TTTGCTGAGTAATGTGTAGGTTTTTAAATGCAATGCCATACATCT	45	M1 dock/sticky-ends
CO-B-L3*	TTTATTAGATACATTTGCTAGATTTAGTTTGACCTTT	38	Blocking
CO-B-L4*	TTTATCAAAAAGATTAAGAAAGCAAAGCGGATTGCTTT	38	Blocking
CO-B-L5*	ATGCTATAACGCCAAAAGGAACAATAATGCAGATACTGTAT	42	sticky-ends
CO-B-L6*	ATTCGGATATTCATTACCCAAATCTTGACAAGAACCGTGTAT	42	sticky-ends
CO-B-R1	ATTCGAATAAGTTTATTTTGTGCGCAAAGACACCACGGTGTAT	42	sticky-ends
CO-B-R2	ATGCTTGTAGCGGTTTTTCATGCCTTTAGCGTCAGACTGTAT	42	sticky-ends
CO-B-R3	TTTAATTTACCGTTCAGTGAAGCGCAGTCTCTGTTT	38	Blocking
CO-B-R4	TTTGGTTTAGTACCGCCACATCACCGTACTCAGGATTT	38	Blocking
CO-B-R5	TTTGCATAAAGGAATTGCGAAGAAATAGAAAGGAACAATACATCT	45	M1 dock/sticky-ends
CO-B-R6	AACAGGAGGACTAAAGACTTTGCGGTACAGAGGCTTTATACATCT	45	M1 dock/sticky-ends
CO-B-U1	ATGTCTCTGAACAAGAAAAATCAACAATAGATAAGATACATCT	45	M1 dock/sticky-ends
CO-B-U2	ACACTTTCACCCAGCTACAAAAGATTAGTTGCTATTATACATCT	45	M1 dock/sticky-ends
CO-B-U3	TTTAATAATAAGAGCAAGAGAATTGAGTTAAGCCCTTT	38	Blocking
CO-B-U4	TTTGTGAGGGGACGACGAACCGTGCATCTGCCATTT	38	Blocking
CO-B-U5	TGAACCCCGGTACCGAGGTCTCGACTCTAGAGGATCTGTAT	42	sticky-ends
CO-B-U6	TTACGAGCTGATTGCCCTCACAGTGAGACGGCAACTGTAT	42	sticky-ends

### Passivation Edge Strands

CO-A-R1 / B-D1	TTTGTTAAATAAGAATAAAGTGTGATAAATAAGGCTTT	38	Blocking
CO-A-R2 / B-D2	TTTAAATCGTCGCTATTAAATAACCTTGCTTCTGTTTT	38	Blocking

CO-A-R3 / B-D3	TTTAAATAAAGAAATTGCGTTAGCACGTAACAGTTT	38	Blocking
CO-A-R4 / B-D4	TTTTATTCCTGATTATCAGAGCGGAATTATCATCATTT	38	Blocking
CO-A-R5 / B-D5	TGCTGAACCTCAAATAATCTAAAGCATCACCTAATACATCT	41	M1 Dock
CO-A-R6 / B-D6	ACATTGGCAGATTCACCTGAAATGGATTATTTAATACATCT	41	M1 Dock
CO-A-D1 / B-L1	CGTTAATATTTTGTAAATATTTAAATTGTAAAAATACATCT	41	M1 Dock
CO-A-D2 / B-L2	TGAGTAATGTGTAGGTTTTTAAATGCAATGCCAATACATCT	41	M1 Dock
CO-A-D3 / B-L3	TTTATTAGATACATTTGCTAGATTTAGTTTGACCTTT	38	Blocking
CO-A-D4 / B-L4	TTTATCAAAAAGATTAAGAAAGCAAAGCGGATTGCTTT	38	Blocking
CO-A-D5 / B-L5	TTTATAACGCCAAAAGGAACAATAATGCAGATACTTT	38	Blocking
CO-A-D6 / B-L6	TTTGGATATTCATTACCCAATCTTCGACAAGAACCTTT	38	Blocking

**Table 2.8 Strand sequences for DNA-PAINT imager strands**

**Imager Strands**

M1' - Cy3b	CTAGATGTAT/Cy3b/	16	M1' Imager Strand
M2' - Cy3b	ACTCACAAAGT/Cy3b/	16	M2' Imager Strand

CHAPTER THREE: INVESTIGATIONS OF STRAND DEFECTS IN DNA ORIGAMI  
WITH CORRELATIVE DNA-PAINT AND ATOMIC FORCE MICROSCOPY

Christopher M. Green<sup>a</sup>

William L. Hughes<sup>a</sup>

Elton Graugnard<sup>a</sup>

Wan Kuang<sup>b</sup>

Accepted for publication in:

Journal TBD

Date TBD

*<sup>a</sup>Micron School of Materials Science & Engineering,  
Boise State University, 1910 University Dr., Boise, ID 83725, USA*

*<sup>b</sup>Department of Electrical & Computer Engineering,  
Boise State University, 1910 University Dr., Boise, ID 83725, USA*

### 3.1 Introduction

DNA-directed self-assembly offers precise spatial control when arranging molecules and particles at the nanoscale.<sup>1-4</sup> The utility of DNA origami has been demonstrated through multiple applications,<sup>5</sup> such as plasmonic and photonic devices,<sup>6-14</sup> localized chemical reaction networks for sensing and DNA computation,<sup>15-24</sup> lithographic masks for semiconductor devices,<sup>25-30</sup> and protein/enzyme-based biosensors.<sup>16,17,20,21,31,32</sup> Many of these applications rely on the inclusion of addressable (i.e. chemically “active”) sites for post-assembly modification; the availability of such sites on the origami is critical to the synthesis of functional structures. Despite significant improvements in the design and synthesis of DNA origami,<sup>12,33-44</sup> over 10% of addressable sites are consistently defective (i.e. inactive) and adversely affect performance. While the source of defective sites has been attributed to unincorporated staple strands,<sup>39</sup> defective tethers,<sup>8</sup> and steric hindrance of conjugated molecules,<sup>8,10</sup> a systematic study of the root cause has yet to be carried out.

The challenge of identifying and overcoming factors that limit DNA origami site availability is exacerbated by a lack of characterization techniques that enable direct and reliable defect metrology on the scale of single staple strands.<sup>45</sup> Common high-resolution techniques, such as atomic force microscopy (AFM) and electron microscopies, provide detailed topographic and structural images of DNA nanostructures, though the availability of individual sites cannot be directly determined. Conversely, DNA-PAINT super-resolution microscopy (SRM) enables high-resolution optical characterization of addressable sites on DNA origami,<sup>39,46-52</sup> though defective sites are indicated by a lack of observation, providing little information on the source of defects and the structure of the origami near defects. The combination of DNA-PAINT and AFM through correlative microscopy overcomes these limitations.

While certain super-resolution techniques have been combined with AFM,<sup>53</sup> prior to this work, correlative DNA-PAINT and high-resolution AFM has not been possible due to incompatible sample preparation for the individual techniques. Here, we introduce a simple and flexible method to selectively bind DNA origami, and not short ssDNA imager strands, directly to cover glass, enabling correlative DNA-PAINT/AFM imaging with no loss in quality of the individual techniques. We employed high-resolution, correlative microscopy to characterize DNA origami—achieving spatial correlation in super-resolution optical and topographic images that exceeded the mean localization uncertainty for the super-resolution image. Unavailable sites were directly identified in DNA-PAINT and subsequently examined in AFM for structural defects. The results show little correlation between inactive (unresolved) DNA-PAINT sites and unincorporated staple strands. Overall, less than 15% of inactive sites were the result of unincorporated sites. The results suggest that strand incorporation has a smaller role in DNA origami site yield than previously reported,<sup>39</sup> and defects are likely due to the unavailability of incorporated staple strands. Further, structural defects were observed on active DNA-PAINT sites more often than at non-DNA-PAINT sites, suggesting that DNA-PAINT may locally increase the susceptibility of DNA origami to damage during imaging or rinsing.<sup>54,55</sup> The availability of addressable sites was improved with staple strand purification methods, suggesting further improvements are possible.

## **3.2 Results**

### **3.2.1 Cross-compatible Substrate for Correlative Imaging**

For correlative DNA-PAINT/AFM microscopy, a substrate and sample preparation method were needed that met the individual requirements of the techniques, namely

transparency, low surface roughness, favorable DNA origami adsorption, and low affinity for single-stranded DNA in solution. For DNA-PAINT, protein-functionalized cover glass is commonly used to immobilize DNA origami and passivate the surface.<sup>46</sup> However, the protein surface is generally too rough to obtain high resolution AFM. Inspired by a previous study by Takabayashi et al. demonstrating pH-dependent DNA origami adsorption to thermally-grown silica after hydrofluoric acid etching,<sup>28</sup> we investigated hydroxylated silica for DNA-PAINT imaging in the absence of a protein layer for binding and passivation. Materials and methods can be found in Section 3.5.1, and details on DNA origami cross-tile design and synthesis (adapted from Aghebat et al.)<sup>56,57</sup> are provided in Section 3.5.1.1-4. Borosilicate cover glasses, commonly used in fluorescence microscopy, were hydroxylated by exposure to glow discharge and prepared for DNA-PAINT imaging (Figures 3.1a, 3.6-8). Total internal reflection fluorescence (TIRF) imaging was performed on the substrates with and without DNA origami to determine the degree of interaction between imager strands and the hydroxylated surface; the results revealed near complete passivation of the surface to imager strands and favorable absorption of DNA origami (Figure 3.7). During DNA-PAINT imaging, fluorescent events were detected at a signal-to-noise ratio higher than 36 dB and a nominal rate of non-specific events, notably achieved without additional surface functionalization or passivation (Figures 3.7,8). High-resolution AFM images were acquired in buffer conditions identical to that used for DNA-PAINT (Figures 3.1 and 3.9),

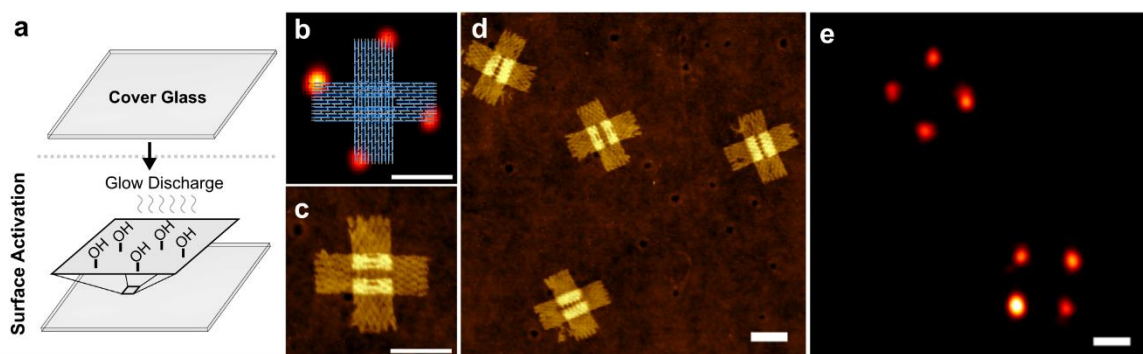


**Figure 3.1** Hydroxylated cover glass for DNA-PAINT and AFM imaging of DNA origami. (a) Depiction of cover glass preparation for imaging. Pre-cleaned borosilicate cover glass were exposed to glow discharge in a reduced atmosphere of air to activate the surface through hydroxylation. (b) Strand diagram overlaid on DNA-PAINT image, (c) high resolution AFM image, (d) areal AFM image, and (e) DNA-PAINT image of DNA origami cross-tiles on hydroxylated cover glass. Scale bars, 50 nm.

demonstrating the simplicity and efficacy of the method for both DNA-PAINT and AFM characterization of DNA origami.

### 3.2.2 Correlative DNA-PAINT/AFM Microscopy

For correlative imaging, cover glass substrates were prepared with registration and fiducial markers prior to hydroxylation by glow discharge, as described in Section 3.5.1.5. Immediately after hydroxylation, substrates were assembled into fluid wells, and DNA origami were deposited on the surface and incubated for 30 minutes to promote adhesion. DNA-PAINT and AFM were performed stepwise, and inscribed registration marks were used to optically locate the region of interest. DNA-PAINT images of  $55\ \mu\text{m} \times 55\ \mu\text{m}$  were acquired using protocols described in Section 3.5.1.9. High- and low-resolution AFM images ranging from  $2\ \mu\text{m} \times 2\ \mu\text{m}$  to  $20\ \mu\text{m} \times 20\ \mu\text{m}$  were acquired to assess the quality of correlation between DNA-PAINT and AFM images and the stability of DNA origami during imaging. The experimental procedure can be found in Section 3.5.1.10 and Figure

3.12, along with representative results of correlative DNA-PAINT/AFM imaging of DNA origami in Figure 3.2.

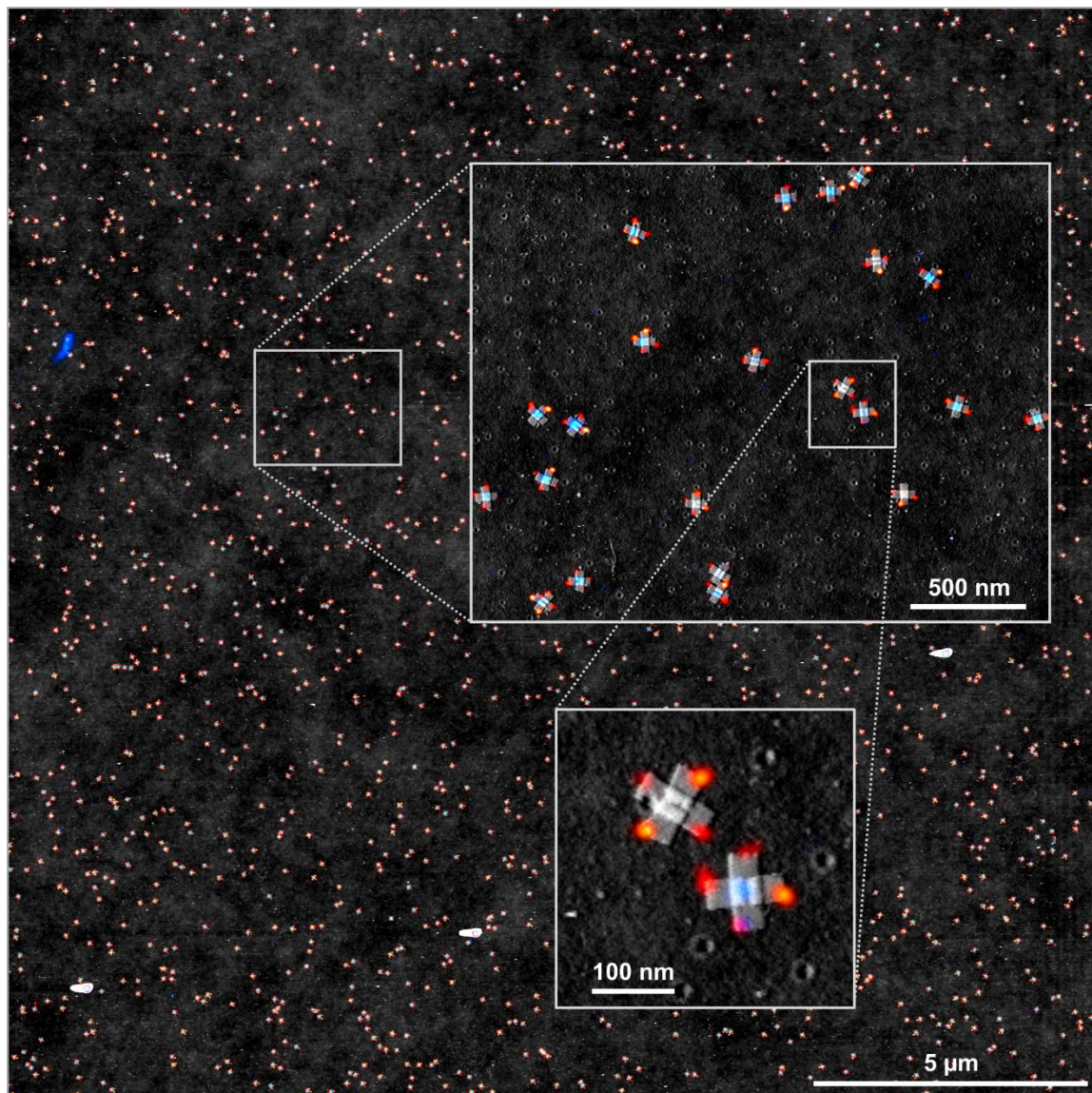


**Figure 3.2** 20  $\mu\text{m}$  x 20  $\mu\text{m}$  correlative DNA-PAINT/AFM image of DNA origami cross-tiles. The large area AFM image was acquired with 10 nm pixel size, and the inset images were acquired with 2.5 nm pixel size. To distinguish features on the surface in AFM images, the height and amplitude error channels were superimposed.

Individual origami were well-correlated in DNA-PAINT/AFM after correcting for global image distortions that arise from image aberrations of the individual techniques,

such as field curvature in optical microscopy and thermal drift in AFM (Figures 3.12-19).<sup>53</sup> Two sets of correlated DNA-PAINT and AFM images were examined for differences in the relative positions of docking sites within the images. Two-dimensional (2D) dispersion was calculated for each image to quantify the quality of correlation (Figure 3.3). For 286 docking sites resolved in the DNA-PAINT and AFM images, the mean spatial deviation in docking site positions was  $5 \pm 3$  nm (Figure 3.19). The deviations were independent of position (Figure 3.3c) and can be fully accounted for by the mean uncertainty of localizations in the super-resolved image ( $\sigma_{xy} = 6 \pm 2$  nm, Figure 3.19), suggesting that adsorbed origami were completely immobile on the surface. These results demonstrate that optimal performance of the individual techniques can be maintained during correlative imaging with no observable movement of individual origami, enabling a 1:1 mapping of DNA-PAINT to AFM topography and validating correlative imaging for single-strand defect metrology.

### 3.2.3 Correlative Defect Metrology

Unresolved DNA-PAINT docking sites were investigated in correlative images to determine whether two docking site defect scenarios, as shown in Figure 3.4b, could be distinguished: (1) incorporated but inactive sites—strands that are present in the origami but lack an active docking site, and (2) unincorporated sites—strands that are missing entirely from the origami.<sup>39</sup> Prior to this work, it has not been possible to distinguish inactive sites from unincorporated sites. By itself, DNA-PAINT detection indicates only that a site is active and therefore must be incorporated. For sites designed to be incorporated but lack a signal, either defect scenario is possible. With high resolution AFM images, we

are able to distinguish incorporated sites from unincorporated sites (see Figures 3.23-25).

However, the activity of sites cannot be determined from AFM images alone.

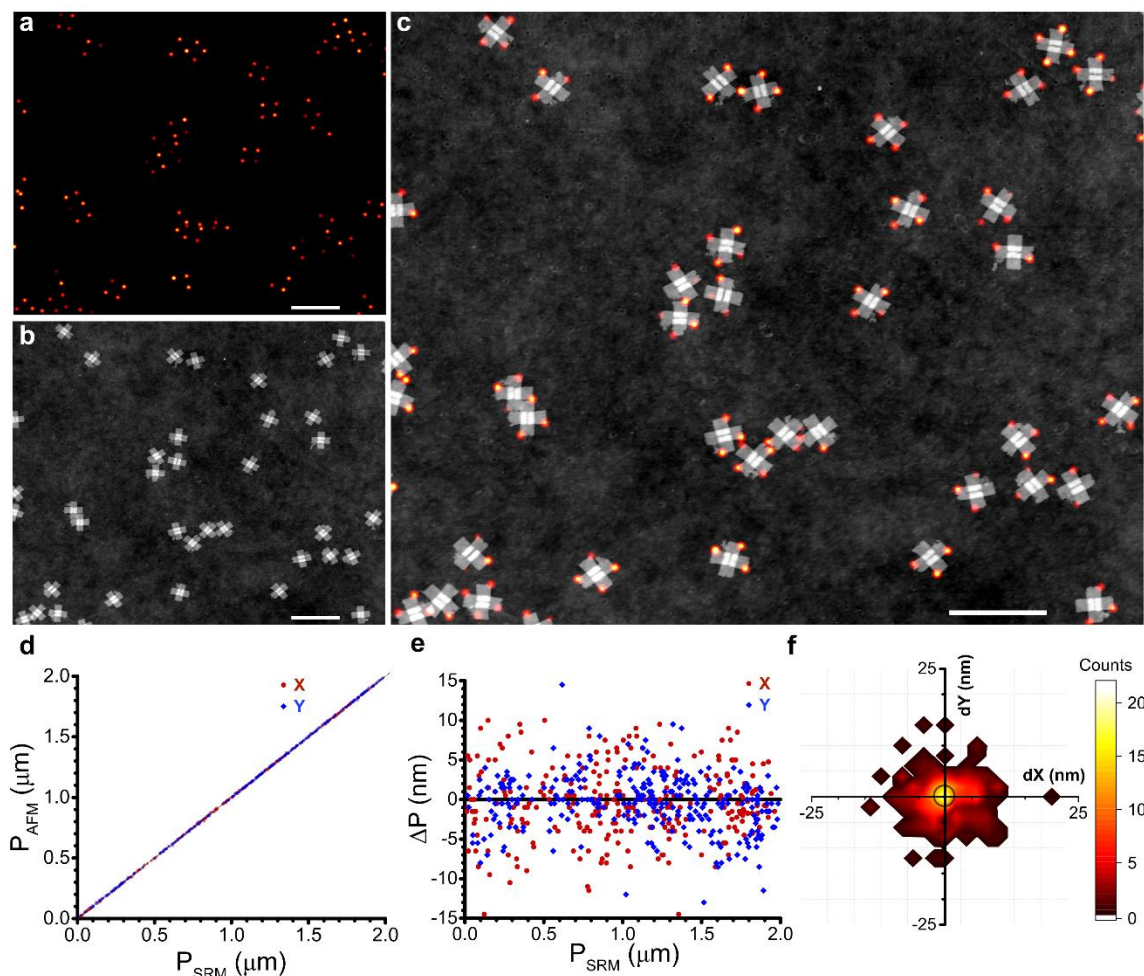


**Figure 3.3** Spatial correlation of docking sites in DNA-PAINT and AFM images. (a) DNA-PAINT SRM, (b) AFM, and (c) correlative DNA-PAINT/SRM image of DNA origami cross-tiles. Scale bars, 250 nm. (d-f) Spatial correlation, dispersion, and 2D dispersion histogram, respectively, of 286 docking sites in two correlated DNA-PAINT and AFM images (Figure 3.26).  $P_{AFM}$  and  $P_{SRM}$  represent the positions of corresponding docking sites in AFM and SRM images, respectively, with horizontal (X, red) and vertical (Y, blue) positions indicated.  $\Delta P$  represents the deviation in position of corresponding sites in DNA-PAINT and AFM.  $dX$  and  $dY$  represent the relative deviation between corresponding sites in the x and y axes, respectively. The mean spatial deviation between the images was  $5 \pm 3$  nm, depicted by a black circle near the origin.

By combining the capabilities of each technique, correlative DNA-PAINT/AFM imaging overcomes the limitations of the individual techniques, providing a reliable means to determine the activity and incorporation of individual docking sites.

Single defect site characterization with DNA-PAINT and AFM is inherently sensitive to variations in imaging conditions, and the fidelity of the individual techniques must be ensured to reduce the rate of false detections. For DNA-PAINT, site detections occur stochastically during image acquisition. As a result, total acquisition time must be at a duration that enables all available sites to be detected. To ensure complete image acquisition for correlative defect analysis, we quantify the progress of imaging and approximate the fraction of active sites resolved in the final rendered image (see Section 3.5.2.3). Using this approach, DNA-PAINT imaging typically surpassed 99% completion in 60 minutes for imager strand concentrations of 3 nM. These results were independently supported by equilibrium reaction rate calculations and the time evolution of site detection efficiencies (see Section 3.5.2.3 and Figure 3.20).

To ensure that unincorporated sites could be reliably detected in topographic images, we performed a series of imaging optimization experiments on DNA origami designed to have both incorporated and unincorporated sites. We determined the probability of unincorporated site detection using DNA origami cross-tiles synthesized with several staple stands intentionally removed, simulating unincorporated site defects, and imaged with correlative DNA-PAINT/AFM (Figures 3.23 and 3.24). For defects located on the corners of tile arms, symmetric to DNA-PAINT sites, all missing strand defects were observed in high-resolution AFM images, indicating a low probability of false negative defect detection with AFM under similar conditions (Figure 3.25). While structures are still

susceptible to damage during imaging and rinsing, potentially increasing the rate of false positive defect detections, correlation with DNA-PAINT provides a means to distinguish imaging-induced and pre-existing defects.

We investigated unresolved docking sites on DNA origami cross-tiles to quantify the distribution of defects and shed light on the mechanisms contributing to current observed addressability yield. The results are shown in Figure 3.4, along with the results of defect analysis for the regions of interest. For 344 docking sites examined in two correlated images, 47 inactive sites ( $14 \pm 2\%$ ) were identified in DNA-PAINT, and 60 structural defects ( $17 \pm 1\%$ ) were identified in AFM. Of all the sites examined, only 6 sites ( $1.7 \pm 0.5\%$ ) were identified as both inactive in DNA-PAINT and having structural defects in AFM. Put another way,  $98.3 \pm 0.5\%$  of docking sites were incorporated in the origami and  $86 \pm 2\%$  were both active and incorporated. Thus, approximately 7 out of 8 inactive docking sites were, in fact, physically incorporated into the origami.

Interestingly, structural defects were observed more often at active DNA-PAINT sites ( $18 \pm 2\%$ ) than at inactive sites ( $13 \pm 3\%$ ), suggesting that active docking sites were more susceptible to damage post-DNA-PAINT imaging than inactive sites. While the presence of a docking site might locally impact the stability of origami, it is unlikely that similar defects would not occur prior to DNA-PAINT imaging and appear as unincorporated sites; see Section 3.5.2.6 for a more detailed discussion. Rather, the results suggest that damage was induced during DNA-PAINT imaging, possibly by photo-induced oxidation of nucleotides near the docking sites.<sup>54</sup> Oxidative damage to the scaffold or staple strands could decrease the local stability of origami and increase the likelihood of damage during subsequent rinsing and imaging steps.<sup>55</sup>

The results of correlative defect analysis suggest that inactive docking sites play a significant role in limiting the addressability of DNA origami, and we speculate that local defects in the docking sites, such as oxidative damage, sequence errors, or truncations,

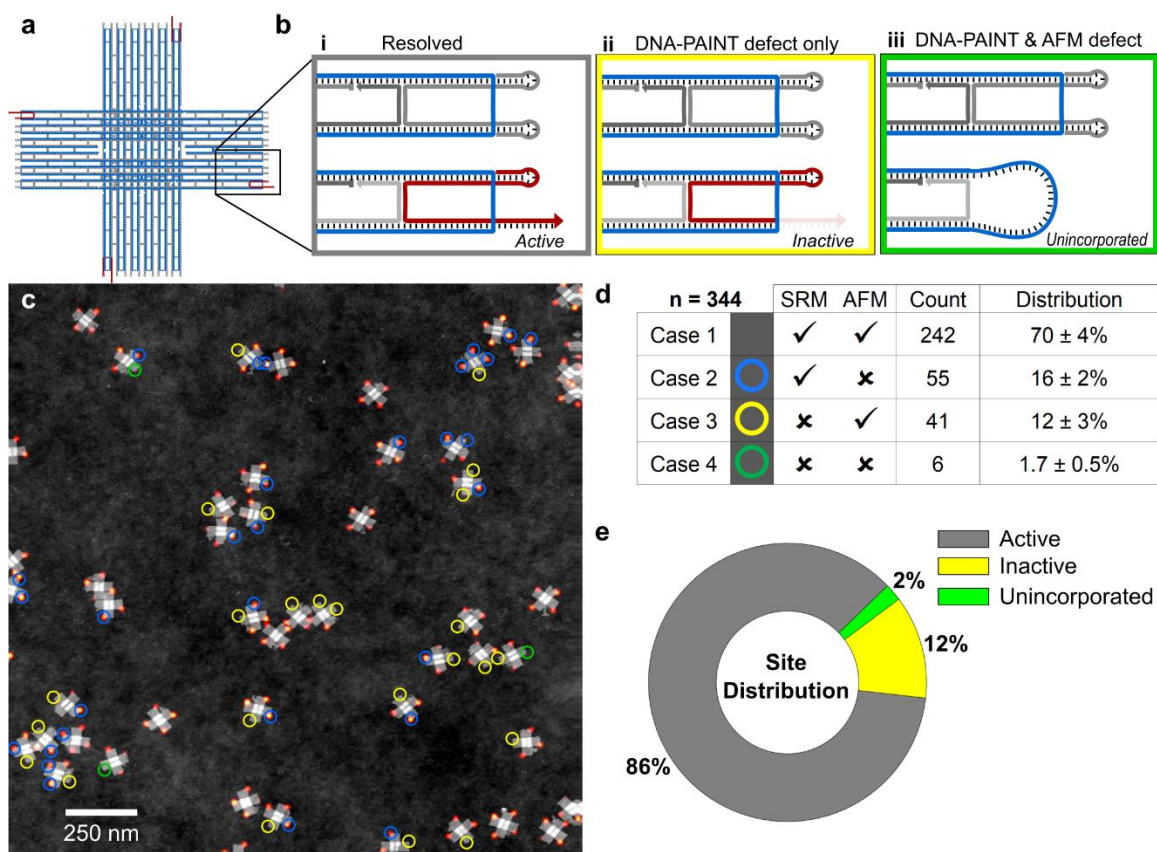


**Figure 3.4** Correlation of defects in DNA-PAINT and AFM images. (a) Strand diagram of the DNA origami cross-tile depicting the positions of docking sites (red) at one corner of each arm. (b) Magnified strand diagram depicting (i) active docking sites that are successfully imaged with DNA-PAINT, (ii) inactive docking sites that do not appear in DNA-PAINT images but appear in AFM images, and (iii) unincorporated docking sites that do not appear in both DNA-PAINT and AFM images. (c) Superimposed DNA-PAINT center-of-mass and AFM topography image with unresolved sites (yellow), AFM defects (blue), and unresolved sites correlated to AFM defects (green). Full resolution images can be found in Figures 3.23 and 3.24. (d) Tables summarizing the results of defect quantification for the images in c and d, respectively. The four cases are distinguished by the states of docking sites in DNA-PAINT and AFM images (✓ - no defect, ✗ - defect). (e) Donut chart of the site distribution corresponding to the three possible states of docking sites depicted in b.

might account for the population of inactive sites. To quantify the impact of local docking site defects on detection efficiency, cross-tiles were folded with docking site staple strands purified by polyacrylamide gel electrophoresis (PAGE) and compared to cross-tiles with unfiltered staple strands. Additionally, two sequence-dependent PAGE filtrations of staple strands were explored to increase the accessibility of docking sites: (1) Acrydite-immobilization of small, complementary (7 nt) ssDNA on the acrylamide matrix (Figure 3.28),<sup>58</sup> and (2) small domain (8/9 nt) duplexing of the docking site to long, sacrificial ssDNA strands (Figure 3.29). Cross-tiles with docking sites filtered with the two sequence-dependent techniques were synthesized as well as unfiltered docking sites for comparison. DNA-PAINT detection efficiencies revealed modest improvements in the availability of docking sites, increasing from  $82.2 \pm 0.7\%$  detection efficiency for unfiltered sites to  $84.6 \pm 0.2\%$  for PAGE-filtered sites,  $86.0 \pm 0.1\%$  for sites filtered by duplex-PAGE, and to  $87.2 \pm 0.2\%$  for sites filtered by Acrydite-ssDNA-PAGE (Figure 3.30). With a maximum detection efficiency of only 87%, despite over 98% incorporation, these results suggest that other mechanisms, yet to be identified, likely contribute to inaccessible sites.

### 3.3 Conclusion

We have developed methods for correlative DNA-PAINT/AFM microscopy that enable the acquisition of high-resolution optical and topographic images of DNA origami without compromising the image quality of the individual techniques. We achieved high quality correlation between structures in DNA-PAINT and AFM images, observing an average spatial deviation which could be fully accounted for by the localization uncertainty of the super-resolution image. Investigations of unresolved docking sites showed little correlation to structural defects observed with AFM, revealing that most site defects occur

on strands that are present on the structure. We employed staple strand purification methods to improve the addressability of docking sites, however the results do not identify all possible causes, and more work is needed to further increase the site addressability of DNA origami.

### 3.4 References

- 1 Li, X. J., Yang, X. P., Qi, J. & Seeman, N. C. Antiparallel DNA double crossover molecules as components for nanoconstruction. *JACS* 118, 6131-6140, doi:DOI 10.1021/ja960162o (1996).
- 2 Mirkin, C. A., Letsinger, R. L., Mucic, R. C. & Storhoff, J. J. A DNA-based method for rationally assembling nanoparticles into macroscopic materials. *Nature* 382, 607-609, doi:10.1038/382607a0 (1996).
- 3 Seeman, N. C. Nucleic acid junctions and lattices. *J. Theor. Biol.* 99, 237-247, doi:Doi 10.1016/0022-5193(82)90002-9 (1982).
- 4 Seeman, N. C. DNA nanotechnology: novel DNA constructions. *Annu. Rev. Biophys. Biomol. Struct.* 27, 225-248, doi:10.1146/annurev.biophys.27.1.225 (1998).
- 5 Rothmund, P. W. Folding DNA to create nanoscale shapes and patterns. *Nature* 440, 297-302, doi:10.1038/nature04586 (2006).
- 6 Kuzyk, A., Jungmann, R., Acuna, G. P. & Liu, N. DNA Origami Route for Nanophotonics. *ACS Photonics* 5, 1151-1163, doi:10.1021/acsp Photonics.7b01580 (2018).
- 7 Pilo-Pais, M., Acuna, G. P., Tinnefeld, P. & Liedl, T. Sculpting light by arranging optical components with DNA nanostructures. *MRS Bull.* 42, 936-942, doi:10.1557/mrs.2017.278 (2017).
- 8 Bui, H., Onodera, C., Kidwell, C., Tan, Y., Graugnard, E., Kuang, W., Lee, J., Knowlton, W. B., Yurke, B. & Hughes, W. L. Programmable periodicity of

- quantum dot arrays with DNA origami nanotubes. *Nano Lett.* 10, 3367-3372, doi:10.1021/nl101079u (2010).
- 9 Schreiber, R., Do, J., Roller, E. M., Zhang, T., Schuller, V. J., Nickels, P. C., Feldmann, J. & Liedl, T. Hierarchical assembly of metal nanoparticles, quantum dots and organic dyes using DNA origami scaffolds. *Nat Nanotechnol* 9, 74-78, doi:10.1038/nnano.2013.253 (2014).
- 10 Ko, S. H., Gallatin, G. M. & Liddle, J. A. Nanomanufacturing with DNA Origami: Factors Affecting the Kinetics and Yield of Quantum Dot Binding. *Adv. Funct. Mater.* 22, 1015-1023, doi:10.1002/adfm.201102077 (2012).
- 11 Shen, B., Kostianen, M. A. & Linko, V. DNA Origami Nanophotonics and Plasmonics at Interfaces. *Langmuir*, doi:10.1021/acs.langmuir.8b01843 (2018).
- 12 Gur, F. N., Schwarz, F. W., Ye, J., Diez, S. & Schmidt, T. L. Toward Self-Assembled Plasmonic Devices: High-Yield Arrangement of Gold Nanoparticles on DNA Origami Templates. *ACS Nano* 10, 5374-5382, doi:10.1021/acsnano.6b01537 (2016).
- 13 Klein, W. P., Schmidt, C. N., Rapp, B., Takabayashi, S., Knowlton, W. B., Lee, J., Yurke, B., Hughes, W. L., Graugnard, E. & Kuang, W. Multiscaffold DNA origami nanoparticle waveguides. *Nano Lett.* 13, 3850-3856, doi:10.1021/nl401879r (2013).
- 14 Takabayashi, S., Klein, W. P., Onodera, C., Rapp, B., Flores-Estrada, J., Lindau, E., Snowball, L., Sam, J. T., Padilla, J. E., Lee, J., Knowlton, W. B., Graugnard, E., Yurke, B., Kuang, W. & Hughes, W. L. High precision and high yield fabrication of dense nanoparticle arrays onto DNA origami at statistically independent binding sites. *Nanoscale* 6, 13928-13938, doi:10.1039/c4nr03069a (2014).
- 15 Simmel, F. C., Yurke, B. & Singh, H. R. Principles and Applications of Nucleic Acid Strand Displacement Reactions. *Chem. Rev.*, doi:10.1021/acs.chemrev.8b00580 (2019).

- 16 Chandrasekaran, A. R. DNA origami and biotechnology applications: a perspective. *J. Chem. Technol. Biotechnol.* 91, 843-846, doi:10.1002/jctb.4826 (2016).
- 17 Voigt, N. V., Topping, T., Rotaru, A., Jacobsen, M. F., Ravnsbaek, J. B., Subramani, R., Mamdouh, W., Kjems, J., Mokhir, A., Besenbacher, F. & Gothelf, K. V. Single-molecule chemical reactions on DNA origami. *Nat Nanotechnol* 5, 200-203, doi:10.1038/nnano.2010.5 (2010).
- 18 Chatterjee, G., Dalchau, N., Muscat, R. A., Phillips, A. & Seelig, G. A spatially localized architecture for fast and modular DNA computing. *Nat Nanotechnol* 12, 920-927, doi:10.1038/nnano.2017.127 (2017).
- 19 Bui, H., Shah, S., Mokhtar, R., Song, T., Garg, S. & Reif, J. Localized DNA Hybridization Chain Reactions on DNA Origami. *ACS Nano* 12, 1146-1155, doi:10.1021/acsnano.7b06699 (2018).
- 20 Chao, J., Zhu, D., Zhang, Y., Wang, L. & Fan, C. DNA nanotechnology-enabled biosensors. *Biosens. Bioelectron.* 76, 68-79, doi:10.1016/j.bios.2015.07.007 (2016).
- 21 Pei, H., Zuo, X. L., Pan, D., Shi, J. Y., Huang, Q. & Fan, C. H. Scaffolded biosensors with designed DNA nanostructures. *Npg Asia Materials* 5, e51, doi:10.1038/am.2013.22 (2013).
- 22 Thubagere, A. J., Li, W., Johnson, R. F., Chen, Z., Doroudi, S., Lee, Y. L., Izatt, G., Wittman, S., Srinivas, N., Woods, D., Winfree, E. & Qian, L. A cargo-sorting DNA robot. *Science* 357, doi:10.1126/science.aan6558 (2017).
- 23 Gothelf, K. V. Chemical modifications and reactions in DNA nanostructures. *MRS Bull.* 42, 897-903, doi:10.1557/mrs.2017.276 (2017).
- 24 Kotani, S. & Hughes, W. L. Multi-Arm Junctions for Dynamic DNA Nanotechnology. *JACS* 139, 6363-6368, doi:10.1021/jacs.7b00530 (2017).
- 25 Galatsis, K., Wang, K. L., Ozkan, M., Ozkan, C. S., Huang, Y., Chang, J. P., Monbouquette, H. G., Chen, Y., Nealey, P. & Botros, Y. Patterning and templating

- for nanoelectronics. *Adv. Mater.* 22, 769-778, doi:10.1002/adma.200901689 (2010).
- 26 Gao, B., Sarveswaran, K., Bernstein, G. H. & Lieberman, M. Guided deposition of individual DNA nanostructures on silicon substrates. *Langmuir* 26, 12680-12683, doi:10.1021/la101343k (2010).
- 27 Gates, E. P., Dearden, A. M. & Woolley, A. T. DNA-templated lithography and nanofabrication for the fabrication of nanoscale electronic circuitry. *Crit. Rev. Anal. Chem.* 44, 354-370, doi:10.1080/10408347.2014.910636 (2014).
- 28 Takabayashi, S., Kotani, S., Flores-Estrada, J., Spears, E., Padilla, J. E., Godwin, L. C., Graugnard, E., Kuang, W., Sills, S. & Hughes, W. L. Boron-Implanted Silicon Substrates for Physical Adsorption of DNA Origami. *Int J Mol Sci* 19, doi:10.3390/ijms19092513 (2018).
- 29 Liddle, J. A. & Gallatin, G. M. Lithography, metrology and nanomanufacturing. *Nanoscale* 3, 2679-2688, doi:10.1039/c1nr10046g (2011).
- 30 Liddle, J. A. & Gallatin, G. M. Nanomanufacturing: A Perspective. *ACS Nano* 10, 2995-3014, doi:10.1021/acsnano.5b03299 (2016).
- 31 Grossi, G., Jaekel, A., Andersen, E. S. & Sacca, B. Enzyme-functionalized DNA nanostructures as tools for organizing and controlling enzymatic reactions. *MRS Bull.* 42, 920-924, doi:10.1557/mrs.2017.269 (2017).
- 32 Samanta, A. & Medintz, I. L. Nanoparticles and DNA - a powerful and growing functional combination in bionanotechnology. *Nanoscale* 8, 9037-9095, doi:10.1039/c5nr08465b (2016).
- 33 Castro, C. E., Kilchherr, F., Kim, D. N., Shiao, E. L., Wauer, T., Wortmann, P., Bathe, M. & Dietz, H. A primer to scaffolded DNA origami. *Nat. Methods* 8, 221-229, doi:10.1038/nmeth.1570 (2011).
- 34 Douglas, S. M., Marblestone, A. H., Teerapittayanon, S., Vazquez, A., Church, G. M. & Shih, W. M. Rapid prototyping of 3D DNA-origami shapes with caDNAno. *Nucleic Acids Res.* 37, 5001-5006, doi:10.1093/nar/gkp436 (2009).

- 35 Dunn, K. E., Dannenberg, F., Ouldridge, T. E., Kwiatkowska, M., Turberfield, A. J. & Bath, J. Guiding the folding pathway of DNA origami. *Nature* 525, 82-86, doi:10.1038/nature14860 (2015).
- 36 Kosinski, R., Mukhortava, A., Pfeifer, W., Candelli, A., Rauch, P. & Sacca, B. Sites of high local frustration in DNA origami. *Nat Commun* 10, 1061, doi:10.1038/s41467-019-09002-6 (2019).
- 37 Song, J., Arbona, J. M., Zhang, Z., Liu, L., Xie, E., Elezgaray, J., Aime, J. P., Gothelf, K. V., Besenbacher, F. & Dong, M. Direct visualization of transient thermal response of a DNA origami. *J. Am. Chem. Soc.* 134, 9844-9847, doi:10.1021/ja3017939 (2012).
- 38 Stahl, E., Martin, T. G., Praetorius, F. & Dietz, H. Facile and scalable preparation of pure and dense DNA origami solutions. *Angew. Chem. Int. Ed. Engl.* 53, 12735-12740, doi:10.1002/anie.201405991 (2014).
- 39 Strauss, M. T., Schueder, F., Haas, D., Nickels, P. C. & Jungmann, R. Quantifying absolute addressability in DNA origami with molecular resolution. *Nat Commun* 9, 1600, doi:10.1038/s41467-018-04031-z (2018).
- 40 Tikhomirov, G., Petersen, P. & Qian, L. Fractal assembly of micrometre-scale DNA origami arrays with arbitrary patterns. *Nature* 552, 67-71, doi:10.1038/nature24655 (2017).
- 41 Zadegan, R. M. & Norton, M. L. Structural DNA nanotechnology: from design to applications. *Int J Mol Sci* 13, 7149-7162, doi:10.3390/ijms13067149 (2012).
- 42 Pan, K., Bricker, W. P., Ratanalert, S. & Bathe, M. Structure and conformational dynamics of scaffolded DNA origami nanoparticles. *Nucleic Acids Res.* 45, 6284-6298, doi:10.1093/nar/gkx378 (2017).
- 43 Kozyra, J., Ceccarelli, A., Torelli, E., Lopiccio, A., Gu, J. Y., Fellermann, H., Stimming, U. & Krasnogor, N. Designing Uniquely Addressable Bio-orthogonal Synthetic Scaffolds for DNA and RNA Origami. *ACS Synth Biol* 6, 1140-1149, doi:10.1021/acssynbio.6b00271 (2017).

- 44 Veneziano, R., Ratanalert, S., Zhang, K., Zhang, F., Yan, H., Chiu, W. & Bathe, M. Designer nanoscale DNA assemblies programmed from the top down. *Science* 352, 1534, doi:10.1126/science.aaf4388 (2016).
- 45 Mathur, D. & Medintz, I. L. Analyzing DNA Nanotechnology: A Call to Arms For The Analytical Chemistry Community. *Anal. Chem.* 89, 2646-2663, doi:10.1021/acs.analchem.6b04033 (2017).
- 46 Schnitzbauer, J., Strauss, M. T., Schlichthaerle, T., Schueder, F. & Jungmann, R. Super-resolution microscopy with DNA-PAINT. *Nat Protoc* 12, 1198-1228, doi:10.1038/nprot.2017.024 (2017).
- 47 Jungmann, R., Steinhauer, C., Scheible, M., Kuzyk, A., Tinnefeld, P. & Simmel, F. C. Single-molecule kinetics and super-resolution microscopy by fluorescence imaging of transient binding on DNA origami. *Nano Lett.* 10, 4756-4761, doi:10.1021/nl103427w (2010).
- 48 Jungmann, R., Avendano, M. S., Woehrstein, J. B., Dai, M., Shih, W. M. & Yin, P. Multiplexed 3D cellular super-resolution imaging with DNA-PAINT and Exchange-PAINT. *Nat. Methods* 11, 313-318, doi:10.1038/nmeth.2835 (2014).
- 49 Jungmann, R., Avendano, M. S., Dai, M., Woehrstein, J. B., Agasti, S. S., Feiger, Z., Rodal, A. & Yin, P. Quantitative super-resolution imaging with qPAINT. *Nat. Methods* 13, 439-442, doi:10.1038/nmeth.3804 (2016).
- 50 Graugnard, E., Hughes, W. L., Jungmann, R., Kostianen, M. A. & Linko, V. Nanometrology and super-resolution imaging with DNA. *MRS Bull.* 42, 951-959, doi:10.1557/mrs.2017.274 (2017).
- 51 Iinuma, R., Ke, Y., Jungmann, R., Schlichthaerle, T., Woehrstein, J. B. & Yin, P. Polyhedra self-assembled from DNA tripods and characterized with 3D DNA-PAINT. *Science* 344, 65-69, doi:10.1126/science.1250944 (2014).
- 52 Green, C. M., Schutt, K., Morris, N., Zadegan, R. M., Hughes, W. L., Kuang, W. & Graugnard, E. Metrology of DNA arrays by super-resolution microscopy. *Nanoscale* 9, 10205-10211, doi:10.1039/c7nr00928c (2017).

- 53 Odermatt, P. D., Shivanandan, A., Deschout, H., Jankele, R., Nievergelt, A. P., Feletti, L., Davidson, M. W., Radenovic, A. & Fantner, G. E. High-Resolution Correlative Microscopy: Bridging the Gap between Single Molecule Localization Microscopy and Atomic Force Microscopy. *Nano Lett.* 15, 4896-4904, doi:10.1021/acs.nanolett.5b00572 (2015).
- 54 Blumhardt, P., Stein, J., Mucksch, J., Stehr, F., Bauer, J., Jungmann, R. & Schwille, P. Photo-Induced Depletion of Binding Sites in DNA-PAINT Microscopy. *Molecules* 23, doi:10.3390/molecules23123165 (2018).
- 55 Kielar, C., Xin, Y., Xu, X., Zhu, S., Gorin, N., Grundmeier, G., Moser, C., Smith, D. M. & Keller, A. Effect of Staple Age on DNA Origami Nanostructure Assembly and Stability. *Molecules* 24, doi:10.3390/molecules24142577 (2019).
- 56 Liu, W., Zhong, H., Wang, R. & Seeman, N. C. Crystalline two-dimensional DNA-origami arrays. *Angew. Chem. Int. Ed. Engl.* 50, 264-267, doi:10.1002/anie.201005911 (2011).
- 57 Aghebat Rafat, A., Pirzer, T., Scheible, M. B., Kostina, A. & Simmel, F. C. Surface-assisted large-scale ordering of DNA origami tiles. *Angew. Chem. Int. Ed. Engl.* 53, 7665-7668, doi:10.1002/anie.201403965 (2014).
- 58 Rehman, F. N., Audeh, M., Abrams, E. S., Hammond, P. W., Kenney, M. & Boles, T. C. Immobilization of acrylamide-modified oligonucleotides by copolymerization. *Nucleic Acids Res.* 27, 649-655 (1999).

### 3.5 Supporting Information

#### 3.5.1 Materials and Methods

Unmodified DNA oligonucleotides (Tables 3.1-3.3) were purchased from Integrated DNA technologies. Cy3b modified DNA oligomers (Table 3.4) were purchased from Bio-Synthesis. M13mp18 scaffold was purchased from Bayou Biolabs (cat: P-107). Agarose (cat: R0492), 10X TBE (cat: FERB52), 100X Tris-EDTA (cat: BP1338-1), magnesium chloride hexahydrate (cat: AC197530010), nickel (II) chloride hexahydrate (cat: 50-901-14780), and SYBR™ gold nucleic acid gel stain (cat: 3.5.11494) were purchased from Fisher Scientific. 20% Ficoll® solution (cat: F5415-50ML) was purchased from Sigma Aldrich. 30% Acrylamide/Bis solution 29:1 (cat: 1610156) was purchased from Bio-Rad. Tetramethylethylenediamine (TEMED, cat: BP150-100) and ammonium persulfate (APS, cat: AC327081000) were purchased from Fisher Scientific. Cover glass mounts were designed and machined in house. Gold Seal® #1 cover glass (cat: 260341) were purchased from Ted Pella. 150 nm silane polymer-coated spherical AuNPs (part: E11-150-Silane-2.5) were custom ordered from Nanopartz. Alconox™ Liquinox™ (cat: NC9906065) and methanol (cat: AA19393K2) were purchased from Fisher Scientific. Type-F immersion oil (cat: MOIL-30) was purchased from ThorLabs. Bruker FastScan D AFM tips (cat: FASTSCAN-D) were purchased from Bruker. Fluoroelastomer X-profile o-rings (cat: 6450K126) and 2-56 flathead screws (cat: 92210A076) were purchased from Grainger.

##### 3.5.1.1 Optical Setup

Optical imaging was performed on a modified Nikon Eclipse TiU microscope equipped with a Nikon Total Internal Reflection Fluorescence (TIRF) illuminator and CFI Apo TIRF 100x NA 1.49 objective. A 561 nm Coherent Sapphire laser was used for excitation with a 0.5x stop down (approx. 8 mW TIRF illumination), and spectral filtration

was performed with a Chroma TRF49909 ET-561 nm filter set. An additional 1.5x magnification was used to achieve a total magnification of 150x and pixel size of 107 nm. Images were acquired using a Princeton Instruments ProEM Electron-Multiplying Charge Coupled Device (EMCCD) camera controlled by the imaging software LightField, set to 100x EM gain with low analog gain and 150 ms/frame (6.67 Hz) acquisition. The area captured within each image is  $55 \times 55 \mu\text{m}^2$  with a  $512 \times 512$  px sensor ROI. Focal drift was corrected in real time with an optical setup and feedback loop controlling a Mad City Labs (MCL) Nano-Drive piezo stage. Precise stage movements for registration were performed with an MCL Micro-Drive stepper motor stage.

#### 3.5.1.2 AFM Setup

AFM images were acquired in fluid on a Bruker Dimension FastScan with fluid tapping mode and Bruker FastScan D AFM tips. Sample cover glass were mounted on sticky silicone pads for AFM imaging. Typical scanning parameters were  $11 \mu\text{m/s}$  tip velocity with  $1 \text{ px/nm}$  resolution for image areas up to  $2 \times 2 \mu\text{m}^2$ , and  $40 \mu\text{m/s}$  tip velocity with  $2000 \times 2000$  px images acquired for areas up to  $20 \times 20 \mu\text{m}^2$ .

#### 3.5.1.3 Reusable fluidic chamber construction

For recovery of the substrate after TIRF imaging, reusable cover glass mounts were designed to enable construction and deconstruction of the fluidic chamber without damaging the cover glass substrate. The cover glass mounts (Figure 3.6b) were machined out of aluminum, and x-shaped o-rings were used to seal the open-backed fluidic chamber upon assembly. With this design, the cover glass is held in place by compression against the o-ring and can be easily removed from the mount after TIRF imaging.

#### 3.5.1.4 DNA origami synthesis

Cross-shaped DNA origami tiles (Figure 3.5, Tables 3.1-3.3) were prepared with 10 nM M13mp18 scaffold, 50 nM unmodified oligomers, and 500 nM docking oligomers in 0.5X TBE buffer (44.5 mM Tris, 44.5 mM boric acid, 1 mM EDTA, pH 8.3) with 12.5 mM MgCl<sub>2</sub>. Thermal annealing was performed in an Eppendorf Mastercycler Nexus Gradient thermal cycler using a previously reported recipe, provided in Table 3.5. After annealing, cross-tiles and sharp triangles were stained with 0.1X SYBR<sup>TM</sup> Gold and mixed with loading buffer (0.5X TBE, 20% Ficoll<sup>®</sup> solution in water) at 5:1 origami solution to loading buffer. DNA origami were filtered by agarose gel electrophoresis (0.8% agarose, 0.5X TBE, 8 mM MgCl<sub>2</sub>) at 7 V/cm for 90 minutes uncooled. Filtered DNA origami structure bands were identified under 305 nm UV light illumination and cut from the gel, and origami were extracted from the gel by compressing the agarose between glass slides. DNA origami concentrations were determined using a Thermo Scientific<sup>TM</sup> NanoDrop<sup>TM</sup> One microvolume UV-Vis spectrophotometer.

#### 3.5.1.5 Cover glass substrate preparation

Prior to cleaning, No. 1 cover glass (22 mm x 22 mm) were lightly inscribed with a fine-tip diamond scribe in the upper corner of each slide for orientation of the cover glass, and cross-marks were inscribed at the center of each slide to enable registration during imaging. Cover glass were then submerged in DI water with 0.1% Liquinox<sup>TM</sup> surfactant and cleaned by ultrasonic agitation (sonication) for 1 min to remove contaminants. Following sonication, cover glass were removed from the surfactant solution, submerged in DI water several times, then sonicated again for 1 min in DI water. Cover glass were placed in custom mounts and centrifuged at 1000 rcf for 5 min to remove excess water, then baked in an incubator at 40°C for > 30 min to remove any remaining water.

After cleaning and drying, 50  $\mu$ L of 200 fM silanized AuNPs in methanol were deposited on the cover glass and incubated for 10 min. During incubation, methanol was added as needed to prevent complete evaporation of the solution. Cover glass were rinsed with methanol, then submerged several times in DI water and dried by slowly withdrawing the cover glass from the water bath. Excess water was wicked from the surface with a lab wipe, then the cover glass were placed in the incubation chamber at 40°C and stored until use.

#### 3.5.1.6 Cover glass hydroxylation

To prepare cover glass for sample deposition, substrates were placed with the functionalized surface face up in a glow discharge vacuum chamber (Figure 3.6a), and the chamber was pumped down to 2 torr. Valves into the chamber were closed to maintain pressure statically, then the glow discharge was activated for 75 seconds to hydroxylate the surface. After glow discharge treatment, the chamber was vented slowly, then the cover glass was assembled into a reusable fluidic chamber for DNA origami deposition and imaging.

**Note:** It is best to minimize the amount of time that treated substrates are exposed to air and/or heat. The hydroxyl groups appear to relax at an accelerated rate when exposed to air and when heated. If covered with buffer at room temperature, the surface should remain functional for > 8 hours. This is particularly important for DNA-PAINT imaging; after the surface has reverted, imager strands will begin to adsorb to the surface.

All optical imaging steps were performed with identical buffer conditions, referred to as the working buffer (0.5X TBE with 18 mM MgCl<sub>2</sub>, pH 8.3).

### 3.5.1.7 DNA origami deposition

After coverslip hydroxylation and assembly of the fluid well, DNA origami solution (100 uL of DNA origami at 0.1 nM in working buffer) was deposited directly onto the surface (surface area ~ 1.77 cm<sup>2</sup>), then the fluidic chamber was sealed to prevent evaporation and the sample was incubated at room temperature for 30 minutes. After incubation, the DNA origami solution was wicked from the fluidic chamber, then the surface was rinsed twice with 200 uL working buffer. Excess buffer was then added to the sample and covered until use.

**Note:** The surface concentration of DNA can be controlled by the concentration of DNA origami, the divalent cation concentration, and the incubation time. High DNA concentrations (>1 nM for 100 uL volume) result in saturation of the surface with origami, and the degree of surface coverage is dependent on the concentration of MgCl<sub>2</sub>. Below 72 mM MgCl<sub>2</sub> only a single layer of origami is observed; aggregation does not occur given sufficient hydroxylation of the surface. Origami bound to the surface are highly stable and adsorption appears to be effectively irreversible in the buffer conditions described (0.5X TBE with 6 mM to 72 mM MgCl<sub>2</sub>).

**Note:** DNA-PAINT can be performed within approximately 8 hrs of preparation, but the best results are achieved immediately after preparation. If DNA-PAINT will not be performed, the sample can be stored significantly longer, though it is suggested to rinse the surface with filtered buffer prior to storage to reduce adsorption of contaminants to the surface.

### 3.5.1.8 Optical registration of region of interest (ROI)

After sample preparation, the fluidic chamber was mounted on the microscope. The additional 1.5x magnification was removed to provide a larger field of view to locate the inscribed registration marks. The registration mark was identified in brightfield, and the center of the cross-point was aligned to the center of the sensor ROI. Steps of 70  $\mu\text{m}$  were performed in the X and Y axes to move the imaging ROI away from the inscribed registration mark, and images were captured for each move and stitched together to provide a full view of the registration mark and desired ROI. Once the desired ROI was found, the 1.5x magnification was added and illumination was changed to the 561 nm laser for TIRF imaging.

### 3.5.1.9 DNA-PAINT imaging

For DNA-PAINT imaging, several imaging and rinsing buffers were prepared. Imaging solutions M1' and M3' (Table 3.4) were prepared with 3 nM of Cy3b-labeled imager strands M1' or M3', respectively, in working buffer. A passivation solution was prepared with M1 ssDNA (complementary to imager strand M1) at 3  $\mu\text{M}$  in working buffer, and excess working buffer was prepared for additional rinsing steps. For two-color image acquisition, 400  $\mu\text{L}$  of imaging solution M1' was first added to the fluidic chamber. 24,000 frames were acquired with 150 ms/frame for a total of 1 hr acquisition. 400  $\mu\text{L}$  of M1 passivation buffer was added to the fluidic chamber and incubated for 2 minutes, then the chamber was rinsed with 400  $\mu\text{L}$  of working buffer. 400  $\mu\text{L}$  of imaging solution M3' was added to the chamber, and image acquisition was performed. After imaging, the fluidic chamber was rinsed twice with 400  $\mu\text{L}$  of filtered working buffer, then the sample was transferred for AFM imaging.

#### 3.5.1.10 AFM imaging

The fluidic chamber was deconstructed to provide access to the substrate, and the cover glass was placed on a silicone pad and mounted on the AFM stage. The sample was rinsed with 300  $\mu\text{L}$  of filtered working buffer, then 300  $\mu\text{L}$  of filtered working buffer with 1 mM  $\text{NiCl}_2$  was deposited on the surface and incubated for 5 min. For imaging, 300  $\mu\text{L}$  of filtered working buffer was deposited on the surface. The AFM tip was aligned over the center of the registration mark, then steps of 70  $\mu\text{m}$  were performed in the X and Y axes to relocate the correct ROI, accounting for any changes in the orientation of the substrate. The sample was then engaged, and high-resolution AFM images (1 nm/px and 1  $\mu\text{m}$  or 2  $\mu\text{m}$  per side) were captured. 50  $\mu\text{L}$  of DI water was added to the sample every 30 minutes to counteract evaporation. Large area AFM images (5  $\mu\text{m}$ , 10  $\mu\text{m}$ , and/or 20  $\mu\text{m}$  per side, 2000 x 2000 px) were then acquired, centered on the original ROI.

#### 3.5.1.11 Super-resolution localization and post-processing

Image localization, fiducial-based xy-drift correction, and image post-processing were performed with the ThunderSTORM plugin for ImageJ, which is available for download at <http://zitmen.github.io/thunderstorm/>.<sup>1,2</sup> The images were filtered to remove localizations with uncertainty greater than 15 nm and exported at 20x magnification (5.35 nm/px) for rough alignment to AFM images. Corresponding DNA-PAINT ROI were identified for each AFM image and rendered at the resolution of the AFM image.

#### 3.5.1.12 AFM image processing

AFM images were processed with Gwyddion (available at <http://gwyddion.net/>) using a simple three-step leveling and scar removal procedure.<sup>3</sup> Images were leveled initially by ‘mean plane subtraction’, then rows were aligned using the ‘median’ method. Lastly,

horizontal stroke scars were removed, and the images were rendered at the captured resolution using a grayscale LUT for correlated images.

#### 3.5.1.13 Alignment of DNA-PAINT and AFM images

Initial alignment of DNA-PAINT and AFM images was performed by manual alignment of AuNP fiducial markers identified in the DNA-PAINT and large area AFM images. Within the full DNA-PAINT field of view, ROI were identified corresponding to each AFM image, and each ROI was rendered in ThunderSTORM at a resolution matching the defined AFM image. Next, the MATLAB script cpselect (Control Point Selection tool) was used to identify corresponding points of interest (POI) in the images, generate a geometric transformation to minimize global offsets, and transform the AFM image for overlay on the corresponding SRM image; details can be found at <https://www.mathworks.com/help/images/ref/cpselect.html>. It was found that topographic images up to  $5 \times 5 \mu\text{m}^2$  were well aligned using a projective transformation; for larger images, locally-weighted mean transformations were required on occasion, likely due to stage drift during AFM imaging. The transformation was applied to the DNA-PAINT image and cropped to the boundaries of the corresponding AFM image. The corrected DNA-PAINT image was then overlaid on the AFM image using ImageJ. See Figure 3.15 for reference.

#### 3.5.1.14 PAGE filtration of docking sites

For native PAGE filtration, a 10% native PAGE gel (10% 29:1 acrylamide/bis-acrylamide, 0.1% w/v PSA, 0.064% v/v TEMED, 1x TBE, 1.5 mm thickness and 10 cm length) was prepared and ran for 30 minutes with 1x TBE buffer. ssDNA samples (50  $\mu\text{M}$  ssDNA, 1x TBE, 6% Ficoll) were loaded onto the gel and ran uncooled for 120 minutes

with 150 V applied voltage. The completed PAGE gel was imaged on a phosphor plate with 254 nm illumination, then the main sample bands were cut from the gel, crushed, and submerged in 150 uL of 1x TE buffer. After 24 hours, the samples were centrifuged for 5 min @ 10,000 rcf, and the supernatant was extracted from each sample.

#### 3.5.1.15 PAGE filtration with Acrydite-immobilized ssDNA (seqPAGE)

For docking site-targeted PAGE filtration, short Acrydite-labeled ssDNA strands (sequence M1') were added to a 10% native PAGE gel at 3  $\mu$ M concentration prior to polymerization of the gel (10% 29:1 acrylamide/bis-acrylamide, 0.1% w/v PSA, 0.064% w/v TEMED, 1x TBE, 12.5 mM MgCl<sub>2</sub>, 3  $\mu$ M Acry-5T-M1', 1.5 mm thickness and 10 cm length). Acrydite, an acrylamide phosphoramidite, polymerizes with acrylamide upon the addition of the polymerizing agents APS and TEMED, covalently binding Acrydite-labelled ssDNA into the gel.<sup>4</sup> The immobilized ssDNA was synthesized with a 7 nt domain complementary to M1 docking sites, thus staple strands with an active docking site could transiently hybridize to immobilized ssDNA, slowing progression through the gel. The gel was cooled to 5 C and ran for 30 minutes at 150 V with 1x TBE and 12.5 mM MgCl<sub>2</sub>. ssDNA samples (100  $\mu$ M ssDNA, 1x TBE, 12.5 mM MgCl<sub>2</sub>, 6% Ficoll) were loaded onto the gel and ran for 120 minutes with 150 V applied voltage, cooled to 5 C. The completed PAGE gel was imaged on a phosphor plate with 254 nm illumination (Figure 3.28), then the main sample bands were cut from the gel, crushed, and submerged in 150 uL of 1x TE buffer. After 24 hours, the samples were centrifuged for 5 min @ 10,000 rcf, and the supernatant was extracted from each sample.

#### 3.5.1.16 PAGE filtration of weakly duplexed strands (dpxPAGE)

A second method for docking site-targeted PAGE filtration was demonstrated on docking site staple strands using the formation of weak duplexes at the docking site. Staple strands were mixed 1:1 with duplexing strands (53 nt total length, 46/47 nt poly-thymine with 3' 8/9 nt M1' domain) at 200  $\mu$ M in 1x TBE with 12.5 mM MgCl<sub>2</sub> and 6% Ficoll, and the mixture was heated to 90 C and cooled to 20 C over 20 minutes. A 10% native PAGE gel (10% 29:1 acrylamide/bis-acrylamide, 0.1% w/v PSA, 0.064% w/v TEMED, 1x TBE, 12.5 mM MgCl<sub>2</sub>, 1.5 mm thickness and 10 cm length) was prepared, cooled to 5 C, and ran for 30 minutes at 150 V with 1x TBE and 12.5 mM MgCl<sub>2</sub>. The annealed ssDNA samples were loaded onto the gel and ran for 120 minutes with 150 V applied voltage, cooled to 5 C. The completed PAGE gel was imaged on a phosphor plate with 254 nm illumination (Figure 3.29), then the main sample bands were cut from the gel, crushed, and submerged in 150  $\mu$ L of 1x TE buffer. After 24 hours, the samples were centrifuged for 5 min @ 10,000 rcf, and the supernatant was extracted from each sample.

### 3.5.2 Characterization and Analysis

#### 3.5.2.1 TIRF image signal-to-noise ratio (SNR)

The SNR of fluorescent events in TIRF images was determined from parameters of the fitted symmetric 2D gaussian point spread function ( $PSF_G$ ) for individual events:

$$PSF_G(x, y, i) = \frac{I_i}{2\pi\sigma_i^2} \exp\left(-\frac{(x - X_i)^2 + (y - Y_i)^2}{2\sigma_i^2}\right) + B_i \quad (1)$$

where  $I_i$  is the total intensity of event  $i$ ,  $\sigma_i$  is the spread,  $X_i$  and  $Y_i$  are the localized sub-pixel coordinates of point source  $i$ , and  $B_i$  is the local background intensity offset. The SNR was calculated with  $I_i$  as the signal and  $B_i$  as the noise for individual events:

$$SNR (dB) = 20 * \log_{10}\left(\sqrt{\frac{\sum I_i^2}{\sum B_i^2}}\right) \quad (2)$$

### 3.5.2.2 Quantifying 2D dispersion in correlated images

To quantify the 2D dispersion of correlated points in DNA-PAINT and AFM images, the MATLAB `cselect` script was adapted for manual identification of positions of corresponding POI in the corrected DNA-PAINT image and the original AFM image. 286 corresponding POI were identified in two sets of correlated images (Figures 3.16 and 3.17) with 1 nm/px image resolution. The spatial deviation of each DNA-PAINT POI from the corresponding AFM POI was calculated, and the 2D dispersion was calculated as the standard deviation of DNA-PAINT sites from AFM,

$$\sigma_{xy} = \sqrt{\frac{1}{n-1} \sum ((x_m - X_m)^2 + (y_m - Y_m)^2)} \quad (3)$$

where  $x_m, y_m$  are the x/y coordinates of site  $m$  in the AFM image,  $X_m, Y_m$  are the x/y coordinates of site  $m$  in the DNA-PAINT image, and  $n$  is the total number of sites examined. For the sites examined,  $\sigma_{xy} = 5 \pm 3$  nm. The offsets were also plotted as a function of position to ensure uniform alignment across correlated images. The results are shown in Figures 3.3 and 3.18.

### 3.5.2.3 Progression of DNA-PAINT imaging

To calculate the fraction of active sites detected during DNA-PAINT imaging, a full field view of a DNA-PAINT image was rendered at 5.35 nm/pixel. Maxima were identified in the rendered image with an intensity threshold of two localizations. The list of positions of maxima within the image was exported. To calculate the number of localizations per POI as a function of time, a MATLAB script was created to perform a search of the full localizations list and identify localizations corresponding to individual POI. Each POI was assigned a search radius  $R$  as a function of the average localization uncertainty  $\bar{\sigma}_{loc}$  for all

events in the localization list,  $R = 2\bar{\sigma}_{loc}$ . A time-resolved POI list was generated containing the position of each POI and a count of the cumulative localizations per minute for each POI. The cumulative number of first detections of POI (i.e., the total number of unique docking sites detected) in time was calculated from the time-resolved list. The cumulative first detections,  $N(t)$ , was approximated with a two-part exponential decay,

$$N(t) = A_1(1 - \exp(-k_1t)) + A_2(1 - \exp(-k_2t)), \quad (4)$$

where  $k_1$  and  $k_2$  are the detection rate constants for two independent populations of reaction sites with binding rates  $k_1$  and  $k_2$ , assuming pseudo-first order kinetics.<sup>5</sup> For DNA origami cross-tiles imaged with standard imaging buffer, it was found that the secondary population of reaction sites was large ( $A_2 \gg A_1$ ) with a low rate constant ( $k_2 \ll k_1$ ). Given that the number of active POI is fixed during imaging, the secondary population was speculated to be the result of nonspecific imager strand interactions with the substrate. For  $t \ll 1/k_2$ , the cumulative first detections associated with the second population of sites can be approximated to be linear with respect to time,

$$\text{for } t \ll \frac{1}{k_2}, \quad A_2(1 - \exp(-k_2t)) \cong A_2k_2t. \quad (5)$$

The cumulative first detections can thus be approximated,

$$N(t) = N_{total}(1 - \exp(-k_1t)) + ct, \quad (6)$$

where  $N_{total}$  and  $k_1$  are the total number of active sites and the reaction rate constant, respectively, for DNA-PAINT, and  $c$  is the correction factor for nonspecific events, approximated as  $c = A_2k_2$ . The fraction of active sites detected,  $\theta(t)$ , as a function of time for DNA-PAINT was thus approximated as

$$\theta(t) = \frac{N(t) - ct}{N_{total}} = 1 - \exp(-k_1t). \quad (7)$$

For comparison, the reaction rate constant can also be approximated from the total number of detections ( $D_{total}$ ), the number of unique POI identified ( $N_{total}$ ), the association rate constant ( $k_{on}$ ), and the dissociation rate constant ( $k_{off}$ ) assuming the system has reached thermodynamic equilibrium, indicated by a constant flux of imager strands. The rate equation can then be expressed,

$$\frac{dI}{dt} = k_{on}[I][P] - k_{off}[IP] = 0 \quad (8)$$

where  $[I_e]$ ,  $[P_e]$ , and  $[IP_e]$  are the equilibrium concentrations of imager strands, active POI, and bound imager strands, respectively. For active sites  $P$  and bound imager strands  $IP$  confined to a surface,  $[P]$  and  $[IP]$  were approximated from the experimentally determined  $N_{total}$  and the average detections per frame for the case where  $[P_e] \gg [IP_e]$ ,

$$[P_e] = \frac{N_{total}}{Area} - [IP_e] \approx \frac{N_{total}}{Area} \quad (9)$$

and

$$[IP_e] \approx \frac{D_{total}}{Area} * \frac{dt}{t_{total}} = \frac{\bar{D}}{Area} \quad (10)$$

and the reaction rate constant,  $k_1$ , for DNA-PAINT was calculated,

$$k_1 = k_{on} * [I_e] = k_{off} \frac{[IP_e]}{[P_e]} = k_{off} \frac{\bar{D}}{N_{total}}. \quad (11)$$

The reaction rate constant and the total imaging time can then be used to approximate the fraction of active sites detected during DNA-PAINT imaging with eq. 7. For the DNA origami cross-tile sample analyzed in Figure 3.19, the reaction rate constant  $k_1 = 0.00273 \text{ s}^{-1}$ , in close agreement with the value calculated from the cumulative first detections,  $k_1 = 0.00263 \text{ s}^{-1}$ .

#### 3.5.2.4 Calculation of the site detection efficiency

To calculate the site detection efficiency for each DNA-PAINT sample, DNA-PAINT images were rendered at 20x with ThunderSTORM, and maxima were identified with a threshold of two localization events, generating a binary image of maxima. To reduce the probability of incorrect counts caused by overlapping structures, points in the binary image were dilated by 50 nm, causing structures to overlap if a structure is located within 100 nm of another structure. To remove overlapping structures, the dilated structures were filtered by total area, and structures with area greater than expected for an individual structure were filtered out of the image (Figure 3.20). The center of mass was calculated for the remaining structures, then a list of the center of masses was exported from ImageJ. A MATLAB script was created to identify individual structures in the maxima image using the center of mass list and generate input vectors for classification by neural pattern recognition (NPR) using the MATLAB `nprtool` (Figure 3.21); details can be found at <https://www.mathworks.com/help/deeplearning/gs/classify-patterns-with-a-neural-network.html>.

To train the network, SRM images of DNA origami cross-tiles were examined manually to identify tiles with two, three, and four resolved docking sites, as well as overlapping structures with greater than four sites resolved. A minimum of 500 training images were identified for each case, and additional training images were generated by rotational and mirror transformations of the manually selected training images. To reduce the size of the input vector for each structure and improve the performance of NPR, unique input vectors consisting of 53 elements were constructed for each structure. The input vectors were generated by concatenating the radial distribution function of each image with the count of the total number of sites detected. The NPR tool was used to generate a neural

network with 10 hidden neurons, and the network was trained to classify tiles by the number of sites resolved using over 4000 training images for each class. Performance testing during training found less than 1% error for classified structures.

Structures were classified by the number of sites resolved, and structures with uncertain classifications or less than two sites resolved were discarded as they cannot be distinguished from non-specific binding of imager strands to the substrate. The remaining distribution of classified structures was fitted with a binomial probability distribution function,

$$f(x|4, p) = N \binom{4}{x} p_{det}^x (1 - p_{det})^{4-x} \quad (12)$$

for  $2 \leq x \leq 4$  to calculate the probability of detection ( $p_{det}$ ) of individual sites for each sample. To ensure consistent performance of the automated structure classification, 5 images, each containing 500 structures, were classified manually, and the results were compared to automated classification. For the five images, the maximum deviation in  $p_{det}$  between manual and automated classification was less than 1% (Figure 3.21).

After training the network, classification could be performed on all qualifying structures in a DNA-PAINT image (typically several thousand structures) in a few seconds. Manual classification of the same structures would be impractical. With this method, the detection efficiency could be calculated as a function of time, and the progression shown in Figure 3.19c was determined from classification of over 60,000 structures. Automated classification was also used to determine the detection efficiencies reported in Figure 3.30.

#### 3.5.2.5 AFM detection of unincorporated strands

To determine the fidelity of unincorporated site detection with AFM, DNA origami cross-tiles were synthesized with unincorporated sites by intentionally excluding strands

P-L6 and P-R1 (Table 3.3) during synthesis. All docking sites were included in the synthesis; the excluded strands, located on two opposite corners of tile arm LR, served solely as passivation against blunt-end stacking interactions between tiles. Following synthesis, cross-tiles were filtered with agarose gel electrophoresis (section 3.5.1.4). Samples were prepared for correlative DNA-PAINT/AFM microscopy and imaged according to the protocols described in sections 3.5.1.5 to 3.5.1.13. During AFM imaging, two images were captured (Figures 3.22, 23) at 1 nm/px and 2 nm/px, respectively, to determine the imaging resolution necessary to detect unincorporated sites.

For defect analyses, edge detection methods were utilized in Gwyddion to enhance the visibility of features on tile edges. Cross-tiles within the AFM images were examined for edge defects, indicated by a shortened tile edge which appears as an indentation in the corner of a tile arm or rounding of the corner. Within the images shown in Figures 3.22 and 3.23, all intentional unincorporated sites were detected and are indicated by white circles. The edge lengths of unincorporated sites were measured and compared to tile edges without apparent defects, and the results are provided in Figure 3.24. The observed variation in edge length was  $6 \pm 2$  nm, in close agreement with the value expected for a change of 16 nt (5.4 nm). The results indicate that unincorporated sites can be reliably detected with AFM under similar conditions.

#### 3.5.2.6 Correlative defect metrology

For correlative defect analysis, DNA-PAINT and AFM images were examined independently to identify and locate docking site defects, indicated by unresolved (inactive) sites in DNA-PAINT and missing (unincorporated) sites in AFM. Unincorporated docking sites can be detected with both techniques and were identified as

such, though correlated defects may occur by chance if structural defects occur during or after DNA-PAINT imaging, such as AFM tip-induced defects, resulting in AFM defect detections that do not correspond to unincorporated sites. All possible states for docking sites imaged with DNA-PAINT can be expressed by the probabilities of docking site incorporation ( $p_{Inc.}$ ), activity of an incorporated site ( $p_{Act.}$ ), and detection of an active and incorporated site ( $p_{Det.}$ ),

$$1 = \underbrace{p_{Inc.} * p_{Act.} * p_{Det.}}_{p_{on}} + \underbrace{p_{Inc.} * p_{Act.} * (1 - p_{Det.}) + p_{Inc.} * (1 - p_{Act.}) + (1 - p_{Inc.})}_{p_{off}} \quad (13)$$

where  $p_{on}$  is the probability of resolving a docking site and  $p_{off}$  accounts for all other scenarios in which docking sites were unresolved in DNA-PAINT. It was found that  $p_{Det.}$  approaches 1 after 60 minutes of image acquisition for the experimental conditions (3.5.2.3, Figure 3.19), thus  $p_{on}$  and  $p_{off}$  can be approximated as the limit where  $p_{Det.} \rightarrow 1$ ,

$$p_{on} \approx p_{Inc.} * p_{Act.} \quad \text{and} \quad p_{off} \approx p_{Inc.} * (1 - p_{Act.}) + (1 - p_{Inc.}) \quad (14)$$

Similarly, all possible states of docking sites in AFM images can be expressed by the probability of detection of existing defects in AFM images ( $p_{dDet.}$ ), the probability of characterization-induced defects on active sites ( $p_{dImg.}$ ), and  $p_{Inc.}$ ,

$$1 = \underbrace{p_{Inc.} * (1 - p_{dImg.}) + (p_{Inc.} * p_{dImg.} + (1 - p_{Inc.})) * (1 - p_{dDet.})}_{\text{no defect detected } (p_{nD})} + \underbrace{(p_{Inc.} * p_{dImg.} + (1 - p_{Inc.})) * p_{dDet.}}_{\text{defect detected } (p_{dD})} \quad (15)$$

where  $p_{nD}$  is the probability of not detecting a defect on a site and  $p_{dD}$  accounts for all other scenarios in which defects are detected. It was found that  $p_{dDet.}$  was close to 1 for AFM images acquired under similar experimental conditions (see Figures 3.22-3.24), thus  $p_{nD}$  and  $p_{dD}$  can be approximated as the limit where  $p_{dDet.} \rightarrow 1$ ,

$$1 = \underbrace{p_{Inc.} * (1 - p_{dImg.})}_{no\ defect\ detected\ (p_{nD})} + \underbrace{p_{Inc.} * p_{dImg.} + (1 - p_{Inc.})}_{defect\ detected\ (p_{dD})} \quad (16)$$

The possible states of docking sites observed with both DNA-PAINT and AFM can then be expressed by adapting the AFM state equation to account for active and inactive incorporated sites and substituting  $p_{on}$  and  $p_{off} = 1 - p_{on}$ ,

$$1 = \underbrace{p_{on} * (1 - p_{dImg.})}_{p_{11}} + \underbrace{p_{on} * p_{dImg.}}_{p_{10}} + \underbrace{(p_{Inc.} - p_{on}) * (1 - p_{dImg.})}_{p_{01}} + \underbrace{(p_{Inc.} - p_{on}) * p_{dImg.} + (1 - p_{Inc.})}_{p_{00}} \quad (17)$$

where  $p_{11}$  and  $p_{10}$  are the probabilities of resolving the docking sites in DNA-PAINT without and with observing AFM defects at the same location, respectively, and  $p_{01}$  and  $p_{00}$  are the probabilities of unresolved sites in DNA-PAINT without and with AFM defects, respectively. The probabilities, determined directly from the correlated defect counts, can also be expressed as a system of equations with  $p_{on}$  as determined from the DNA-PAINT image and unknown variables  $p_{Inc.}$  and  $p_{dImg.}$ ,

$$\begin{aligned} p_{11} &= p_{on} * (1 - p_{dImg.}) && \Rightarrow \text{Resolved in SRM, No defect in AFM} \\ p_{10} &= p_{on} * p_{dImg.} && \Rightarrow \text{Resolved in SRM, Defect in AFM} \quad (18) \\ p_{01} &= (p_{Inc.} - p_{on}) * (1 - p_{dImg.}) && \Rightarrow \text{Not resolved in SRM, No defect in AFM} \\ p_{00} &= (p_{Inc.} - p_{on}) * p_{dImg.} + (1 - p_{Inc.}) && \Rightarrow \text{Not resolved in SRM, Defect in AFM} \end{aligned}$$

To solve the state equations, it was initially assumed that characterization-induced defects were randomly distributed among all incorporated sites and thus  $p_{dImg.}$  would be equivalent for resolved and unresolved sites. In this case,  $p_{dImg.}$  can be solved from  $p_{11}$  and  $p_{10}$ ,

$$p_{dImg.} = \frac{p_{10}}{p_{on}} \quad (19)$$

and applied to directly determine the probability of site incorporation and activity of incorporated sites,

$$p_{Inc.} = \frac{p_{01}}{(1 - p_{dmg.})} + p_{on} \quad \text{and} \quad p_{Act.} = \frac{p_{on}}{p_{Inc.}} \quad (20)$$

For docking sites on the DNA origami cross-tile (Figure S25), it was found that  $p_{11} = 0.70$ ,  $p_{10} = 0.16$ , and  $p_{01} = 0.12$ . Solving for  $p_{dmg.}$ ,  $p_{Inc.}$ , and  $p_{Act.}$  using equations 19 and 20, it was found that the experimental values produced non-physical results with a probability of incorporation exceeding 1:  $p_{dmg.} = 0.19$ ,  $p_{Inc.} = 1.01$ , and  $p_{Act.} = 0.85$ . It was speculated that this resulted from an incorrect assumption that  $p_{dmg.}$  was equivalent for active and inactive docking sites and could be calculated from the experimental results for active sites alone. If we define an independent value for the probability of characterization-induced defects for inactive sites ( $p'_{dmg.}$ ) and assume as a boundary condition that  $p_{Inc.} \rightarrow 1$ , we approximate a maximum value for  $p'_{dmg.}$ ,

$$\frac{p_{00}}{p_{00} + p_{01}} = \frac{(p_{Inc.} - p_{on}) * p'_{dmg.} + (1 - p_{Inc.})}{(p_{Inc.} - p_{on}) * p'_{dmg.} + (1 - p_{Inc.}) + (p_{Inc.} - p_{on}) * (1 - p'_{dmg.})} \quad (21)$$

and applying the boundary condition,

$$\text{for } p_{Inc.} \rightarrow 1, \quad \frac{p_{00}}{p_{00} + p_{01}} = p'_{dmg.} \quad (22)$$

From the experimental results, it was found that the maximum value for  $p'_{dmg.} = 0.12$ , less than the value calculated for active sites,  $p_{dmg.} = 0.19$ . The results suggest that the probability of characterization-induced damage varies between active and inactive sites, and thus the value of  $p_{Inc.}$  cannot be directly calculated. Instead, the values reported for  $p_{Inc.}$  throughout this work will represent the minimum value for  $p_{Inc.}$ , determined for the boundary condition in which  $p'_{dmg.} \rightarrow 0$  and  $p_{Inc.} = 1 - p_{00}$ .

## 3.5.3 Supplemental Figures

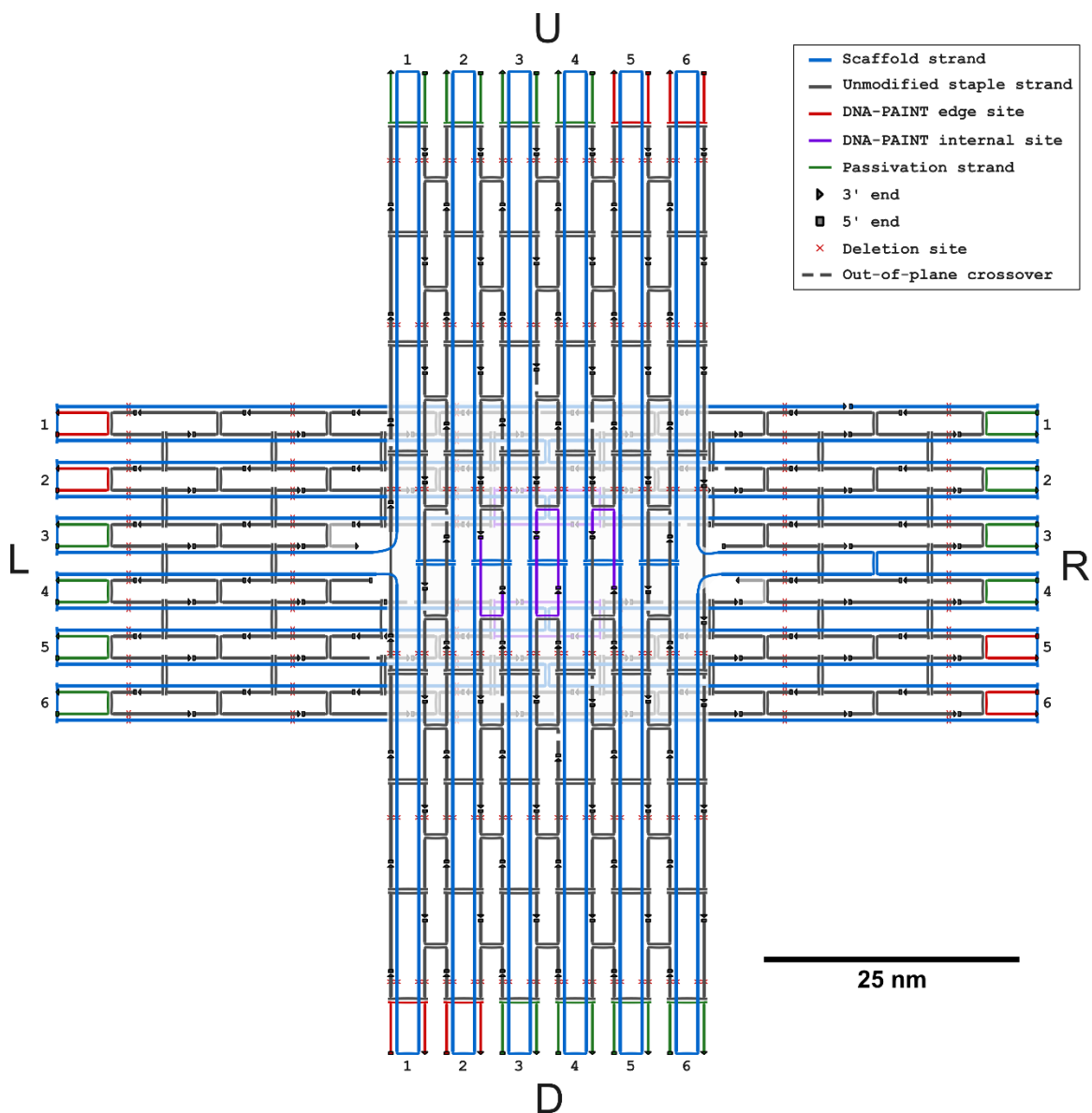


**Figure 3.5** DNA origami cross-tile caDNAno schematic.<sup>6</sup> Modified caDNAno schematic of the twist-corrected DNA origami cross-tile,<sup>7,8</sup> altered to more closely depict the geometry of the intended structure. Individual staple strand sequences can be found in Tables 3.1-3.3.

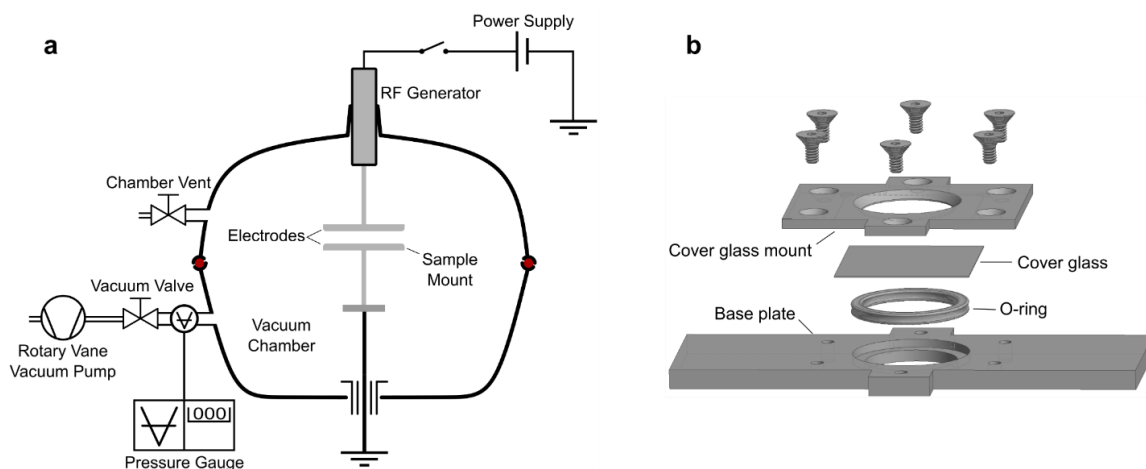


**Figure 3.6** Schematic of glow discharge vacuum chamber and fluidic well. (a) Schematic diagram of the custom glow discharge vacuum chamber used for hydroxylation of cover glass.<sup>9</sup> For glow discharge treatment, power to the RF (radio frequency) generator was supplied for 75 seconds, during which the chamber pressure was held at 2 torr. (b) 3D CAD model of custom, reusable fluidic well, designed and machined in house. The base plate and cover glass mount were machined from aluminum, and the screws, o-ring, and cover glass were purchased separately.

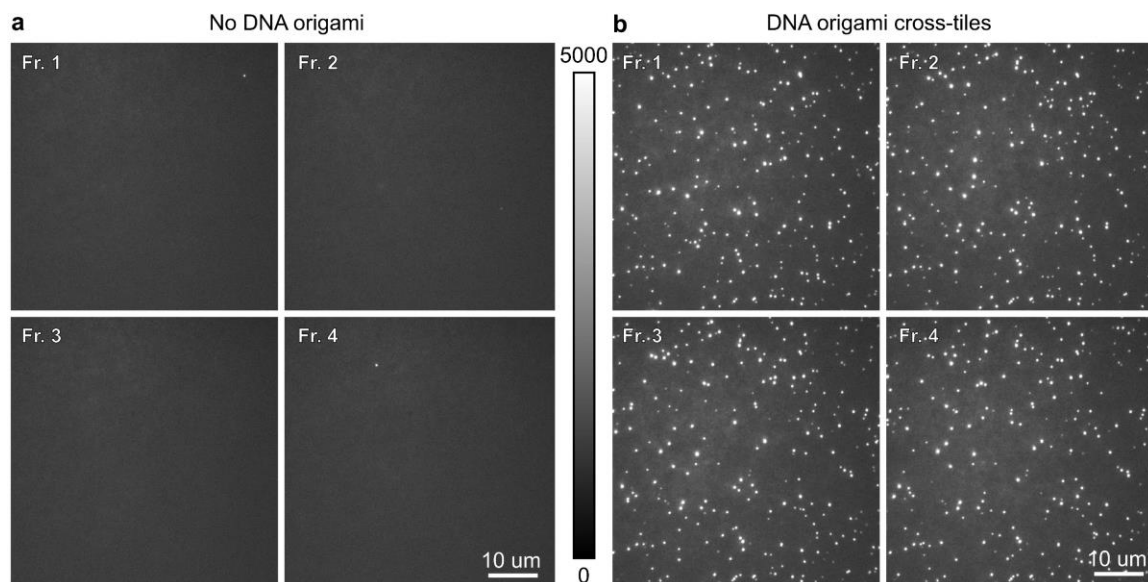


**Figure 3.7** Selective passivation of cover glass by hydroxylation. The first four TIRF frames of image acquisition of hydroxylated cover glass (a) without DNA origami and (b) with DNA origami cross-tiles adsorbed onto the surface. The imaging buffer for both samples was 0.5X TBE with 35 mM MgCl<sub>2</sub>, pH 8.3, and 3 nM Cy3b-labeled imager strands. The samples were imaged under identical experimental conditions, and the color range is identical for all images.

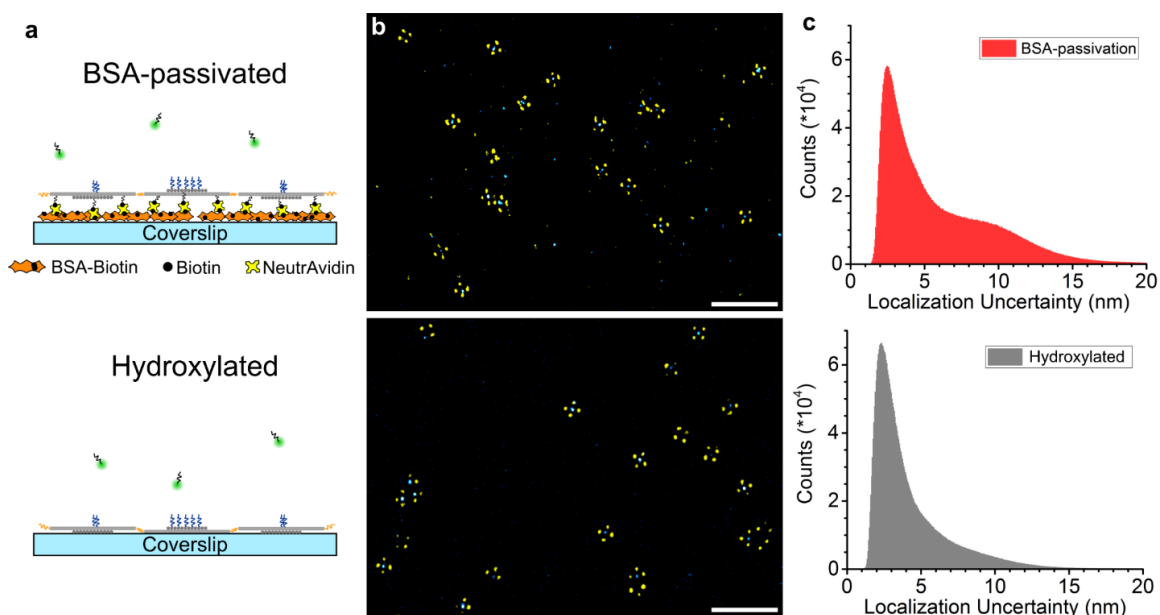


**Figure 3.8 Comparison of DNA-PAINT images on BSA-passivated and hydroxylated cover glass. (a) Depiction of DNA origami cross-tiles bound to cover glass by protein-binding (top) and by hydroxylation (bottom), with (b) multiplexed DNA-PAINT imaging and (c) localization uncertainty distributions shown for each, respectively. The localization lists corresponding to the images in (b) were corrected for xy-drift and rendered at 5.35 nm/px; no filters were applied to the list prior to image rendering. Nonspecific binding events are indicated in DNA-PAINT images by localizations randomly distributed between structures and in the localization uncertainty distribution by a second population of events with higher localization uncertainty. The second population of events was speculated to result from nonspecific binding events lasting less than one full frame of acquisition. Scale bars, 500 nm.**

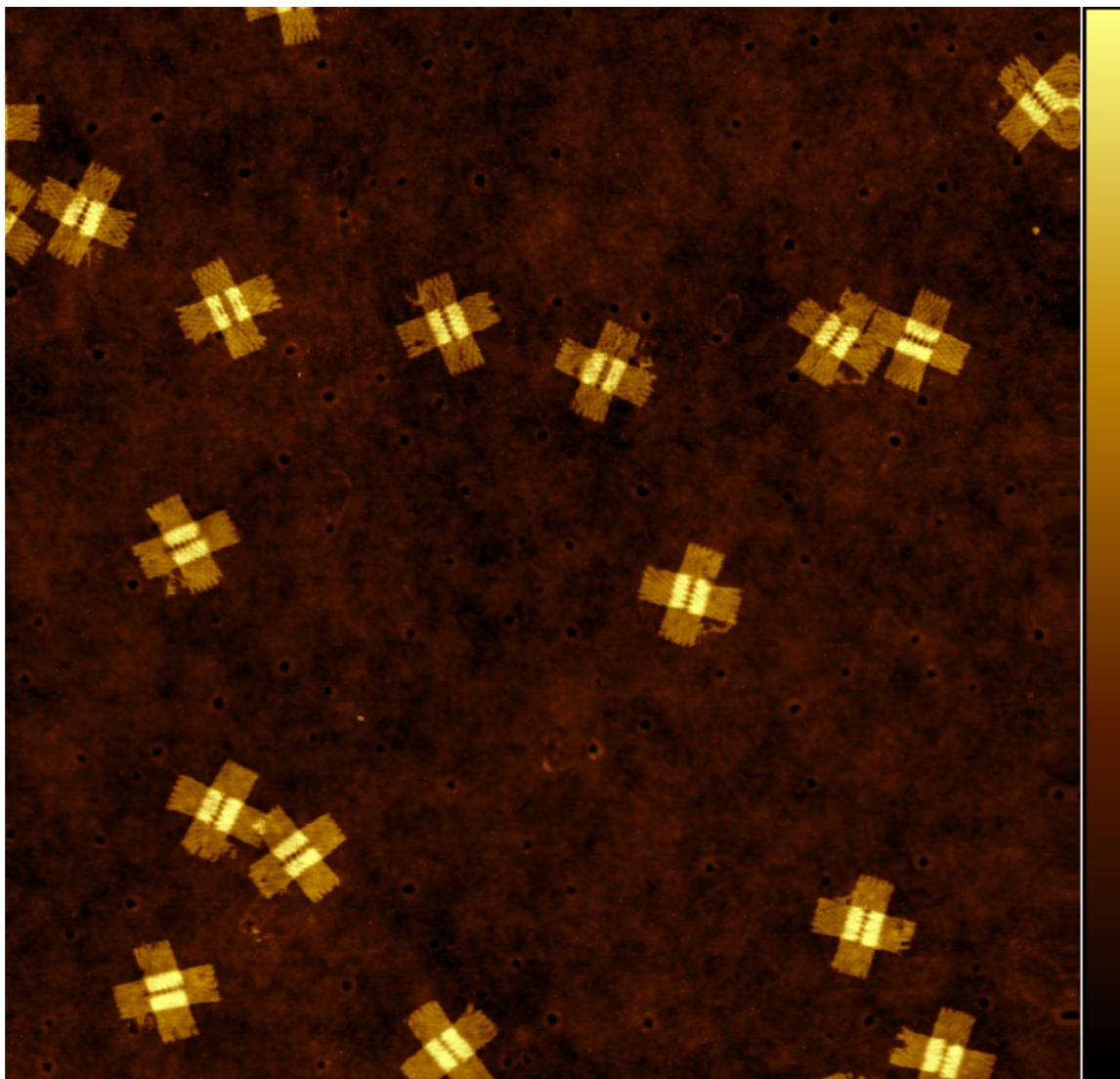


**Figure 3.9** High resolution AFM topography image of DNA origami cross-tiles on hydroxylated cover glass. Tapping mode topography images were acquired in fluid (0.5x TBE, 18 mM MgCl<sub>2</sub>). The image shown is 1  $\mu\text{m}$  x 1  $\mu\text{m}$  and was captured with 1000 pts/line and 3 Hz scan rate. The pores observed on the surface were suspected to result from phase separation during cooling of the borosilicate glass after formation. AFM height scale bar, 4.2 nm.

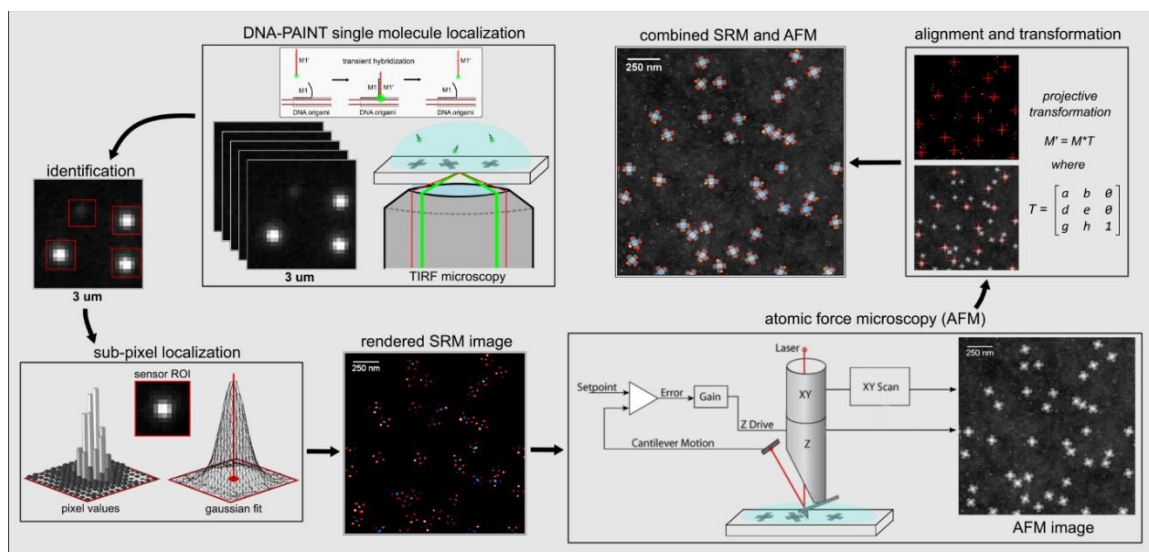


**Figure 3.10** Schematic depicting correlative DNA-PAINT/AFM imaging. For correlative imaging, samples were mounted on an inverted microscope and viewed in brightfield to locate substrate registration marks and perform a programmed stage movement to a specified ROI. DNA-PAINT images of origami within the ROI were then acquired in TIRF illumination by a 561-nm laser source. Fluorescent events were identified in each frame and localized to sub-pixel coordinates, then the positions of each event were corrected for xy-drift by tracking fiducial markers as a function of time and generating a translational correction for events in each frame. Super-resolution microscopy (SRM) images were rendered from the corrected localization list, and pseudo-colors were assigned to each image to indicate the imager strand used. After SRM imaging, substrates were removed from the fluidic chamber and transferred for AFM characterization in fluid. The substrate was viewed optically to identify registration marks and move to the ROI imaged with SRM. Topographic images were acquired in fluid tapping mode using protocol provided in the methods. After AFM imaging and image processing, SRM and AFM images were roughly aligned using corresponding structures in the images. The positions of corresponding docking sites in each image were used to generate a projective transformation to transform SRM to AFM and correct for global image aberrations (Figure 3.14). The corrected SRM and AFM images were then combined by averaging. AFM schematic adapted from Bruker Dimension Icon/FastScan Bio help files.<sup>10</sup>

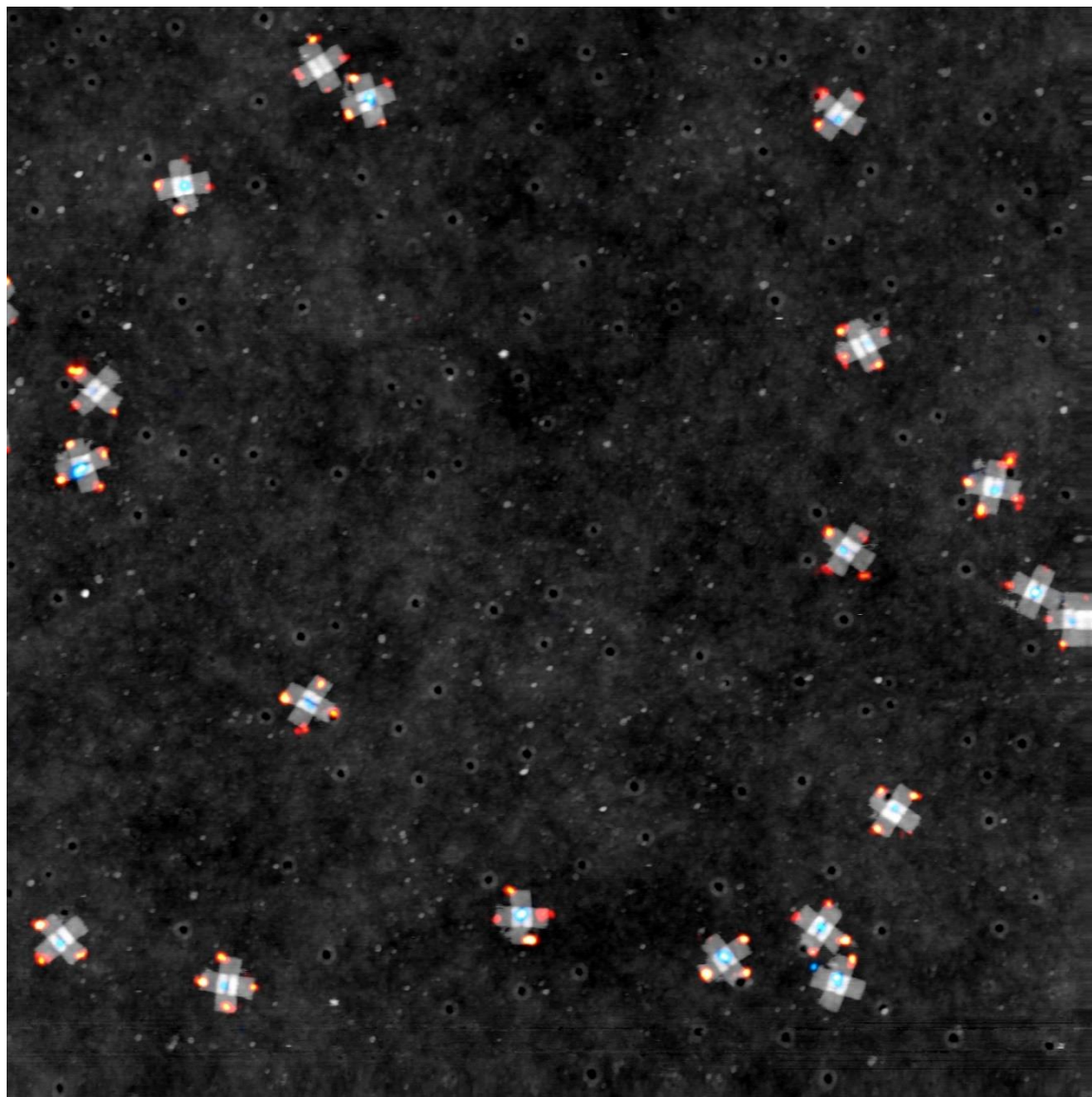


**Figure 3.11** 2  $\mu\text{m}$  x 2  $\mu\text{m}$  correlative DNA-PAINT/AFM image. Correlative SRM/AFM image of DNA origami cross-tiles on cover glass. Two color DNA-PAINT imaging was performed on the sample with imager strands M1' (red/yellow) and M3' (cyan). The AFM image was captured with 1  $\text{nm}^2$  pixel size and rendered in greyscale.

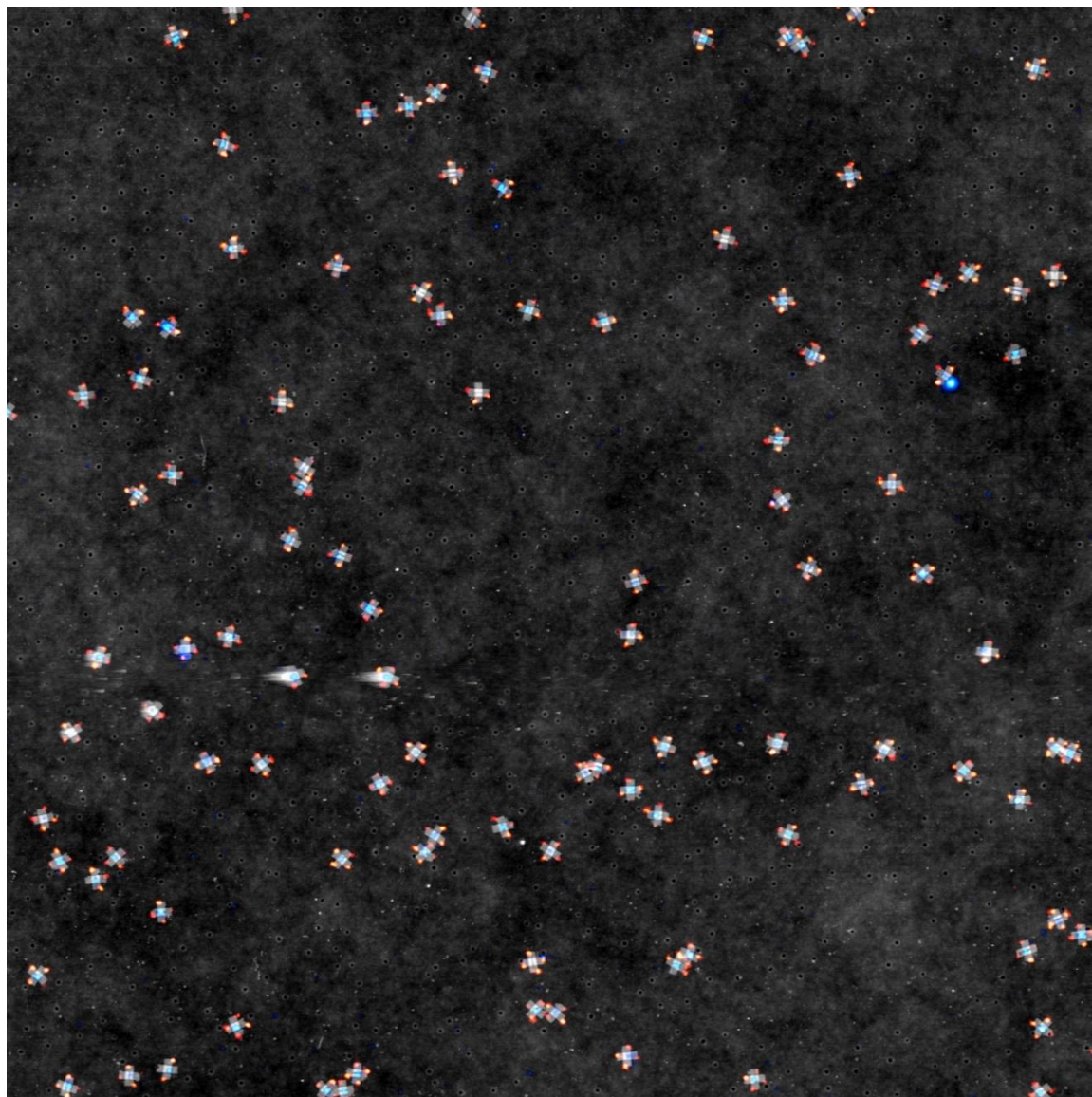


**Figure 3.12** 5  $\mu\text{m}$  x 5  $\mu\text{m}$  correlative DNA-PAINT/AFM image. Correlative SRM/AFM image of DNA origami cross-tiles on cover glass. Two color DNA-PAINT imaging was performed on the sample with imager strands M1' (red/yellow) and M3' (cyan). The AFM image was captured with 2.5 nm x 2.5 nm pixel size and rendered in greyscale.

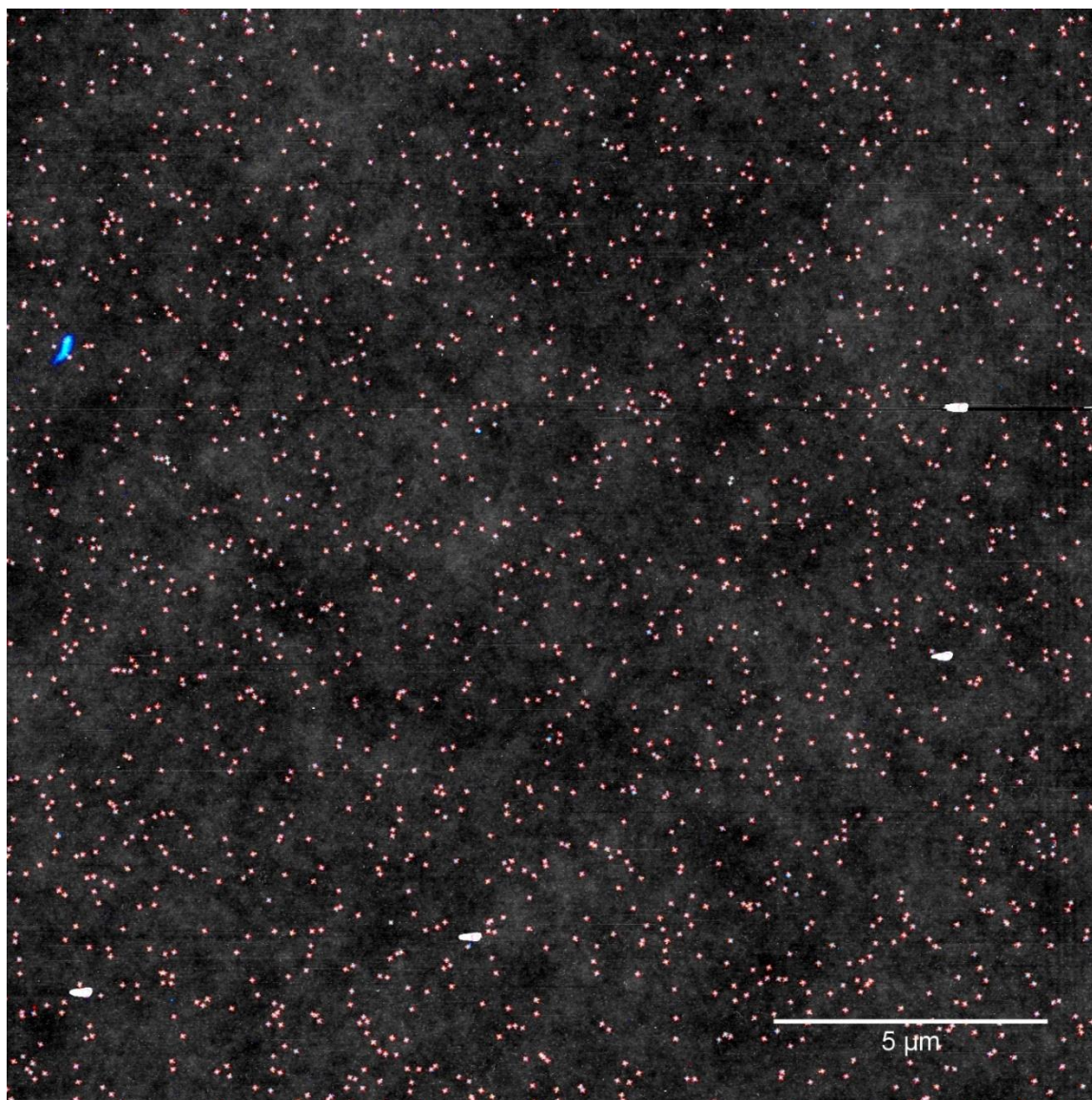


**Figure 3.13** 20 μm x 20 μm correlative DNA-PAINT/AFM image. Correlative SRM/AFM image of DNA origami cross-tiles on cover glass. Two color DNA-PAINT imaging was performed on the sample with imager strands M1' (red/yellow) and M3' (cyan). The AFM image was captured with 10 nm x 10 nm pixel size and rendered in greyscale.

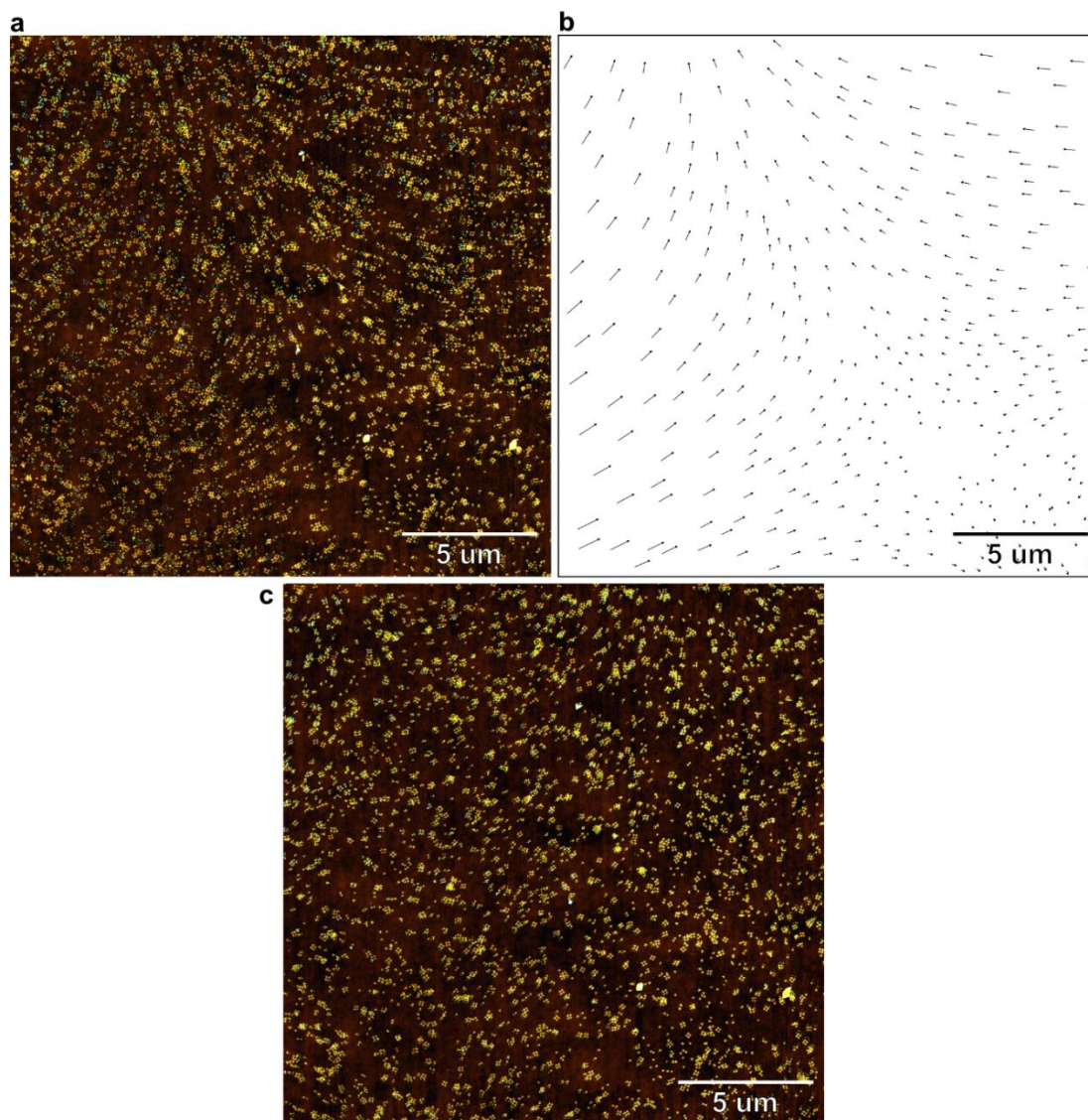


**Figure 3.14** Nonlinear deviations between AFM and SRM images. Global image aberrations often occur in optical and topographic images due to optical aberrations and suboptimal AFM imaging conditions. The aberrations manifest as nonlinear deviations between images acquired on different systems and should be corrected to better represent the correlation between images. (a) Correlative SRM/AFM image of DNA origami cross-tiles with nonlinear deviation in the positions of individual structures within the images. (b) Vector field visualizing the deviation in position of a subset of structures within the image; vectors begin on the AFM structure and end on the SRM structure. (c) Correlative SRM/AFM image from (a) after correcting for global image aberrations. Deviations between individual structures in the image were small and randomly oriented after the correction.

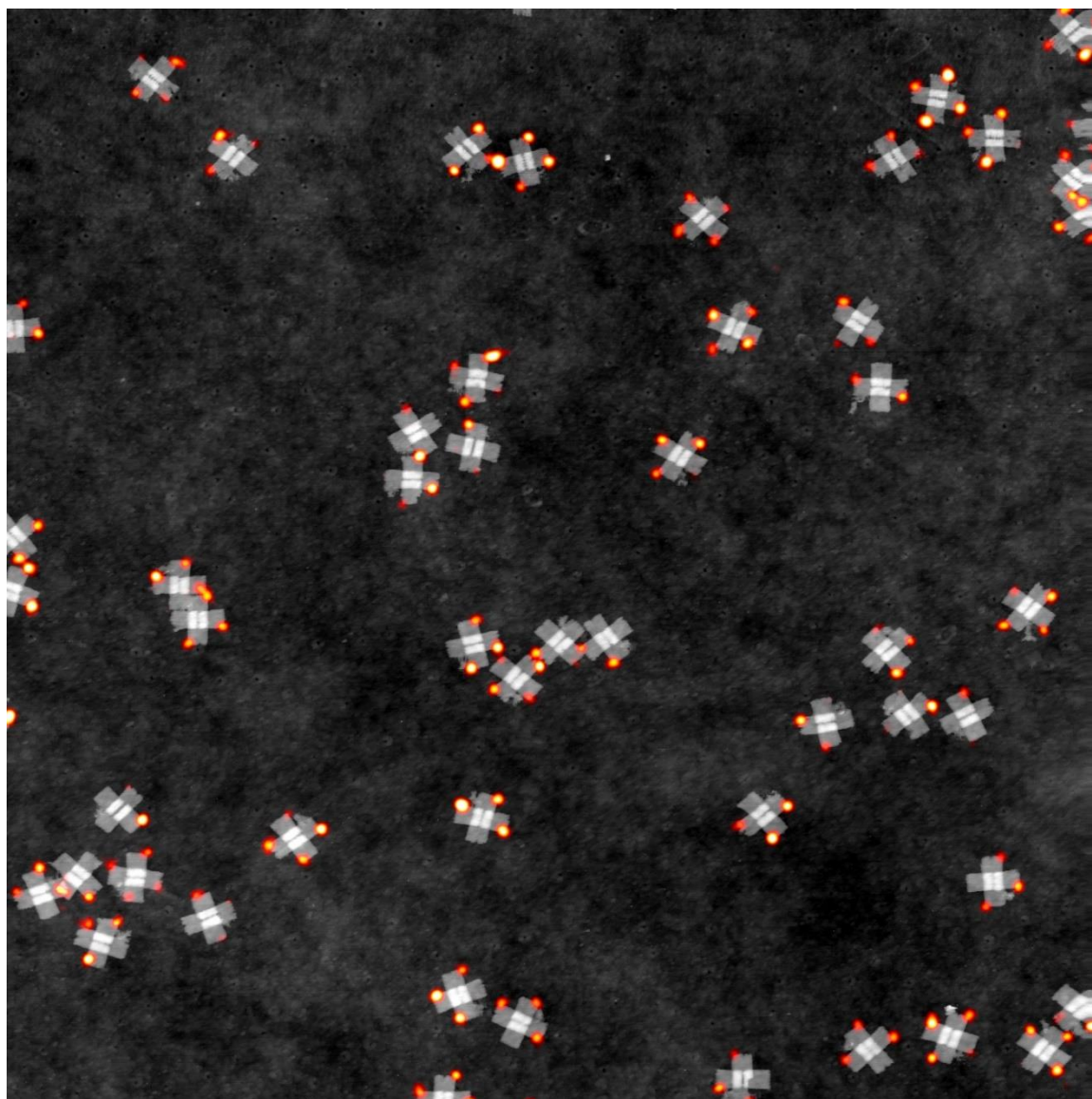


**Figure 3.15** Correlative DNA-PAINT/AFM image 1a. High-resolution, correlative SRM/AFM image of DNA origami cross-tiles on cover glass for quantifying spatial correlation and single-site defect metrology. Two-color DNA-PAINT imaging was performed on the sample with imager strands M1' (red/yellow) and M3' (cyan). The AFM image was captured with 1 nm<sup>2</sup> pixel size and rendered in greyscale. Image is 2 x 2 μm<sup>2</sup>.

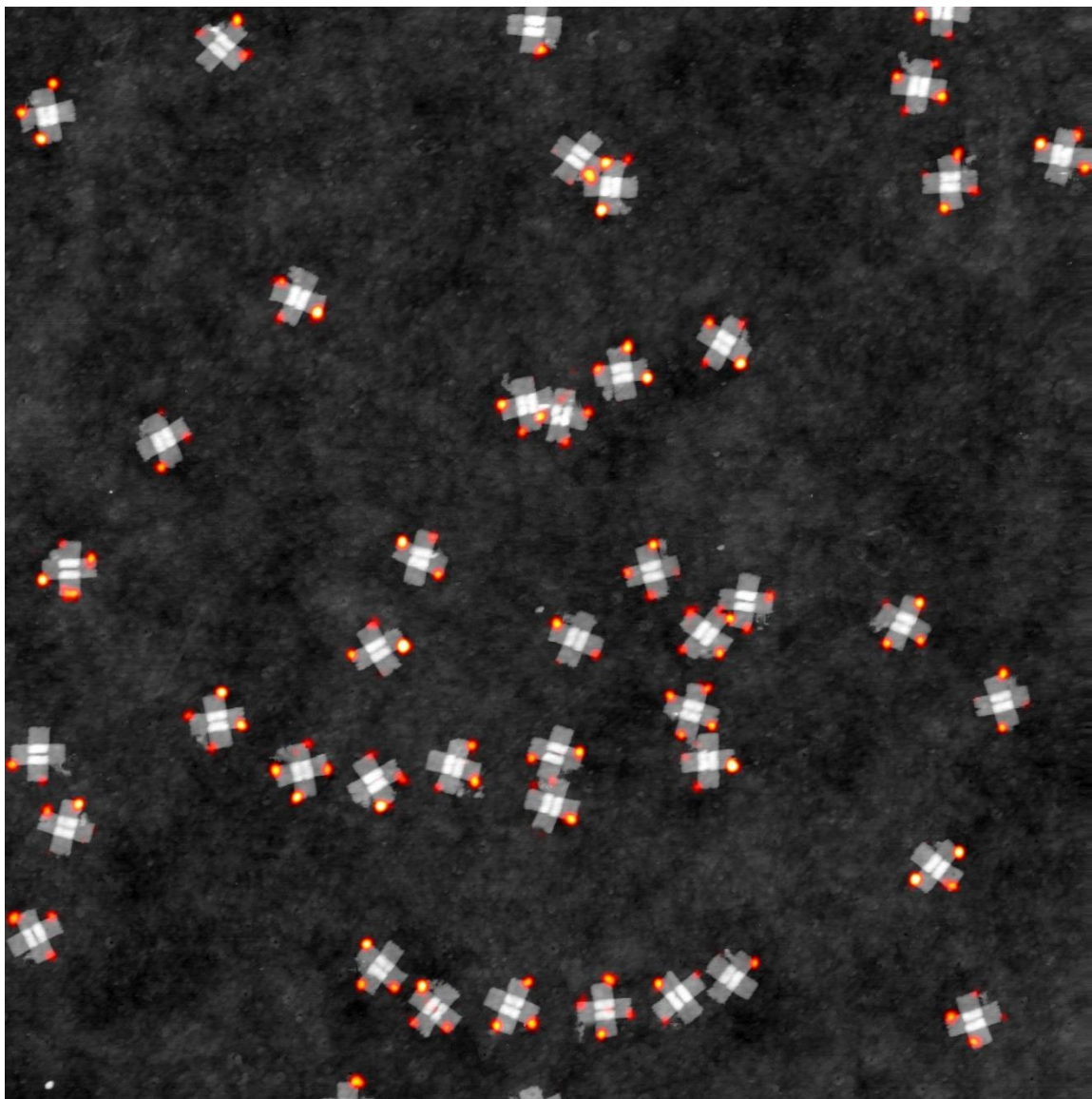


**Figure 3.16** Correlative DNA-PAINT/AFM image 1b. Second correlated image of the DNA origami cross-tile sample from Figure 3.15. Identical imaging parameters and dimensions.

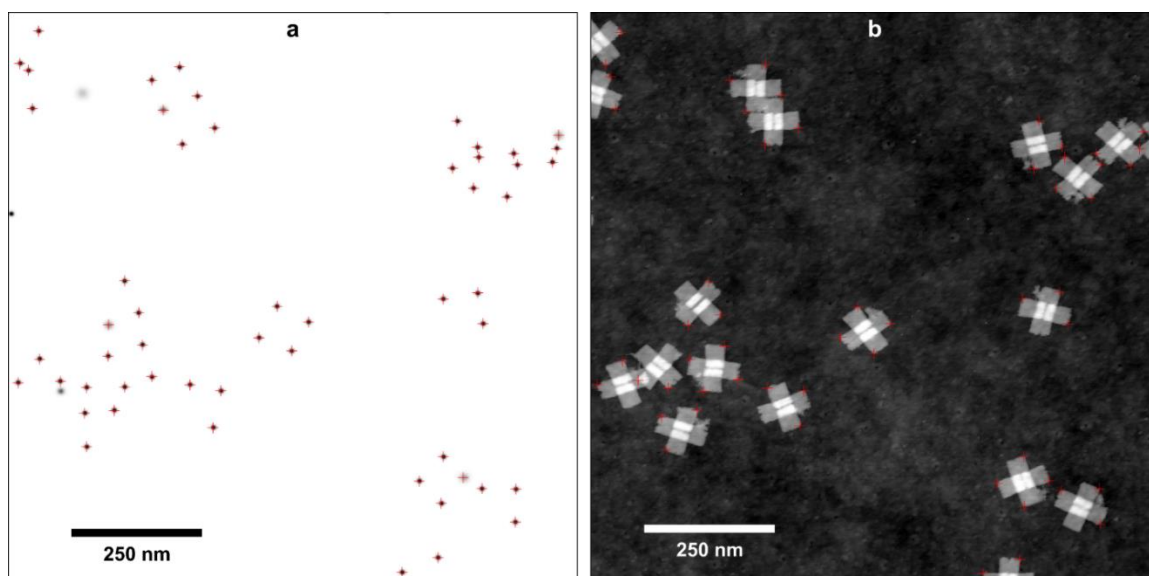


**Figure 3.17** Locating docking sites in DNA-PAINT and AFM images. To quantify the quality of correlation between SRM and AFM images, the positions of docking sites were identified independently in SRM images (a) and AFM images (b), depicted by red cross-marks in each image. For DNA-PAINT images, POI were identified within the images and mapped to the localization list to identify all events corresponding to each POI. The position of individual POI were then determined from the average position of the corresponding events. For AFM images, the positions of docking sites were approximated based on the design of the origami. The relative positions and deviations in position for the images are plotted in Figure 3.18.

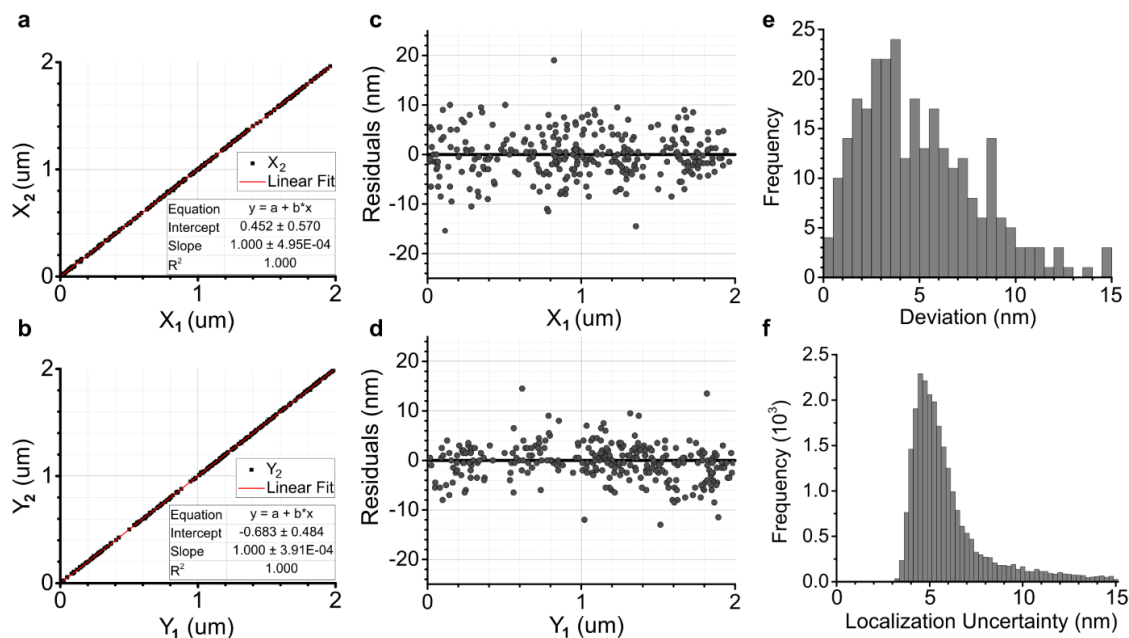


**Figure 3.18** Correlation of docking site positions in AFM and DNA-PAINT images. (a,b) Plots of the x and y coordinates of 286 sites in the AFM images ( $X_1$ ,  $Y_1$ ) relative to the SRM images ( $X_2$ ,  $Y_2$ ). The correlation between individual sites within the images is represented by the slope of the fitted lines; for both fits, the slope  $b = 1.000$  and  $R^2 = 1.000$ . The results show strong correlation between the images with deviations randomly distributed in the x and y directions. (c,d) Plots of the regular residuals for the fits in (a,b). The residuals provide a better visualization of the position-dependence of deviations between the images. (e) Histogram of the magnitude of deviations for sites within the images. The standard deviation in site positions between the SRM and AFM images was 5.85 nm. (f) Histogram of the localization uncertainty for events in the SRM image corresponding to the correlated images. The root mean square localization uncertainty was 6.5 nm.

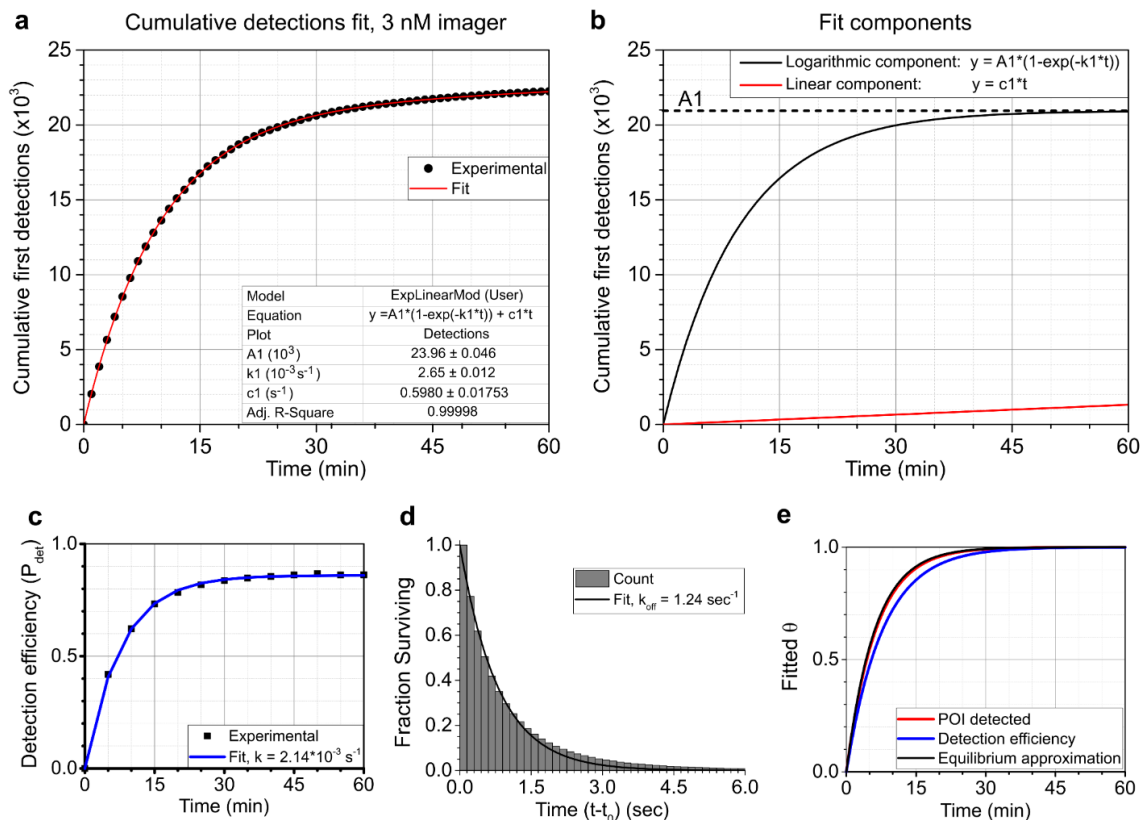


**Figure 3.19** Cumulative first detections of DNA-PAINT sites. (a) Plot of the cumulative first detections for an SRM image of DNA origami cross-tiles acquired in standard imaging buffer with imager strand M1'. The experimental data was fitted to extract the exponential and linear components; the exponential component was found to have a rate constant of  $k_I = 0.00267 \text{ sec}^{-1}$ . (b) Plot of the extracted exponential and linear components. The exponential component, representing the cumulative first detections of active docking sites, surpasses 99% of the predicted population of active sites by 60 minutes of imaging. (c) Plot of the detection efficiency ( $p_{det}$ ) measured for SRM images rendered every 5 minutes. For the fitted exponential decay, the rate constant  $k = 0.00214 \text{ sec}^{-1}$ . (d) Histogram of fluorescent event lifetimes. The dissociation rate constant ( $k_{off}$ ) was calculated from the exponential decay fit to be  $k_{off} = 1.24 \text{ sec}^{-1}$ . From the list of POI,  $[IP_e] / [P_e]$  was found to be 0.0022, and  $k_I = 0.00277 \text{ sec}^{-1}$ . (e). Plot comparing the progressions of DNA-PAINT detection predicted with each method.

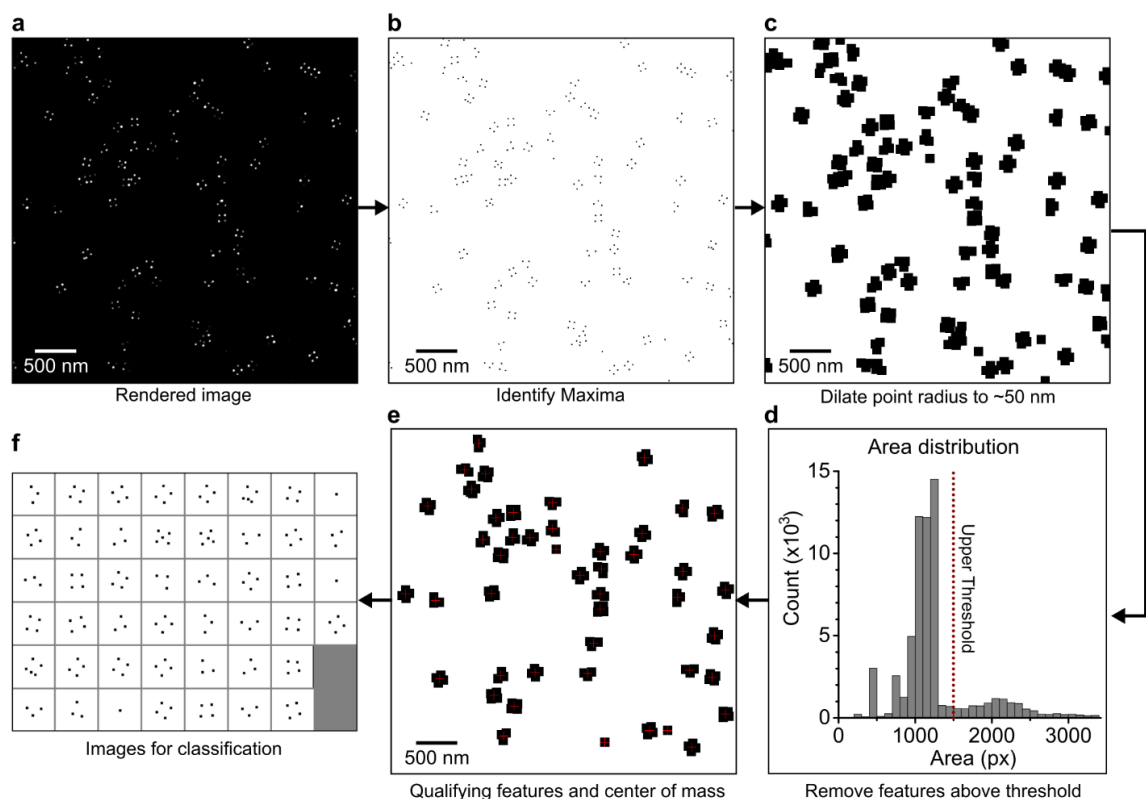


**Figure 3.20** Point-masking procedure for structure classification. (a) DNA-PAINT images were rendered at 20x magnification. (b) Maxima in the images surpassing a threshold of two detections were identified, generating a binary image of maxima. (c) Points within the maxima image were dilated to 50 nm squares, causing structures within 100 nm of other structures to be joined. (d) Structures in the dilated image were filtered by area, removing structures with areas larger than expected for a single structure. (e) Filtered image of dilated structures. The center of masses of filtered structures within the image were recorded. (f) The coordinates of filtered structures were used to generate a montage image of structures meeting the criteria for classification.

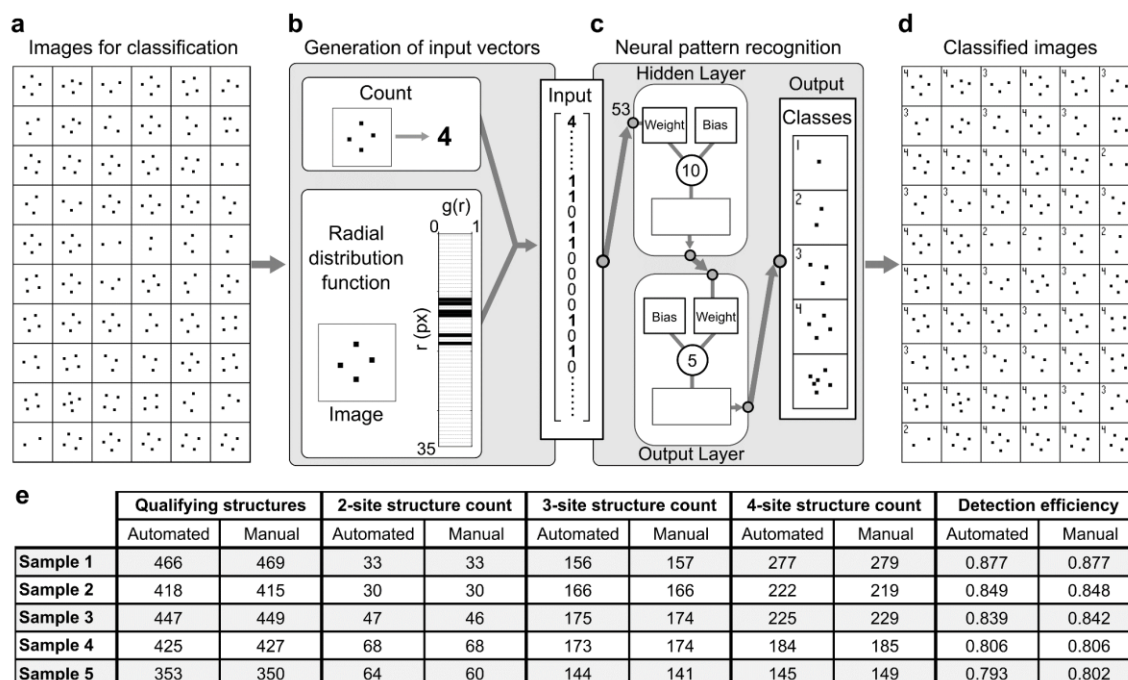


**Figure 3.21** Neural pattern recognition for structure classification. (a) Subset of structures identified with the method described in Section 3.5.2.4 and depicted in Figure 3.20, chosen for automated classification. (b) An input vector is generated for each image. The count of maxima in the image is determined, then the radial distribution is calculated for the image. For the input, the count is vertically concatenated with the radial distribution, generating a row vector for the image. The final input matrix contains the input for individual images separated by column. (c) The inputs are fed into a neural network for classification. The output distinguishes between 5 classes for input images. The network was trained using over 4000 images per class. (d) The montage of input images labelled with the results of classification. The class values represent the number of POI detected for each structure. With this method, thousands of structures can be classified in seconds. (e) Table of the results of automated and manual counting of five image samples containing 500 structures each. For all five samples, the detection efficiency determined from automated classification was within 1% of the value obtained by manual classification.

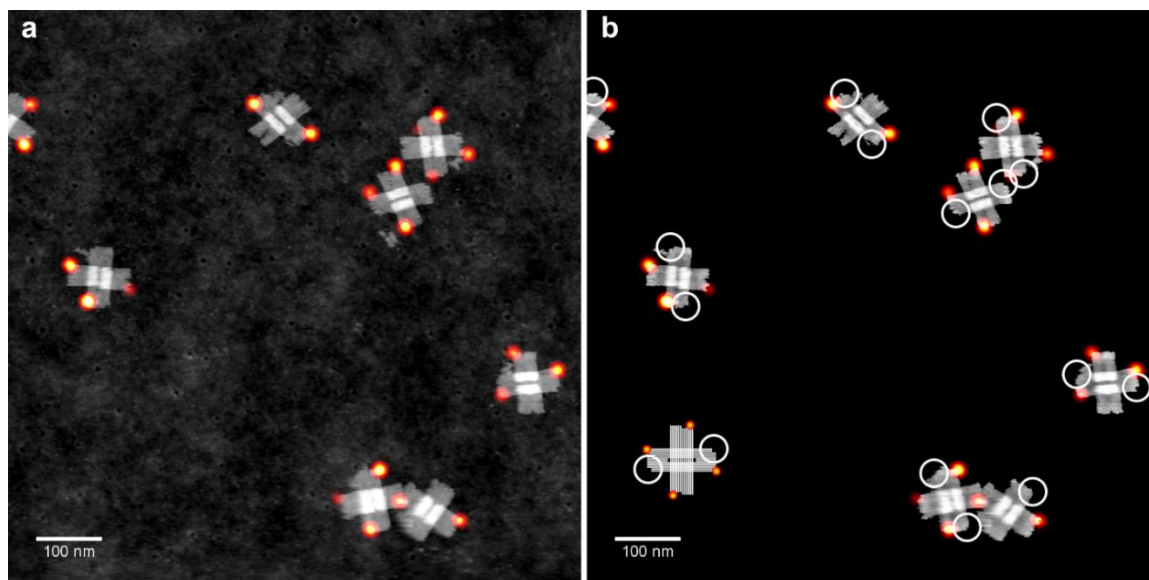


**Figure 3.22** AFM detection of unincorporated sites – Image 2a. Correlative SRM/AFM image of DNA origami cross-tiles synthesized with intentional unincorporated site defects. The DNA-PAINT image was rendered with detections located at the average position of the associated POI for improved visualization. The positions of the defects on individual origami are indicated by the structure diagram in the bottom left, along with simulated SRM detections. Within the image, unincorporated sites which were correctly identified are marked by white circles. One tile arm was obscured by imaging artifacts, but all other unincorporated sites were successfully detected.

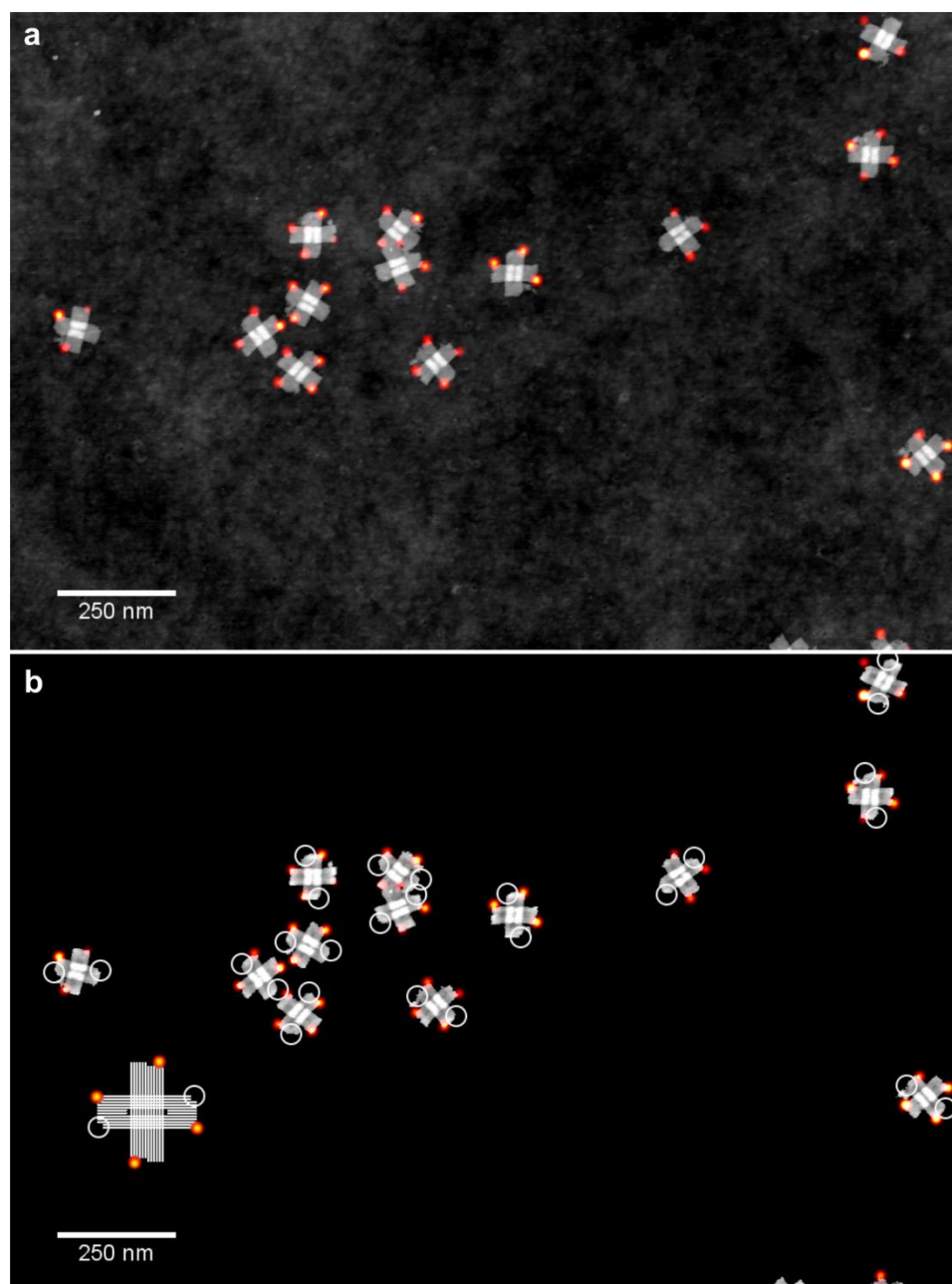


**Figure 3.23** AFM detection of unincorporated sites – Image 2b. Second correlated image of DNA origami cross-tiles with intentional defects. Within the image, unincorporated sites which were correctly identified are marked by white circles. All 24 sites within the image were correctly identified.

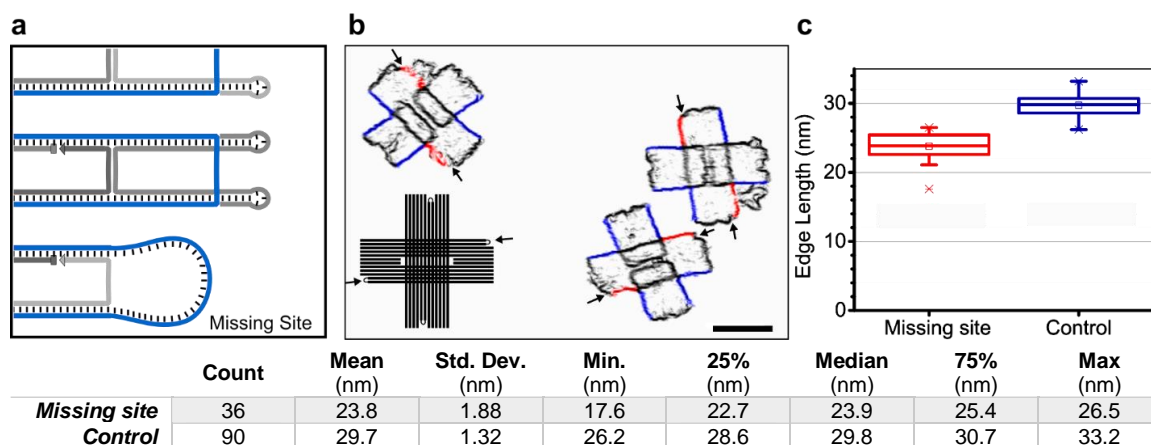


**Figure 3.24** Quantifying unincorporated site detection with AFM. (a) DNA origami cross-tile strand diagram depicting an unincorporated site defect. (b) To quantify the structural difference between incorporated and unincorporated sites on DNA origami, the edge lengths of DNA origami cross-tiles were measured for intentional unincorporated sites (red) and sites without apparent defects (blue). The image shown is an inverted local slope image to aid visualization, and unincorporated sites are indicated by black arrows, corresponding to the structure diagram in the bottom left. Scale bar, 50 nm. (c) Box and whisker plots summarizing the distribution of edge lengths for unincorporated sites ('Missing site', red) and incorporated sites ('Control', blue), with a box spanning the 50<sup>th</sup> percentile and split by the median line, connected to the minimum and maximum values. The mean is indicated by a small box, and one outlier in the Missing site measurements is indicated by an 'x'. (d) Table of the values from the box and whisker plot. The means are separated by greater than three standard deviations, indicating a significant difference between the edge length of incorporated and unincorporated sites. For the unincorporated sites examined, the double-stranded helix edge length was expected to be reduced by 5.4 nm (16 nt) by the defect, in close agreement with the measured  $6 \pm 3$  nm difference in the means.

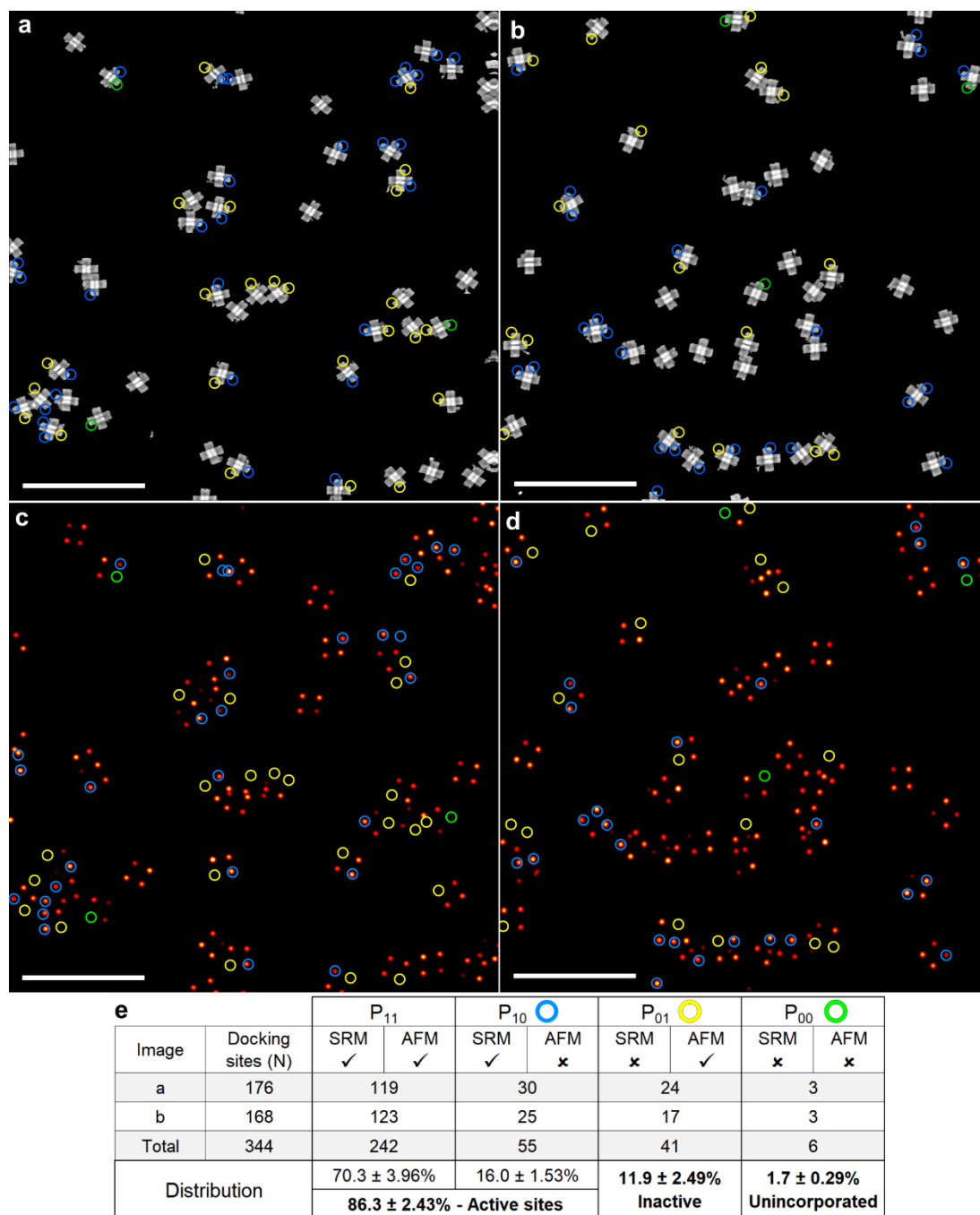


**Figure 3.25** Correlative defect metrology of DNA origami cross-tiles. AFM topography images with local contrast enhanced and background removed (a,b) and DNA-PAINT images (c,d) with colored circles indicating AFM defects (blue), inactive DNA-PAINT sites (yellow), and correlated defects (green) identified independently in AFM and SRM images, prior to correlation. The DNA-PAINT image was rendered with detections located at the average position of the associated POI for improved visualization. (e) Table of the results of defect quantification. The fraction of inactive DNA-PAINT sites correlated to AFM defects was 0.23, less than the value expected to result from false AFM detections alone. The results suggest that the fraction of

inactive sites missing from the structure is lower than the detectable limit for the experiment, and the rate of strand incorporation for the sites examined was greater than 0.97. For structures within the ROIs shown in (b) and (d), the detection efficiency of DNA-PAINT sites was 0.86; for the full SRM image, the detection efficiency was 0.815 (Section 3.5.2.4).

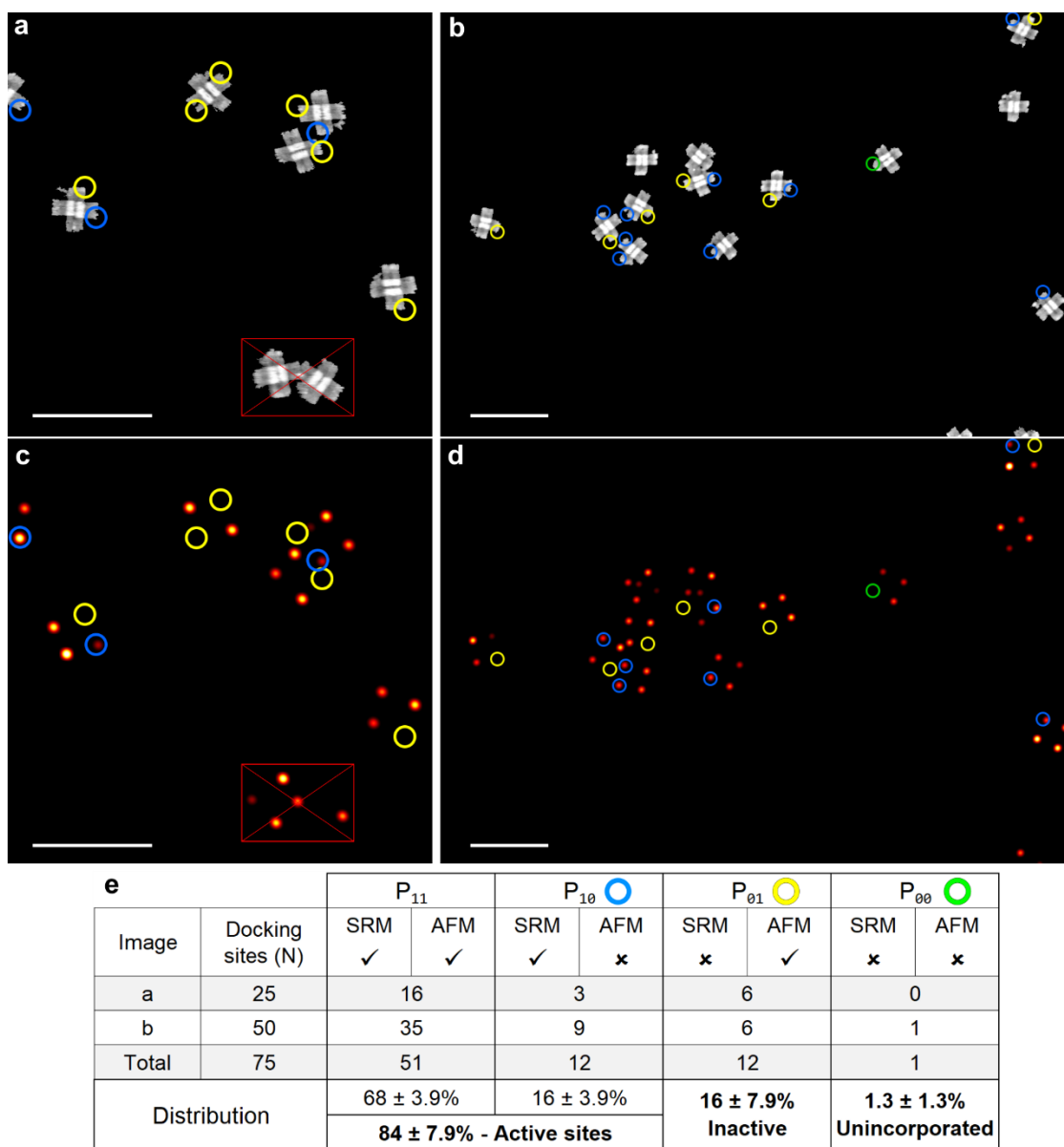


**Figure 3.26** Correlative defect metrology of DNA origami cross-tiles. Correlative defect metrology as described in Figure 3.25, performed on a second tile sample. The percentage of inactive DNA-PAINT sites correlated to AFM defects was 7.7%, and the rate of strand incorporation for the sites examined was greater than 0.98. Scale bars, 250 nm.

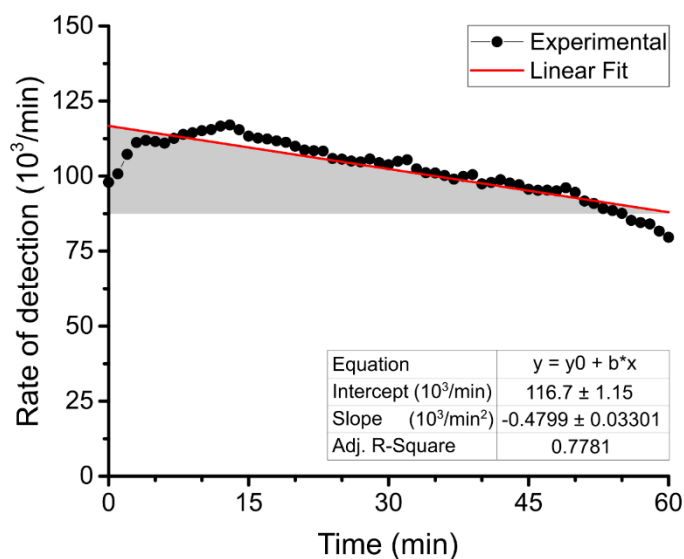


**Figure 3.27** Rate of detection plot. The rate of observed detections for the sample shown in Figure 3.25 decreased by  $24.7 \pm 1.7\%$  over the course of DNA-PAINT image acquisition, close to the fraction of active DNA-PAINT sites with defects in AFM ( $18 \pm 2\%$ , Figure 3.25). Based on the results of a recent study demonstrating photo-induced depletion of docking sites during DNA-PAINT imaging,<sup>11</sup> it is speculated that the decrease in detection rate resulted from photo-induced damage to docking sites. Individual fluorophores can also become photo-bleached during imaging, though fluorophores exposed to TIRF illumination while imaging represent only about 1 in  $10^5$  of the total population for the given sample.

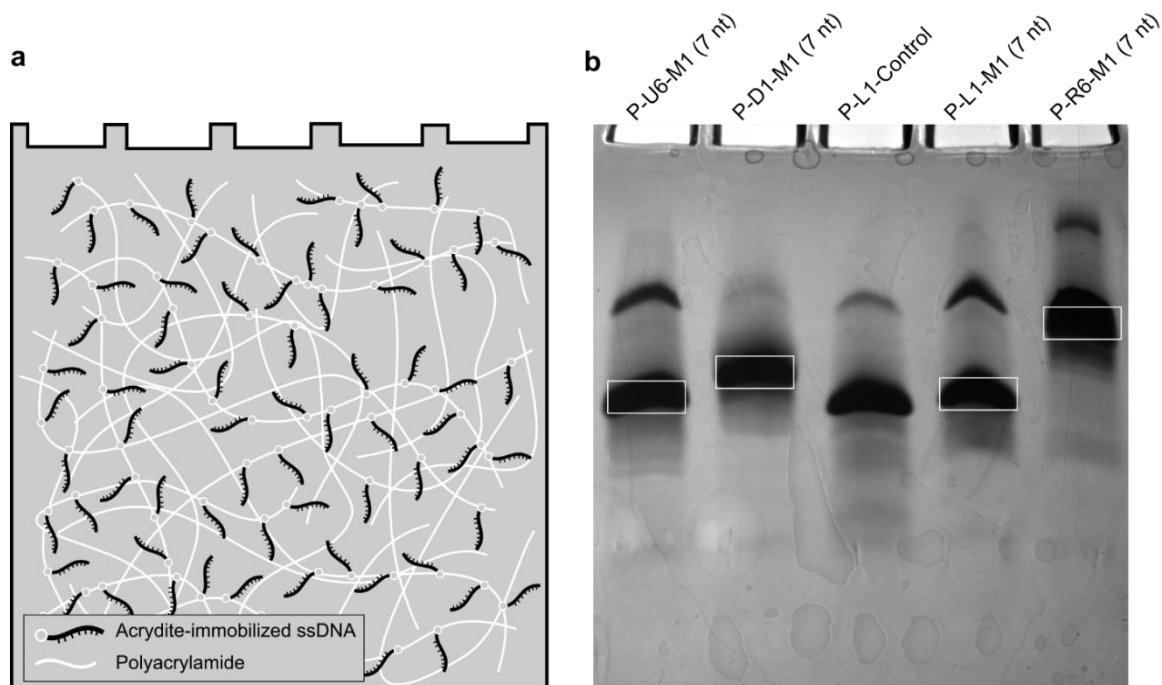


**Figure 3.28 Docking site-targeted filtration – seqPAGE.** (a) Depiction of Acrydite-immobilized ssDNA in a polyacrylamide matrix. For docking site-targeted PAGE filtration, Acrydite-modified ssDNA was incorporated in a polyacrylamide gel at a concentration of  $3 \mu\text{M}$ . The modified ssDNA polymerizes with acrylamide during polymerization of the gel, immobilizing the strands in the gel. A 7 nt domain of the ssDNA was complementary to docking site M1; migrating strands interact weakly with the immobilized strands if the docking site is present. (b) seqPAGE gel image of docking site strands. 5 nmoles of the indicated strands were added to the wells. The docking site length was 7 nt, White boxes indicate the bands removed from the gel after filtration.

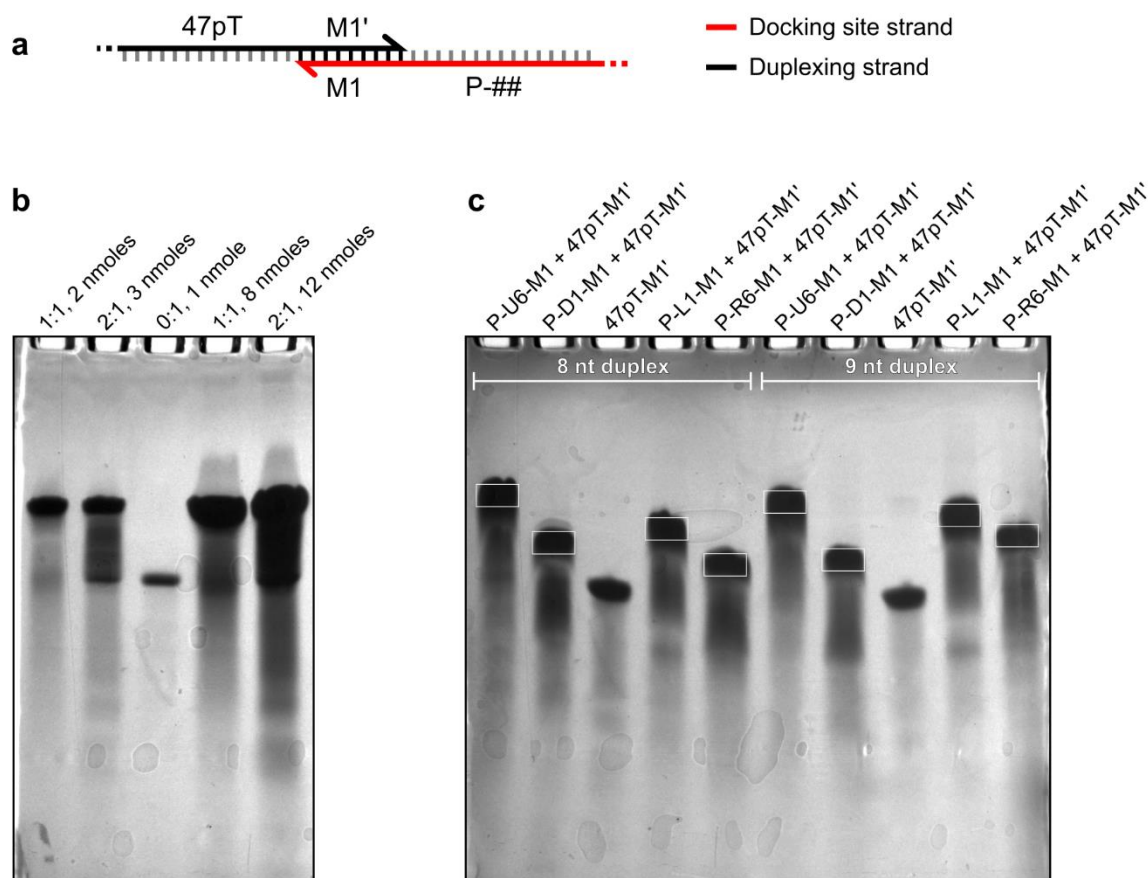


**Figure 3.29** Docking site-targeted filtration – dpXPAGE. (a) Strand diagram depicting docking site strands hybridized to duplexing strands. The 8 nt hybridized domain was found to be stable during PAGE filtration when cooled to 5 C in 0.5x TBE with 12.5 mM MgCl<sub>2</sub>. (b) dpXPAGE filtration of 1:1 and 2:1 strand concentrations [47pT-M1']:[47pt-M1] for 1 nmole and 4 nmole of strand 47pT-M1 added to the wells. The total mass of ssDNA added to each well, from left to right, was 33.4 ng, 50.2 ng, 16.7 ng, 134 ng, and 201 ng. Sharp duplexed bands were observed for ratios of 1:1 and 2:1 for up to 50 ng of ssDNA added to the wells. (c) dpXPAGE filtration of docking sites with 8 nt and 9 nt duplexed domains. The duplexing strand 47pT-M1' was included in the 3<sup>rd</sup> and 8<sup>th</sup> wells for reference. Docking sites and duplex strands were mixed at 1:1 ratio (3 nmoles total) and annealed from 90 C to 20 C over 20 minutes, then the annealed solutions were added to each well. White boxes indicate the bands removed from the gel after PAGE filtration.

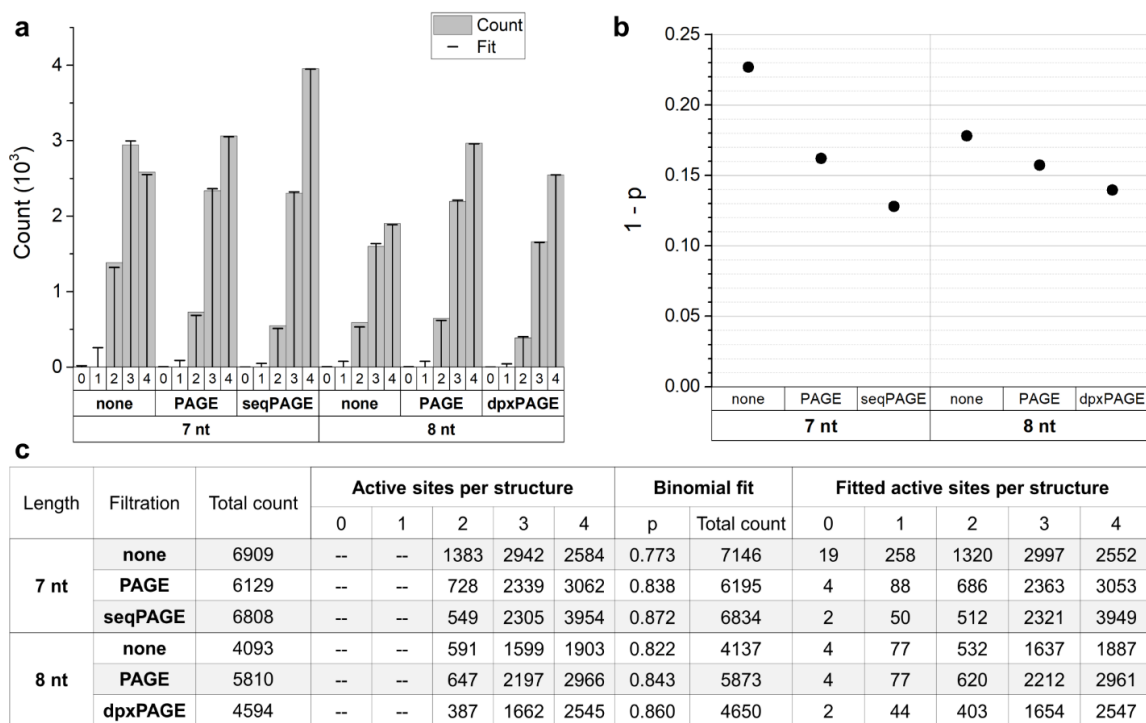


**Figure 3.30 Results of docking site-targeted filtration.** Six sets of DNA origami cross-tiles were synthesized with 7 nt or 8 nt docking sites with no filtration, PAGE-filtration, seqPAGE-filtration (7 nt only), or dpxPAGE-filtration (8 nt only). DNA-PAINT imaging was performed on each set and classified to calculate the detection efficiency ( $p$ ) for docking sites filtered by each method. (a) Histogram of the experimental counts of classified structures with two, three, or four active docking sites (grey bars), and the counts expected for a binomial distribution fitted to the results (black bars). The parameters of the binomial distribution for each sample can be found in (c). (b) Plot of the rate of SRM defects ( $1-p$ ) for each origami set. For both 7 nt and 8 nt docking sites, the rate of defects decreased after PAGE-filtration, and the lowest rates of defects were achieved for the docking site-targeted filtration methods.

### 3.5.4 Supplemental Tables

**Table 3.1 List of internal staples for DNA origami cross-tile.**

Name	Sequence	Notes
LR-A1	GACAACTCGTATTAACCTTTACAACAATTC	
LR-A2	AGTACCTTTTACATCGATGAATATACAGTAAC	
LR-A3	GATAGCTTAGATTAAGTCCTTGAAAACATAGC	
LR-A4	AACGAGAATGACCATATTTAACAGTTCAGAA	
LR-A5	AAAGTACGGTGTCTGGTTTTAAATATGCAACT	
LR-A6	TGTAATACTTTTGCGGAAAAACATTATGACCC	
LR-B1	GTATTAGTCCTTTGCCCGAACGCAGGTTTA	
LR-B2	ACGTCAGGGAGAAAACAATAACGAATTTTCC	
LR-B3	CTTAGAAAACGCTGAGAAGAGTCATCCCCCT	
LR-B4	CAAATGCAATCAAAAATCAGGCTGTAGCT	
LR-B5	CAACATGAAGTTTCATTCCATATAAATCGG	
LR-B6	TTGTACCGAGAAGCCTTTATTCAACGCAA	
LR-C1	TTTAAAAGGATAATACATTTGAGGATTTAGAA	
LR-C2	TGATTGCTAAATTGCGTAGATTTTTTATTAAT	
LR-C3	ATTTATCAATCGTCGTATTAATTGATTCGCC	
LR-C4	TGACTATTCATAAATATTCAATGAAATAGTGA	
LR-C5	GATTCCAATTGCTGAATATAATGCTTTACCC	
LR-C6	GGATAAAACCTCAGAGCATAAAGCTAACAGTT	
LR-D1	CGTCAATATTTGAGTAACATTATCTAAAACAG	
LR-D2	AAATAAAGTTGAATACCAAGTTACAACCTTGC	
LR-D3	TTCTGTAAAAATCATAGGCTGAGAATACTGC	
LR-D4	GGAATCGTATAGTCAGAAGCAAAGGATGGCTT	
LR-D5	AGAGCTTAATTCTGCGAACGAGTAAAATTAAG	
LR-D6	CAATAAAGATTTTGTAGAACCCTCATATATTT	
LR-E1	GGAACAAAACCTAACAATAATAGATTAGAGC	
LR-E2	CGCAGAGGAAAATTATTTGCACGATTTTGC	
LR-E3	CTTTTTAATATATGTGAGTGAATAAAATCG	
LR-E4	CATCAAAAGACTGGATAGCGTCCAGACTAC	
LR-E5	TTTGACCAGAGGTCATTTTGCAGGATTTG	
LR-E6	TAAATGCAGGCAAAGAATTAGCAGATTTAG	
LR-F1	TTAGGAGCGAAACCACCAGAAGGATAGAACCCT	
LR-F2	ACCATATCCGAATTATTCATTTCAACAGTACA	
LR-F3	TAAATCAACCTCCGGCT	
LR-F4	AGTAAAATGTTTAAGATTAAGAGGAAGCCTTGCTCCT	
LR-F6	ACAGGCAAATGCCTGAGTAATGTGTAGGTAAA	
LR-G1	ATCATCATTGAGGAAGGTTATCTAAAATATCT	
LR-G5	ATAACCTGTAGAGAGTACCTTTAA	
LR-G6	GATTCAAATAGCATTAAACATCCAAAATGGTCA	
LR-H1	AAGGAATATTCTTGATTATCAGTTTGGATT	
LR-H2	ATACTTCAAGATGATGAAACAAAATTTTCAAT	
LR-H5	TCAGGATTTTAGCTATATTTTCTTCTACTA	
LR-H6	ATAGTAGAGGGTGAGAAAGGCCGGAGACAG	
LR-I2	AAAACAAATGTCGTGCCAGCTGCATTCCAAGTC	
LR-I4	AGCGAACCCGCCATTCAGGCTGCGCAGGCAA	
LR-J3	GGGAAACCATTAATTACATTTAACACATCAAG	
LR-J5	GCGCCATTAGACCGAAGCAAACCTAGCTTCAA	

LR-K1	GTCAAAGCCTCAAATATCAAACCTCAATC	
LR-K2	ATCGGCCAAGTGTGTTCCAGTTCTCCAAC	
LR-K5	AAAATAATTCTGGTGCCGAAACCAACTGT	
LR-K6	TCTAGCTGCGCATTAAATTTTTGGCCATCA	
LR-L1	TTGCTGAAGCGAAAAACCGTCTATGCCCGAGA	
LR-L2	TAGGGTTGACGCGCGGGGAGAGGC	
LR-L6	TTAAAATTATAATTAATGCCGGAGAGGGTAG	
LR-M1	TGGCCACAAATGAAAAATCTAAAGCATCACC	
LR-M3	CACCCTCAGAGCCAATGAGTGAGCTAACTGGTTGCG	
LR-M4	ATTACGCCATTGGCCTT	
LR-M5	GCTTTCATGATCGCACTCCAGCCATCTTCGCT	
LR-M6	CTATTTTTTAAATTGTAACGTTATGTAGCCA	
LR-N1	CAGCAGCTACGTGAACCATCACTCGGCAAA	
LR-N2	ATCCCTTGCCAGGGTGGTTTTTAAGCCTGG	
LR-N3	GGTGCTGCCACCAGAACCACCGAGGCAGG	
LR-N4	TCAGACGAGCTGGCGAAAGGGGTATCGCC	
LR-N5	TCAGGAACAACATTAATGTGAGTATAAGC	
LR-N6	AAATATTGAGAGATCTACAAAGGCTATCAG	
LR-O1	AGTTTTTGAAGGGAAGTCCACGCTGAGAGC	
LR-O2	CAGTGAGAGATGGTGGTCCGAAACCAATCA	
LR-O3	CGCCGCCATCCCCGGTACCGAGCGGTCGACT	
LR-O4	GCAAGGCGATTAAGTTGGTAACGGTGCATCT	
LR-O5	CAACCCGTGAGGGGACGACGACAGGATGTGCT	
LR-O6	GTCATTGCCAAAAACAGGAAGATTGCGAGTAA	
LR-P1	CGAGAAAGGGGGTCGAGGTGCCGTGGCGAAAA	
LR-P2	TCCTGTTTCGGGCAACAGCTGATTACACAACA	
LR-P3	TACGAGCCGGAAGCATAAAGTGTACTTTTCAC	
LR-P4	CTAGAGGAGCATTGACAGGAGTTACCAGAGC	
LR-P5	GCCAGTTTCGGATTCTCCGTGGGAATAATCAG	
LR-P6	AAAAGCCCCTGAGAGTCTGGAGCAAACAAGA	
LR-Q1	TAAATCGGACGGGGAAAGCCGGCGAACGTGG	
LR-Q2	ACCGCCTGTGGTTTGCCCGCAAAAAGCAC	
LR-Q3	CGTAATCATCCGCTCACAAATCCGCCCTTC	
LR-Q4	TTTCCAGGCTTGCAATGCCTGCATCGAATT	
LR-Q5	GCGGATTGGGGCGCATCGTAACCCAGGGT	
LR-Q6	GAATCGATTATGTACCCCGTTGACAAAACG	
LR-R1	CCCGATTTAGAGCTTGAACCCATAAGGGAGCC	
LR-R2	AGCAAGCGGTCCACGCGCCTGAGAGAGTTGC	
LR-R3	CTGTGTGAAATTGTTATGGTCATAGCTGTTTC	
LR-R4	CGACGGCCAGTGCCAATCACGACGTTGTAAAA	
LR-R5	TCACGTTGGTGTAGATACCGTAATGGGATAGG	
LR-R6	ACTAGCATGTCAATCAGAACGGTAATCGTAAA	
UD-A1	AACTAATGCAGATACATAGGAATACCACATTC	
UD-A2	CAAGAACC GGATATTCTCAAGAGTAATCTTGA	
UD-A3	GAAGGCACCAACCTAATACGTAATGCCACTAC	
UD-A4	TTAATTGTATCGGTTTGCTCCAAAAGGAGCCT	
UD-A5	TAGCAAGCCCAATAGGCCCTCATTTTCAGGGA	

UD-A6	CTTGAGTAACAGTGCCTTAACGGGGTCAGTGC	
UD-B1	AAAAGGAATTACGAGGCATAGTAATTACAGGT	
UD-B2	AAATCAACTCATCAGTTGAGATTTAACGCC	
UD-B3	GAGGCAAAGCTGGCTGACCTTCAATTACCC	
UD-B4	TGCTTTCGATTAACGGGTAAAAACGAAA	
UD-B5	GTACCGTAATCTCCEAAAAAAGATCAGCT	
UD-B6	ACAGTTAACCTCAGAGCCACCAAAACCCAT	
UD-C1	AGAAAGATGTAACAAAGCTGCTCACAGACCAG	
UD-C2	GCGCATAGAGAATACTAAAAACATCATGAGG	
UD-C3	AAGTTTCCAGGTGAATTTCTTAAATTTTTTCA	
UD-C4	CGTTGAAAACACTGAGTTTCGTCAACCCTCAG	
UD-C5	AACCGCCATGCCCTGCCTATTTTGATGATA	
UD-C6	CAGGAGTGTACTGGTAATAAGTTTCGTATAA	
UD-D1	CTATCATAACCTCGTTTACCAGTTAATAA	
UD-D2	ATAAGGCTTAACGGAACAACATTAGAGCAACA	
UD-D3	TGACCCCCACAGATGAACGGTGTATTAGTGA	
UD-D4	TACCGATAAGGACTAAAGACTTTTCTCATCTT	
UD-D5	AACTACAAGAATTGCGAATAATAACAGCTTGA	
UD-D6	ATTATTCTCACCTCAGAACCGCCAGTACA	
UD-E1	AACGAACTGCCCTGACGAGAAACAACCTTG	
UD-E2	AAAGAGGAGCGATTATACCAAGGCTACAGA	
UD-E3	GGCTTTGGTTGCGCCGACAATGAAGGAACA	
UD-E4	ACTAAAGCGCTGTAGCATTCCGAGGTTTA	
UD-E5	GTACCGCGAAACATGAAAGTATTACCGTTC	
UD-E6	CAGTAAGCGTCATACATGGCTTTCGGAACCT	
UD-F1	AAAAACAAAATAGCGAGAGGCTTTACCAGTC	
UD-F2	CGAGTAGTGGGAAGAAAAATCTACACGACGAT	
UD-F3	AAAGTACAAGGGAACCGAACTGACCACCAGAA	
UD-F5	CCCTCATAGCGGAGTGAGAATAGAACAACAA	
UD-F6	TGAGACTCGTATCACCGTACTCAGACAGACAG	
UD-G1	AGGACGTTAAATTTGGGCTTGAGATCAGACGGT	
UD-G4	AGTTTCAGTTAGCGTAACGATCTATAGCCCG	
UD-G6	ATGGAAGCGCAGTCTCTGAATTTAAGAGGC	
UD-H1	AAGTTTTGCCAGAGGGGTATTTTTTTTTTGGGTTATA	
UD-H3	ATAAATTGAGCCGGAACGAGGCGGGTTTAA	
UD-H4	GCTGAGGCCGTACCCCTCAGCAGTCGCCTG	
UD-H5	TGTCGTCTGGATTTTGCTAAACATTTCGGTC	
UD-H6	CGGGGTTTAGGGTTGATATAAGTAAAGTTT	
UD-HI6	AATAAATCCTCATTGGATTAG	
UD-I2	TGTTACTTTGTCGAAATCCGCGACGAACAAGC	
UD-I3	TGCGGGATTTGCAGGGAGTTAAAGGAAACGAT	
UD-I4	TCTGTATGTTCCAGACGTTAGTAACGCAATAA	
UD-J3	AAGCCGTTGTACCGCACTCATCGACTGCTCCA	
UD-J4	TTTTTGTATCCCAATCCAAATAAGCCGCTTT	
UD-J5	TAACGGAAGGAAACCGAGGAAAAATGAATTT	
UD-JK1	TAACATATGTAATCAACAGT	
UD-K1	AGGGCTTATGTAATTTAGGCAGCGGGTATT	

UD-K2	AAACCAATTTATTTTCATCGTAACAGCCAT	
UD-K3	ATTATTTTAAACGTCAAAAATGAGAACAAG	
UD-K4	TTACCAGTACCCAAAAGAACTGGGTGAATT	
UD-K6	GAACCGCCACCCTCAGAGCCTTTTTTTTTTTCACAAACA	
UD-L1	AAATCCAATCGCAAGACAAGAATATACAAA	
UD-L3	ACCGCGCCTTATCATTCCAAGAAAGGCATTT	
UD-L6	TACCATTAGAAATTATTCATTAAGCATGATT	
UD-M1	TTCTTACCCTAATAAGAGAATATATAATCGGC	
UD-M2	TGCTTTCCCAATAGCAAGCAAATTTCCAGA	
UD-M4	TTTAAGAATTATTACGCAGTATGTAAGGTAAA	
UD-M5	TATTGACGGCAAGGCCGAAACGTAGCCACCA	
UD-M6	CCGGAACCGCCTCCCTCAGAGCCGAGCACCAT	
UD-N1	AAACTTTTTCAAATATATTTTAGTCTAGAAAA	
UD-N2	GACAAAAGTAGTATCATATGCGTCGCGAGA	
UD-N3	AGAAGGCTGTAGAAACCAATCAAAGTACC	
UD-N4	GAAGCGCACGCTAACGAGCGTCTCAGATAT	
UD-N5	CGTAGAAAAAGCTATCTTACCGAAACAGG	
UD-N6	GAAACCATCCGATTGAGGGAGGGTAGCAAA	
UD-O1	AGCCTGTTGTAAAGTAATTCTGTCCCTAATTT	
UD-O2	ACGAGCATTATCCGGTATTCTAAGTCCTGAAT	
UD-O3	CTTACCAATTAGACGGGAGAATTAACAATG	
UD-O4	AAATAGCAATACATACATAAAGGTAAAGGGCG	
UD-O5	ACATTCAACGATAGCAGCACCGTAATCTTTTC	
UD-O6	ATAATCAAATCACCAGCAACAGCACCAAT	
UD-P1	TCTTCTGACCTAAATTTAATGGTTAAATAAG	
UD-P2	GACAATAAACCGGAATCATAATTATAATTTCA	
UD-P3	GCGTTTTAAAAAATAATATCCCATCAGACGAC	
UD-P4	CCCTGAACCCAGCTACAATTTTAAACGCGAG	
UD-P5	ATAAAAGACAATAATAAGAGCAAGACTGAACA	
UD-P6	CGACAGAAACCAGCGCAAGACAGGCAACAT	
UD-Q1	AATAAACACAACATGTTTCAGCTTAAGTCTT	
UD-Q2	GAACAAGGCGAACCTCCCAGTAGTTGCTA	
UD-Q3	TTTTGCAAAAGTCAGAGGGTAAGAATTGAG	
UD-Q4	TTAAGCCAACGCAAGACACCAAAATTCAT	
UD-Q5	ATGGTTTTCAAGTTTGCCTTTATTCGGTCA	
UD-Q6	TAGCCCCCTTATTAGCGTTTGCCATCAGTAG	
UD-R1	GTGATAAATAAGGCGTTTGAAATACCGACCGT	
UD-R2	GTTTATCAACAATAGAAATGCAGAACGCGCCT	
UD-R3	GCCTTAAATCAAGATTTGCGGGAGGTTTTGAA	
UD-R4	GAGAGATAACCCACAATTGAGCGCTAATATCA	
UD-R5	TGTCACAATCAATAGACGGAATAAGTTTATTT	
UD-R6	CGTTTTTCATCGGCATTGCGTCAGACTGTAGCG	
CX-1a	TTTGATAATTAGATACATTTCTTTCAAAG	
CX-1b	TTTCAACTAGAACTGGCTATTATTGTTGCATAAATCAT	
CX-2a	TCGAGCCAAGTATAAAGCCAACGCTGCTTTGGTGCGGAATT	
CX-2b	AGCAAAAGTGAATAATGGAAGTTTTGATGC	
CX-3a	CGAAAGACTTTTATTAATCATGTGAATTATTTAAC	

CX-3b	GCGATTTTTCAAATATCGCGTTTTAATTCGCCAACAGG	
CX-4a	AACGCCTTTTTTTAATGGAAATTACCTG	
CX-4b	TTGAATTACCTTAACAATTGAGAATCGCCATACCTTAT	
CX-5a	CAATCATAACGGAGATTTCAAATTTGGGG	
CX-5b	GCTCATTTGAAAAGGTGGCATTGTTGTATCACGAAAGAC	
CX-6a	GCCTTTACGCCAGTTACAAAATAAGGATTTTGATGATGGC	
CX-6b	GAGTCCACAATATAATCCTGATTATCATT	
CX-7a	GCCTAATTAGTTGGCAAATCAACAGTTGA	
CX-7b	AATATCTGGTCTTTTTAGAGAGAATAACATAAAAGCCCTT	
CX-8a	TCAAATCACCATTCCCAACGAGGGTAGCAACGCGGAAAC	
CX-8b	CCATCGTTTCAATATGATATTCAACCGT	
CX-9a	CGCGAGCTTTAACCAATAGGTTTTCAAC	
CX-9b	AGCATCGGACGCATAACCGATATAACTTTAACTTAAATCA	
CX-10a	AATTCTCTATTAAGAAGCGTTTAGATAGCCAAATAGCA	
CX-10b	AAGACTCCAAGTAAGCTTGGATGGAACAA	
CX-11a	TGGGAAGGGCGTTGAGTGCTCAGTACCAGGCGTTTGGGA	
CX-11b	CCGTCTTATCGGTGCGGGCCGCTTTCCG	
CX-12a	ATTAGATTTGCGTTGCGCTCACTGCCCGCTTAAATGA	
CX-12b	CACATTAATTGCCTCACCAGCTTGAGCCAGATAAGTG	
CX-13a	GCACCGCTTCGCGCTGGCCTTTTGCCAGA	
CX-13b	GAATAGGTCTCAAGAGAAGGATTAATAATTTCCATATTTG	
CX-14a	ATCACCGAGCAAATCACCAGTCCATTATACAGGGCGCA	
CX-14b	TATTGGGCATAAATCAAAGATTTCCCTCA	

**Table 3.2 List of internal docking staples for DNA origami cross-tile.**

Name	Sequence	Notes
LR-I2_M2-8	AAAACAAATGTCGTGCCAGCTGCATTCCAGTCTTACTTGTGA	8 nt M2 dock
LR-J5_M2-8	GCGCCATTAGACCGGAAGCAAAGCTTCAATTACTTGTGA	8 nt M2 dock
LR-I4_M2-8	AGCGAACCAGCCATTCAGGCTGCGCAGGCAAATTACTTGTGA	8 nt M2 dock
LR-J3_M2-8	GGGAAACCATTAATTACATTTAACACATCAAGTACTTGTGA	8 nt M2 dock
UD-I2_M2-8	CTCATCGACTGCTCCATGTTACTTTGTGCGAAATTACTTGTGA	8 nt M2 dock
UD-I3_M2-8	CCAAATAAGCCGCTTTGCGGGATTTGCAAGGTTACTTGTGA	8 nt M2 dock
UD-J4_M2-8	AGTTAAAGGAAACGATTTTTGTTATCCCAATTTACTTGTGA	8 nt M2 dock
UD-J5_M2-8	GTTAGTAACGCAATAATAACGGAAAAGGAACTTACTTGTGA	8 nt M2 dock
UD-I4	CGAGGAAAATGAATTTCTGTATGTTCCAGAC	
UD-J3	TCCGCGACGAACAAGCAAGCCGTTGTACCACA	

**Table 3.3 List of edge staples for DNA origami cross-tile.**

Name	Sequence	Notes
P-U1	GTGTCGTAGACACGTGATAAATAAGGCCTTTGAAATACCGACCGTGTGTCGTAGACAC	Hairpin passivation
P-U2	GTGTCGTAGACACGTTTATCAACAATAGAAATGCAGAACGCGCCTGTGTCGTAGACAC	Hairpin passivation
P-U3	GTGTCGTAGACACGCCTTAAATCAAGATTTGCGGGAGGTTTTGAAGTGTGTCGTAGACAC	Hairpin passivation
P-U4	GTGTCGTAGACACGAGAGATAACCCACAATTGAGCGCTAATATCAGTGTGTCGTAGACAC	Hairpin passivation
P-U5	GTGTCGTAGACACTGTCACAATCAATAGACGGAATAAGTTTATTTGTGTCGTAGACAC	Hairpin passivation
P-D2	GTGTCGTAGACACCAAGAACCGGATATTCTCAAGAGTAATCTTGAGTGTGTCGTAGACAC	Hairpin passivation
P-D3	GTGTCGTAGACACGAGGACCAACCTAATACGTAATGCCACTACGTGTGTCGTAGACAC	Hairpin passivation
P-D4	GTGTCGTAGACACTTAATTTGATCGGTTTGCTCCAAAAGGAGCCTGTGTCGTAGACAC	Hairpin passivation
P-D5	GTGTCGTAGACACTAGCAAGCCAATAGGCCCTCATTTTCAGGGAGTGTGTCGTAGACAC	Hairpin passivation
P-D6	GTGTCGTAGACACCTTGAGTAACAGTGCCTTAACGGGGTCAGTGCGTGTGTCGTAGACAC	Hairpin passivation
P-L2	GTGTCGTAGACACAGTACCTTTTACATCGATGAATATACAGTAACGTGTGTCGTAGACAC	Hairpin passivation
P-L3	GTGTCGTAGACACGATAGCTTAGATTAAGTCCTTGAAAACATAGCGTGTGTCGTAGACAC	Hairpin passivation
P-L4	GTGTCGTAGACACAACGAGAATGACCATAATTAACAGTTCAGAAGTGTGTCGTAGACAC	Hairpin passivation
P-L5	GTGTCGTAGACACAAAGTACGGTGTCTGGTTTTAAATATGCAACTGTGTCGTAGACAC	Hairpin passivation
P-L6	GTGTCGTAGACACTGTAATACTTTTTCGCGAAAACATTATGACCCGTGTGTCGTAGACAC	Hairpin passivation
P-R1	GTGTCGTAGACACCCGATTTAGAGCTTGAACCTTAAAGGGAGCCGTGTGTCGTAGACAC	Hairpin passivation
P-R2	GTGTCGTAGACACAGCAAGCGGTCCACGCGCCTGAGAGAGTTGCGTGTGTCGTAGACAC	Hairpin passivation
P-R3	GTGTCGTAGACACCTGTGTGAAATGTTATGGTCATAGCTGTTTCGTGTCGTAGACAC	Hairpin passivation
P-R4	GTGTCGTAGACACCGACGCCAGTGCCAAACACGACGTTGTAAGTGTGTCGTAGACAC	Hairpin passivation
P-R5	GTGTCGTAGACACTCACGTTGGTGTAGATACCGTAATGGGATAGGGTGTGTCGTAGACAC	Hairpin passivation
P-U5_M1-7	GTGTCGTAGACACTGTCACAATCAATAGACGGAATAAGTTTATTTGTATACATCA	7 nt M1 dock
P-U6_M1-7	GTGTCGTAGACACCGTTTTTCATCGGCATTGCGTCAGACTGTAGCGGTATACATCA	7 nt M1 dock
P-U6_M1-8	GTGTCGTAGACACCGTTTTTCATCGGCATTGCGTCAGACTGTAGCGTTATACATCT	8 nt M1 dock
P-D1_M1-7	GTGTCGTAGACACAACCTAATGAGATACATAGGAATACCACATTCGTATACATCA	7 nt M1 dock
P-D1_M1-8	GTGTCGTAGACACAACCTAATGAGATACATAGGAATACCACATTCATACATCT	8 nt M1 dock
P-D2_M1-7	GTGTCGTAGACACCAAGAACCGGATATTCTCAAGAGTAATCTTGAGTATACATCA	7 nt M1 dock
P-L1_M1-7	GTGTCGTAGACACGACAACCTCGTATTAACCTTTACAAAACATTCGTATACATCA	7 nt M1 dock
P-L1_M1-8	GTGTCGTAGACACGACAACCTCGTATTAACCTTTACAAAACATTCATACATCT	8 nt M1 dock
P-L2_M1-7	GTGTCGTAGACACAGTACCTTTTACATCGATGAATATACAGTAACGTATACATCA	7 nt M1 dock
P-R5_M1-7	GTGTCGTAGACACTCACGTTGGTGTAGATACCGTAATGGGATAGGGTATACATCA	7 nt M1 dock
P-R6_M1-7	GTGTCGTAGACACACTAGCATGTCAATCAGAACGGTAATCGTAAAGTATACATCA	7 nt M1 dock
P-R6_M1-8	GTGTCGTAGACACACTAGCATGTCAATCAGAACGGTAATCGTAAATATACATCT	8 nt M1 dock

**Table 3.4 List of modified oligomers for imaging and filtration.**

Name	Sequence	Notes
M1'	CTAGATGTAT/Cy3b/	Imager for dock M1
M2'	ACTCACAAGT/Cy3b/	Imager for dock M2
M3'	AGGATACCTT/Cy3b/	Imager for dock M3
Ac-5T-M1' -7	/5Acryd/TTTTTAGATGTAT	Acrydite-labelled, 7 nt M1'
47pT-M1' -8	TTAGATGTAT	Duplexing strand, 8 nt M1'

**Table 3.5 Thermocycler recipe for DNA origami synthesis.**

Step	Initial temp.	Cycles	$\Delta T$ / Cycle	Time / Cycle
#	(°C)	#	(°C)	(min)
1	70	1	0	15
2	70	50	-0.1	0.75
3	65	50	-0.1	0.75
4	60	50	-0.1	0.75
5	55	50	-0.1	2
6	50	50	-0.1	2
7	45	50	-0.1	2
8	40	50	-0.1	1.5
9	35	50	-0.1	1.5
10	30	20	-0.5	0.5
11	20	1	0	Hold

### 3.5.5 References

- 1 Ovesny, M. Computational methods in single molecule localization microscopy, Charles University in Prague, (2016).
- 2 ImageJ (U.S. National Institute of Health, Bethesda, Maryland, USA, 1997-2019).
- 3 Nečas, D. & Klapetek, P. Gwyddion: an open-source software for SPM data analysis. *Open Physics* **10**, doi:10.2478/s11534-011-0096-2 (2012).
- 4 Rehman, F. N. *et al.* Immobilization of acrylamide-modified oligonucleotides by co-polymerization. *Nucleic Acids Res.* **27**, 649-655 (1999).
- 5 Scheible, M. B., Pardatscher, G., Kuzyk, A. & Simmel, F. C. Single molecule characterization of DNA binding and strand displacement reactions on lithographic DNA origami microarrays. *Nano Lett.* **14**, 1627-1633, doi:10.1021/nl500092j (2014).
- 6 Douglas, S. M. *et al.* Rapid prototyping of 3D DNA-origami shapes with caDNAno. *Nucleic Acids Res.* **37**, 5001-5006, doi:10.1093/nar/gkp436 (2009).
- 7 Liu, W., Zhong, H., Wang, R. & Seeman, N. C. Crystalline two-dimensional DNA-origami arrays. *Angew. Chem. Int. Ed. Engl.* **50**, 264-267, doi:10.1002/anie.201005911 (2011).
- 8 Aghebat Rafat, A., Pirzer, T., Scheible, M. B., Kostina, A. & Simmel, F. C. Surface-assisted large-scale ordering of DNA origami tiles. *Angew. Chem. Int. Ed. Engl.* **53**, 7665-7668, doi:10.1002/anie.201403965 (2014).
- 9 Aebi, U. & Pollard, T. D. A glow discharge unit to render electron microscope grids and other surfaces hydrophilic. *J Electron Microsc Tech* **7**, 29-33, doi:10.1002/jemt.1060070104 (1987).
- 10 Bruker Dimension Icon/FastScan Bio help files.
- 11 Blumhardt, P. *et al.* Photo-Induced Depletion of Binding Sites in DNA-PAINT Microscopy. *Molecules* **23**, doi:10.3390/molecules23123165 (2018).

## CHAPTER FOUR: SUMMARY AND FUTURE WORK

In conclusion, two techniques for nanoscale quantitative characterization of DNA origami have been developed and applied to study defects in DNA origami: (1) embedded structural and defect metrology for hierarchical assembly of DNA origami into arrays, enabling visualization of the spatial arrangement of origami within arrays, internal array defects, and grain boundaries between arrays, and (2) correlative DNA-PAINT/AFM for high-resolution optical and topographical imaging of DNA origami, providing information on both the structure and activity of individual sites on DNA origami. Both studies have addressed needs that are critical to the integration of DNA nanotechnology in high volume manufacturing. In addition, correlative imaging provided key insights into the nature of addressable site defects on DNA origami and identified potential routes to overcome the current limits of addressable site yield.

The key developments and insights attained from the studies of DNA arrays with embedded defect metrology are listed below (Chapter 2):

1. Introduced a versatile optical metrology technique for stepwise, selective characterization of DNA arrays by means of DNA-PAINT and state-dependent docking sites. The demonstrated technique provides an approach for large area, inline, defect detection and classification for DNA arrays with the statistical analysis relevant for high volume manufacturing.
2. Revealed grain boundaries between tile arrays and the periodic structure of tiles within arrays, enabling reconstruction of arrays observed in Xtal-PAINT images. Reconstruction was performed on a polycrystalline tile array that was

found to consist of approximately 81 tiles in three arrays, or ‘grains’, separated by low-angle grain boundaries.

3. Demonstrated the ability to image and quantitatively analyze tile arrays and gain insight critical to improving array formation. Point correlation methods were employed to characterize the size and crystallinity of arrays within large array DNA-PAINT images.
4. Monte Carlo simulations were employed to approximate the radial distribution function for unique, finite tile arrays, enabling determination of array yield through linear decomposition of experimental spectra into the component spectra determined through simulations.
5. Studies of the dependence of array defects on thermal annealing temperature identified an inverse relationship between quality and yield in tile arrays, where the quality of arrays increased with temperature.

While this work demonstrated techniques for quantitative characterization of DNA arrays, Xtal-PAINT alone does not provide a means to directly identify the cause of defects in tile arrays. In addition, the method does not facilitate investigations into the nature of single-site defects observed in DNA-PAINT images. To expand on the capabilities of DNA-PAINT-based characterization techniques, methods to combine DNA-PAINT with high-resolution AFM were developed and employed to study single-site defects in DNA origami. The fundamental developments and insights realized through the investigations of single-site defects with correlative DNA-PAINT/AFM are listed below (Chapter 3):

1. Developed a simple and flexible method to selectively bind DNA origami, and not single-stranded DNA, directly to coverglass, providing a substrate that is

simultaneously compatible with DNA-PAINT and high-resolution AFM. High-resolution AFM images were demonstrated in which the ‘weave’ of double-stranded DNA in DNA origami cross-tiles could be observed with resolution of approximately 1 nm. In addition, a significant decrease in background noise was observed for DNA-PAINT imaging relative to that achieved by protein-binding.

2. High-resolution, correlative microscopy was performed to characterize DNA origami cross-tiles. Spatial correlation in super-resolution optical and topographic images of  $5 \pm 3$  nm was achieved, in close agreement with the localization uncertainty of super-resolution images ( $6 \pm 2$  nm). This result suggested that DNA origami are fixed on the surface during imaging, validating correlative imaging for studies of single-site defects in DNA origami.
3. Analytical methods and neural pattern recognition tools were employed to quantify the progress of DNA-PAINT imaging and the detection efficiency of individual docking sites on DNA origami during DNA-PAINT imaging. The results revealed that approximately 99% completion could be achieved in one hour of imaging, ensuring that the majority of unresolved sites do not result from insufficient imaging time.
4. Quantified the sensitivity of AFM to unincorporated strand defects by synthesizing and imaging DNA origami with intentionally unincorporated sites. Within the images, all unincorporated sites were successfully detected,

demonstrating that unincorporated sites could be reliably detected in AFM images acquired under similar imaging conditions.

5. Correlative defect metrology was employed on DNA origami cross-tiles, and docking sites were examined in DNA-PAINT and AFM images for correlation of defects. Investigations showed little correlation of unresolved DNA-PAINT sites to structural defects on DNA origami ( $13 \pm 3\%$ ), revealing that most unresolved site defects occur on strands that are present in the structure, contrary to prior reports.
6. Observed structural defects more often at successfully resolved DNA-PAINT sites than at unresolved sites. In combination with reports in the literature, namely of photo-oxidative damage incurred during DNA-PAINT and reduced stability of DNA origami due to staple aging, the results suggest that the structural stability of DNA origami was decreased during DNA-PAINT imaging.
7. Developed and employed two techniques for docking-site-targeted PAGE purification of docking site strands. DNA origami cross-tiles were synthesized with docking sites purified by each technique in addition to PAGE-purified and unfiltered docking site strands for comparison. The docking site detection efficiency increased from 82% for unfiltered sites to 87% for strands purified with sequence-targeted methods. Given that the maximum detection efficiency achieved was 87%, despite over 98% incorporation, the results suggest that other mechanisms, yet to be identified, likely contribute to inaccessible sites.

Overall, the presented work demonstrated the development and application of advanced characterization techniques for DNA nanostructures, which will accelerate fundamental research and applications of DNA nanotechnology. The flexibility of the techniques reported here facilitate many applications in future studies, and several directions that could be pursued are listed below:

1. Inline optical and topographic characterization of nanophotonic devices templated by DNA origami. Prior studies of photonic and plasmonic structures required deposition on mica to enable optical and topographic imaging, a method that is not conducive to DNA-PAINT imaging. Instead, such structures could be deposited on hydroxylated coverglass and characterized with DNA-PAINT and AFM prior to the addition and characterization of the optically-active components on the DNA origami.
2. Simultaneous correlative DNA-PAINT/AFM performed using a microscope capable of both optical and topographic imaging. A setup in which the optical field of view and AFM tip could be aligned for simultaneous imaging would significantly reduce the difficulty of registration of optical and topographic images, the biggest challenge encountered during the studies in Chapter 3.
3. Masked hydroxylation of coverglass for selective deposition of active DNA origami. Glow discharge, UV, and ozone exposure were all found to sufficiently hydroxylate the coverglass surface and enable DNA-PAINT imaging. The pH-dependent binding of DNA origami to hydroxylated coverglass could be utilized to selectively passivate areas of the coverglass prior to DNA origami deposition. For example, inactive ‘masking’ DNA

origami could be deposited in acidic buffer conditions, preventing adsorption to the hydroxylated surface but enabling adsorption elsewhere. Active DNA origami could then be deposited in basic buffer conditions to enable adsorption to the hydroxylated surface.

4. State-dependent indexing for nucleic acid memory on DNA origami arrays. For 1D or 2D arrays of unique origami spatially encoded with docking sites, sticky-ends could be modified to serve as docking sites with unique edge locations such that a break in a 1D or 2D array could be identified by the index displayed. Such indexing would increase the data storage density on individual origami.